Essential role of *Plasmodium* Topoisomerase III & its unique charged domain

A Thesis Submitted to the University of Hyderabad for the award of a Ph.D. degree in the Department of Biotechnology and Bioinformatics
School of Life Sciences

SHEPHALI BANSOD
(14LTPM01)

Under the Supervision of
Dr. Sunanda Bhattacharyya

Department of Biotechnology and Bioinformatics

School of Life Sciences
University of Hyderabad
Hyderabad-500046
Telangana, India

April-2021

University of Hyderabad
School of Life Sciences
Department of Biotechnology and Bioinformatics

DECLARATION

I, **Shephali Bansod**, hereby declare that this thesis entitled **"Essential role of *Plasmodium* Topoisomerase III & its unique charged domain"** submitted by me under the guidance and supervision of **Dr. Sunanda Bhattacharyya**, is an original and independent research work. I also declare that it has not been submitted previously in part or in full to this University or any other University or Institution for the award of any degree or diploma

Signature of the Student
Shephali Bansod (14LTPM01)

Signature of the Supervisor
Dr. Sunanda Bhattacharyya
Dr. Sunanda Bhattacharyya
LECTURER
Dept. of Biotechnology
School of Life Sciences
University of Hyderabad
Gachibowli, Hyd-500 046, India

Date 30 - 04 - 2021

University of Hyderabad
School of Life Sciences
Department of Biotechnology and Bioinformatics

CERTIFICATE

This is to certify that this thesis entitled **"Essential role of *Plasmodium* Topoisomerase III & its unique charged domain"** submitted by **Ms. Shephali Bansod** bearing registration number **14LTPM01** for award of Doctor of Philosophy in the Department of Biotechnology and Bioinformatics, School of Life Sciences, is a bonafide work carried out by her under my supervision and guidance.

This thesis is free from plagiarism and has not been submitted previously in part or in full to this or any other University or Institution for award of any degree or diploma.

Parts of this thesis have been:

A. Published in the following journal:

- **Shephali Bansod**, Navneet Bung, Priyanka Singh, Niranjan Suthram, Himashree Choudhary, Arijit Roy, Gopalakrishnan Bulusu, and Sunanda Bhattacharyya. Elucidation of an essential function of the unique charged domain of *Plasmodium* topoisomerase III. **Biochemical Journal 2020** doi: 10.1042/BCJ20200318

- **Shephali Bansod**, Navya Raj, Amjesh R, Achuthsankar S Nair, and Sunanda Bhattacharyya. Molecular docking and molecular dynamics simulation identify a novel Radicicol derivative that predicts exclusive binding to *Plasmodium falciparum*. **J Biomolecular Structure and Dynamics** 2021 doi: 10.1080/07391102.2021.1891970.

B. Presented in the following conferences:

a) Shephali Bansod and **Sunanda Bhattacharyya**. Quest to find a small molecule inhibitor targeting PfTopoVIB. Bioquest 2017. Oral presentation, held at the University of Hyderabad, Hyderabad, India.

b) Shephali Bansod and **Sunanda Bhattacharyya.** Radicicol derivatives showing selective
binding towards *Plasmodium falciparum* Topoisomerase VIB but not to PfHsp90. International conference on innovation in pharma and biopharma industry (ICIPBI), UoH 2017, held at University of Hyderabad, Hyderabad, India.

c)Shephali Bansod and **Sunanda Bhattacharyya.** Identification of unique charged amino acid rich residues essential for *Plasmodium falciparum* topoisomerase III activity. International Symposium on Malaria Biology & 29th National Congress of Parasitology on Basic and Applied Aspects (ISMBNCP-2018) 2018. Abstract No. 44, held at

University of Hyderabad, Hyderabad, India.

Further, the student has passed the following courses towards fulfilment of coursework requirement for the PhD

Course code	Name	Credits	Pass/Fail
BC 801	Research Methodology/Analytical Techniques	4	Passed
BC 802	Research ethics, biosafety, data analysis and biostatistics	4	Passed
BC 803	Research Proposal and scientific writing	4	Passed

Supervisor
Dr. Sunanda Bhattacharyya
LECTURER
Dept. of Biotechnology
School of Life Sciences
University of Hyderabad
Gachibowli, Hyd-500 046. India

Head 30/4/21
Department of Biotechnology
and Bioinformatics

HEAD
Dept. of Biotechnology & Bioinformatics
University of Hyderabad
Hyderabad.

Dean
School Life Sciences

DEAN
School of Life Sciences
University of Hyderabad
Hyderabad - 500 046.

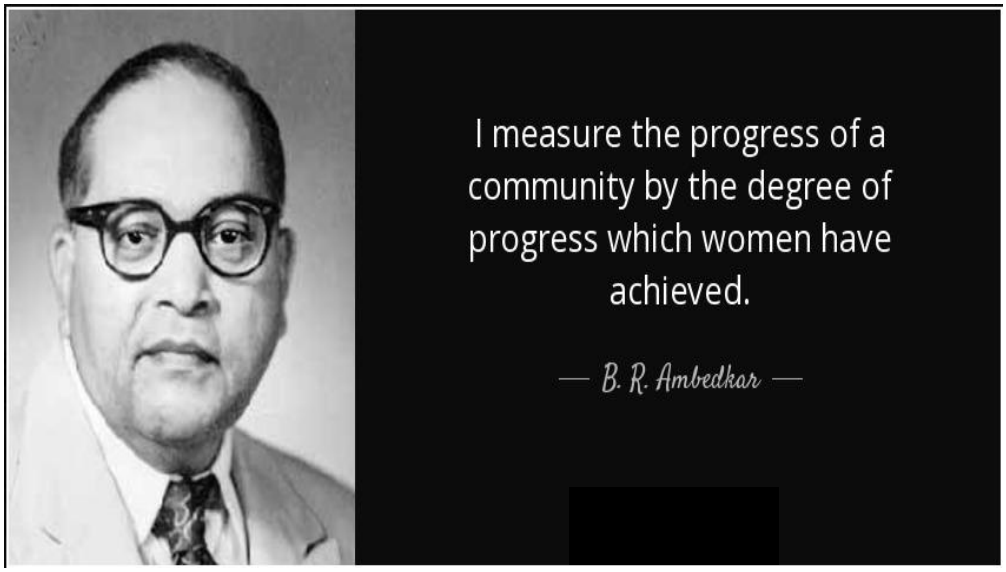

Dedicated to Dr. Babasaheb Ambedkar

ACKNOWLEDGEMENTS

I want to take this opportunity to thank all those people who made this thesis possible.

First and foremost, I would like to gracefully acknowledge my thesis advisor, **Dr. Sunanda Bhattacharyya,** for giving me the chance to work with her. I thank her sincerely for her excellent scientific guidance and valuable suggestions during this work.

I'm grateful to **Prof. Mrinal Kanti Bhattacharyya** for data interpretation in research work and for extending his lab facilities. I am also thankful for his critical inputs and for providing beneficial suggestions during lab meetings.

I wish to express my sincere thanks to my doctoral committee members, **Prof. Arun Kumar** and **Prof. Mrinal Kanti Bhattacharyya,** for their valuable suggestions during my project presentations.

I thank the Head of Biotechnology and Bioinformatics department, **Prof. K.P.M.S.V. Padmasree**, and the former heads **Prof. Niyaz Ahmed, and Prof. Anand Kondapi,** for allowing me to use all the research facilities.

I thank the Dean of School of Life Sciences, **Prof. S Dayananda**, and the former Deans, **Prof. P Reddanna,** and **Prof. KVA Ramaiah,** for providing all the research facilities.

I thank **Dr. Navya Raj, Dr. Amjesh R, Dr. Achuthsankar S. Nair**, Department of Computational Biology, Kerala, and **Dr. Navneet Bung**, **Dr. Gopalakrishnan Bulusu**, **Dr. Arijit Roy**, TCS innovation labs for helping me with *in silico* analysis.

I thank all the teaching and non-teaching staff members of the School of Life Sciences for their help and support.

I thank **CSIR** for all its financial support for five years of my research.

I thank funding agencies **DBT**, **DST-SERB**, **CSIR**, **DST-FIST**, and **UGC-SAP** for the financial assistance to the lab.

I thank **DST-FIST**, **DBT-CREBB, UGC-SAP, DST-PURSE** for funding to school and departments towards common facilities that aided my research work.

I thank my lab mates **Dr. Niranjan, Dr. Suresh**, **Dr. Nidhi**, **Dr. Tanvi, Dr. Nabi**, **Dr. Vydyam Pratap**, **Dr. Purna Chandra**, **Wahida**, **Payal**, **Abhilasha**, **Tanishka**, **Nupur**, **Priyanka**, and **Khushboo** for their timely help, support, and I thank them for keeping the lively environment in the lab.

I thank all the previous and present **M.Sc. Project students** from the lab of Dr. Sunanda Bhattacharyya and Prof. Mrinal Kanti Bhattacharyya for their help and co-operation.

I thank our lab attender Mr. Ramesh, for his help in the lab.

I'm grateful to all my **friends Siddharth, Niranjan, Poorvaja, Deeksha and Sushree** for scientific discussions, suggestions, and fun chats in the corridors.

I thank the Health Center staff, the University of Hyderabad, for helping me whenever needed.

I'm immensely grateful to my family for their invaluable support and encouragement, without which I could not have completed my Ph.D. My parents and my sisters have been a great source of constant motivation during my Ph.D.

Finally, I would like to thank **Dr. Babasaheb Ambedkar** for giving me the strength, knowledge, ability, and opportunity to undertake this research study and persevere and complete it satisfactorily.

Shefphali Prashant Bansod

CONTENTS

CHAPTER 3: FUNCTIONAL CHARACTERIZATION OF PfTopoIII AND ITS UNIQUE CHARGED DOMAIN

List of tables:

ABBREVATIONS

Ade	Adenine
AM1-BCC	Atomic charges1-bond charge corrections
BLASTP	Basic Local Alignment Search Tool - Protein
CGenFF	CHARMM General Force Field
CHARMM36 FF	CHARMM36 additive force field
CHARMM36	Chemistry at Harvard Macromolecular Mechanics 36
DEPC	Diethylpyrocarbonate
DMSO	Dimethyl sulfoxide
DNase	Deoxyribonuclease
DS	Discovery Studio
DSB	Double Strand Break
dsDNA	Double stranded DNA
DTT	Dithiothreitol
gDNA	Genomic DNA
EDTA	Ethylene diamine tetra acetic acid
farPPI	Fast Amber Rescoring for Protein-Protein Interacting Inhibitors
ff14SB	Force field 14 Stony Brook
GAFF2	General AMBER Force Field
GPU	Graphics processing unit

GROMOS	GROningenMOlecular Simulation
GSK299423	GlaxoSmithKline 299423
HR	Homologous Recombination
His	Histidine
IC_{50}	Half maximal inhibitory concentration
IPTG	IsoPropyl-β-D-1-Thio Galacto-pyranoside
iRBC	Infected Red blood cell
IUPAC	International Union of Pure and Applied Chemistry
kDa	Kilo Dalton
Leu	Leucine
MMS	Methyl methanesulfonate
Mg	Milligram
mM	Millimolar
min	Minutes
ml	Milliliter
mV	Milli Volt
nM	Nanomolar
NPT ensembles	moles (N), pressure (P) and temperature (T)
OD	Optical Density
PAGE	Poly-acrylamide gel electrophoresis

PCIA	Phenol chloroform isoamyl alcohol
PDB	Protein Data Bank
PEG	Polyethylene glycol
PMSF	Phenyl-methyl-sulfonyl-fluoride
PY	Pyrimethamine
RMSD	Root-Mean-Square Deviation
RNA	Ribonucleic acid
RNase	Ribonuclease
ROS	Reactive Oxygen Species
Rpm	Rotations per minute
RPMI	Roswell park memorial institute medium
SAVES	Structural Analysis and Verification Server
SAR	Structure-Activity Relationship
SC	Synthetic complete
SDS	Sodium Dodecyl Sulfate
SMTL	Swiss-Model Template Library
SDSA	Synthesis Dependent Strand Annealing
SSA	Single Strand Annealing
ssDNA	Salmon sperm DNA
TIP3P	Transferable intermolecular potential with 3 points

UniProtKB	Universal Protein Knowledgebase
UCLA-DOE	University of California, Los Angeles-Department of Energy
WHO	World health organization
WT	Wild Type
XRCC4	X-Ray Cross complementing factor 4
YNB	Yeast nitrogen base
YPD	Yeast extract, peptone, dextrose
µF	Micro Faraday
µg	Microgram
µl	Microliter
µm	Micrometer
µM	Micromolar
Ura	Uracil

CHAPTER-1

INTRODUCTION

Malaria is one of the most dangerous diseases caused by the *Plasmodium* species transmitted to people through the bites of infected female Anopheles mosquitoes referred to as 'malaria vectors.' The five known species inflicting human malaria are *P. vivax, P. falciparum, P. ovale, P. malariae*, and *P. knowlesi*, out of which *P. falciparum* and *P. vivax* are the most dangerous ones. In the 20th century alone, malaria claimed between 150 million and 300 million lives, accounting for 2 to 5 percent of all deaths (1). Although its chief sufferers today are the poverty-stricken places of sub-Saharan Africa, Asia, the Amazon basin, and other tropical regions, 40 percent of the world's population still lives in areas where malaria is transmitted. In 2018, there were an estimated 228 million malaria cases and 405 000 malaria deaths. Pregnant women and children below age of five are the most affected group. In 2018 alone, they accounted for 67% (272 000) of all malaria deaths worldwide (2).

1.1. History of Malaria

Malaria has a long history. In Indian writings malaria was called as 'king of diseases' during Vedic period (1500 to 800 BC) (3). Europe's history marked a turning point when malaria first arrived in Rome during the first century AD. A large group of historians suspect that fall of Rome was because of the deadliest *P. falciparum* malaria species. In South Asian countries like India and China, population growth and humid temperature favoured malaria growth (4).

1.2. Breakthroughs in malaria research

Malaria was named after Roman fever which means "bad air". Due to three species involvement like, *P. falciparum*, female Anopheles mosquitos and humans, it took years to understand the complex physiology of malaria.

1.2.1. Discovery of Malaria Parasite

Malaria parasite was discovered by Charles Laveran a French army doctor. He saw a crescent-shaped bodies nearly transparent except for a tiny dot of pigment as a parasite. He examined blood specimens from 192 malaria patients and saw pigment-containing crescents in 148 sufferers (5). Laveran distinguished four well-defined shapes in infected human samples. Those were the female and male gametocyte, schizont, and trophozoite stages. Later he received the Nobel Prize for discovering the single-celled protozoan that caused malaria.

1.1.2. Discovery of Malaria's Mosquito Stages

The first evidence of malaria parasites were the preserved mosquitos found from the Palaeogene period (30 million years ago) (6). Ronald Ross of the British Indian Medical Services discovered Anopheles mosquitos as a vector for malaria. Ross designed experiments using *P. relictum*, the malaria parasite of sparrows and crows, where he identified sporozoites in the salivary glands of mosquitoes. He later infected 21 of 28 fresh sparrows through these mosquitoes (7). In 1902, Ross received the Nobel Prize for discovering the mosquito stages of malaria.

1.2.3. Discovery of the Parasite in Human Tissue

Even after understanding the malaria parasite and its mosquito stage infection, the major question was to understand; where sporozoites develop in human hosts? Years later, in 1948, malaria parasites were detected in the infected liver of rhesus monkeys (7). Later similar stages were found in liver of humans volunteers infected with *P. vivax* and *P. falciparum* (7).

1.3. The life cycle of the *Plasmodium* parasite

The life cycle of the *Plasmodium* parasite is extraordinarily complex and is mainly conserved across its lineage. They require many specialized proteins for intracellular and extracellular survival in both invertebrate and vertebrate host environments. Asexual reproduction occurs in humans, also known as an intermediate host, and obligatory sexual reproduction occurs in a mosquito called the definitive host.

The parasite's life cycle starts when an infected female Anopheles mosquito takes a blood meal and thereby injects sporozoites into the skin, which is the starting point of infection (Figure 1). After surpassing the host immune and lymphatic system, sporozoites enter the hepatocytes to undergo exoerythrocytic schizogony or endoreduplication to form merozoites, which are the invasive stage of erythrocytes (8). Endoreduplication is defined as replication of the nuclear genome in the absence of mitosis for extreme population growth within a brief span, which is critical for their continued transmission and pathogenesis in the host (9). These merozoites invade other red blood cells (RBCs) to produce three distinct developmental stages rings, trophozoite, and schizont (Figure 1). The second round of endoreduplication takes place at the schizont stage called erythrocytic schizogony. This asexual replication cycle produces up to 32 nuclei cells (segmenters), which eventually burst out to produce many merozoites. Through repeated rounds of invasion and growth, these merozoites establish acute and chronic infections. In species such as *P. vivax* and *P. ovale*, merozoites do not form schizonts; instead, they enter a latency period by forming a non-replicating hypnozoite. These hypnozoites lead to relapses which ultimately help parasite's survival for longer period of time (10).

Plasmodium completes its life cycle only when few asexual parasites undergo a series of changes that generate a sexually competent parasite. This maturation is termed gametocytogenesis. Gametocytogenesis produces male and female gametocytes, the only transmission stage from the human to the mosquito. These gametocytes travel to the mosquito's midgut and undergo maturation. The male gamete divides rapidly (nuclear division) and differentiates into eight motile flagellated microgametes through exflagellation (11), whereas the female gamete matures to become enlarged and spherical macrogamete. Later both forms fertilize and produce zygote which is diploid in nature., which further develops into an ookinete (Figure 1). The motile ookinete crosses the midgut epithelium and settles in basal lamina to produce immotile oocyst. The last process of endoreduplication takes place at this stage where they undergo meiosis to produce thousands of haploid daughter cells referred to as sporozoites (12). These immature sporozoites moves to the salivary glands of mosquito and settle there in order to infect other humans.

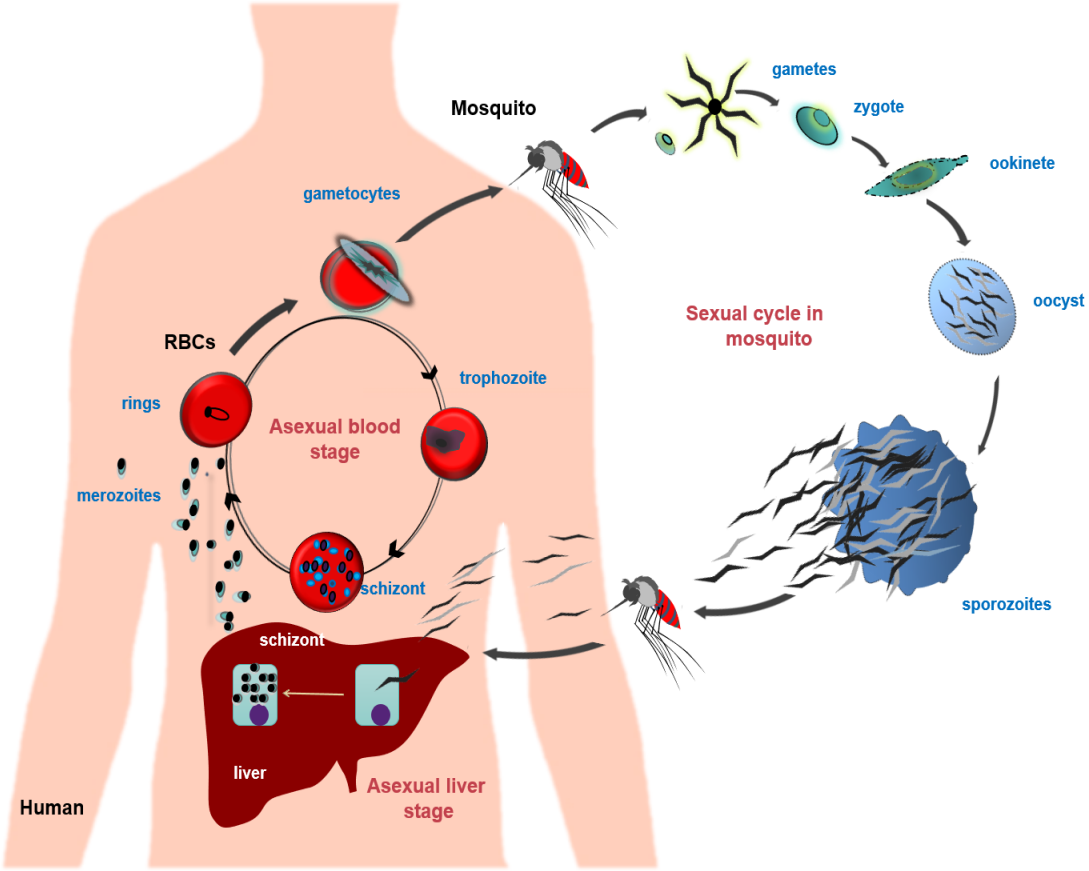

Figure 1: Life cycle of *Plasmodium falciparum*

1.4. Challenges in the malaria control strategy

Already a century has passed, knowing *Plasmodium falciparum* as the causative agent of malaria, but it still exists and threatens the global efforts for its control and elimination. The following are the main reasons why malaria continues to kill thousands and infects millions.

1.4.1. Drug resistance

Anti-malarial drug resistance is a massive blow to the ongoing control programs to curb this deadly disease. During the 1950s and 1960s, chloroquine and sulfadoxine-pyrimethamine (SP) were the first among all to get resistant against malaria (2). Artemisinin-based combination therapies (ACTs) introduced in the year 1994 are still in use to treat malaria. There are five types of WHO adopted ACTs, namely: artesunate-amodiaquine (ASAQ), artemether-lumefantrine (AL), artesunate-sulfadoxine pyrimethamine (ASSP), dihydro-artemisinin piperaquine (DP), and artesunate-mefloquine (ASMQ) (13). Recent reports suggest that resistance has emerged to all the five types of ACTs, and hence there is an immediate need to develop a novel drug target to treat malaria (14). Two main mechanisms through which *Plasmodium* derives its resistance to any anti-malarial drugs. The first one is mutation in the transporter gene (*Pfcrt* in case of chloroquine resistance) or increase in number of transporter gene copies (*pfmdr1* copy number in mefloquine resistance). This increases the capacity of parasite to efflux the drug away from the site of action The second one is the mutation in the parasite target gene, examples are *dhfr* and *dhps* in sulfadoxine-pyrimethamine resistance and mutation in *cytochrome b* gene that occurs in atovaquone resistance.

1.4.2. Antigenic variations

Antigenic variation is a mechanism through which an infectious organism alters its immunogenic epitopes to bypass the antibody response from the host immune system. Parasites utilize antigenic variation to increase the successful transmission of infection. This primary antigen is expressed on the surface of infected red blood cells (RBCs) by a set of a gene family called the var gene (15). There are 45-90 var genes in the natural isolates of *P. falciparum* which efficiently changes their surface antigens by expressing a different set of var genes (16,17). Erythrocyte membrane protein one (PfEmp1) is an example of one such highly variable protein. These proteins have a variable number of functional domains that adhere to the host endothelium, thereby allowing the parasites to avoid systemic circulation and clearance by the spleen. So far, researchers have understood that malaria parasites have evolved lots of strategies to escape the host immune system.

1.4.3. The economic and social burden of malaria

Where malaria prospers the most, human societies have prospered the least (18). Malaria's economic and social burden is so huge that it shadows all the measures taken on the right path to control it. The African region disappoints the most by sharing a high global malaria burden. In 2018, Africa had 93% of total malaria cases and 94% of malarial mortalities (2). Malaria has been forced to degrade economic costs beyond the direct medical cost and the persistent income of an individual. Nevertheless, its epidemic nature has made countries suffer a loss of trade, tourism, migration, and foreign investments.

In India, during 1964, malaria cases have significantly declined to just 100,000. However, the following decade experienced a comeback by 1976, where malaria

flourished again to touch the 6.4 million mark. Since then, India is experiencing a gradual rise in malaria cases every year(19).

1.4.4. Failure of Vector control strategies and Global warming

Vector control refers to the measures taken against mosquitoes to limit their ability of disease transfer. In the 1950s and 1960s, dichlorodiphenyltrichloroethane (DDT) was effective against malaria eradication [10]. Although later, it was discontinued due to its serious health hazards. Currently, malaria management programs widely rely on indoor residual spraying (IRS) and long-lasting insecticidal nets (LLIN). But still, almost 91 countries are epidemic for malaria [6], and millions suffer from its disease burden. Many scientists believe a direct correlation between temperature rise and the survival of both *Plasmodium* parasites and mosquitoes (20). For the optimal breeding of Anopheles mosquitoes, the temperatures should be around 20 to 30 degrees centigrade. They also require high humidity, small stagnant pools of water, and food availability (20). Recent reports suggest an increase in malaria incidence has occurred in East African highlands, some Asian and South American countries due to global warming (21). Hence, it is likely that global warming will result in malaria spread even in those areas where previously it did not exist.

1.5. Current scenario

Malaria has continued to be a dreadful disease for ages. The main reasons are resistance to anti-malarial drugs, uncontrolled breeding of mosquitoes, lack of awareness in developing countries, and environmental changes. In the current scenario, the only approved vaccine against malaria is RTS SA/AS018, which is

against the circumsporozoite protein but has a low efficacy rate of only 39% (22). In the mid-nineties, the world saw sulfadoxine, pyrimethamine, and chloroquine failing at their end (23). So, Artemisinin-based combination therapies (ACTs) became the frontline treatment against malaria. But unfortunately, drug resistance to artemisinin and its derivatives had emerged in many pockets of the world (23).

This alarming situation highlights the need for constant basic research related to the essential biological pathways of *P. falciparum* to identify areas of vulnerability in the parasite. For instance, targeting asexual replication may lead to disruption of the parasite's life cycle. Similarly, targeting proteins required for gametogenesis will also lead to non-compatible gamete formation (Transmission blockage strategy) (24). Once a new target is found and validated, the next job is to generate new therapeutics that target the parasite proteins uniquely. Replication proteins such as DNA polymerase, ORC1 (25), and topoisomerases (26,27) are essential for parasites' survival.

Topoisomerases are one of the essential class of protein that govern many DNA metabolic processes. They perform multifaceted roles and are required during replication, transcription, recombination, chromatin segregation, and meiosis. They have proved to be a vital lead to generate anti-cancer compounds, for example, doxorubicin, camptothecin (28,29), and anti-bacterial drugs like quinolones and ciprofloxacin (30,31). Topoisomerase inhibitors work by two mechanisms (Figure 2); firstly, they target the ATP binding site of the enzyme, thereby inhibiting ATP hydrolysis; examples are Novobiocin and Radicicol. Secondly, they form a ternary complex with the enzyme and DNA, thereby irreversibly hampering the re-ligation reaction step in the broken part of DNA.

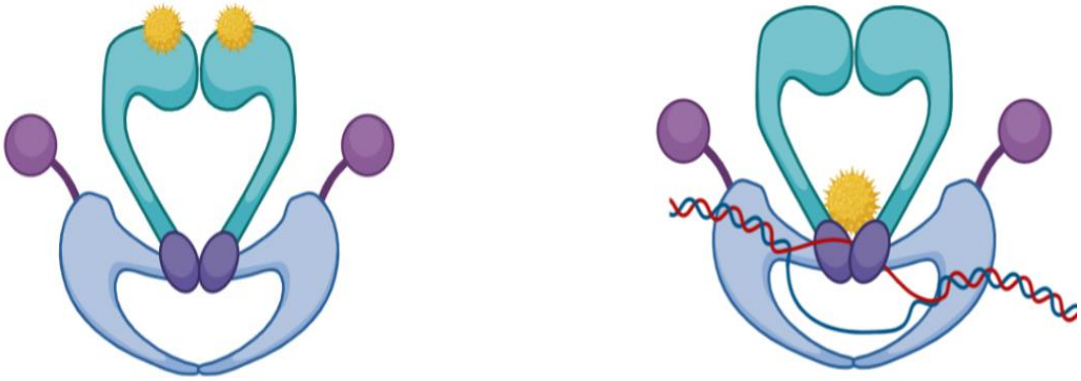

A. **B.**

Figure 2: Mechanism of Topoisomerase inhibitors: A) Targeting active catalytic site of the enzyme. B) Forming ternary complex with enzyme and the DNA. The yellow circular structure represents the inhibitor.

1.6. Introduction to Topoisomerases

1.6.1. Discovery

With the discovery of DNA double-helix, many questions were asked related to its functioning. To this, the famous Watson and Crick quoted - "Since the two chains in our model are intertwined, they need to untwist if they are to separate" (32). Their entire prediction stands correct, to separate the DNA double helix, a cell requires a set of specialized proteins known as topoisomerases.

The discovery of topoisomerases was led by James C Wang in 1971 (33) while studying negative supercoiling. He isolated *E. coli* topoisomerase I protein through chromatography and named it ω (33). Wang also discovered topoisomerase II, a DNA-dependent ATPase (34). He referred to the topoisomerases as "Magicians among magicians; known to open and close gates in DNA without leaving a trace enabling two DNA strands or duplexes to pass each other as if the physical laws of spatial exclusion do not exist" (35).

1.6.2. Cellular Functions

Compact DNA structure must maintain the integrity of the genetic information, but DNA metabolism like replication, transcription require overwinding (positive supercoiling) or underwinding (negative supercoiling) of DNA. Nature has provided Topoisomerases as a solution for resolving the topological problems accruing due to different DNA metabolism processes (36). These processes need access to the information stored in the DNA. During replication as fork progress, over winding of the dsDNA creates difficulties for the polymerase to move forward. As DNA wraps tighter and tighter the process of replication stops ultimately hampering the fork progression. Inside the cell,

these problems are taken into consideration by topoisomerases. They are specialized to relieve local topologies such as supercoiling, knotting, catenation, and precatenane formation. They function to maintain the condensed form of the chromosome by introducing positive supercoiling. On the other hand, topoisomerases also tend to participate in chromosome segregation during cell division (37,38). They play an essential role during the segregation of both the nuclear (39) and mitochondrial genomes (40).

1.6.3. Classification of topoisomerases

Topoisomerase enzyme maintains DNA integrity by resolving complex structures that occur during different DNA metabolic pathways such as replication, repair, and transcription. To perform their functions, they form a phosphor-tyrosine intermediate between the enzyme's catalytic tyrosine residue and the scissile phosphoryl group of the DNA backbone. Primarily they are classified based on the number of strands they cut: Type I and Type II enzymes cut one and two DNA strands, respectively. Type I topoisomerases cleave a single strand of duplex DNA and alter the linking number by 1. Type II topoisomerases break both strands of duplex DNA, thereby changing the linking number by ±2. Further, they are subdivided into A and B subfamilies by the differences in their mechanism of catalysis.

1.6.3.1. Type I Topoisomerases

Type I topoisomerases are proficient in cutting a single strand of DNA. They do not require ATP to function; instead, they utilize the potential energy already stored in DNA. Further, they are divided into two subfamilies based on the polarity with which the catalytic tyrosine attaches to the DNA.

1.6.3.1.a. Type IA Topoisomerases

This group requires an exposed single-stranded region within the substrate DNA to form a covalent linkage between the catalytic tyrosine and the 5' phosphoryl group. Mg (II) acts as an essential co-factor for its activity. Single-stranded negative but not positive supercoils are the characteristic substrate for this group of enzymes, where the linking number changes in steps of one. Hyper-thermophilic archaea make an exception to this group where the reverse gyrase introduces positive supercoils in an ATP-dependent manner (41). Type IA subfamily members function by the strand passage mechanism. The enzyme binds to a dsDNA's denatured region, creating a transient nick on one of the strands followed by passing the uncut strand through the nicked DNA then resealing both the broken strands (42). However, many scientists believe there is an alternative mechanism known as the enzyme bridging model. Here, the enzymes bind covalently to one end of the broken strand and noncovalently to the other, creating a bridge through which the entire DNA strand passes (43). This enzyme-bridging mechanism explains the catenation/de-catenation of two circular molecules (44).

These enzymes are proficient at catalyzing the knotting, unknotting, and interlinking of single-stranded circles. They are also known to act upon catenation and de-catenation of gapped or nicked duplex DNA circles. Type IA topoisomerase includes Topoisomerase I, Topoisomerase III, and reverse gyrase, they all are monomeric proteins (45). *Methanopyrus kandleri* reverse gyrase makes an exception to the above group (45). X-ray crystallographic data confirms the toroidal shape of *E. coli* topoisomerase I (PDB 1ECL) (46) and topoisomerase III (PDB 1D6M) (47) with four domains (I, II, III, and IV). Key amino acids from the domain I, III, and IV together form the active site of the

enzyme. Active site tyrosine is present in domain III cleaves the single-stranded DNA (46,47). The gap between domains I and III allows the passage of the other DNA strand that is subsequently captured by the enzyme clamp followed by the ligation of the cleaved DNA strand (Figure 3B).

Although EcTopoI enzymes relaxes DNA supercoils, but the complete relaxation will only occur if the substrate is negatively supercoiled (48). They bind to three Zn(II) with three tetra-cysteine motifs to perform the above function (49). In contrast to topoisomerases I, topoisomerases III require a hyper negatively supercoiled DNA substrate for relaxation. This is because topoisomerases III have a lower affinity for single stranded DNA and is therefore less able to facilitate the opening of the helix on DNA binding (45,48). However, topoisomerases III enzymes are more efficient in performing the functions like the catenation and decatenation of gapped DNA circles.

Many studies in bacteria and eukaryotes suggest that topoisomerases III proteins are functionally associated with helicases. Hence, topoisomerase III proteins are involved in unwinding the partially single stranded intermediates formed by helicases during recombination, repair, and replication (43,48).

Topoisomerase III has been identified and annotated in the genome sequence of *Plasmodium falciparum* as a sole member of the Type IA family of topoisomerases (50,51). However, there are no reports available about the biochemical and functional characters of *Plasmodium* topoisomerase III till now. We have studied for the first time the functional role of *Plasmodium* topoisomerase III.

1.6.3.1.a.a. Topoisomerase III

TopoIII was identified in Cozzarelli's lab when they performed experiments on Type I topoisomerases as it had a cleavage pattern entirely different from that of Topo I (52,53). Type IA subfamily members share a common structural core that ensures a proper DNA strand passage reaction (54). However, many structural characteristics models TopoIII as a unique enzyme. *E. coli* topoisomerases I and III show that the two proteins are very similar, but there are few structural differences that allows them to function differently. The domain organizations of TopoI and TopoIII have been represented in Figure 3A. *E. coli* TopoIII enzyme is made up of four domains (I–IV) that forms a toroidal-shape with a centre hole of approximately 25 Å. Domain I (residues 1–216) is the catalytic Toprim domain, which occurs commonly in type I-A, type II topoisomerases, RecR proteins, OLD family nucleases, and DnaG-type primases (55). Toprim domain consists of conserved amino acid residues that bind to the metal ion co-factor. In human counterparts, these acidic residues are Asp148, Asp150, and Glu152 (55). Domain II (residues 218–287 and 418–488) is intercalated within the domain III sequences consisting of mostly β fold which form a central hole (Figure 3C). Domain III (residues 288–417) is mainly helical and contains the catalytic tyrosine residue responsible for the covalent attachment with the 5'-phosphate group (42). This domain opens and then closes during a catalytic cycle. Domain III is associated with both domains I and IV (Figure 3C).

Mechanistically, domain III has to separate from domain I to expose the active site for cleavage and open a gate for entry/exit of the other DNA strands into the central cavity. Once the domains separate, the acidic residues in domain I get involved in magnesium binding. These highly conserved amino acids are

spatially arranged in such a fashion that they adapt the geometry appropriate for the interaction. The last domain IV (residues 489–609) is the main body of the protein that is associated with domain I and III.

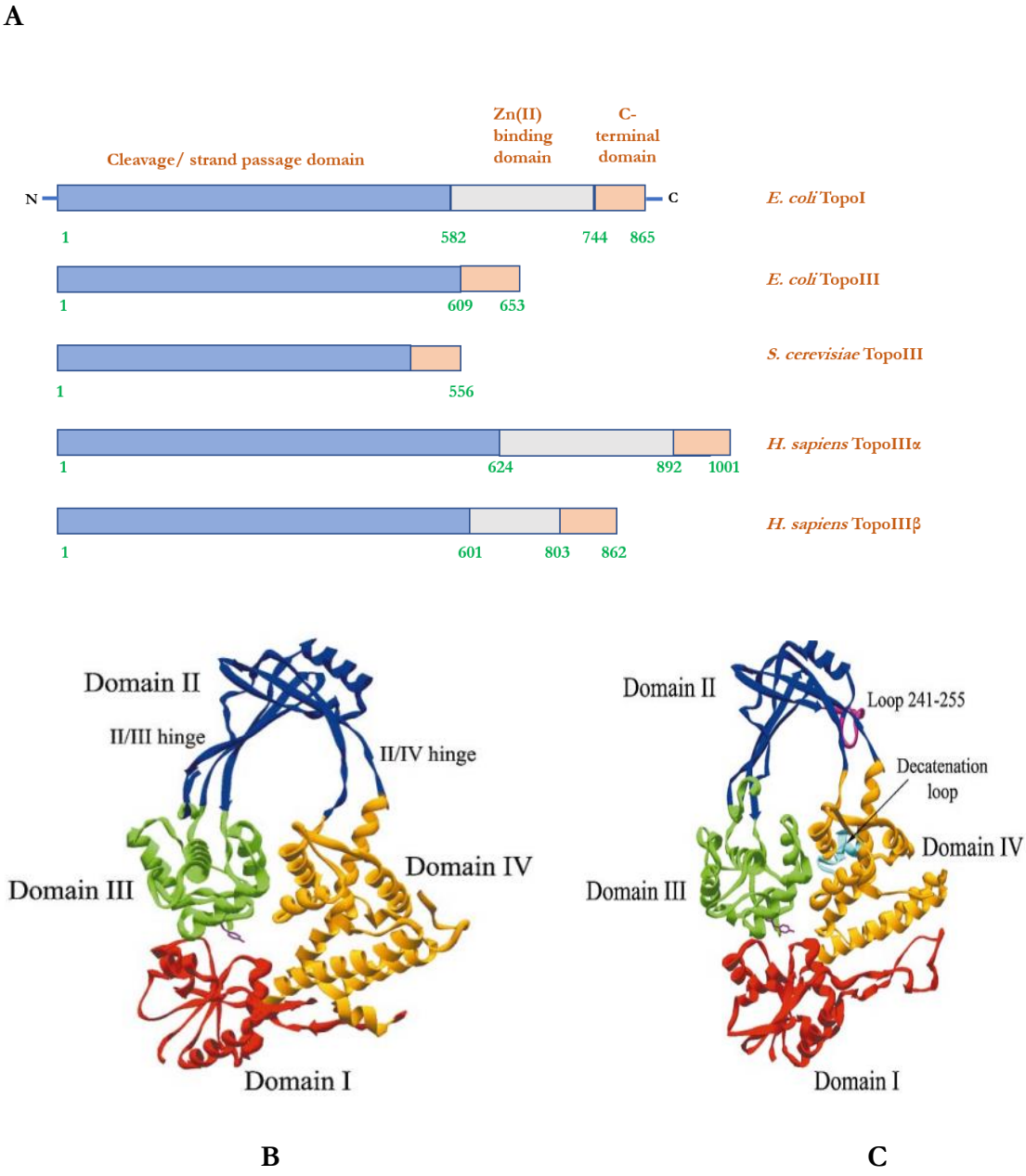

Figure 3: Domain organisation of Type IA topoisomerases. A) Domain structure of type IA topoisomerases. The sequences of the Type IA topoisomerases from the indicated organisms were aligned based on homology (54,56,57). The boxes corresponding to the various domains are coded as follows: blue, cleavage/strand passage domain; grey, Zn (II) binding domain found in *E. coli* Topo I, Human topoisomerases IIIα/β (58); orange, C-terminal domain. B) Structure of Topoisomerase I PDB entry 1ECL (46). C) Structure of Topoisomerase III PDB entry 1D6M (47).

Studies in *E. coli* have shown that topoisomerase III enzymes are more efficient at decatenating substrate than topoisomerase I, which happens to be more efficient at relaxing supercoiled DNA (59). This is due to one difference, TopoIII consists of the so-called "decatenation loop" in between domain III but lacks Zn (II) binding domain, which is important for relaxation (Figure 3C). This loop contains 17 positively charged amino acids, comprising several arginine and lysine residues facing the central hole (60). The charged character of the loop suggests that it is a DNA-binding region, and its removal will affect the decatenation activity but relaxation activity will be unaffected (61). The loop enables topoisomerase III to perform multiple decatenation reactions. The proposed model in *E. coli* suggests that decatenation loop promotes the entry and binding of a duplex DNA segment inside the cavity of the enzyme closed form before binding the single-stranded segment (61). This complex then binds to a single-stranded region of a gapped circle, and after cleavage, the duplex DNA segment is passed through the break. The decatenation loop would then promote rebinding to double-stranded DNA, leading to yet another cycle of decatenation. Therefore it has been suggested that topoisomerase III is likely to be involved in the unlinking of nascent daughter chromosomes (59). *E. coli* topoisomerase III cleaves and decatenates RNA molecules unlike, the Topoisomerase I (62). However, this region is absent in yeast and higher eukaryotic topoisomerase III (61). In our domain mapping studies, we found that the PfTopoIII enzyme also consists of positively charged amino acid regions similar to the *E. coli* TopoIII. Hence, we were interested in understanding its functional relevance in our study.

TopoIII has been extensively studied in other orthologs. In higher eukaryotes, topoisomerase III is present as two different isoforms TopoIIIα and TopoIIIβ.

Although they have similar enzymatic activities (56,63), their cellular functions are different. TopoIIIα functions during homologous recombination to repair cleaved double-stranded DNA. TopoIIIα is essential for development in drosophila (63), whereas in mouse, deletion of *TopoIIIα* leads to embryonic lethality (64). The heterozygous *topoIIIα*$^{+/-}$ mutant mice phenotypically resembled *TOPIIIα*$^{+/+}$ littermates; however, *topoIIIα*$^{-/-}$ homozygotes were not viable (65). In contrast, studies have shown that TopoIIIβ is dispensable for life (64,66). It has a unique developmental pattern in drosophila; TopoIIIβ only expresses during the first few hours of embryogenesis and later once again during adulthood but is not essential for survivability and fertility (56).

Studies have shown that yeast TopoIII is dispensable for vegetative growth, but essential for completing meiosis as mutant for the topoIII topoisomerase does not achieve the first meiotic division (67). ⊿*topoIII* cells result in pleiotropic traits such as slow growth phenotype, defective sporulation, increased mitotic and meiotic chromosome nondisjunction and, hyper-recombination between repeated sequences (67,68). The slow growth defect in the absence of TopoIII is due to the accumulation of cells with an undivided nucleus in the neck of an elongated bud. An extended G2/M phase results in the delay of chromosome segregation suggests that TopoIII is involved directly in the separation of replicated chromatids (67).

The mammalian TopoIIIα gene codes for two different forms of protein by using alternative translation initiation sites; first one is the shorter form with the nuclear localization signal at the C-terminal for exclusive localization in the nuclei, and second on is the longer form, having a mitochondrial import sequence at the N-terminus (63). Both forms of Topo IIIα fully rescue *top3α* null mutant's viability, suggesting the Topo IIIα's functions in nuclei are essential

for survival. *⊿topoIIIa M1L* flies only survive till adolescence; they show 4 to 15 fold reduction in the mitochondrial DNA copy number and 2 to 3 fold reduction in ATP content of ovaries/testes. This gives strong indication that Topo IIIα of *Drosophila* plays a crucial role in maintaining mitochondrial genome and male germ-line stem cells (69). Another recent study shows that TopoIIIα is necessary to decatenate and segregate human mitochondrial DNA following replication (70).

TopoIII enzyme requires RecQ helicases to perform its function, and the interplay between these two proteins is conserved among all the kingdoms of life. The proposed model indicates that RecQ helicases unfolds the DNA into an accessible single-stranded conformation upon which topoisomerase III acts to resolve stalled and converging replication forks. Studies indicate that TopoIII physically interacts with RecQ-type helicases in *S. cerevisiae* (71,72), *S. pombe* (73), and *H. sapiens* (74,75). Yeast TopoIII acts with Sgs1 to resolve the stalled replication fork and suppresses the genetic crossover (76). In humans, TopIIIα acts with BLM, a RecQ helicase that is mutated in the cancer predisposition disorder Bloom's syndrome. Topoisomerase IIIα collaborates with BLM, a RecQ-type helicase (77) and the RMI1/2 factor in mammals (78) to resolve Double Holliday Junctions (DHJs), to avoid the generation of crossover products that create chromosome rearrangements and genome instability in mitotic cells (79,80). Together, TopIIIα, RecQ helicase, and Rmi1(RMI1) proteins form the minimal DHJ dissolvasome. Mutation in any component of this complex results in genomic instability (78,81,82).

TopoIII resolves the late replication intermediates and catenated dimmers at the end of the replication. Bacterial TopoIII remains physically associated with the actively replicating fork and unlinks the catenated and pre-catenated DNA

rings that result during DNA replication (83). Apart from its function during mitosis, the TopoIII enzyme plays an essential role during meiosis, as they aid in the processing of molecules generated during meiotic recombination. They are involved in the resolution of Holliday junction by decatenating single-stranded DNA, which allows the two alleles after recombination to separate, thereby completing the sexual cycle. In yeast, *topo3*$^{-/-}$ diploid cells are unable to sporulate, leading to cell death (67).

1.6.3.1.b. Type I B Topoisomerases:

The members of the type IB subfamily are unique as they do not resemble structurally and functionally with any known topoisomerases. Type IB topoisomerase includes eukaryotic topoisomerase I, topoisomerase V and, poxvirus DNA topoisomerase. The active site tyrosine residue present in these enzymes covalently attached to the 3' phosphate end of dsDNA. Unlike the type IA, they neither require Mg (II) ions nor a partially single-stranded substrate for their catalysis activity. Type IB subfamily members can efficiently relax positive as well as negative supercoils as their activity is independent of the substrate's supercoiling state (84). The relaxation of type IB topoisomerase is mediated by strand rotation mechanism, where the two domains of the enzyme encircle DNA to form a clamp [38] and generate a single-strand break through the formation of a covalent bond between its active site tyrosine and 3' phosphate in the DNA backbone leaving the 5'-OH end of the broken strand free (85). The broken strand is then free to rotate around the intact strand before being re-ligated. Type IB topoisomerase helps during replication fork progression by relaxing supercoiled DNA ahead of it (86).

TopIB was first purified and characterized from infected erythrocytes in *Plasmodium berghei* (87). Later, the gene encoding the PfTopIB was discovered (88). It consists of three structural domains: (i) the N-terminus domain (134 amino acids), which is poorly conserved, (ii) 500-residue long conserved amino acids with a high level of homology to the core domain of the human protein, and (iii) the C-terminal domain, with the conserved active tyrosine at position 798, which makes the enzyme fully active. Tosh and colleagues in 1999 showed that PfTopIB is developmentally regulated during the various stages of the *Plasmodium* life cycle. But its mRNA expression levels are high during the trophozoite stage but not in schizonts (89).

1.6.1.2. Type II Topoisomerases

Contrary to the type IA and type IB enzymes, the type II DNA topoisomerases resolve compact DNA structures by moving one DNA double helix through another in an ATP-dependent fashion (90). Type II enzymes resolve topological complexities which occur during various DNA metabolic processes. For instance, their substrates are catenated/decatenated DNA products formed during replication. They relax both positive and negative supercoiled DNA. Different type II family members are distinguished by their relative proficiency at DNA relaxation versus decatenation (or catenation). This property likely reflects their specialized roles in the cell. Among all known Type II enzymes, DNA gyrase is the only enzyme capable of using ATP hydrolysis energy to introduce negative supercoils into the DNA (45). The type II enzymes contain two different subunits, all prokaryotic enzymes are mostly hetero-tetrameric, whereas eukaryotic enzymes are all homodimers. These dimers cleave the dsDNA by forming a 5' phosphotyrosine bond. They perform their function

when a conformational change moves apart the two ends of the cleaved duplex DNA to create an opening called gated segment (G-segment) DNA. The second region of duplex DNA, also known as a transported segment (T-segment) from either the same molecule (relaxation, knotting, or unknotting) or a different molecule (catenation or decatenation), is passed through the open DNA gate. This leads to an explanation that why the linking number changes in steps of two when the supercoiling of a circular DNA is changed (91,92). Type II topoisomerases function in order to successfully remove super helical twists from DNA and resolve knotted or tangled duplex molecules in numerous DNA processes. The major ones include recombination, the separation of daughter chromosomes, condensation/de-condensation, and maintaining proper chromosome structure (48,93).

This group is again divided into type IIA and type IIB subfamilies. Type IIB subfamilies share common mechanistic features with the type IIA enzymes, but there are distinct structural differences between the two subfamilies (94).

1.6.1.2.a. Topoisomerase IIA

Type IIA topoisomerases are present in all possible domains of life and are essential for an organism's growth and survival. They include gyrase, TopoIV of *E. coli*, TopoII of *S. cerevisiae,* and eukaryotic TopoIIα and TopoIIβ. Type IIA topoisomerases are made up of the following regions: N-terminal GHKL ATPase domain, a central DNA-binding core, and a variable C-terminal domain. The Toprim domain consists of the three invariant acidic residues that coordinate with magnesium ions to allow DNA cleavage and re-ligation (55).

Type IIA enzymes are essential for maintaining the double-helical structure and segregation of daughter chromosomes post DNA replication (92,95). They

condense chromosomes during apoptosis in mammals (96). Many studies have also shown *S. cerevisiae* TopoII as a cell cycle regulator (97). Topo IIα enzymes are present in the proliferating cell types, and their expression is highest during the G2 and M phases of the cell cycle. Similarly, Topo IIβ enzymes are present in almost all cell types, but their expression is constant throughout the cell cycle (98).

In *Plasmodium,* two type IIA family topoisomerases are present, DNA gyrase and TopoII. DNA gyrases are involved in apicoplast replication whereas, TopoII enzymes are essential during nuclear replication (99). Both Gyrase A (*PfGYRA*) and Gyrase B (*PfGYRB*) enzymes have been expressed and functionally characterized. Interestingly, the intrinsic ATPase activity of PfGyrB follows a linear pattern of ATP hydrolysis that differs EcGyrB. PfGyrB but not PfGyrA was able to complement the *E. coli* gyrase temperature sensitive strain. PfGyrB exhibits DNA cleavage and DNA supercoiling activity when combined with EcGyrA or PfGyrA (100).

Furthermore, PfGyrA contains a unique leucine heptad repeat that might be responsible for dimerization. Also, a unique 45-amino acid region in the Toprim domain of PfGyrB was identified, which is responsible for DNA binding activity, DNA-stimulated ATPase activity, and DNA cleavage activity (101). The C-terminal region of PfGyrA and EcGyrA share a similar DNA wrapping activity, and Asn-region of PfGyrA is dispensable for its activity since its deletion did not show any effect (102).

Plasmodium Topoisomerase II was expressed in cell-free extracts in soluble form. The plasmid relaxation and decatenation activity of Topoisomerase II is conserved. Moreover, bacterial gyrase inhibitors, GSK299423, ciprofloxacin, and etoposide exhibited 15-, 57-, and 3-fold selectivity for the malarial enzyme

over human Topoisomerase II (103). A dsRNA targeting the coding region of *Plasmodium* Topoisomerase II combined with chitosan nanoparticle was able to inhibit the *in vitro* growth of *Plasmodium falciparum* efficiently (104).

1.6.1.2.b. Type IIB Topoisomerases

Type IIB subfamily includes only two enzymes, topoisomerase VI and topoisomerase VIII. Topoisomerase VI is present in archaea (94), plants (105), and *Plasmodium (106)* whereas, topoisomerase VIII is present in archaea and bacteria (107). Although the Type IIB subfamilies share standard mechanistic features with the type IIA enzymes, but there are definite structural differences between them. Firstly, the double-strand breaks formed by TopoVI have a 2-bp stagger whereas, other type IIA enzymes create 4-bp stagger that marks structurally different cleavage sites (108). Secondly, A subunit of TopoVI lacks a post-strand passage cavity, unlike type IIA topoisomerases (109). TopoVI possesses the N and G-gate only, whereas, in Type IIA topoisomerases, there are three gates, N, G, and C-gate (110).

1.6.1.2.b.a. Topoisomerase VI

For the first time, Topoisomerase VI was characterized in thermophilic archaea *Sulpholobus shibatae* (111) and later in plants such as *Arabidopsis thaliana*, *Oryza sativa* (105,112,113). Recently, a study in mice identified Topoisomerase VIB-like protein (TopoVIBL) with a similar conserved GHKL domain as that of TopoVIB. It interacts with Spo11(a TopoVIA like protein) to perform its biological functions during meiosis (114). Histological analysis of *topo6bl*−/− testis sections showed disrupted spermatogenesis, spermatocytes were strongly depleted, and spermatids could not be detected, suggesting a

defect during the meiotic prophase. Hence, the conserved structure and function of TOPOVIBL proteins demonstrate that there is a notable biochemical and evolutionary relationship between the type IIB family of topoisomerases and meiotic DSB activity.

TopoVI enzymes are hetero-tetrameric (A2B2) enzymes, consisting of topoisomerase VIA and topoisomerase VIB subunits. This structural arrangement suggests that the A subunit dimer separates during G-segment opening. The B subunits act as bridging elements to span the broken G-segment and prevent dsDNA break formation. They undergo a simple 'two-gate' mechanism where transported DNA enters through a nucleotide-dependent 'entry' gate comprised of the two B subunits and leaves through an 'exit' gate on the opposite side of the protein, formed by the two A subunits. In the proposed mechanism for this reaction, ATP binding by the B subunit stimulates DNA cleavage by a bipartite CAP/Toprim active site in the A subunit (55,94).

Although TopoVIA has two conserved domains, the CAP and the Toprim, it shows no structural homology with any other topoisomerases (115). Instead, TopoVIA is a homolog of Spo11, a protein responsible for creating dsDNA breaks to initiate meiotic recombination (116,117). The mechanism and generation of DNA breaks are similar in both Spo11 and TopoVIA. However, *Sulfolobous shibatae* TopoVIA alone cannot cleave DNA but generates a double-strand break along with TopoVIB (113).

Knock-out experiments in *Arabidopsis* topoVIA or VIB subunits resulted in the plant's extreme dwarf phenotype, reduced size of hair roots, yellowish leaves and, reduced trichome (leaf hair) size (118). Reduction in ploidy and cell death after 4 to 5 days was also observed (118,119). Plant cells are known to increase their ploidy numbers through an alternative cell cycle called endoreduplication,

a process in which genome replicates but cell division does not happen (120). The inability of these mutants to increase its ploidy suggests that TopoVI is essential during the endoreduplication process. *P. falciparum* undergoes endoreduplication three times, once in the host mosquito and twice in the human host (in the liver and RBC) (121,122). Schizogony paves a path for malaria parasites to expand its pathogen biomass and infectivity.

The *S. shibatae* Topo VIB (PDB 2ZBK) crystal structure indicates the presence of ATP binding domain, the H2TH (helix 2 turn helix) domain, and the transducer domain (Figure 4) (123,124). The transducer domain helps to communicate between the N terminal ATPase domain and the C-terminal domain of TopoVIB (125). Studies have indicated that it also interacts with the TopoVIA N-terminus region (Figure 4) (123). H2TH domain function is not clearly understood and is not present in any other topoisomerases. The ATPase domain of TopoVIB resembles the large family of proteins with GHKL domain (**G**yrase, **H**sp90, Histidine **K**inase, and Mut**L**). ATPase domain has a characteristic 3D fold, known as Bergerat fold which gets involved in ATP binding and its hydrolysis to provide the energy required for proper functioning of the cell. Radicicol is a competitive inhibitor of ATP; it hampers ATP hydrolysis by binding to the Bergerat fold/ ATPase pocket of Topoisomerase VIB (Figure 4) (126).

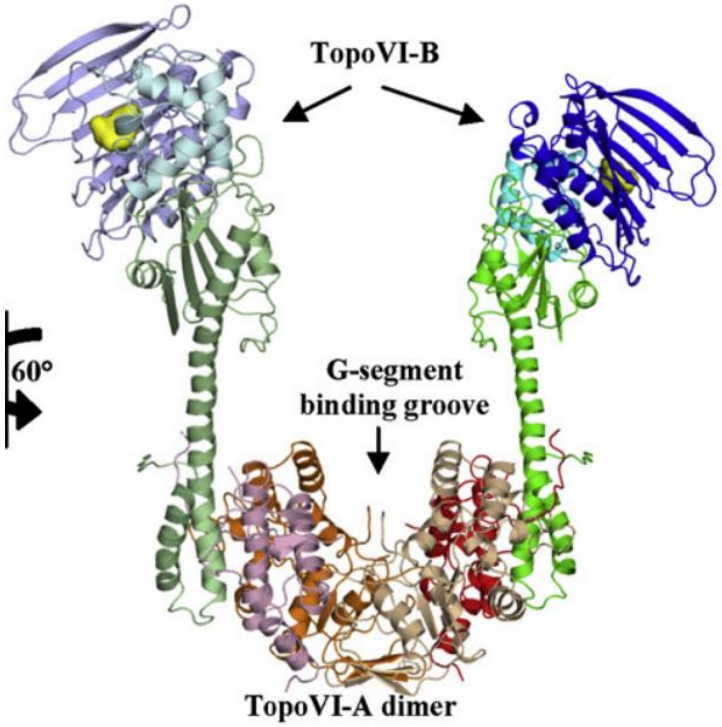

Figure 4. Structure of the *S. shibatae* Topo VI A2B2 heterotetramer enzyme as ribbon representation (124). The radicicol drug bound to Topo VIB is shown in yellow space filling. Topo VIB subunit is represented as a dimer with N-terminal GHKL motif (blue) and C-terminal transducer domain (green) (115,123). Topo VIA subunit is also present as a dimer with G-segment binding groove represented in magenta colour, the N- terminal domain (red) interacts with C terminal domain of Topo VIB.

Radicicol is an antifungal antibiotic originally isolated from the *Monosporium bonorden.* Earlier reports of *Sulpholobus shibatae* TopoVIB suggest that Radicicol has a binding affinity towards the Bergerat fold, which in turn inhibits the ATP hydrolysis and dimerization of the enzyme (126). Biochemical experiments on *SsTopo*VIB also confirm that Radicicol inhibits its relaxation and decatenation activities (126). Radicicol also inhibits the decatenation activity of *Haloforax volcanni* archaea affecting its growth (127).

Following the above findings, our lab has also established the function of *Plasmodium falciparum* Topoisomerase VIB during the schizogony development stage of the parasite [26, 27]. Sequence alignment analysis have shown a considerable homology between PfTopoVIB and its orthologs (plant and archaea) predominantly in the core ATPase domain, especially within the Bergerat fold.

It was observed that Radicicol treatment manifested two different phenotypes in the parasite. Higher concentration (8 μM) leads to a significant reduction of the parasite counts as they were unable to multiply from schizont to ring stage. It was also observed that the newly formed rings and trophozoites had extreme delayed development, which causes parasite death. Whereas, with sublethal doses of Radicicol (1.5 μM) a delay in the transition from the schizont to the ring stage of the parasite was observed (128). Radicicol treatment causes an increase in the expression of PfTopoVIB at the transcript and protein levels. This induction could be due to the compensatory mechanism which cells offer to maintain the active TopoVIB level in the cell.

Radicicol specifically reduces the mitochondrial genome content of the parasite without affecting the nuclear genome content (26). It was further observed that yeast TopoII function could be complemented by the presence of both

PfTopoVIB and PfTopoVIA [27]. Using the cell-free yeast extract that harbours PfTopoVIB-TopoVIA, it was found that the decatenation activity of the enzyme is inhibited by Radicicol [27].

Earlier studies have shown that Hsp90 has a similar GHKL motif as that of TopoVIB. Radicicol binding to the Hsp90's ATPase domain leads to proteasomal degradation (129) and loss in tumor cell growth (130). Hence, to further understand the function of TopoVIB in *Plasmodium* biology, we aimed at designing specific analogs of Radicicol that will have a biased binding towards PfTopoVIB and not to PfHsp90.

1.7. SIGNIFICANCE

Today's new world is facing a challenge towards malaria control strategies. Although a lot of research is going on to find a novel drug target against malaria, somehow, we are failing at our ends. Because every time there emerges a more powerful resistant strain against the conventional drug system, it is essential to keep on finding other drug targets that can potentially disrupt the functioning of this unicellular organism *Plasmodium*. Keeping that in mind, my laboratory is motivated to understand the biological significance of *P. falciparum* topoisomerase proteins. My thesis work is associated with two such topoisomerase proteins, Topoisomerase III and Topoisomerase VIB.

Our study demonstrates an essential role of PfTopoIII during replication of the parasite. We find that this enzyme is expressed explicitly during the onset of replication of the parasite and is localized in both nucleus and mitochondria, indicating its involvement in replicating both the genomes of the parasite. Using yeast as a surrogate system, we have shown that PfTopoIII can complement the function of yeast TopoIII. We have demonstrated that PfTopoIII physically interacts with both the RecQ helicases of *Plasmodium,* namely *PfBLM* and *PfWRN*. We find a direct involvement of PfTopoIII during replication stress given to the parasite. We observe that the parasites cannot replicate, and their growth is arrested even in the presence of a low dose of hydroxyurea. However, the transgenic parasites harboring PfTopoIII expressing plasmid show survival advantage during replication stress. We have identified a unique, highly charged low complexity region in the enzyme, which is not present in its human ortholog. To analyze the structure-function relation of PfTopoIII, we have deleted that region from the enzyme, and by employing series of genetic studies,

we have established that this region is indispensable for the proper functioning of PfTopoIII. Together, our results establish the importance of TopoIII during *Plasmodium* replication and emphasize the essential requirement of the charged domain in PfTopoIII function. The presence of this unique 85 amino acid region affirms the enzyme as an attractive target for the design of anti-malarial agents.

Our second project revolves around *Plasmodium falciparum* Topoisomerase VIB. Earlier, we have shown that Radicicol inhibits the decatenation activity of PfTopoVI protein. But there are similar studies indicating Hsp90 is also inhibited by Radicicol, since it possesses a similar GHKL motif as TopoVIB. Bioinformatics data confirms that Radicicol fits comfortably in the ATP-binding pocket of both PfTopoVIB and PfHsp90 (26). As most of the replication proteins are essential for survivability, and generation of conditional knock-outs in *Plasmodium* is technically challenging, it is important to identify highly specific chemical inhibitors of PfTopoVIB in order to delineate the precise biological role of this protein in *Plasmodium*. Hence to reduce the off-target activity of Radicicol, we have designed different Radicicol analogs that showed preferential binding toward PfTopoVIB but not PfHsp90. Our in-silico docking analysis has predicted that one such analog, namely, Analog 2, that binds specifically to PfTopoVIB and not PfHsp90.

1.8. SPECIFIC AIMS

I. Functional characterization of PfTopoIII and its unique charged domain

1. Domain analysis of PfTopoIII and its comparison with HsTopoIII
2. To study the expression and localization of PfTopoIII in asexual stages of the parasite
3. To study the structure-function relation of PfTopoIII using yeast as a surrogate system
4. To evaluate PfTopoIII function during replication
5. To evaluate the role of PfTopoIII when replication stress is given to the parasite

II. To predict a small molecule inhibitor targeting PfTopoVIB

1. To identify a specific analog of Radicicol by the computational method that predicts stronger association towards *Plasmodium* topoisomerase VIB but not with PfHsp0

CHAPTER-2

MATERIALS AND METHODOLOGY

2.1 MOLECULAR BIOLOGY METHODS

2.1.1. Bacterial plasmid DNA isolation by alkaline lysis method

The bacterial colony harboring the recombinant plasmid was inoculated in 5 ml of LB medium and was incubated overnight at 37ºC and 200 rpm. The culture was centrifuged at 4000 rpm for 15 minutes to pellet the cells. The supernatant was discarded, and the pellet was resuspended in 200 µl of solution I (Tris 25 mM pH 8, EDTA 10 mM). It was transferred to a micro-centrifuge tube and incubated on ice for 5 minutes. Then 200 µl of solution II (NaOH, 1 % SDS) was added to the tube and mixed by inverting 4-5 times, followed by 5 mins incubation for less than 5 minutes at room temperature. Next, 150 µl of chilled solution III (3M sodium acetate) was added to the tube and again incubated on ice for 5 minutes with intermittent mixing. The sample was then centrifuged at 12000 rpm for 15 minutes at room temperature. The supernatant was collected in another fresh micro-centrifuge tube, and the pellet was discarded. 2.2 volume of absolute alcohol was then added to the tube, mixed well, and kept at -20ºC for 45 minutes. After incubation, the sample was centrifuged at 12000 rpm at 4ºC to precipitate the DNA. The pellet was washed by adding 70 % alcohol followed by air drying, and the supernatant was discarded. The dried pellet was then re-suspended in 50 µl of 1X Tris-EDTA buffer. To remove RNA, the sample was subjected to RNase treatment at 37ºC for 30 minutes. After that, an equal volume of phenol-chloroform isoamyl alcohol (25:24:1) mixture was added to it, and it was vortexed for 2 minutes. This solution was then centrifuged at 12000 rpm for 15 minutes, and the upper aqueous layer containing DNA was precipitated by adding 1/10th volume of solution III and 2.2 volumes of 100 % ethanol. This solution was then incubated at - 80ºC for 2

hours. After incubation, the tube was then centrifuged at 12000 rpm, 4^{o}C, for 30 minutes to precipitate the plasmid DNA, subsequently washed using 70 % alcohol. The pellet was then air-dried and re-suspended in 30 µl 1X TE buffer.

2.1.2. Bacterial competent cell preparation

A single bacterial colony was inoculated in 10 ml of LB overnight at 37^{o}C. The next day, a secondary culture was inoculated with 500 µl of the overnight culture. The culture was then incubated at 37^{o}C till the OD_{600} reached 0.5. The culture was centrifuged at 8000 rpm, 4^{o}C for 8 minutes to harvest the cells. The supernatant was discarded, and the pellet was then very gently re-suspended in 12.5 ml of ice-cold $CaCl_2$ (0.1 M) solution. The suspension was centrifuged at 8000 rpm, 4^{o}C for 8 minutes, and the supernatant was discarded. The pellet was gently resuspended in 12.5 ml of ice-cold $CaCl_2$ (0.1 M) and incubated on ice for 4-8 hours to make cells competent. After incubation, the cells were harvested by centrifuging the culture at 8000 rpm, 4^{o}C for 8 minutes. The pellet was then re-suspended in 1.070 ml of ice-cold $CaCl_2$ (0.1 M) and 170 µl of glycerol. This cell suspension was divided into 100 µl aliquots in pre-chilled eppendorf tubes, and liquid nitrogen treatment was given. The frozen tubes were stored in a -80^{o}C refrigerator.

2.1.3. Bacterial transformation

25-50 ng of DNA was layered on the Top10 competent cells and was incubated on ice for 30 minutes. This suspension of cells was given heat shock for 30 seconds. The tubes were incubated on ice for 2 minutes immediately after heat shock. 1 ml of Luria Broth was added to the cells and incubated at 37^{o}C for 1 hour with shaking. The cells were given a short spin, most of the supernatant

was removed, and the pellet was re-suspended in the left-over supernatant. The cell suspension was then spread on a Luria agar plate containing the appropriate antibiotic. The plates were incubated at 37ºC for (12-16) hours.

2.1.4. Recombinant protein expression in *Escherichia coli*

The clone *PfTOPOIII/pET28a* was transformed into each of the bacterial strains (BL21DE3*, pLysS, Rosetta, and Codon Plus competent cells). 10 ml Luria broth containing respective antibiotics was added to the above mixture and incubated at 37ºC overnight. Then next day, 10 ml secondary culture was inoculated with the appropriate amount of the primary culture. After the absorbance of the cells reached 0.6 OD_{600}, the protein was induced with 1 mM IPTG (Isopropyl β-D-1-thiogalactopyranoside) (Sigma) by 4 hours incubation. The equal number of cells was taken from un-induced and induced cultures and resuspended in 1x Laemmli loading buffer. Their expression was compared on SDS-PAGE gels and empty vector induced and un-induced samples after staining with Coomassie brilliant blue R (Sigma).

2.1.5. RNA isolation from yeast

Yeast cells grown in 10 ml of suitable media were taken at mid-log (OD_{600} 1) for RNA isolation. Cells were harvested by spinning them for 5 minutes at 3500 rpm. The obtained pellet was re-suspended in 500 µl of DEPC treated water. After re-suspension, cells were given a short spin, and the supernatant was discarded. To the pellet, 400 µl of TES (10 mM Tris-Cl pH 7.5, 10 mM EDTA, and 0.5% SDS) solution, 400 µl of phenol (H_2O buffered) was added, and vortexed for 10 seconds. Then samples were incubated for 60 minutes on a dry bath with a temperature of 65°C and vortexed in between every 15 minutes.

Further, samples were immediately transferred to the ice for 5 minutes and spun for 10 minutes at 14000 rpm, 4°C. The obtained aqueous layer was aliquoted to a new tube, and to this, 400 µl of chloroform was added. After chloroform addition, samples were vortexed for 10 seconds and spun for 10 minutes at 14000 rpm, 4°C. The aqueous layer obtained was transferred to a new microfuge tube. Precipitation of RNA was done by adding 2.2 volumes of pre-chilled 100% ethanol and 1/10th volume of 3 M NaOAc pH 5.2. The samples were kept at -80°C for 1 hour. After incubation, samples were spun for 10 minutes at 14000 rpm, 4°C, and the pellet was washed with 500 µl of 70% alcohol (prepared with DEPC water). After washing, cells were spun for 10 minutes at 14000 rpm, 4°C. The pellet was air-dried and re-suspended in 50 µl of DEPC water. The RNA sample's integrity was checked by formaldehyde agarose gel electrophoresis, and the concentration by measuring OD_{260} (OD_{260} of 1 is equal to a concentration of 40 µg/ml).

2.1.6. Semi-Quantitative PCR

About 10 µg of total RNA was reverse transcribed using oligo dT primer (Sigma Aldrich) and reverse transcriptase (Omniscript kit, Qiagen). RNase inhibitor (Qiagen) was used in this process. The resulting cDNA was first quantified, diluted appropriately to normalize, and then subjected to PCR amplification (27 cycles) using gene-specific primers. The PCR products were run on 1.4% ethidium bromide (Hi-media) containing agarose gel.

2.1.7. Real-time RT-PCR

Equal amounts of RNA (10 mg) from rings, trophozoite, and schizont stage parasites were first subjected to DNase I (Fermentas) digestion for 15 min at

room temperature. Then, DNase I was inactivated by incubation with 25 mM EDTA at 65°C for 10 min. The absence of genomic DNA was verified by amplification with gene-specific primers before the reverse-transcriptase step. Next, each RNA sample was reverse-transcribed with oligo dT primer (Sigma–Aldrich) using reverse transcriptase (Omni Script; Qiagen, Hilden, Germany) (131).The resulting cDNA was subjected to semi-quantitative reverse transcription RT-PCR to detect the transcript level of *P. falciparum TopoIII* in all of the asexual stages.

Similarly, the expression of *PfBLM* was measured by amplifying 149 bp gene-specific regions using the primer pairs OMKB 332 and OMKB 333. *PfWRN* expression was measured by amplifying 225 bp gene-specific regions using the primer pairs OMKB 334 and OMKB335. For real-time PCR, cDNA from each stage was diluted (1:50) and used for PCR using an RT-PCR kit (Roche). Real-time analyses were conducted using the Applied Biosystems 7500 Fast Real-Time PCR system. The threshold cycle (Ct) value of each sample's ARP transcript was used to normalize the corresponding Ct values of the *PfTOPOIII* transcripts. The normalized Ct values of *PfTOPOIII* from different samples were compared with obtain ΔCt values. The relative levels of mRNA were deduced from the formula: change in mRNA level = 2ΔCt. The primers OSB 337 and OSB 335 were designed to amplify a 254 bp gene-specific region of *PfTOPOIII*, and OSB 94 and OSB 95 were used to amplify a 300 bp gene-specific region of *P. falciparum* aspartate-rich protein *(PfARP)* (131). To further investigate the mRNA levels of *PfTOPOIII* under HU conditions, RNA was isolated under treated and untreated conditions from late schizonts stage parasites. The same procedure was followed to check the expression of

PfTOPOIII. *PfRAD51* was used as a positive control. The primers OMKB 198 and OMKB 17 were used to amplify 314 bp gene specific regions of *PfRAD51*.

2.2. YEAST GENETIC METHODS

2.2.1. Protein isolation from Yeast by TCA method

Yeast cells were inoculated in 5 ml of appropriate medium and grown overnight at 30ºC at 200 rpm. The secondary inoculum was given in 20 ml of the appropriate medium. The culture was grown till the OD_{600} reaches 0.5. The cells were then centrifuged and re-suspended in autoclaved milli-Q water. The cell suspension was transferred to a 2 ml eppendorf tube to centrifuge again, and the residual medium was discarded. This obtained pellet was first washed with 0.5 ml of 20 % TCA and centrifuged. The pellet was again re-suspended in 200 µl of 20 % TCA, and glass beads were added and vortex thoroughly. The supernatant was transferred into a new 1.5 ml tube, washed twice with 200 µl of 5 % TCA followed by mixing (132). This suspension was centrifuged again, and the TCA precipitated proteins were dissolved in 60 µl 1X sample buffer [Tris-HCl, pH 6.8, 2 % SDS (Fisher Scientific) and bromophenol blue (Qiagen). The sample was then boiled for 8 minutes, centrifuged at top speed for 5 minutes, and used for further analysis.

2.2.2. Yeast competent cell preparation

A single colony of desired yeast strain was inoculated in 5 ml of yeast growth medium and incubated overnight. The next day secondary culture was grown in 40 ml medium, and culture was incubated at 30°C till the final absorbance reached OD 0.6 (for knockout experiments, O.D taken is 0.8). The cells were

harvested and then washed by suspending them in 10 ml sterilized water. The cells were finally re-suspended in 300 µl Lithium solution (1X Tris-EDTA, 1X Lithium Acetate), and thus competent yeast cells were prepared.

2.2.3. Yeast transformation

About 0.5-1 µg of the sample DNA and 10 µg of carrier DNA were added to the eppendorf tube. 200 µl of competent yeast cells was added gently over the DNA mixture in each transformation tube. To each tube, 1.2 ml of PEG solution [10X LiOAc (Sigma), 10X TE, 50% PEG 2000 (Sigma)] was added, and the solution was incubated for 30 minutes with shaking. Heat shock was given at 42°C followed by ice incubation. The cells were then collected by centrifugation at 10000 rpm for 10 seconds. The pellet was re-suspended in 200 µl 1X Tris-EDTA buffer and then spread on appropriate plates. The plates were incubated at 30°C till transformed colonies were seen.

2.2.4. Yeast Two-Hybrid Assay

For yeast two-hybrid analysis, we monitored *ADE2* and *HIS3* reporter gene expression as the readout of protein-protein interaction. pGBDUC1 plasmid with gene of interest was fused to the binding domain, and the second gene was fused to the activation domain in pGADC1 plasmid. The presence of both the plasmid was confirmed by transforming them into the PJ69-4A strain. The cells were grown up to 0.5 OD_{600} and then serially diluted, as shown in the figure (Figure **). 3 µl of each diluted sample was spotted simultaneously on two plates; one lacking uracil and leucine and the other lacking uracil, leucine, and his (132). The weak interaction was scored on SC-Ura-Leu–His plate. Self-activation of the gene was checked by transforming either empty bait or prey

vectors and respective plasmids containing the gene of interest. Growth on these plates was scored after 5 days of incubation at 30ºC

A list of yeast strains used in this study is mentioned in Table 3. PMY3 strain that harbors empty pGADC1 and pGBDUC1 vectors was used as a negative control [31]. To study the interaction between PfTopoIII and PfBlm and/or PfWrn, the HCY1 and HCY2 strains were created by transforming *Prey-PfBLM + Bait-PfTOPOIII*, and *Prey-PfWRN + Bait PfTOPOIII* constructs into the PJ69-4A strain, respectively. Similarly, to study the interaction between *PftopoIII(⊿259–337)* and PfBlm as well as PfWrn, strains HCY3 and HCY4 were generated by transforming the Prey-*PfBLM + Bait-Pf(⊿259–337)topoIII* and *Prey-PfWRN + Bait-Pf(⊿259–337)topoIII* constructs, respectively into the PJ69-4A strain. The strains HCY7, HCY8, HCY9, and HCY10 were used as controls. These strains were generated by transforming empty *Prey + Bait-PfTOPOIII, Prey-PfBLM + empty Bait, Prey-PfWRN + empty Bait, and empty Prey + Bait-Pf(⊿259–337)topoIII* vectors respectively into the PJ69-4A strain.

2.2.5. Yeast genomic DNA isolation

10 ml culture was grown overnight at 30ºC in a shaker incubator. The following day, the cells were harvested at 3000 rpm (RT). The cell pellet was suspended in 0.5 ml autoclaved double distilled water and centrifuged for 10 seconds. The supernatant was removed, and the pellet was suspended through vortexing for 5 minutes. 200 µl breaking buffer [Triton X-100 (2%) (Qiagen), SDS (1%), NaCl (0.1M)], glass beads (Sigma), and 200 µl of Phenol/Chloroform mixture were added to the suspension. 200 µl 1X Tris-EDTA buffer (10 mM Tris-HCl, 1 mM EDTA pH 8.0) was then added, and the mixture was centrifuged at maximum speed for 5 minutes at room temperature. The supernatant was transferred into

a new tube. To this 1 ml 100 % absolute ethanol was added and incubated at -20ºC for 30 minutes. The DNA was precipitated by centrifugation at 12000 rpm for 5 minutes, and the pellet was dissolved in 400 µl of 1X Tris-EDTA buffer. RNA was removed by RNase (10 mg/ml) (SRL) treatment. Then 10 µl of 4 M NH_4OAc (Fisher Scientific) and 2.2 volume of 100 % absolute ethanol were added to precipitate the DNA, and the mixture was incubated at -20ºC for 1 hour. Genomic DNA was collected by centrifuging at maximum speed for 10 minutes at room temperature (132). The supernatant was discarded, and the pellet was washed with 70 % ethanol. Finally, the genomic DNA pellet was dissolved in 1X Tris-EDTA buffer and used for further processes.

2.2.6. Yeast gene knockout

The strains used in this study are listed in Table 3. The ⊿*SctopoIII* strain was generated by homologous recombination-mediated gene knockout. To that end, a deletion cassette (133) with a *HIS3* gene flanked by 40 bp upstream and 40 bp of the 30 terminal ends of *ScTOPOIII* ORF was amplified using the primer set OSB 348/OSB 385. Then the cassette was transformed in the wild-type strain, and the transformed colonies were selected using histidine drop-out plates. Individual colonies were screened for *SctopoIII* knockout clone by PCR-mediated confirmation using primer pairs OSB 350(-150bp upstream of the gene) and OSB 385. The confirmed colonies should give an expected size of 1.45 kb (HIS3 gene size is 1.3 kb and 150 bp extra upstream region). Unconfirmed colonies will give size of 2.05 kb (*ScTOPOIII* gene size is 1.9kb and 150 bp extra upstream region).

2.2.7. Yeast complementation assay

For a functional complementation study in yeast, we transformed the empty vector (pTA), *pTA-ScTOPOIII, pTA-PfTOPOIII, pTA-PfY421FtopoIII,* and *pTA-Pf(⊿259–337) topoIII* individually into the *⊿topoIII* strain to generate SBY2, SBY3, SBY4, SBY5, and SBY6, respectively. Later, these strains were tested for slow growth phenotype in liquid as well as solid phase.

For liquid state, all strains were grown overnight in tryptophan dropout synthetic medium at 30°C. The next day, secondary culture was grown at 30°C for 15 hours, and after every 3 hours, the survivability was measured. For the solid phase, a similar procedure was followed until secondary OD_{600} reached 0.6. At this stage, all three strains were serially diluted and spotted on TRP- plates.

2.2.8. MMS Sensitivity Assay

MMS sensitivity assay SBY2, SBY3, SBY4, SBY5, and SBY6 were tested for DNA damage sensitivity. All strains were grown overnight in tryptophan dropout synthetic medium at 30°C. The next day, secondary culture was grown until 0.5 OD_{600} at 30°C. After OD600 reached 0.5, the culture was divided into three sets. One set of cells was treated with 0.01% (vol/vol) methyl methanesulfonate (MMS) (Sigma–Aldrich), and the second set of cells was treated with 0.04% MMS and grown at 30°C for 2 h. The third set was continuously grown at 30°C for 2 h without MMS. After this process, approximately 1000 untreated and 1000 treated cells were spread on selective media and incubated at 30°C for 2–3 days. We calculated the percent survival by dividing the number of colonies in the treated plate with untreated ones for each strain.

2.3. BIOCHEMICAL METHODS

2.3.1. Western Blot method:

The protein samples of interest were separated on SDS-PAGE and transferred onto the Poly Vinylidene di Fluoride (PVDF) membrane (132). Before the transfer, the membrane was treated with methanol for 20 seconds, water for 2 minutes, with 1x transfer buffer (5.86 gm glycine, 11.64 gm Tris base, and 0.75 gm SDS) for 5 minutes. A semi-dry transfer method was used, and the transfer conditions were 240mA of current for 80 minutes. After the transfer, blocking of the membrane was done by 5% blocking buffer (5 gm skimmed milk powder, 100ml 1x TBS) for 2 hours at RT. The blot was added with the primary antibody and kept at 4°C overnight in a rocking position. The next day, washing of the blot was done with 1xTBST (0.2 M Tris base, 9% sodium chloride pH 7.6, and 0.1% Tween 20) three times. HRP conjugated antibodies were used for secondary antibody treatment for 2 hours, washed as previously described. The blot was developed by the chemiluminescence system (Pierce) substrate and visualized in a Bio-Rad chemidoc system. The primary antibodies used were mouse anti-hAct1 antibody (Abcam) and rabbit anti-PfTopoIII antibody (KR Instruments and Chemicals) at 1: 5000 dilutions. Anti-PfTopoIII is a peptide antibody against DSNNYSDETDDYYGDEKK of PfTopoIII protein. For subcellular fractionation, we used rabbit anti-histone H3 antibody (Imperial Life Sciences) and mouse anti-Cytochrome C antibody (Allied Scientific) at 1: 5000 and 1: 3000 dilutions, respectively. For secondary antibodies, horseradish peroxide conjugated antirabbit antibody (Promega), and anti-mouse antibody (Santa Cruz Biotechnology Inc. CA, U.S.A) were used at 1: 10 000 dilutions.

To check the expression of the PfTopoIII in the yeast surrogate system, proteins were isolated from the SBY3, SBY4, and SBY5 strains. The primary antibody against anti-ScActin (Abcam) was used at a concentration of 1: 10 000 dilutions. The western blots were developed using a chemiluminescent detection system (Pierce). Every experiment was repeated at least three times, and band intensities were quantified using Image J software. Mean relative densities were plotted using GraphPad prism. We used rabbit anti-GFP antibody (Allied Scientific Products) at 1: 5000 dilutions to detect the expression of GFP fused PfTopoIII and the charged linker deletion mutant in the transgenic parasite. To further study HU's effects on protein levels of PfTopoIII, western blotting analysis was performed on 20 ml *Plasmodium* cultures. The culture was divided equally into two groups: samples treated with 10 mM HU and kept for 20 h at 37°C and an untreated group. After 20 h, parasitized erythrocytes specific to the late-schizont stage were harvested, treated with 0.15% saponin, and washed three times with 1× PBS. Later, the protein was isolated by using standard procedures.

2.3.2. Hydroxy Urea treatment

In survivability assays, HU (Sigma) was added to the highly synchronized late-trophozoite stage of *P. falciparum* culture (~1% parasitemia) at a concentration of 2.5 mM for 30 h at 37°C. Parasitemia was determined via Giemsa staining (Sigma) every 10 h by counting at least 2000 RBCs. For each strain, 3–4 independent assays were conducted. In return-to-growth assays, 1% synchronized parasites were treated with 2.5 mM HU for 6 h. After 6 h treatment with HU, cells were washed twice incomplete RPMI media and allowed to grow for 26 h in complete media. Then 6 h and 26 h slides were

prepared for both HU-treated and untreated samples, and parasitemia were measured. This experiment was repeated three times in 3D7 and strains over-expressing *PftopoIII(⊿259–337)-GFP* and *PfTOPOIII-GFP*.

2.3.3. Site-directed mutagenesis

Point mutations and deletion mutations were introduced in PfTopoIII using the splice overlap extension (SOE) PCR technique. Primer sets with the required mutations were designed to incorporate mutations in *PfTOPOIII* at the desired locations. *Plasmodium* 3D7 genomic DNA was used as a template, and a full-length gene was amplified in two segments to insert a point mutation. To amplify the first and second segments to generate the *PfY421FtopoIII* mutation, the OSB 334/OSB 452 and OSB 453/OSB 335 primer sets were used, respectively. Then full-length PfTopoIII containing the Y421F mutation was amplified using the first two segments along with primer set OSB 334 and OSB 335. Finally, *PfY421FtopoIII* mutant was cloned into pTA yeast expression vector between the BamH1 and SalI sites. After successful cloning, the *PfY421FtopoIII* construct was sequenced to confirm the desired mutation. To generate a Y-to-F mutation at the 421st aa residue, we changed the codons TAC to TTT.

Similarly, to generate the *Pf(⊿259–337)topoIII* mutation, the OSB 334/OSB 450 and OSB 451/OSB 335 primer sets were used, respectively, for amplification, as mentioned earlier. Then full-length PfTopoIII with the deletion of the abovementioned segment was amplified using the first two segments along with the primer set OSB 334/OSB 335. Finally, a *Pf(⊿259–337)topoIII* deletion mutant was cloned into pTA yeast expression vector between the BamH1 and

SalI sites. After successful cloning, the *Pf(⊿259–337) topoIII* construct was sequenced to confirm the desired deletion.

2.3.4. Immunofluorescence assay

Plasmodium culture (6% parasitemia in the late-schizont stage) harboring PfTopoIII-GFP expression vector and that harboring *PftopoIII(⊿259–337)-GFP* expression vector was stained with DAPI and separately with Mitotracker for 30 min at 37°C before imaging. Subsequently, fluorescence levels assessed via DAPI, Mitotracker, and GFP were observed and captured from live cells using a fluorescence microscope (Axio Observer Z1 with Apotome, Carl Zeiss).

2.4 *Plasmodium falciparum* BIOLOGY METHODS

2.4.1 Washing of RBCs:

10 ml of blood was collected from a volunteer in a tube containing 1.4 ml of CPDA (2.63% Trisodium citrate, 0.32% citric acid, 3.19% dextrose, 0.22% $NaH_2PO_4.H_2O$ and 0.02% adenine), and kept at 4^{o}C. Preferably the blood was washed within 6 hours of collection. The collected blood was centrifuged at 1,500 rpm for 15 minutes at 4^{o}C. The upper yellow part (serum) and the white buffy layer at the junction were removed carefully with a Pasteur pipette. The RBC layer volume was checked, and an equal volume of incomplete medium was gently mixed with it. The tube was centrifuged at 2,500 rpm for 10 minutes at 4^{o}C. The supernatant was removed with the help of a Pasteur pipette. The same procedure was repeated twice. Finally, the washed RBC cells were mixed with an equal volume of incomplete medium to make 50% hematocrit (hct) and stored at 4^{o}C. The tube was marked with the blood group and date of wash.

2.4.2. Preparation of complete medium:

RPMI 1640 with L-Glutamine and 25mM Hepes (Lonza) is an incomplete medium. Albumax II (5 mg/ml) (Invitrogen) and hypoxanthine (0.5 mg/ml) (Sigma) are added to the incomplete medium to make it compatible with *Plasmodium* culture. Before using it as a complete medium, it was filter-sterilized using a 0.2-micron filter bottle (Millipore).

2.4.3. Maintenance of *P. falciparum in-vitro* culture:

In vitro, *P. falciparum* culture was maintained by changing the culture's medium every day followed by subculturing every other day. The blood cells settle to the bottom of the culture plate, forming a thin layer. For maintaining the culture, we need to add a fresh medium for that the old culture medium is aspirated out under aseptic condition by not disturbing the cellular layer. Then required amount of pre-warmed (37^{o}C) complete medium was added to the well and mixed gently with the culture. The culture was maintained by the "Candle-jar" method (134). For sub-culture, once the medium was changed, 0.5 ml of the culture was dispensed to the next well; then 0.5 ml of washed RBCs (50 % hematocrit) and 4 ml of complete medium was added to it. Giemsa staining (Sigma) was done to observe the parasites under a microscope.

2.4.4. Thawing of *Plasmodium* parasites from liquid nitrogen:

The frozen parasite vial was taken out from the liquid nitrogen tank and kept for warming in a water bath at 37^{o}C for 3 minutes. Proper care was taken to avoid contamination of the vial. The vial content was transferred into a new 50 ml falcon tube, and 0.2 ml of solution 1 (12% NaCl) was added dropwise (approximately one drop/second) by shaking gently. After adding solution 1,

the sample was left undisturbed for 3-4 minutes. To this, 10ml of solution 2 (1.6% NaCl) was added dropwise with intermittent gentle shaking. The sample was spun for 10 minutes at 2000 rpm at room temperature. The supernatant was aspirated, and to the pellet, 10ml of solution 3 (0.9%NaCl, 0.2% Glucose) was added dropwise by gentle shaking. The sample was spun for 10 minutes at 2000 rpm. The supernatant was discarded, and to the pellet, 0.2ml of fresh RBCs (50% hct), 3 ml of complete medium was added. Finally, the contents in the tube were transferred into a sterile 6 well culture plate and kept in a candle jar which was kept in a 37°C incubator. The volume of solutions added was calculated according to l ml of the sample.

2.4.5. Freezing of *Plasmodium* parasites:

The early ring-stage parasites with a parasitemia of about 2-4% were transferred into a 15 ml falcon tube, centrifuged at 2500 rpm for 10 minutes. The supernatant was aspirated to the estimated PCV (packed cell volume), an equal volume of freezing solution (5% Glycerol, 1.6% sodium lactate, 0.03% KCl, 25 mM Sodium phosphate) was added dropwise (1 drop/second). The contents were mixed gently and left undisturbed for 5 minutes. To the tube, 1.3 volumes of the freezing solution were added dropwise. Finally, 1ml of the sample was transferred into each cryo-vial. These cryo-vials were transferred to a frozen container having iso-propanol for gradual freezing. The freezing container was stored at -20°C overnight. The next day, for long-term storage, the vials were shifted into a liquid nitrogen tank.

2.4.6. Maintenance of *Plasmodium in vitro* culture:

The candle jar method was followed to maintain strains of *P. falciparum in vitro*. The culture was maintained in RPMI-1640 complete media containing Albumax-II (5mg/ml), Hypoxanthine (0.5mg/ml). The hematocrit of RBC was maintained at 5%, and subculture was done once the parasitemia reaches 2.5%. During subculture, parasitemia was diluted to 0.5% by adding fresh media and blood. The volume of the culture was adjusted to 5 ml accordingly. Parasitemia was estimated by counting the Giemsa-stained blood smears.

2.4.7. Synchronization of parasites by sorbitol method:

10 ml ring-stage parasites were centrifuged at 2500 rpm for 10 min at room temperature. The supernatant was removed using a Pasteur pipette, and the pellet was carefully re-suspended in two bed volumes of pre-warmed 5% sorbitol (Sigma) solution at 37°C. The sample was incubated at 37°C for 10 min with intermittent tapping. After that, a pre-warmed incomplete medium was added to a volume of 10 ml, and the sample was centrifuged at 3000 rpm for 10 min. The supernatant was removed, and the pellet was washed thrice with the pre-warmed incomplete medium. Then the parasites were allowed to grow normally until the early ring stage, and sorbitol synchronization was performed again to obtain close to 100% synchronized ring-stage parasites (135). These synchronized parasites were grown further to obtain synchronized trophozoite-stage and synchronized schizont-stage parasites.

2.4.8. Genomic DNA isolation from *Plasmodium* parasites:

The parasite culture of 10 ml having 6-8 % parasitemia was harvested and spun for 10 minutes at 3000 rpm, RT. Two PCV volumes of 0.15% saponin were

added to the obtained pellet and incubated for 30 minutes in a 37°C water bath with intermittent vortexing. Then five pre-warmed incomplete medium volumes were added and centrifuged for 10 minutes at 6000 rpm at 4°C. The obtained pellet was washed with a 1x PBS (phosphate buffer saline) solution to remove saponin remnants. To this pellet, 75 µl of Milli-Q water and 25 µl of lysis buffer (10 mM Tris-HCl pH-8, 20 mM EDTA pH-8, 0.5% SDS, and 0.1mg proteinase K) was added and incubated at 37°C for 3 hrs. with intermittent mixing at every 30 minutes. After incubation, Milli-Q water was added to make the volume 400 µl, and to this, an equal volume of PCIA (phenol, chloroform, isoamyl alcohol) solution was added. The sample was centrifuged at 12000 rpm for 15 minutes at room temperature. The aqueous layer was collected into a new microfuge tube and treated with RNase for 30 minutes at 37°C. After RNase treatment, the PCIA step was repeated. To the aqueous layer obtained, 2.2 volumes of 100% ethanol and 1/10 volume of Solution 3 was added. The sample was kept at -80°C for overnight precipitation. The next day, the sample was spun for 30 minutes at 12000 rpm, 4°C. Finally, the pellet was in the 1xTE buffer, and the integrity of genomic DNA was checked by running agarose gel electrophoresis.

2.4.9. RNA isolation from *Plasmodium* parasites:

The parasite culture of about 10ml was harvested and centrifuged for 10 minutes at 3000 rpm. The supernatant was discarded, and the cell pellet was loosened by tapping. To the pellet, pre-warmed TRIzol (10 pellet volumes for the ring and 20 pellet volumes for trophozoite and schizont) was added. The pellet was shaken thoroughly to avoid clumping. The sample was incubated at 37°C for 5 minutes. After incubation, 0.2 TRIzol volumes of chloroform were

added, and the sample was shaken vigorously. The sample was allowed to settle for 2-3 minutes and centrifuged for 30 minutes at high speed, 4°C. The aqueous layer obtained was shifted to a new microfuge tube, and 1ml of 2-proponal was added. The sample was kept for incubation at 4°C overnight. The next day, the samples were centrifuged at 14000 rpm, 4°C for 30 minutes. The pellet was washed with 75% ethanol (prepared with DEPC treated water) and centrifuged for 30 minutes at 14000 rpm, 4°C. Finally, the pellet was air-dried and re-suspended in 50µl of DEPC water. The integrity of RNA was checked by running formaldehyde agarose gel electrophoresis, and the concentration was determined by measuring OD_{260}.

2.4.10. Cellular fractionation from *Plasmodium falciparum*:

40 ml of *Plasmodium* culture having 8% parasitemia was taken, and the packed volume was estimated. The pellet was re-suspended in two volumes of 0.15 % saponin (Sigma) and was incubated at 37ºC for 15 minutes with intermittent mixing. 5 volumes of incomplete medium were then added to it, and it was centrifuged at 4000 rpm for 10 minutes at 4ºC. The precipitated parasites were washed with 10 ml of 1x PBS thrice. It was then washed with 5 ml of buffer I (0.34 M sucrose, 15 mM NaCl, 0.2 mM EDTA, 0.2 mM EGTA, 15 mM Tri-Cl pH 7.4 and 0.2 mM PMSF). The parasite pellet was finally re-suspended in 5 ml of buffer II (buffer I containing 1 % TritonX-100) and was incubated at 4ºC for 30 minutes. This suspension was homogenized using a Dounce homogenizer using 25 complete strokes. The nuclei were separated by centrifugation at 600 x g for 5 minutes, and the supernatant (carrying organelle and cytosolic fractions) was transferred to a new tube. The obtained nuclei pellet was washed with buffer I and finally was re-suspended in 50 µl of low salt buffer [1.5 mM $MgCl_2$,

0.2 mM EDTA, 20 mM HEPES pH 7.9, 25% glycerol, and 1x protease inhibitor cocktail (Roche)] equal to half the packed nuclear volume and was used for nuclei sample.

The supernatant obtained initially (after nuclei pellet by spun at 600 x g) was subjected to centrifugation at 12000 rpm for 30 minutes at 4ºC to separate organelle fraction and cytosol. The obtained pellet was used an organelle fraction. The above two nuclear and organelle fraction was resuspended in 1X Laemmli buffer (Tris-HCl, 63 mM (pH 6.8), 10% Glycerol, 0.0005% Bromophenol blue, 0.1% 2-Mercaptoethanol). With these fractions, we performed a western blot to locate the localization of PfTopoIII.

2.4.11. Isolation of proteins from *Plasmodium* parasites:

Parasite cultures of about (5-10) ml were collected and centrifuged for 10 minutes at 3000 rpm, at room temperature. 2 PCV (packed cell volume) of 0.15% saponin was added and incubated at 37°C water bath for 20 minutes with intermittent mixing to the pellet. The sample was added with 5 volumes of pre-warmed incomplete medium and centrifuged at 4000 rpm for 10 minutes at 4°C. The obtained parasite pellet was washed with 1x PBS 3-4 times to remove saponin's remnants. Finally, the parasite pellet was resuspended in 1X Laemmli buffer (Tris-HCl, 63 mM (pH 6.8), 10% Glycerol, 0.0005% Bromophenol blue, 0.1% 2-Mercaptoethanol). The quality and integrity of protein preparation were checked by running SDS-PAGE.

2.4.12. Transfection of *Plasmodium falciparum*:

Synchronized early ring-stage parasites having parasitemia around 6-8% were taken for transfection. The desired plasmid (80-100 µg) was resuspended in 50µl

of cytomix solution (10mM K_2HPO_4 pH-7.6, 120mM KCl, 0.15mM $CaCl_2$, 25mM HEPES pH-7.6, 2mM EGTA pH-7.6, and 5mM $MgCl_2$) and kept in 4°C for overnight before the day of transfection. On the day of transfection, 10 ml of the parasite culture was centrifuged at 3000 rpm for 5 minutes at room temperature and, the supernatant was aspirated. The pellet was added with 5ml of pre-warmed cytomix solution and spun for 5 minutes at 3000 rpm. Washing with cytomix was repeated once again. To the pellet, 1250 µl of pre-warmed cytomix was added and pipetted gently. From the re-suspension, 350 µl was taken and added to a microfuge tube containing 50 µl of cytomix re-suspended DNA. The contents from the microfuge tube were transferred to the electroporator cuvette without generating any air bubbles. The cuvette was then placed in the Bio-Rad Gene Pulsar, and pulse was given by selecting the program with 0.31kV and 950 µF. After the pulse, the cuvette sample was mixed with cold complete media and transferred to 6 well culture plate. Pre-warmed complete media of about 3 ml and 100 µl of fresh RBC was added to the 6 well plate. The plate was kept in an incubator containing a candle jar at 37°C. The complete medium was changed daily until the parasitemia reaches up to 4-8 %. After the parasitemia was reached, pyrimethamine containing complete media was added to eliminate non-transfectants and allow only transfectants to grow.

2.5. IN SILICO METHODS

2.5.1. PfTopoIII structure modeling and molecular dynamics.

We used I-TASSER server to model the PfTopoIII structure [33], 4CGY (PDB ID) was used as a template [34]. For residues with no matching template, I-TASSER performs ab initio modeling. To check the stability of the modeled

structure, explicit solvent MD simulation was performed using Gromacs 4.5.5 [35] and CHARMM36 force field [36]. The apo-structure was solvated in an octahedron box with a TIP3P water model [37]. The charges on the protein were neutralized by adding chloride ions. NVT- and NPT-position restrained equilibrations were done for 200 ps and 1 ns, respectively. The modeled apo structure was used for 50 ns molecular dynamics (MD) simulations. A clustering calculation was performed on the last 10 ns of the trajectory from the 50 ns simulation of the PfTopoIII apo-structure. The centre of the largest cluster was chosen as the starting structure for the subsequent simulations. To study the binding of single-stranded DNA in the PfTopoIII structure, the *E. coli* structure was used. The 1I7D (PDB ID) [38] structure was aligned to the PfTopoIII to generate a holo-structure with a single-stranded DNA octamer. The holo structure of PfTopoIII was simulated for 100 ns using a similar procedure as mentioned above. VMD 1.9.2 [39] and Gromacs 4.5.5 [35] were used to analyze the trajectories. The root-mean-square fluctuations (RMSFs) of the Cα atoms of the entire protein were calculated using the grmsf module of Gromacs.

2.5.2. Comparative structure modeling and validation of PfTopoVIB and PfHsp90

The crystal or solution structure for PfTopoVIB is not solved yet. In the case of PfHsp90, although two crystal structures are solved, they are not of the full-length protein. Hence, homology-based structure modeling was carried out for both of the proteins. The sequences of PfTopoVIB and PfHsp90 were retrieved from the UniProtKB/Swiss-Prot database (136), and suitable templates were selected from the SMTL, a large structural database of experimentally determined protein structures, derived from the PDB (137). Target-template

sequence alignment was carried out using BLAST P suite (https://blast.ncbi.nlm.nih.gov/Blast.cgi?PAGE=Proteins). Near-native structures of PfTopoVIB and PfHsp90 were modeled using the automated mode (ProMod3 Version 1.2) integrated into the Swiss-Model server (138). Necessary energy minimization steps were also carried out for the predicted models using the GROMOS 43B1 force field (139) implemented in the Swiss-PDB viewer [http://www.expasy.org/spdbv]. The validation of both the modeled structures was carried out using the PROCHECK server (140) and the Ramachandran plot [http://services.mbi.ucla.edu/SAVES/Ramachandran/]. PROCHECK server checks the stereochemical quality of the modeled structures. The Ramachandran plot shows the residue-by-residue quality and stability of the favored and the disallowed regions in the protein model. ERRAT scores (141) were also predicted for the homology models through the Structural Analysis and the Verification Server (SAVES) [https://servicesn.mbi.ucla.edu/SAVES] of UCLA-DOE Lab.

2.5.3. Design and preparation of Radicicol analogs

The 3D structure of Radicicol, downloaded from the PubChem compound database (142), was used as the reference molecular scaffold for the in-silico design of different derivatives (structural analogs). MarvinSketch tool (https://chemaxon.com/products/marvin), version 16.8.8.0 was used to draw the analogs by modifying different atoms, functional groups, and side chains Radicicol. Our strategy was to modify the structure of Radicicol and design novel analogs by substituting the functional groups, which potentially enhance its inhibition against PfTopoVIB and reduce its inhibition of PfHsp90. The reported Structure-Activity Relationship (SAR) of Radicicol (143) was

considered for selecting the attachment point for the modification, and various functional groups were identified from relevant literature (144-149). We substituted different functional groups at specific attachment points of Radicicol without disturbing the macrocyclic ring required for the bioactivity of Radicicol. The designed analogs were saved along with their 10 conformers each for further preparation. 'Prepare ligand' protocol in Biovia Discovery Studio (DS) 4.0 (150) was used to prepare the analog dataset, which optimizes the charges of common groups, adds hydrogen atoms, generates tautomers/ isomers, and removes duplicate/bad conformers. 'Generate Conformations' protocol, using a quasi-exhaustive systematic search method (FAST conformation generation method) (151) employed in DS 4.0 was used to create all the possible diverse 3D conformers of each analog, and all the resulting diverse conformers were stored as a single file for further docking step.

2.5.4. Structure-based virtual screening of Radicicol analogs against PfTopoVIB and PfHsp90

Along with Radicicol and its analogs, the Adenosine triphosphate (ATP) molecule (downloaded from PubChem compound database) was also used as the positive control for docking studies. Since ATP binds to the monomeric form of TopoVIB, we have used the monomers of PfTopoVIB and PfHsp90 as our template for our docking studies. Two sets of docking were carried out in a site-specific manner. The 3D structures of PfTopoVIB and PfHsp90 served as the receptors, and the Radicicol derivatives with their conformers served as the analog dataset. The docking program LibDock (152,153) implemented in DS 4.0 performs a high-throughput docking by aligning analog conformations to polar and apolar receptor interaction sites (hotspots). The binding site cavities

were analyzed for both the target protein structures using the 'Eraser algorithm' (154) implemented in DS 4.0. A grid with coordinates of -9.153 Å, -79.659 Å, and 25.38 Å for X, Y, and Z, respectively with the spacing of 0.5 Å was used for positioning the binding site. In PfHsp90, the grid coordinates of 21.963, 32.991 and 14.764 for X, Y and Z respectively with spacing of 0.5 Å were used. The grid covered the Bergerat fold residues, which were specified as the target protein site features (termed as HotSpots) by the LibDock program for calculating the binding affinity of analogs with the receptors. Receptor-analog docking study was performed using LibDock protocol against PfTopoVIB as well as PfHsp90. An empirical scoring function, LigScore (155), was employed to score the docked ligand poses, and the complexes were ranked and sorted according to the descending order of the LibDock score. The best-docked pose for each analog towards each protein was identified based on the highest LibDock score and compared with the LibDock score of ATP and Radicicol. The lead molecules were selected based on higher LibDock scores and specific docking with PfTopoVIB and little or no docking with PfHsp90. The interacting amino acids of the complexes were analyzed, and the types of molecular interactions, including conventional hydrogen bonds, carbon-hydrogen bonds, electrostatic interactions, and hydrophobic interactions, were noted.

Table 1: Plasmids used in this study

Name of plasmid	Description about plasmid	Source
pTZ57R/T	TA cloning vector having ampicillin resistance gene.	Thermo Fisher Scientific
pET28a	Bacterial expression vector having T7 promoter and Kanamycin resistance gene. It expresses the protein with N-terminal HIS tag.	Novagen
pGBDUC1	Yeast two-hybrid bait vector having *URA3* marker and ampicillin resistance gene. It is a 2μ plasmid that expresses the binding domain for the Gal4 transcription factor.	(156)
pGADC1	Yeast two-hybrid prey vector with *LEU2* marker and ampicillin resistance gene. It is a 2μ plasmid that expresses the activation domain for the Gal4 transcription factor.	(156)
Pta	Yeast expression vector having GPD/ADH1 promoter. It has a TRP marker and ampicillin resistance gene.	(132)
pPfCENv3	Parasite expression vector having PfCAM promoter. It is a	

	centromeric plasmid with *Blasticidin S deaminase* marker. It expresses the protein with C- terminal GFP tag.	(a gift from Dr. Puran Singh Sijwali, CCMB, Hyderabad) (157)
pFA6a-HIS3	The plasmid was used for gene knockout using *HIS* insertion. It has an ampicillin resistance gene.	(133)

Table 2: List of primers used in this study

S. No.	Name of the primer	Sequence	Purpose
1.	OSB 334	5′TGCGGATCCATGGCACG ACTGAAAGTGTTG 3'	Forward primer to amplify full-length *PfTOPOIII*
2.	OSB 335	5′TGCGTCGACTTATGTAT ATGAGAGCTGATCG 3'	Reverse primer to amplify full-length *PfTOPOIII*
3.	OSB 337	5' TAGGTATAGCCTTAGTAC AATC3'	forward primer to amplify 254 bp of the 3' end of *PfTOPOIII*
4.	OSB 346	5' TGCGGATCCATGAAAGTG CTATGTGTCGC 3'	Forward primer to amplify full length *ScTOPOIII*
5	OSB 455	5' TGCGTCGACTTACATGGA TGCCTTGACAC 3'	Reverse primer to amplify full-length *ScTOPOIII*
6.	OSB 348	5'GCGCTCGCTTCAGCTAC GTAAAGGTGTATTA TAGACAATACGGATCCCC GGGTTAATTAA 3'	Forward primer to amplify the deletion cassette to create *ScTOPOIII* knockout

7.	OSB 385	5' TTACATGGATGCCTTGAC ACGGTCATAAAC TTGCAAGAGAGAATTCGA GCTCGTTTAAAC3'	Reverse primer to amplify the deletion cassette to create *ScTOPOIII* knockout
8.	OSB 350	5' ACATTGGATAATGGCGTG AAC 3'	Forward primer complementary to 150 bp upstream of *ScTOPOIII*
9.	OSB 497	5' TGCAGATCTCCTGTATAT GAGAGCTGATCGGG 3'	Reverse primer to clone *PfTOPOIII* as C-terminal GFP fusion
10.	OSB 452	5' ATAATTGGTTTCTGTTCT AGGAAAACTAATAT AAC 3'	Reverse primer to create *PfY421FtopoIII* mutant
11.	OSB 453	5' AACAAGGGTTATATTAGT TTTCCTAGAACAGAAAC 3'	Forward primer to create *PfY421FtopoIII* mutant
12.	OSB 450	5' GTAAAATCTACAACATTA TCATAATTATTTTCATCAT CCATAG 3'	Reverse primer to create *Pf(⊿1259-337)topoIII* mutant

13.	OSB 451	5' TGAAAATAATTATGATAA TGTTGTAGATTTTACATG GTC3'	Forward primer to create *Pf(Δ1259-337)topoIII* mutant
14.	OMKB 198	5' AGCTAGCTAATAGGCAAT C 3'	Forward primer to amplify 314 bp at the 3' end of *PfRAD51*
15.	OMKB 17	5' ATCGTCGACTTTATTTTTC CTCATAATCTGC 3'	Reverse primer to amplify *PfRAD51*
16.	OMKB 332	5' ATTCGAGATAAAGGAATT ATTGAAG 3'	Forward primer to amplify 149 bp at the 3' end of *PfBLM*
17.	OMKB 333	5' ATGCTTCCTCTTTACATTC ATAG 3'	Reverse primer to amplify *PfBLM*
18.	OMKB 334	5' ATGAACATAGTGTTAATA ATATGC 3'	Forward primer to amplify 225 bp at the 3' end of *PfWRN*
19.	OMKB 335	5' TATAAACGAACTGATCTA ATATATC 3'	Reverse primer to amplify *PfWRN*

20.	OMKB 540	5' GAGTGGATTAAATGCCCAGCC 3'	Forward primer for amplification of fragment A
21.	OSB 251	5' GCATCTCTACAAACTACAGAG 3'	Reverse primer for amplification of fragment A
22.	OSB 493	5' TACTCTGTAGTTTGTAGAGATGC 3'	Forward primer for the amplification of fragment B
23.	OSB 495	5' CCTCACAGCTTTATTCGGTCC 3'	Reverse primer for the amplification of fragment B
24.	OMKB 615	5' CTGGCCTACACTATAAGAACG 3'	Forward primer for amplification of fragment C
25.	OSB 176	5' CATCCCATAGCAAGTATCATAG 3'	Reverse primer for amplification of fragment C
26.	OMKB 616	5' CTACTGGTTTAGAAGTTGATAC 3'	Forward primer for the amplification of fragment D

27.	OMKB 617	5' TACTGGAATAGAGGATAA CAAG 3'	Reverse primer for amplification of fragment D
28.	OMKB 618	5' GTTATCCTCTATTCCAGTA GC 3'	Forward primer for the amplification of fragment E
29.	OMKB 619	5' CATACATCCTAACATTAAT AACG 3'	Reverse primer for amplification of fragment E
30.	OMKB 620	5' CGCTGACTTCCTGGCTAA AC 3'	Forward primer for amplification of fragment F
31.	OMKB 541	5' ATTGTTCTACATTACGAG ATACC 3'	Reverse primer for the amplification of fragment F

Table 3: List of the strains used in this study

Strain	Genotype	Source
SBY1	*MATa leu2-3,112 trp1-1 can1-100 ura3-1 ade2-1 his3-11,15 [phi+] TOPOIII::HIS3*	This study
SBY2	*MATa leu2-3,112 trp1-1 can1-100 ura3-1 ade2-1 his3-11,15 [phi+] TOPOIII::HIS3 pTA*	This study
SBY3	*MATa leu2-3,112 trp1-1 can1-100 ura3-1 ade2-1 his3-11,15 [phi+] TOPOIII::HIS3 pTAScTOPOIII*	This study
SBY4	*MATa leu2-3,112 trp1-1 can1-100 ura3-1 ade2-1 his3-11,15 [phi+] TopoIII::HIS3 pTAPfTOPOIII*	This study
SBY5	*MATa leu2-3,112 trp1-1 can1-100 ura3-1 ade2-1 his3-11,15 [phi+] TopoIII::HIS3 pTAPfY421FtopoIII*	This study
SBY6	*MATa leu2-3,112 trp1-1 can1-100 ura3-1 ade2-1 his3-11,15 [phi+] TOPOIII::HIS3 pTAPf(⊿259-337)topoIII*	This study
PJ69 4a	*MATa trpl-901 leu2-3,112 ura3-52 his3-200 ga14Δ ga180Δ LYS2 :: GALl-HIS3 GAL2-ADE2, met2::GAL7-lacZ*	(158)
PMY 3	*MATa trpl-901 leu2-3,112 ura3-52 his3-200 ga14Δ ga180Δ LYS2 :: GALl-HIS3 GAL2-ADE2, met2::GAL7-lacZ pGADC1,pGBDUC1*	(158)
HCY 1	*MATa trpl-901 leu2-3,112 ura3-52 his3-200 ga14Δ ga180Δ LYS2 :: GALl-HIS3 GAL2-ADE2,*	This study

	met2::GAL7-lacZ pGADC1/PfBLM, pGBDUC1/PfTOPOIII	
HCY 2	*MATa trpl-901 leu2-3,112 ura3-52 his3-200 ga14Δ ga180Δ LYS2 :: GALl-HIS3 GAL2-ADE2, met2::GAL7-lacZ pGADC1/PfWRN, pGBDUC1/PfTOPOIII*	This study
HCY 3	*MATa trpl-901 leu2-3,112 ura3-52 his3-200 ga14Δ ga180Δ LYS2 :: GALl-HIS3 GAL2-ADE2, met2::GAL7-lacZ pGADC1/PfBLM, pGBDUC1/Pf(⊿259-337)topoIII*	This study
HCY 4	*MATa trpl-901 leu2-3,112 ura3-52 his3-200 ga14Δ ga180Δ LYS2 :: GALl-HIS3 GAL2-ADE2, met2::GAL7-lacZ pGADC1/PfWRN, pGBDUC1/Pf(⊿259-337)topoIII*	This study
HCY 7	*MATa trpl-901 leu2-3,112 ura3-52 his3-200 ga14Δ ga180Δ LYS2 :: GALl-HIS3 GAL2-ADE2, met2::GAL7-lacZ pGADC1, pGBDUC1/PfTOPOIII*	This study
HCY 8	*MATa trpl-901 leu2-3,112 ura3-52 his3-200 ga14Δ ga180Δ LYS2 :: GALl-HIS3 GAL2-ADE2, met2::GAL7-lacZ pGADC1/PfBLM, pGBDUC1*	This study
HCY 9	*MATa trpl-901 leu2-3,112 ura3-52 his3-200 ga14Δ ga180Δ LYS2 :: GALl-HIS3 GAL2-ADE2, met2::GAL7-lacZ pGADC1/PfWRN, pGBDUC1*	This study

HCY 10	*MATa trpl-901 leu2-3,112 ura3-52 his3-200 ga14Δ ga180Δ LYS2 :: GALl-HIS3 GAL2-ADE2, met2::GAL7-lacZ pGADC1, pGBDUC1/Pf(⊿259-337)topoIII.*	This study.

CHAPTER-3

FUNCTIONAL CHARACTERIZATION OF PfTopoIII AND ITS UNIQUE CHARGED DOMAIN

3.1. Domain analysis of PfTopoIII and its comparison with HsTopoIII

3.1.1. A unique charged domain in PfTopoIII

The *P. falciparum* genome database (http://www.plasmoDB.org) shows the presence of a putative PfTopoIII (Gene ID: PF3D7_1347100) gene. It has no intron, and it is predicted to code a 710 aa protein. The phylogenetic analyses show that prokaryotic and eukaryotic sequences formed two distinct branches from the root. The TopoIII sequence from *P. falciparum* was close to ScTopoIII and human TopoIIIα (Figure 5A), while the TopoIII sequences from *E. coli*, *V. cholerae*, *V. nereis*, *E. lignolyticus* and *S. enterica* were clustered together.

Multiple sequence alignment of PfTopoIII showed significant homology in the catalytic TOPRIM domain (aa 5 to 150) across various TopoIII sequences (Figure 5B) with two conserved aspartates at positions 118 and 120 and one conserved glutamate at position 122 (red box in the figure). The catalytic tyrosine residue of the enzyme is located at position 421 (blue star) within a highly conserved GYISYPRTET sequence (green box). PfTopoIII lacks a stretch of 30 aa residues at the N-terminal end and an extended 362 aa at the C-terminal domain that are present in human and mouse TopoIIIα. These extended N-terminal and C-terminal regions are also absent from ScTopoIII. However, there is a unique charged amino acid containing region spanning residues 259 to 337, which is absent from other eukaryotic TopoIII (Figure 5C). It showed 75% sequence identity with *Plasmodium berghei* TopoIII and 35–39% sequence identity with other orthologs of TopoIII (Table 4).

Table 4: Similarity and identity amongst Topoisomerase orthologs

Species	*Species*				
	P. falciparum	*P. berghei*	*H. sapiens*	*M. musculus*	*S. cerevisiae*
P. falciparum	*100*	*75(83)*	*39(60)*	*38(61)*	*35(57)*
P. berghei		*100*	*40(62)*	*39(62)*	*35(59)*
H. sapiens			*100*	*87(91)*	*41(58)*
M. musculus				*100*	*41(59)*
S. cerevisiae					*100*

Numbers in parentheses represent % similarity and outside parentheses represents % identity

A.

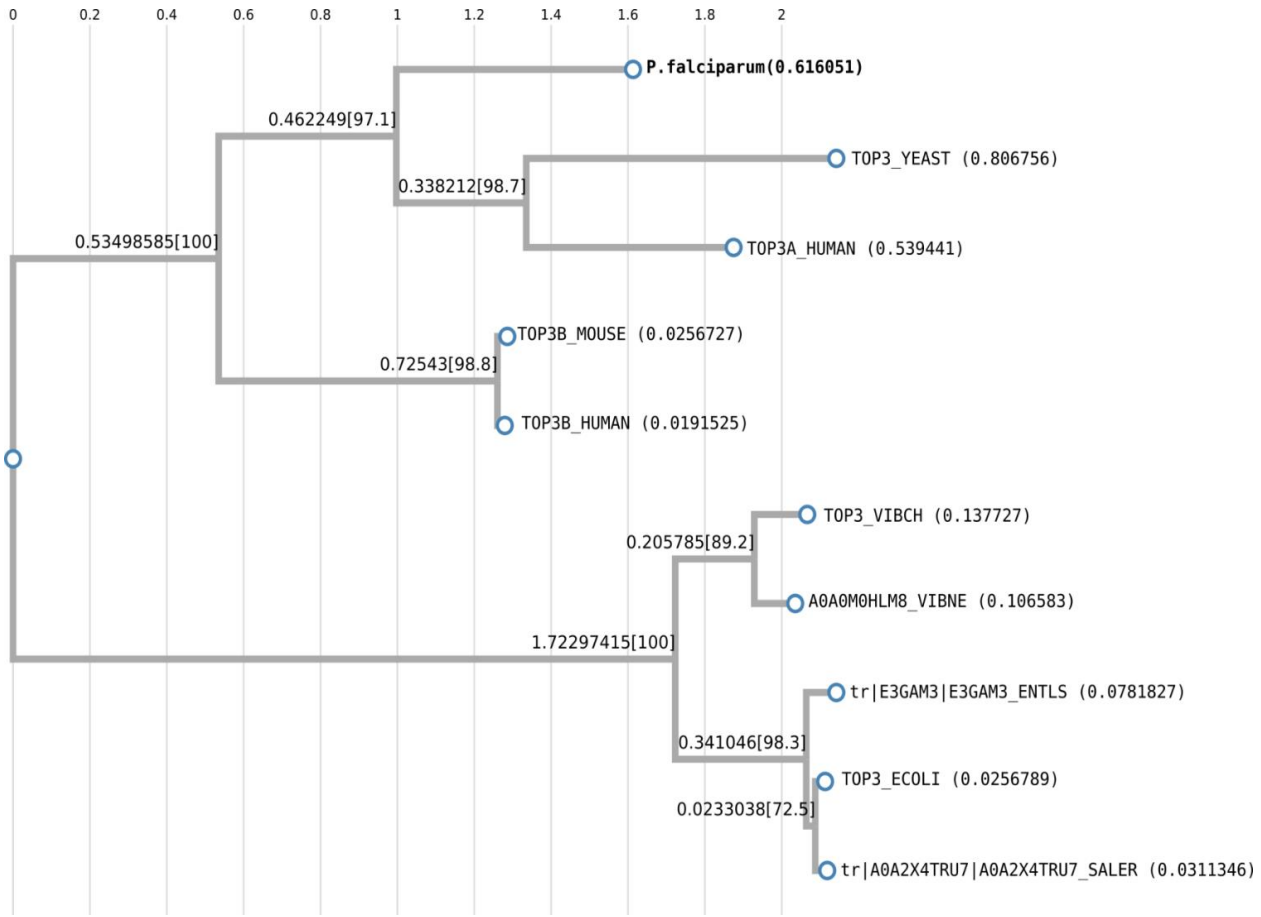
0
0.2
0.4
0.6
0.8
1
1.2
1.4
1.6
1.8
2
P.falciparum(0.616051)
0.462249[97.1]
TOP3_YEAST (0.806756)
0.338212[98.7]
0.53498585[100]
TOP3A_HUMAN (0.539441)
TOP3B_MOUSE (0.0256727)
0.72543[98.8]
TOP3B_HUMAN (0.0191525)
TOP3_VIBCH (0.137727)
0.205785[89.2]
A0A0M0HLM8_VIBNE (0.106583)
1.72297415[100]
tr|E3GAM3|E3GAM3_ENTLS (0.0781827)
0.341046[98.3]
TOP3_ECOLI (0.0256789)
0.0233038[72.5]
tr|A0A2X4TRU7|A0A2X4TRU7_SALER (0.0311346)

B.

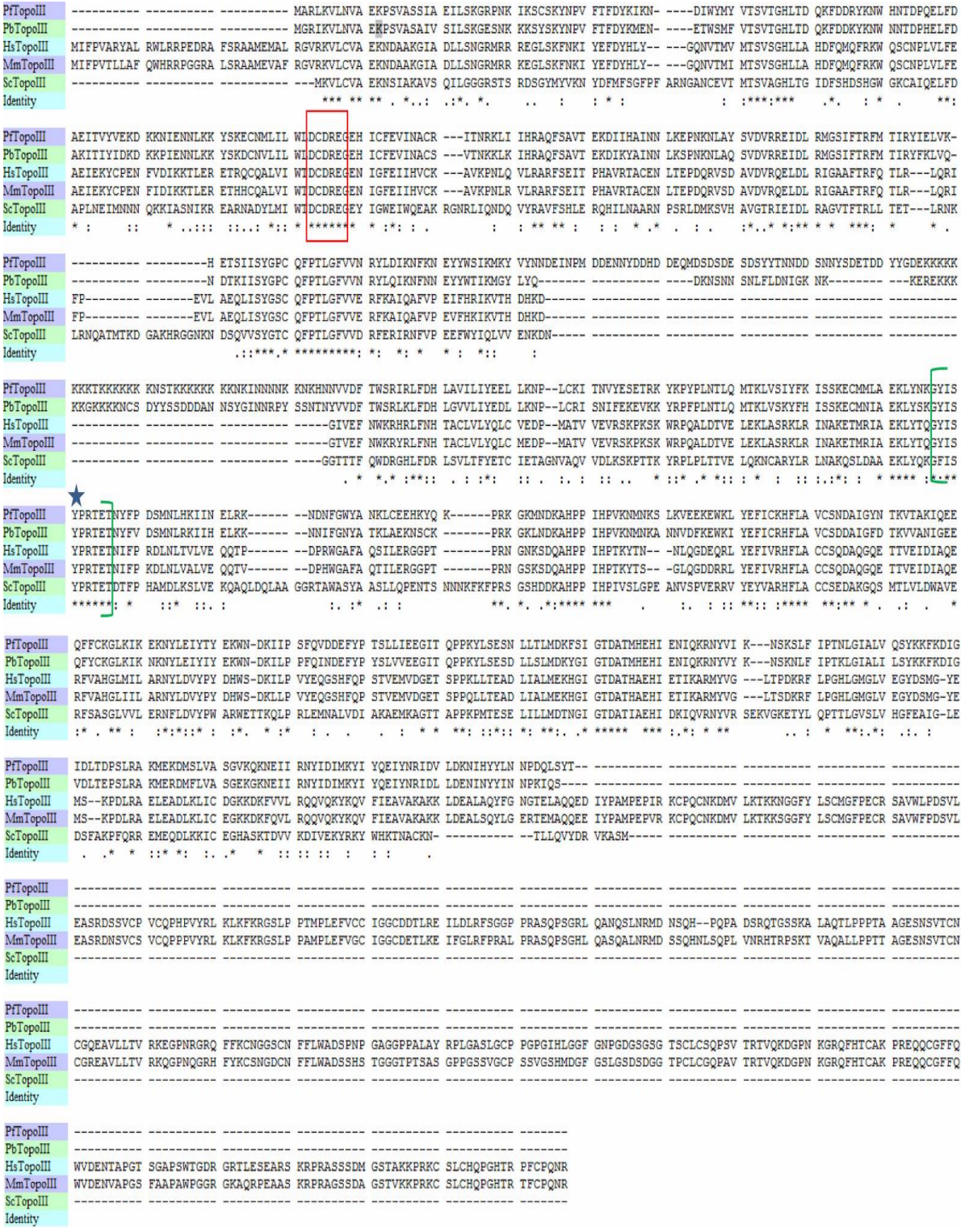
PfTopoIII
PbTopoIII
HsTopoIII
MmTopoIII
ScTopoIII
Identity

C.

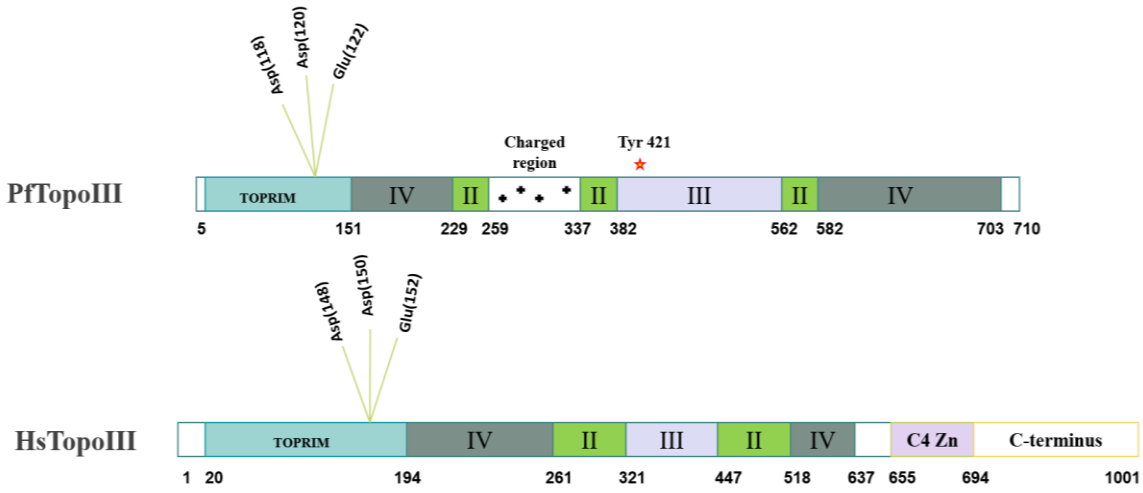

Figure 5: Sequence analysis results show the identification of a unique charged domain in PfTopoIII. A) Phylogenetic analysis of TopoIII protein sequences obtained from various prokaryotic and eukaryotic organisms. B) Multiple sequence alignment of PfTopoIII (*P. falciparum*), PbTopoIII (*Plasmodium berghei*), HsTopoIIIα (*Homo sapiens*), MmTopoIIIα (*Mus musculus*), and ScTopoIII (*Saccharomyces cerevisiae*) shows the presence of two conserved aspartate residues and one glutamate residue in the toprim domain (red box). Moreover, one conserved tyrosine residue (represented by a blue star) is present in the catalytic domain (green box). C) Domain analysis of PfTopoIII and HsTopoIII. The charged region is present at 259-337 amino acid region.

3.1.2. Molecular dynamic simulations (MDS) indicate that the flexible charged domain of PfTopoIII stabilizes upon DNA binding

The following molecular dynamics study has been conducted in collaboration with Dr. Arijit Roy (TCS innovations). This bioinformatics study aimed to predict the structure of the enzyme and understand whether the charged domain is involved in DNA binding. We modeled PfTopoIII using the I-TASSER server by selecting human TopoIIIα as a template (PDB ID: 4CGY) (Figure 6A). Domain analyses of PfTopoIII indicated the presence of an extra charged region within domain II that was disordered and away from the DNA binding region. The stability of the structure was evaluated via MDS for 50 ns. During the simulations, the PfTopoIII structure was stable, but the charged region showed large fluctuations. In a 50 ns apo-PfTopoIII simulation, the charged domain remained away from the DNA binding region (Figure 6B). To understand whether the charged domain had any role in DNA binding, we compared it to the structure of *E. coli* TopoIII, which has a charged loop similar to that of PfTopoIII (61). To that end, the structure of *E. coli* TopoIII (PDB ID: 1I7D) with a single-stranded DNA octamer (5'- CGCAACTT 3') was aligned to the PfTopoIII and the single-stranded DNA octamer was placed in the binding site to generate a structure of PfTopoIII bound with DNA. The holo structure of PfTopoIII was simulated for 100 ns using a similar procedure as mentioned above. RMSFs of the PfTopoIII-DNA complex were computed for the Cα atoms of complete protein to capture the dynamics of individual amino acids. From the RMSF plot, the maximum fluctuations were observed in parts of the charged domain, the Toprim domain, and domain III (Figure 6B). Other fluctuations were also observed in the amino and carboxyl-terminal of

the protein (Figure 6C). The principal component analyses (PCA) were used to identify the dominant motions during the simulations (159), both, PC1 and PC2 showed major fluctuations in the charged domain with similar direction, towards the bindings site of single-stranded DNA (Figure 6D). PC1 also showed fluctuations in parts of Toprim and domain III, which are in the opposite direction, indicating the opening of a central hole of the PfTopoIII protein (Figure 6D).

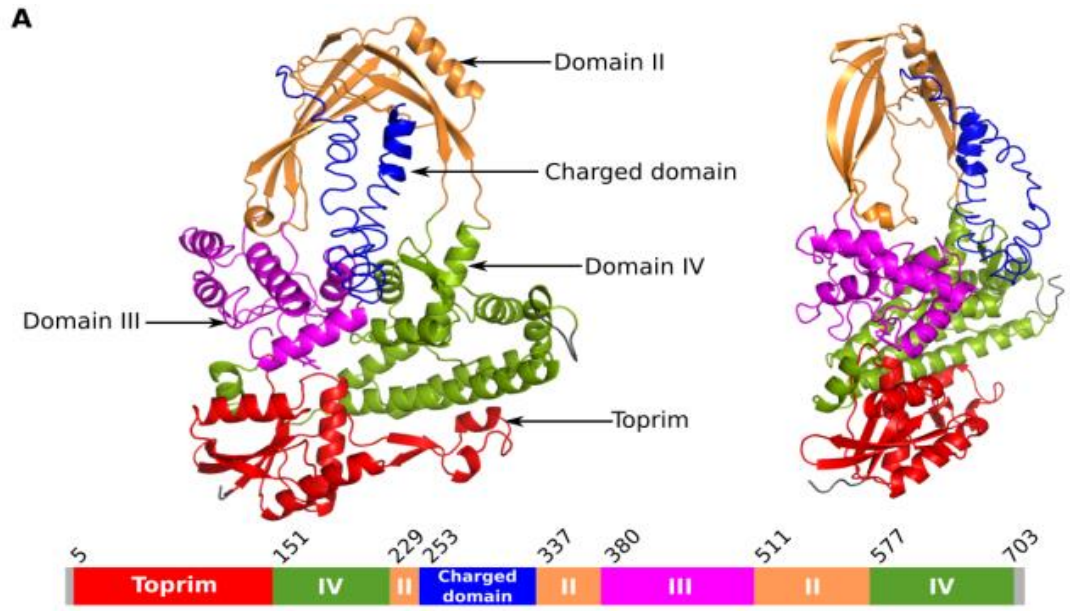
A
Domain II
Charged domain
Domain IV
Domain III
Toprim
5
151
229
253
337
380
511
577
703
Toprim
IV
II
Charged domain
II
III
II
IV

B.

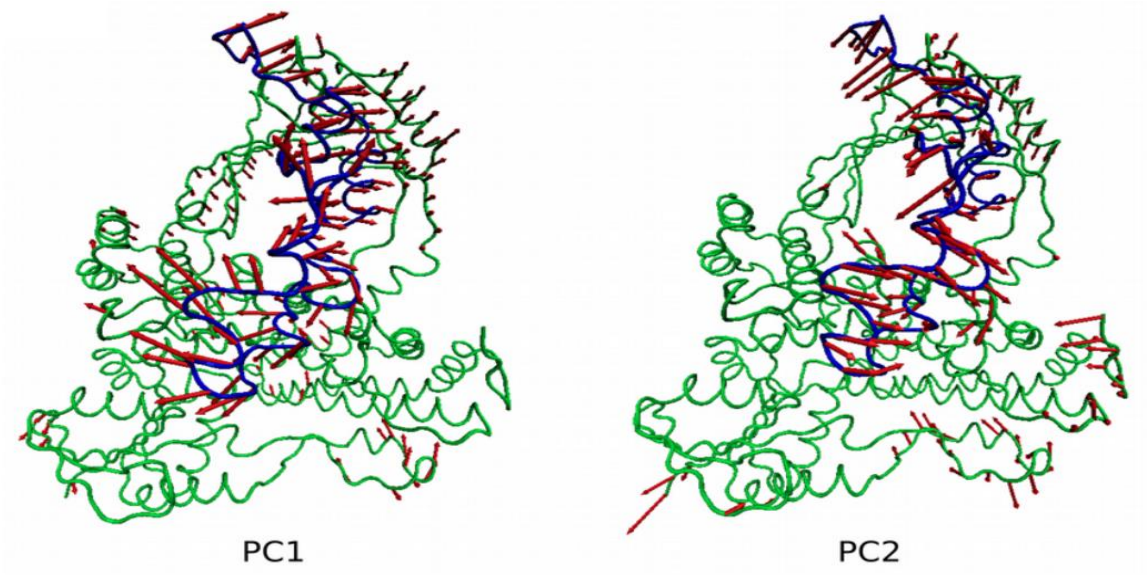
PC1
PC2

C

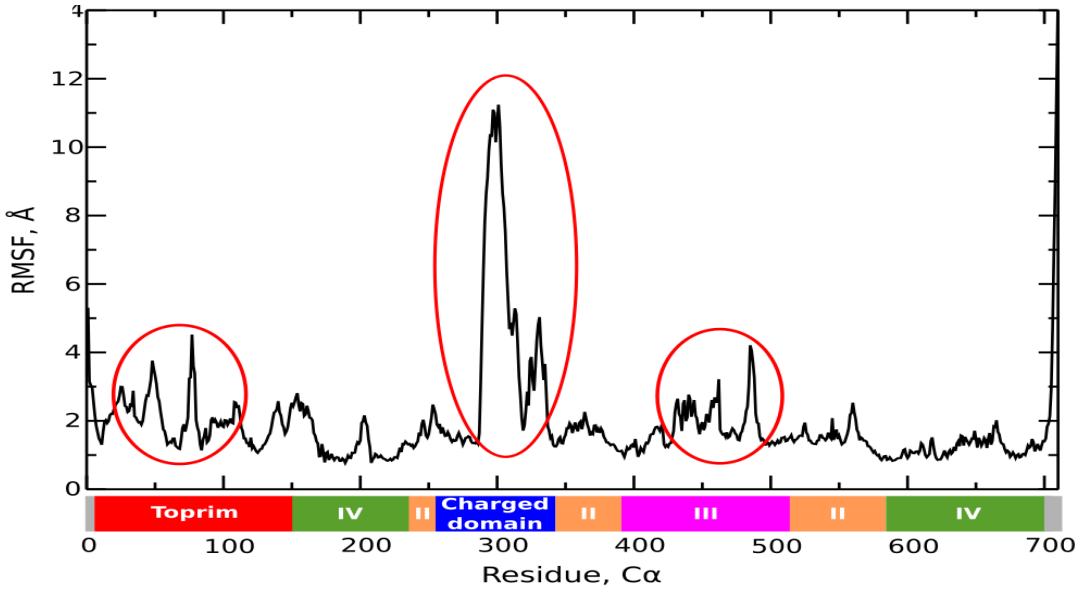
RMSF, Å
0
2
4
6
8
10
12
Toprim
IV
II
Charged domain
II
III
II
IV
0
100
200
300
400
500
600
700
Residue, Cα

D.

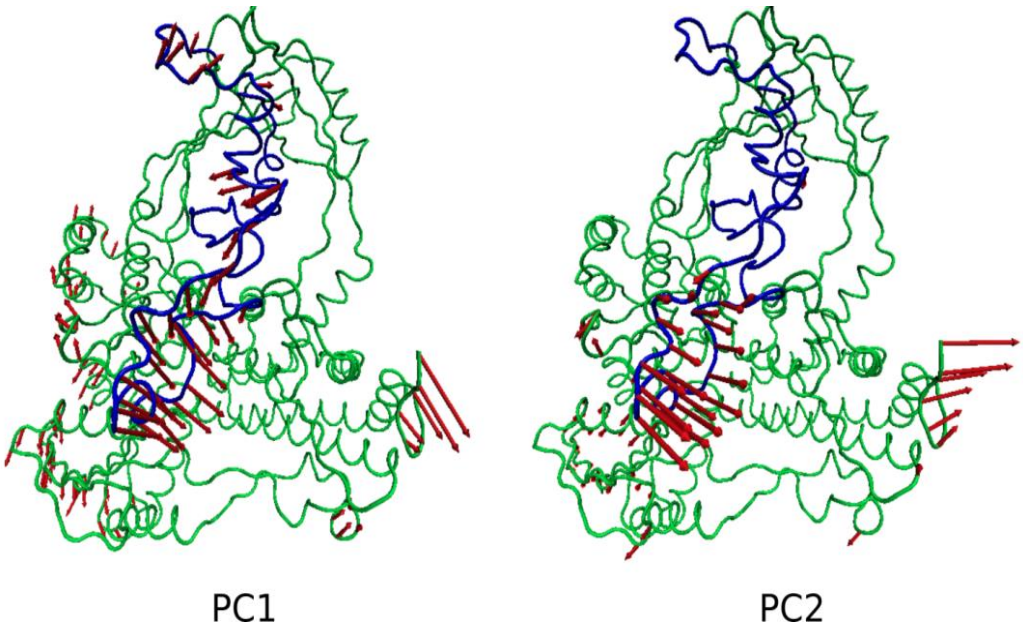
PC1
PC2

From these observations, it can be inferred that there are two major conformational changes in the protein. First, domain III and Toprim domain open up to accommodate the oligonucleotide, and then the charged domain comes closer to and interacts with the oligonucleotide.

The distance between the centres of mass of domain III (residues 380–511) and parts of Toprim domain (residues 12–26 and 152–163) were computed to quantify the movement between these two domains (Figure 6E). The domains moved by a distance of 7 Å compared with the PfTopoIII modeled structure (Figure 6E). In the RMSF and PCA analyses, the charged domain showed high flexibility during MDS. The conformations of the charged domain could largely be clustered into four bins, as can be seen in the free energy landscape (FEL) plot (Figure 6F). During the start of the simulation, the charged domain interacted with parts of domain III, similar to the apo-structure simulation (Figure 6G, red). Around 34 ns, the domain adopted an open conformation to interact with the DNA octamer (Figure 6G, black). At ~46 ns, residues D296, E297, K302, and K304 started interacting with the oligonucleotide (Figure 6G, H). During the latter part of the simulation, the charged domain was in a closed conformation. The charged and aromatic residues in the charged domain interacted with and stabilized the DNA octamer (Figure 6G, H). The residues from this domain (K302, K301, K299 and others) formed hydrogen bonds and stacked interactions with the nitrogenous bases of the DNA octamer (Figure 6G). These interactions helped to stabilize and place the DNA octamer in the cavity for further processing. Thus, the MDS and the structural data established that the charged domain of PfTopoIII stabilizes the binding of single-stranded DNA

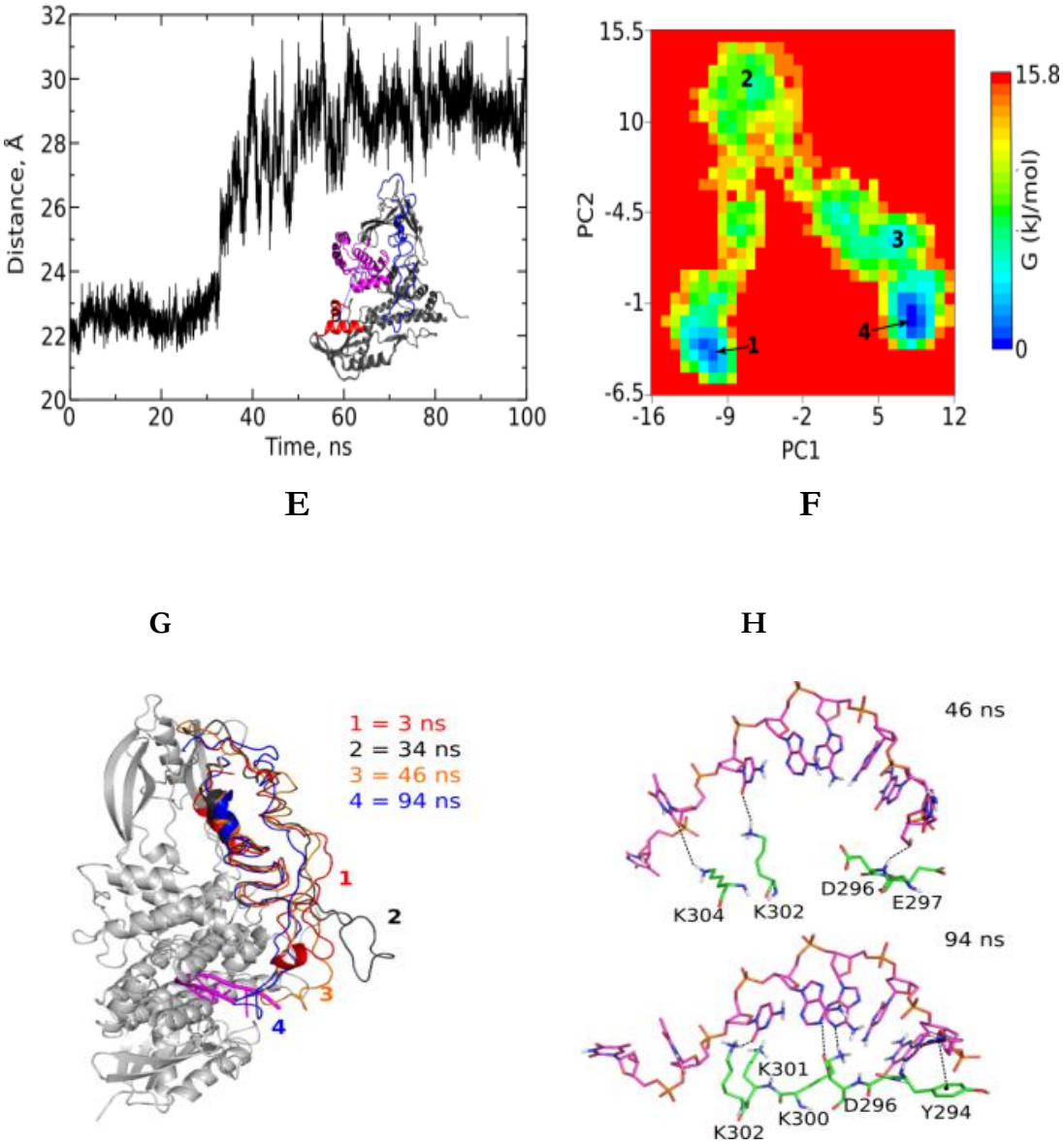

Figure 6. Molecular dynamic simulations indicate that the charged domain of PfTopoIII remains flexible and stabilizes upon DNA binding. A) Structure of PfTopoIII modeled using the I-TASSER. The toprim domain and domain III are colored in red and magenta, respectively. The domains II and IV are colored in orange and green, respectively. The charged domain which is a part of domain II is shown in blue. B) Principal components (PC1 and PC2) obtained from 50 ns simulation of PfTopoIII simulation. The fluctuations greater than 2 Å are shown by red arrows. The protein and charged domain are shown in green and blue trace, respectively. C) The dynamics of holo-PfTopoIII, the RMSF of the Cα atoms of PfTopoIII in presence of DNA octamer. The regions that show high RMSF

are highlighted in red ellipse. D) Principal Components (PC1 and PC2) obtained from 100 ns simulations of PfTopoIII simulation. The fluctuations greater than 2 Å are shown using red arrows. The protein and charged domain are shown in green and blue trace, respectively. E) Graph showing the distance between the centres of mass of parts of toprim (residues 12–26 and 152–163 shown in red) and domain III (residues 380–511 shown in magenta) during the simulation of PfTopoIII holo structure. F) Free energy landscape (FEL) with respect to principal components 1 and 2. G) Major conformations of charged domain (residues 251–337) sampled during 100 ns simulation obtained from FEL have been shown in red, black, orange and blue color, respectively. H) Interactions of charged domain (green) with the DNA octamer (magenta) have been shown.

3.2. To study the expression and localization of PfTopoIII in asexual stages of the parasite

3.2.1. Expression of *PfTOPOIII* and antibody generation

PfTOPOIII with 2133 base pairs were PCR amplified using 3D7 *P. falciparum* genomic DNA as a template (Figure 7A). To generate an antibody against PfTopoIII protein, we attempted to express the full-length protein into pET28a bacterial expression vector having histidine tag. To this end, we transformed the constructs in different bacterial expression strains Rosetta, BL21 DE3* codon plus, and BL21::DE3 pLysS cells and were subjected to IPTG mediated induction at various conditions; the expected size of the band was 78 kDa approximately. Protein expression was not observed with the pET28a:*PfTOPOIII* construct in any given conditions (Figure 7B). Hence, we designed a peptide spanning residues 281–300 of PfTopoIII (DSNNYSDETDDYYGDEKK) and raised antibodies against the peptide. Immune sera analyses showed a specific band near 75 kDa (Figure 7C, right blot), which was absent when probed with pre-immune sera (Figure 7C, left blot)

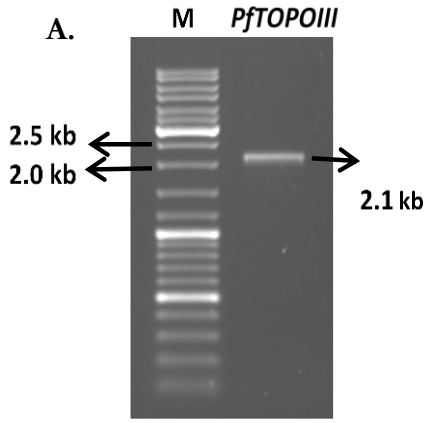
A.
M
PfTOPOIII
2.5 kb
2.0 kb
2.1 kb

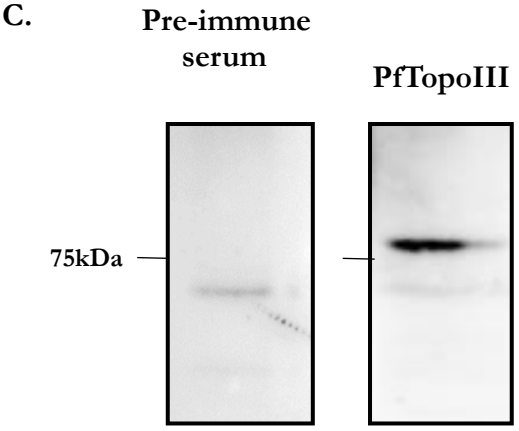
C.
Pre-immune serum
PfTopoIII
75kDa

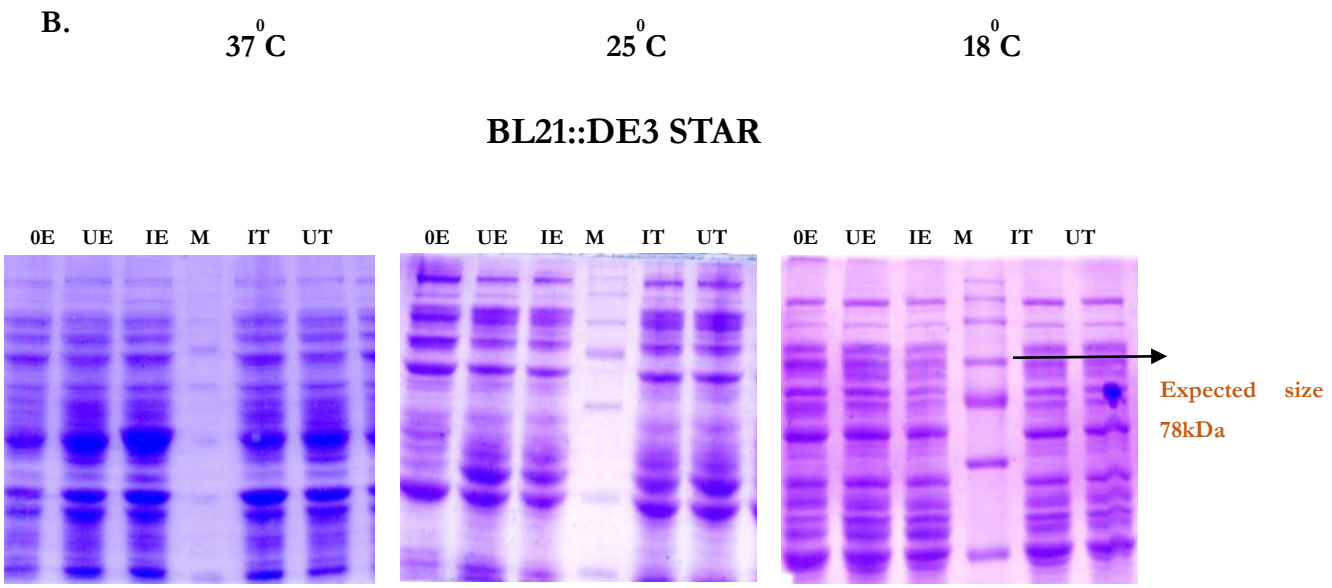
B.
37 0 C
25 0 C
18 0 C
BL21::DE3 STAR
0E UE IE M IT UT
0E UE IE M IT UT
0E UE IE M IT UT
Expected size
78kDa

Codon plus

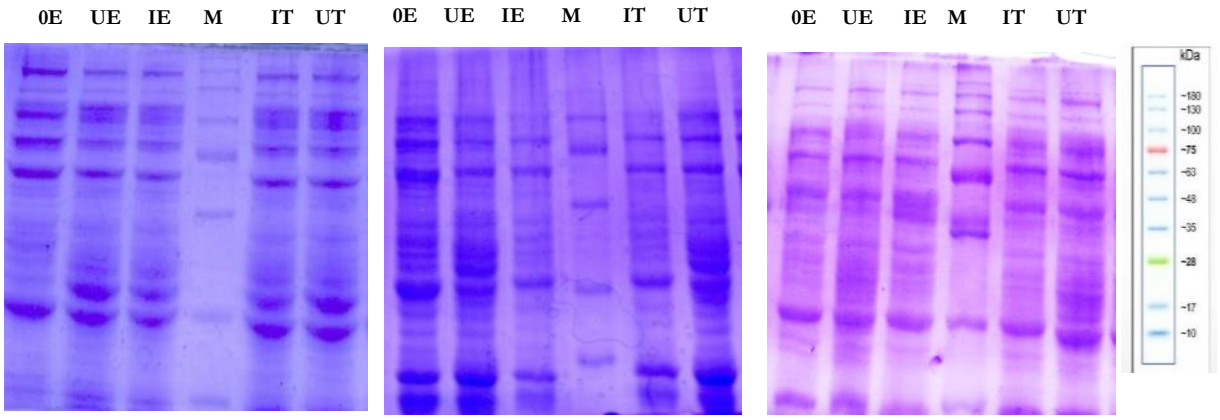

Rosetta

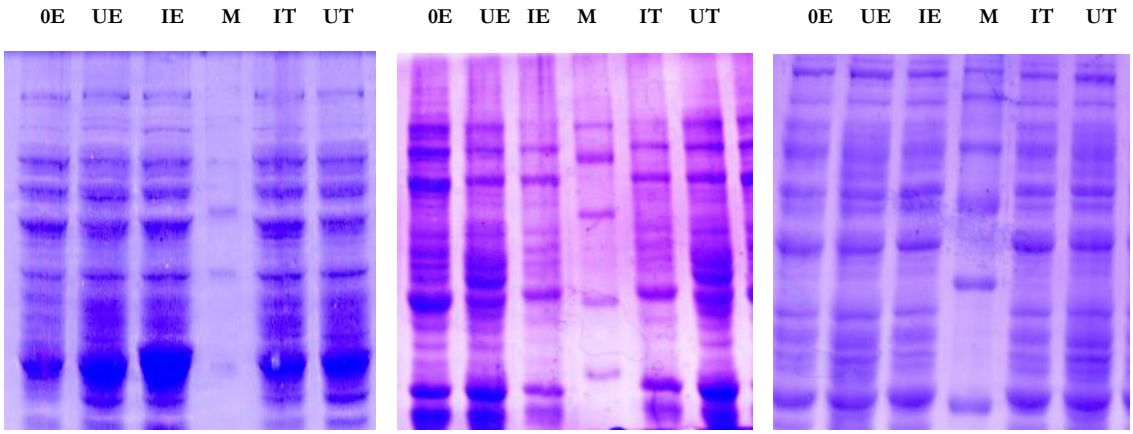

BL21::DE3pLysS

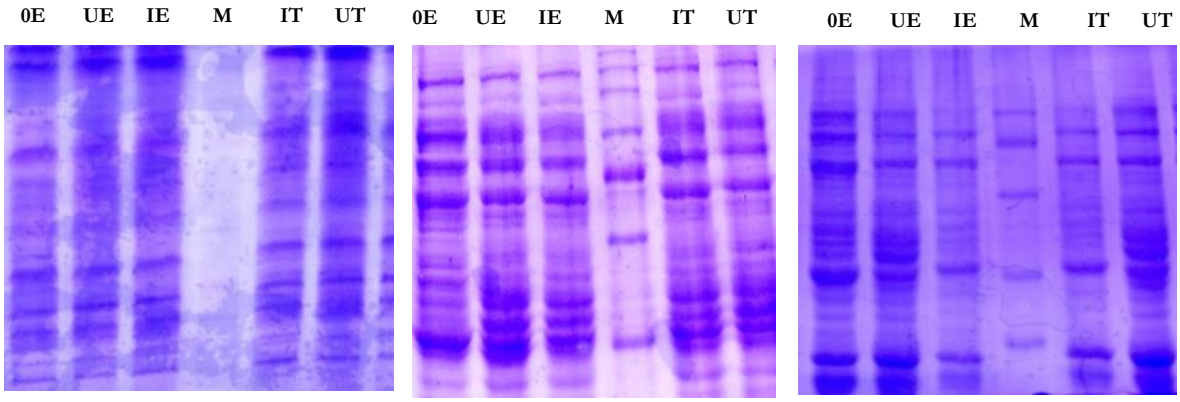

Figure 7: Expression of recombinant proteins PfTopoIII in various host cells which was cloned in bacterial expression vectors pET28a. A) PCR amplification of *PfTOPOIII* is presented. B) SDS-PAGE shows no expression of PfTopoIII as histidine tagged protein in BL21 DE3*, codon plus, Rosetta and BL21::DE3 pLysS strains at 37°C, 25°C and 18°C. C) Western blotting analyses of parasite cell extracts with pre-immune serum (left blot) and with an antibody raised against PfTopoIII (right blot). The molecular weight marker is indicated on the left.

0E: empty induced 0hour **UE: empty uninduced** **IE: empty induced**

M: marker **IT: Test induced** **UT: Test uninduced**

3.2.2. PfTopoIII expression is tightly linked with the replication of the parasite

To understand the specific expression levels of PfTopoIII during blood stages of the parasite, we studied its transcription and protein level expressions. To that end, we performed semi-quantitative RT-PCR, quantitative RT-PCR, and western blotting experiments. We isolated RNA from various synchronized asexual stages of the parasite (ring, trophozoite, and schizont) and performed semi-quantitative RT-PCR and real-time RT-PCR. Our semi-quantitative results indicated that *PfTOPOIII* transcript is expressed in the schizont stage of the parasite (Figure 8A). Aspartate-rich protein (*ARP*), which is constitutively expressed at all stages of the parasite, was used as a loading control. There was no amplicon in each sample before reverse transcriptase treatment (-RT), which tells that the sample preparation is devoid of any genomic DNA. Real-time RT-PCR analyses showed that the schizont stage of the parasite expressed more than 30-fold greater *PfTOPOIII* transcript compared with the ring and trophozoite stages, indicating its direct role during the replication of the parasite (Figure 8B). Using the specific peptide antibody, we performed western blotting

to investigate the stage-specific expression of the protein. We found that PfTopoIII is expressed specifically in the schizont stage (Figure 8C). Actin was used as a loading control. Thus, the expression profiles at the transcript level and protein level corroborated each other.

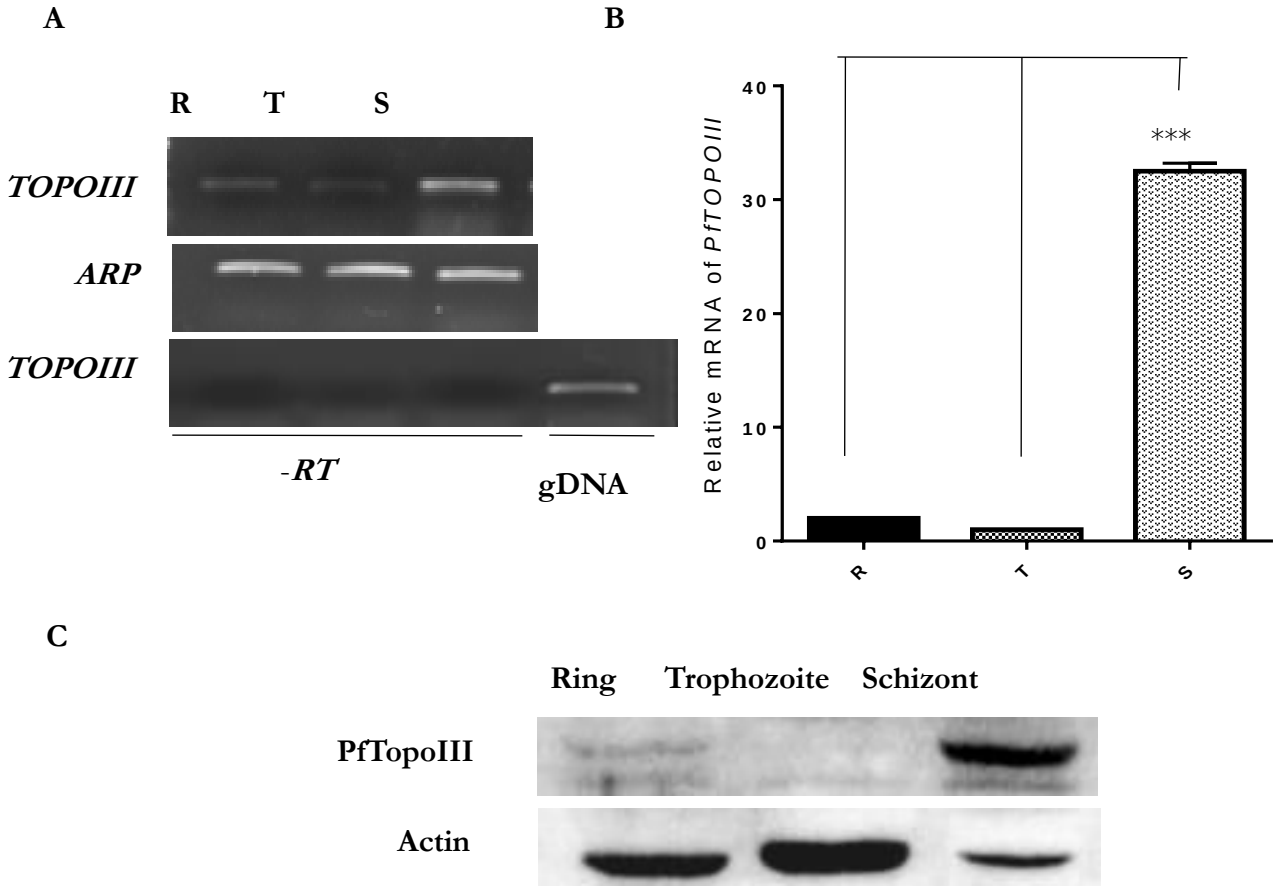

Figure 8. PfTopoIII expression is tightly linked with the replication of the parasite. A) RT-PCR analysis with RNA isolated from the rings (R), trophozoites (T) and schizonts (S) stages. PCR amplification was done using *PfTOPOIII* and *ARP* (Aspartate rich protein) specific primers which amplify 254 bp and 300 bp specific to the 3' end of the transcript, respectively. The bottom panel shows the lack of a *PfTOPOIII* band in the absence of reverse transcriptase (−RT). Genomic DNA (gDNA) served as a positive control. B) Real-time RT-PCR shows the relative abundance of *PfTOPOIII* at various stages of the parasites. Error bars indicate mean ± SD; n= 3; P = 0.0003. C) Stage dependent expression of PfTopoIII in *P. falciparum* lysate has been shown: R, middle rings; T, early/mid trophozoite; S, mid/late schizont. Actin served as a loading control.

3.2.3 Subcellular localization of PfTopoIII

To examine the localization of PfTopoIII in the parasite, the distribution of endogenous PfTopoIII was studied by subcellular fractionation as well as by fluorescence microscopy. We conducted three independent subcellular fractionations of the parasite culture, and one representative image is presented in (Figure 9A). We found that PfTopoIII was present both in the nuclear as well as in the organelle fraction. Histone H3 and cytochrome C were used as nuclear and mitochondrial protein markers, respectively. We generated a transgenic parasite line expressing PfTopoIII-GFP. Western blotting analyses of synchronous parasites in the schizont stage confirmed the expression of PfTopoIII-GFP (Figure 9B) in the parasite. The localization of the GFP-tagged protein was studied by live-cell imaging using a fluorescence microscope (Carl Zeiss). We found that PfTopoIII-GFP showed distinct nuclear foci and was co-localized with DAPI (Figure 9C). PfTopoIII-GFP was also co-localized with MitoTracker dyes (Figure 9D). These results correlate with the subcellular fractionation analyses and confirm its presence in both the nucleus and mitochondria of the parasite.

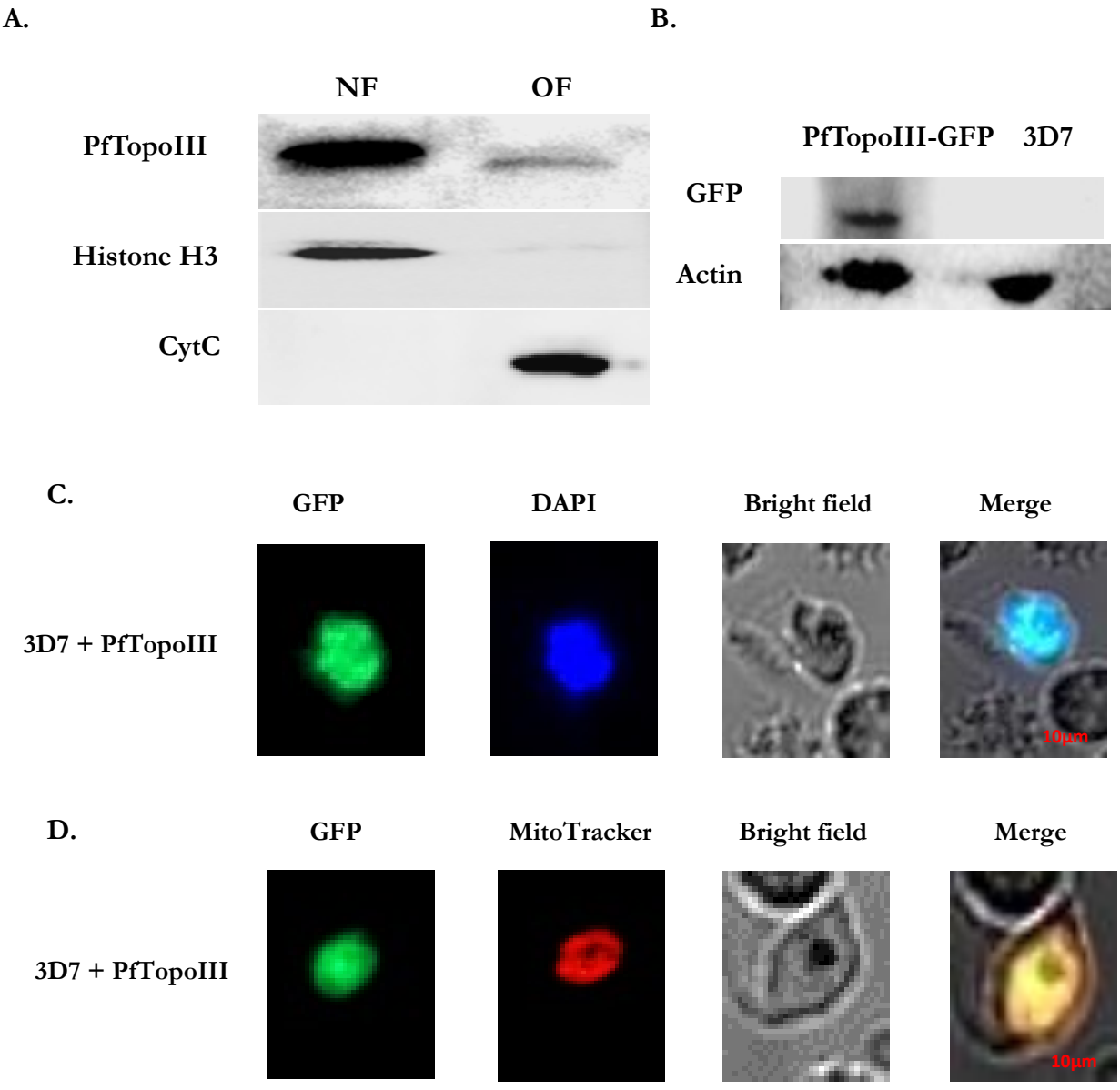

Figure 9. Cellular localization of PfTopoIII. A) Western blotting analyses of the nuclear (NF) and organelle fractions (OF) of 3D7 parasite infected RBC were done using anti-PfTopoIII antibody. Histone H3 and Cytochrome C were used as the nuclear and mitochondrial markers, respectively. B) Western blotting analyses of the total protein extracted from 3D7 and a transgenic parasite strain harbouring PfTopoIII-GFP expression vector were performed using anti-GFP antibody. Actin served as a loading control. C and D) Fluorescence microscopy shows the expression of PfTopoIII-GFP at

the late schizont stage. Parasite nucleus was stained with DAPI (blue) while parasite mitochondria were stained with MitoTracker Red (red).

3.2.4. Subcellular localization of *PftopoIII$^{(\Delta 259\text{-}337)}$GFP*

To determine the functional significance of the charged domain of PfTopoIII, we generated a transgenic parasite that expressed mutant *PftopoIII-GFP* with a deletion of 259–337 charged aa residues from PfTopoIII. We wanted to determine whether the charged linker region is responsible for its nuclear or mitochondrial localisation. We determined the localisation of the mutant enzyme in a similar way as explained above. Western blotting analyses confirmed the expression of mutant *PftopoIII(⊿259–337)-GFP* protein in the parasite (Figure 10A). We performed live cell imaging of the mutant parasite-infected cells and observed that the mutant protein was co-localized with DAPI as well as with MitoTracker, like that of the wild type protein (Figure 10C and 10D).

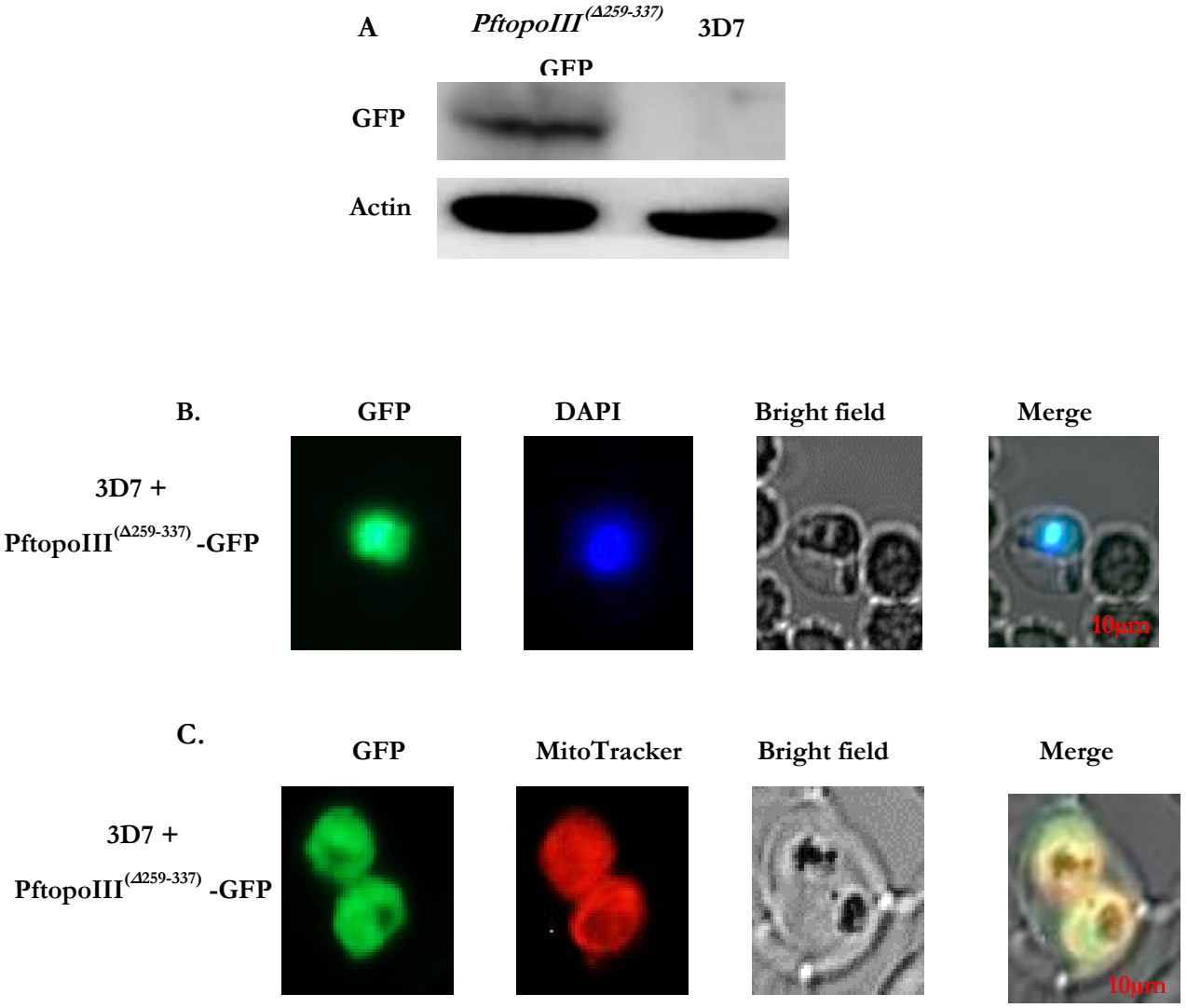

Figure 10. Cellular localization of *PftopoIII*$^{(\Delta 259-337)}$*-GFP*. A) Immunoblot shows the expression of mutant *PftopoIII*$^{(\Delta 259-337)}$*-GFP* protein in the transgenic parasite line. B) and C) Fluorescence microscopic images show the localization of *PftopoIII*$^{(\Delta 259-337)}$*-GFP*. The parasite nucleus was stained with DAPI (blue), and parasite mitochondria were stained with MitoTracker Red (red).

3.3. To study the structure-function analysis of PfTopoIII using yeast as a surrogate system

3.3.1 Generation of *ΔtopoIII* strain of yeast

To determine whether putative PfTopoIII manifests topoisomerase III like functions, we used yeast as a surrogate system. To that end, we generated ⊿*topoIII* yeast knockout through homologous recombination strategy (133). We used *HIS3* cassette flanking with 40 bp UP TopoIII sequence and 30 bp sequence from 3' end of the sequence. The schematic diagram to explain the strategy of confirmation of knockout is presented (Figure 11A). We have screened 6 colonies that were grown in SC medium lacking histidine. Genomic DNA was isolated from each of the conies, and knockout was confirmed through PCR analysis. We used the forward primer which is complementary to the 150 bp upstream of *ScTOPOIII* and the reverse primer which was used for amplifying knockout cassette to confirm the knockout. The expected size for confirmed colony was 1.45 kb (1.3 kb *HIS3* cassette+ 150 bp upstream region) which was obtained in colony 6, others show the amplification of *ScTopoIII* gene in addition with 150 bp upstream region which corresponds to 2.05 kb approximately (Figure 11B).

A.

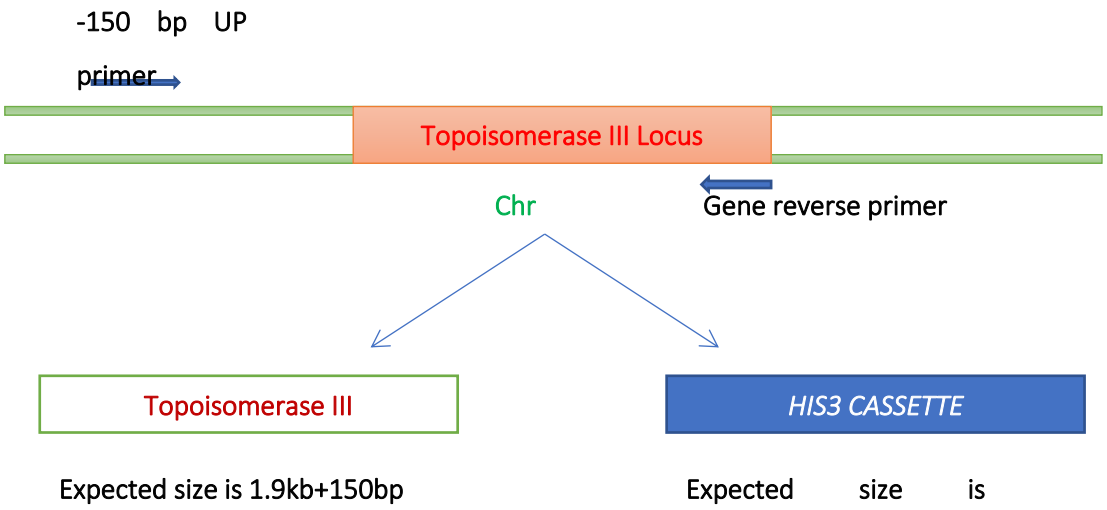

B.

.

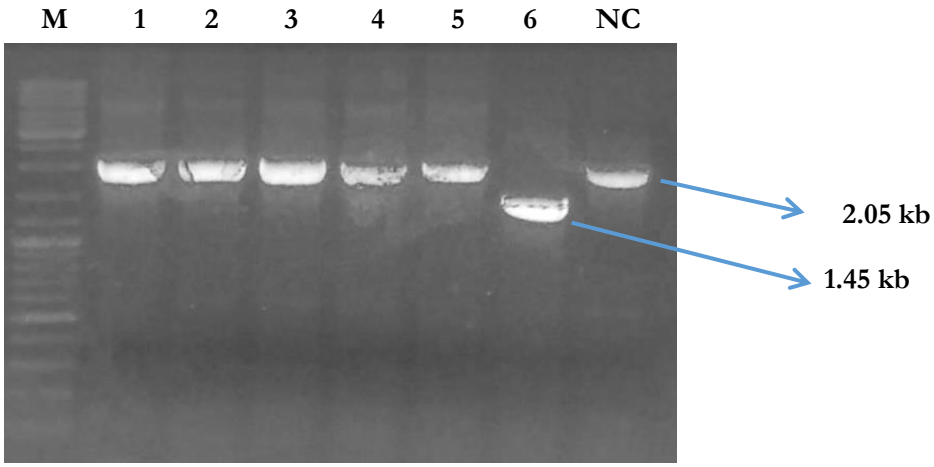

Figure 11. Generation of *ΔtopoIII* strain of yeast. A) Strategy of *ΔtopoIII* knockout using *His3* cassette through homologous recombination in yeast. B) Screening of knockout colonies, colony 6 confirms the *HIS3* knockout, 1-5 colonies are false colonies. NC denotes negative control, *i.e., ScTOPOIII* PCR amplification.

3.3.2. *PfTOPOIII* complements the function of *ScTOPOIII* but *Pf(Δ259–337)topoIII* does not

To decipher the *in vivo* role of PfTopoIII, we used *S. cerevisiae* as a surrogate model system. The schematic presentation of the genetic complementation assay with various positive and negative control strains are shown (Figure 12A). To determine whether full-length PfTopoIII can reverse the slow-growth phenotype of *⊿topoIII* yeast strain we transformed *ScTOPOIII* expressing vector (*pTA-ScTOPOIII*) into the knock-out strain. This strain served as a positive control in our study. We created an isogenic negative control strain that harbours the empty vector. We cloned *PfTOPOIII* in yeast expression vector *(pTA-PfTOPOIII*) and transformed it into the *⊿topoIII* strain to generate an isogenic strain. We also cloned mutants of *PfTopoIII* and transformed it into *⊿topoIII* to generate isogenic strains (Figure 12A). Following that, we performed two kinds of assays to access the slow growth phenotype. Firstly, we individually grew each strain in the fresh liquid media from overnight culture and spotted them onto *TRP* $^{-}$ plates with serial dilutions (Figure 12B). In another assay, we monitored their growth for 15 h at regular intervals (Figure 12C). Both of our assays reflect, that full-length PfTopoIII fully rescued the slow-growth phenotype of the *⊿topoIII* strain to the same extent as that of ScTopoIII (Figure 12B, 12C). To confirm that the growth recovery was not due to any compensatory mechanism, we created an isogenic strain where the putative active tyrosine of PfTopoIII (at the 421st position) was mutated to phenylalanine. The mutant was unable to suppress the slow-growth phenotype of *⊿topoIII* strain, confirming the role of this active tyrosine inside this yeast strain (Figure 12 B, 12C).

To rule out the possibility that loss of complementation is not due to loss of expression of *PftopoIIIY421F*, we checked the expression of wild-type *PfTOPOIII* and *PftopoIIIY421F* both at the RNA level (Figure 12D) and at the protein level (Figure 12E). Both proteins were stably maintained in the *⊿topoIII* strain. Next, we investigated whether the charged domain present in PfTopoIII is essential for its function. To that end, we made a charged domain deletion mutant of PfTopoIII by deleting 259–337 aa and transformed the *pTA-PftopoIII(⊿259–337)* vector into the *⊿topoIII* strain to check whether it would show PfTopoIII-like activity. This mutant failed to rescue the slow-growth phenotype of the *⊿topoIII* strain on plates (SC-trp) and in the liquid medium, suggesting that the charged domain was essential for functional complementation (Figure 12B, 12C). To rule out the possibility that loss of function of the mutant protein was due to the loss of expression of the mutant protein, we studied the mRNA expression of *pTA-PftopoIII(⊿259–337)*; it was detected at the same level as that of other test strains (Figure 12D). However, we could not check its expression at the protein level as the peptide antibody was raised against the charged region of PfTopoIII. This experiment emphasizes the importance of the charged region in the PfTopoIII function.

A.

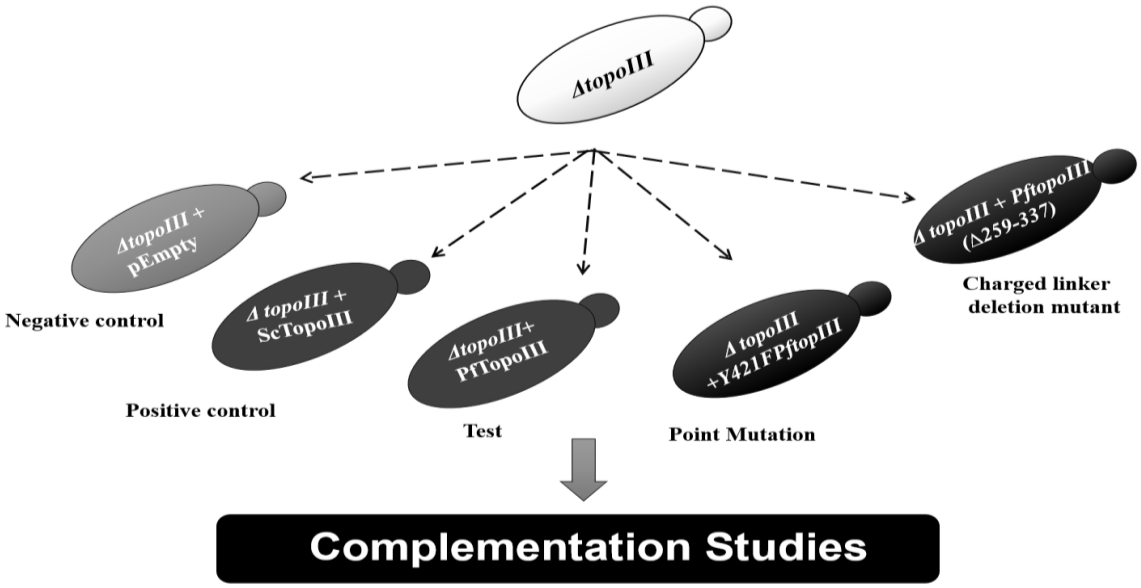
ΔtopoIII
ΔtopoIII + pEmpty
Negative control
Δ topoIII + ScTopoIII
Positive control
ΔtopoIII+ PfTopoIII
Test
Δ topoIII +Y421FPftopIII
Point Mutation
Δ topoIII + PftopoIII (Δ259-337)
Charged linker deletion mutant
Complementation Studies

B.

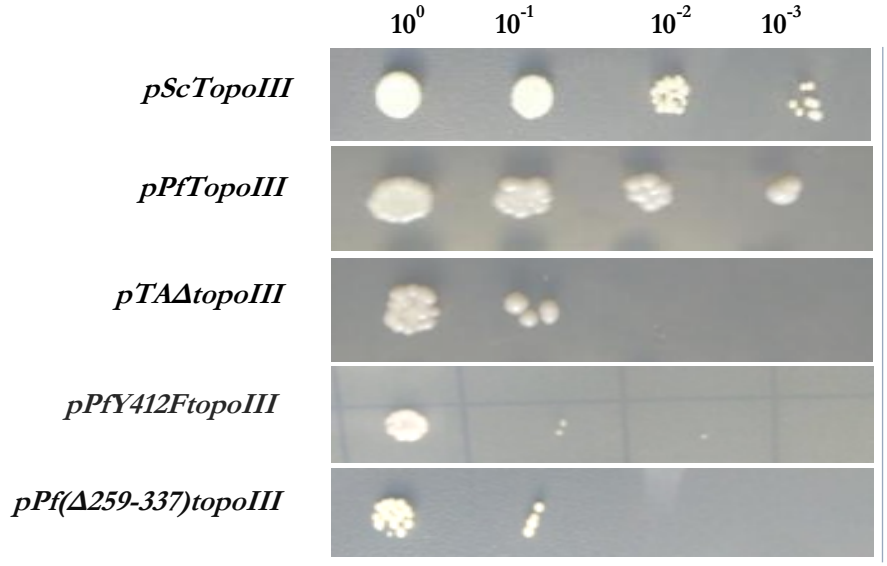
10^0
10^-1
10^-2
10^-3
pScTopoIII
pPfTopoIII
pTAΔtopoIII
pPfY412FtopoIII
pPf(Δ259-337)topoIII

C.

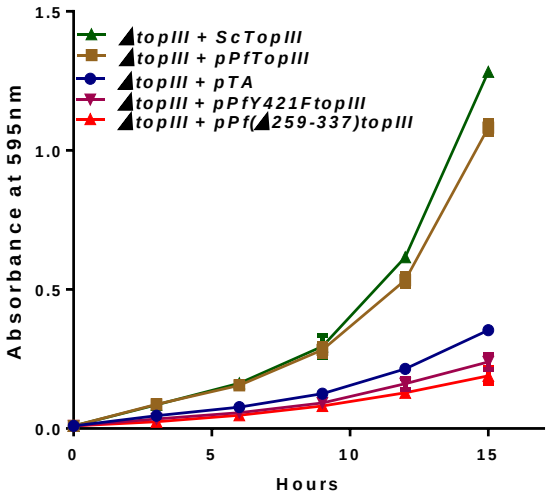
1.5
1.0
0.5
0.0
Absorbance at 595nm
0
5
10
15
Hours
ΔtopIII + ScTopIII
ΔtopIII + pPfTopIII
ΔtopIII + pTA
ΔtopIII + pPfY421FtopIII
ΔtopIII + pPf(Δ259-337)topIII

D.

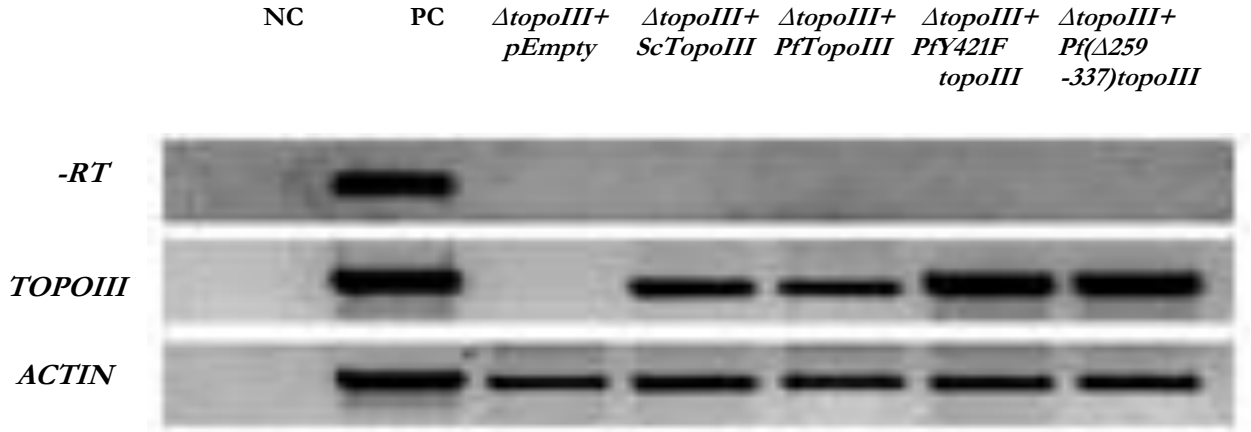
NC
PC
ΔtopoIII+ pEmpty
ΔtopoIII+ ScTopoIII
ΔtopoIII+ PfTopoIII
ΔtopoIII+ PfY421F topoIII
ΔtopoIII+ Pf(Δ259 -337)topoIII
-RT
TOPOIII
ACTIN

E.


WT
PfTopoIII
PfTopoIII Y421F
TopoIII

Figure 12. *PfTOPOIII* can complement the function of *ScTOPOIII,* but *Pf(Δ259–337)topoIII* cannot. A) Diagram showing *S. cerevisiae ΔtopoIII* strain was individually transformed with empty vector, vector expressing *ScTOPOIII, PfTOPOIII, PfY421FtopoIII and Pf(Δ259–337)topoIII.* B) Growth of all the strains on tryptophan lacking plates after 2 days, C) Growth rate of all the strains were measured in liquid synthetic medium lacking tryptophan and the OD_{595} was plotted against time. The results shown represent the mean of three independent experiments. D) The expression of *TOPOIII* from the abovementioned strains was monitored using gene specific primers; Actin served as positive control. NC denotes negative control i.e., *ScTOPOIII* PCR amplification without genomic DNA and PC denotes positive control *i.e. ScTOPOIII amplification* with genomic DNA as a template. E) Total protein was isolated from the strains as indicated at the top and probed with PfTopoIII specific antibody.

3.3.3. Replication block-induced sensitivity in *ΔtopoIII* is rescued by ectopic expression of full-length *PfTopoIII* but not by the charged domain mutant protein

MMS modifies the DNA by adding methyl groups and the methylated DNA subsequently physically blocks replication forks (160). It has been earlier reported that TopoIII along with Sgs1 can eliminate the obstacle during replication fork progression and that deletion of *TOPOIII* causes MMS sensitivity in a dose-dependent manner (161). We assessed whether PfTopoIII could suppress the cytotoxic effects of DNA alkylating agents in a yeast model system. To that end, we exposed the test strains to two different doses of MMS (0.01% and 0.04%) for 2 h, subsequently washed MMS from the media, and then returned them to normal media. The percent survivability of each strain at both the concentration of MMS were evaluated in at least three independent assays and the same was plotted (Figure 13). Our assay shows that the full-length PfTopoIII harboring strain completely rescues the MMS sensitivity of the ⊿*topoIII* strain as that of ScTopoIII harboring strain. We conclude that

PfTopoIII fully complements the function of ScTopoIII during replicative stress.

In contrast to that, mutants of PfTopoIII i.e., *PftopoIIIY421F* and *PftopoIII(⊿259–337)* failed to rescue the replicative stress conditions caused due to MMS. Percent survivability for both the mutants was reduced to less than 50% at 0.01% MMS, and 20% at 0.04% MMS treatment. Both the mutants show similar sensitivity towards MMS as that of the *⊿topoIII* strain. This indicates that not only the Y421 residue of the catalytic domain is of utmost importance for TopoIII functioning but also the charged amino acid rich region of is indispensable for its function.

A.

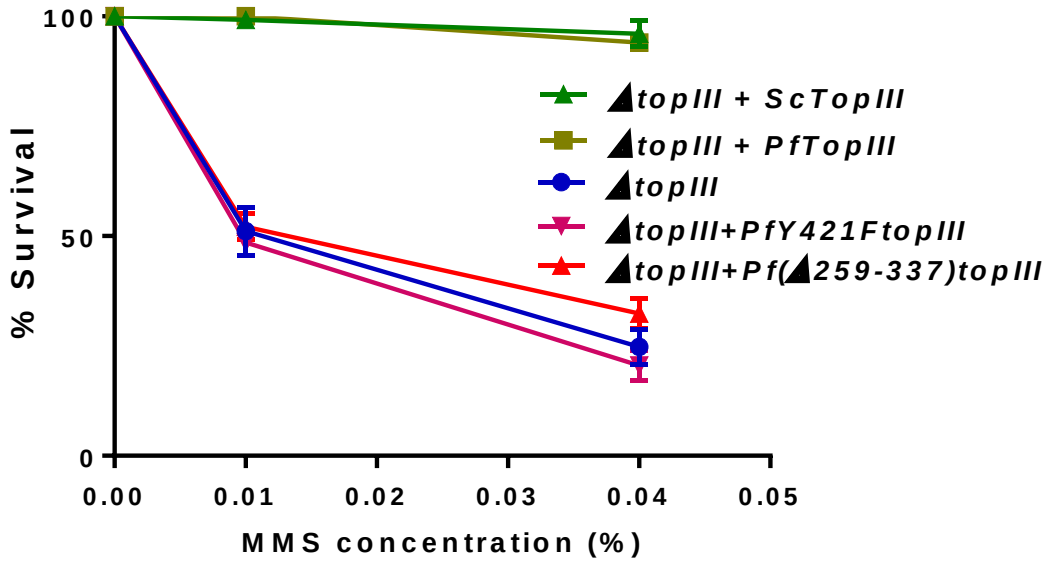

Figure 13. Replication block induced DNA damage sensitivity in *ΔtopoIII* yeast cells is rescued by expression of full length *PfTOPOIII* but not by the expression of mutant protein with deletion in its charged domain. Isogenic strains, as indicated, were grown to early log phase and exposed to 0.01% MMS and 0.04% MMS treatment. The percent survival of each strain was determined. Error bars indicate mean ± SD; n = 3.

3.4. To evaluate PfTopoIII function during replication

3.4.1 PfTopoIII interacts with PfBlm and PfWrn

Studies have shown that TopoIII and RecQ helicases act together to perform its functions in eukaryotes (ref). Specially during fork progression (replication) RecQ helicases tends to forms complex DNA structures that can only be solved by TopoIII. In this study, we were interested to understand whether similar process exists in *Plasmodium*. Hence, we used yeast two-hybrid assay to monitor the interaction between PfTopoIII and the RecQ helicases of *Plasmodium*. We subcloned *PfTOPOIII* in bait vector as a fusion to the Gal4 DNA binding domain and *PfBLM*/*PfWRN* individually to the prey vector as a fusion to the Gal4 activation domain as presented in schematic diagram (Figure 14A). The recombinant bait and prey vectors were transformed in PJ69-4A and the interaction between PfTopoIII and RecQ helicases were scored by monitoring their growth in a medium devoid of histidine. PJ694a strain has three reporter genes namely *HIS3*, *LACZ* and *ADE2* to score the protein-protein interaction. We found that the empty yeast two hybrid vectors as well PfTopoIII fused to the bait vector and PfBlm/PfWrn fused to prey vector individually did not self-activate the *HIS3* reporter gene activity, as they failed to grow in medium lacking histidine (Figure 14B, rows 1–4). However, PfTopoIII interacted with PfBlm as well as with PfWrn as they grew in histidine drop out medium (Figure 14B, rows 5 and 6). This shows weak interaction between PfTopoIII and PfBlm/PfWrn. No growth was observed in adenine dropout medium indicating that their interaction was not strong enough to induce the expression of sufficient adenine.

We also addressed whether the presence of the charged domain in PfTopoIII is essential for mediating the interaction with RecQ helicases. We found that the mutant *PftopoIII(⊿259–337)* interacted with both PfBlm and PfWrn with the same efficiency as that of the full-length protein (Figure 14B, rows 8 and 9), indicating that the charged domain is dispensable for the interaction with RecQ helicases.

Our Y2H data shows that TopoIII interacts with both PfBlm and PfWrn, but we also wanted to determine whether *PfBLM* and/or *PfWRN* are expressed in the parasite during replicative stages as well. To that end, we performed Semi-quantitative RT-PCR to check whether *PfBLM* and *PfWRN* were expressed in the schizont stage of the parasite along with PfTopoIII. Our data suggests that both RecQ helicases were abundantly expressed along with *PfTOPOIII* at the asexual replicative stage of the parasite (Figure 14C). We used the genomic DNA of 3D7, which acts as a positive control and -RT as the negative control where PCR was performed without reverse transcription step. Absence of bands in this lane clearly indicates that the RNA prep is not having genomic DNA contamination (Figure 14C).

A.


PfTopoIII
GAL4-BD
Pf (Δ259-337)topIII
GAL4-BD
PfBLM
GAL4-AD
PfWRN
GAL4-AD

B.

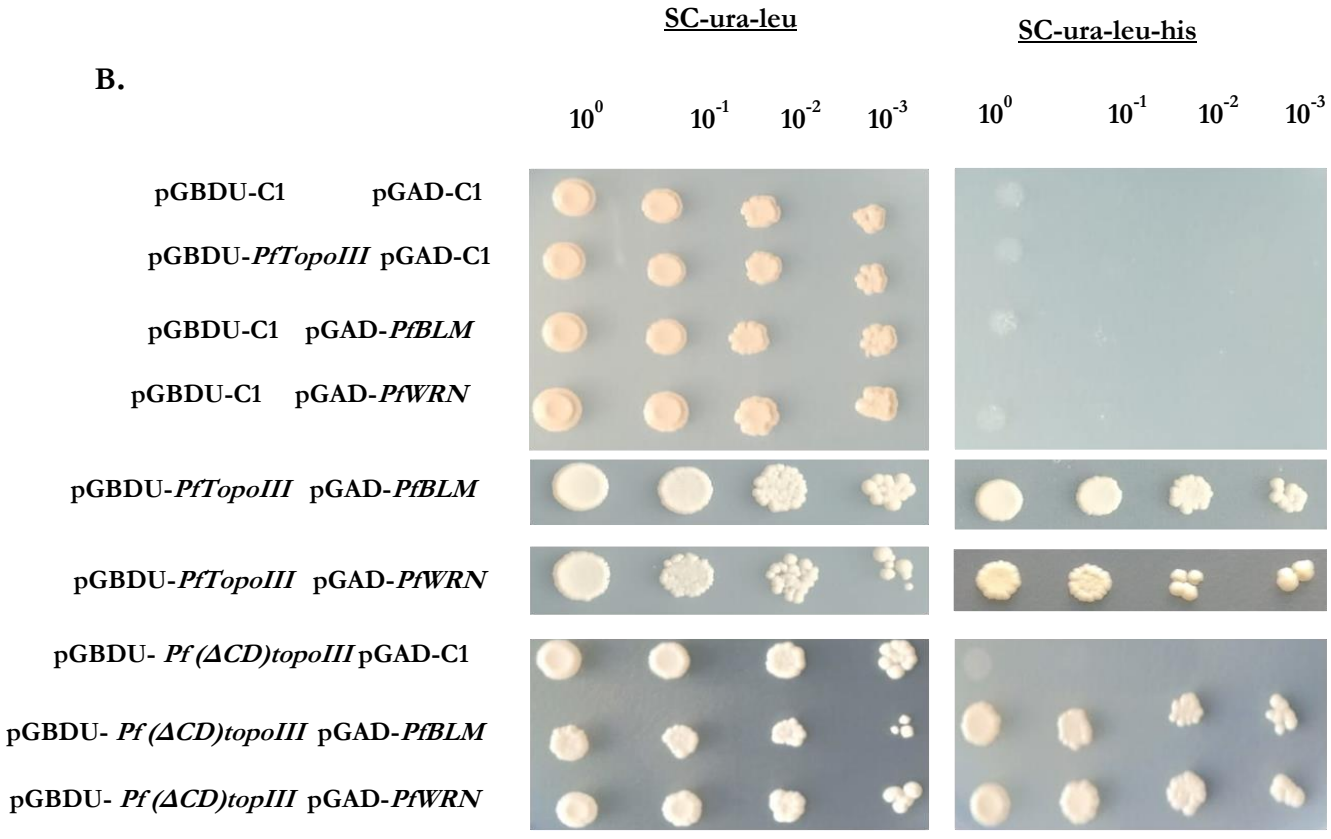
SC-ura-leu
SC-ura-leu-his
10^0
10^-1
10^-2
10^-3
pGBDU-C1 pGAD-C1
pGBDU-PfTopoIII pGAD-C1
pGBDU-C1 pGAD-PfBLM
pGBDU-C1 pGAD-PfWRN
pGBDU-PfTopoIII pGAD-PfBLM
pGBDU-PfTopoIII pGAD-PfWRN
pGBDU- Pf (ΔCD)topoIII pGAD-C1
pGBDU- Pf (ΔCD)topoIII pGAD-PfBLM
pGBDU- Pf (ΔCD)topIII pGAD-PfWRN

C.

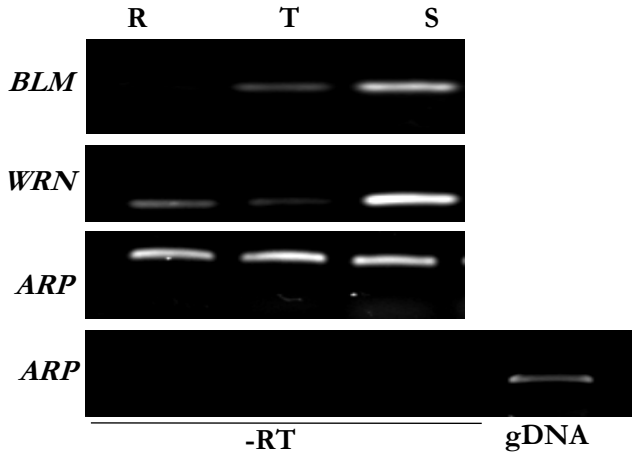

Figure 14. PfTopoIII interacts with PfBlm and PfWrn. A) The schematic representation showing that full length *PfTOPOIII* and *PftopoIII(Δ259–337)* were fused to the Gal4 DNA binding domain generating chimeric constructs in pGBDUC1 bait vector. Similarly, PfBlm and PfWrn were fused to Gal4 activation domain to generate chimeric constructs in pGADC1 prey vector. B) Yeast two-hybrid assays were performed in PJ69-4A strain using *HIS3* as a reporter gene. The left panel represents the spotting of equal number of cells with serial dilution in the medium lacking leucine and uracil while the right panel scores the interaction between respective pairs. C) Semi quantitative RT-PCR shows the expression of *PfBLM* and *PfWRN* at the ring (R), trophozoite (T) and schizont (S) stage of the parasite. Aspartate-Rich Protein (*ARP*) was used as a loading control. PCR without reverse transcriptase (−RT) does not show any amplification except for the positive control i.e., genomic DNA (gDNA).

3.5. To evaluate the role of PfTopoIII when replication stress is given to the parasite

3.5.1. Replication stress-induced expression of *PfTOPOIII*

HU inhibits ribonucleotide reductase, an enzyme that is required for the generation of deoxyribonucleotide triphosphates during the S-phase of the cell cycle. We studied the effects of prolonged HU-mediated replication stress on malaria parasites. We used synchronized 2% trophozoite-stage parasites exposed to 2.5 mM HU to induce replication stress, as established in a previous study (162). The growth and morphology of the parasites were measured in 10 h time intervals (post HU treatment) and compared with that of untreated parasites. The experiment was repeated three times and the survivability at each time point was plotted (Figure 15A). We found a three-fold increase in parasitaemia in untreated parasites at the end of the 30th hour, however, the HU-treated parasites showed severe sensitivity and their survivability was significantly reduced in a time-dependent manner. We also studied the morphology and development of the parasites at three different time intervals (Figure 15B). Untreated parasites mostly form mature schizonts (segmenters) at the end of 20th hour eventually ruptured and produced rings at the end of the 30th hour, which caused an increase in parasitaemia (Figure 15B). However, HU treatment caused an arrest in the development of the parasite; mature schizonts could not develop and eventually died. Next, we studied the effects of short-term exposure to HU on parasite survivability. We used synchronized 1% trophozoite-stage parasites and exposed them to 2.5 mM HU for 6 h. Subsequently, HU was extensively washed and the parasites were returned to

normal media (RTG) and allowed to grow for 26 h. We found a 5-fold increase in parasitaemia in untreated parasites (Figure 15C). However, treated parasites did not show a decrease in survivability; rather their growth was arrested and they remained at the same developmental stage as that at which they started (Figure 15C). It was earlier reported that *⊿topoIII* strain in *Saccharomyces cerevisiae* displays severe sensitivity towards HU (161), which indicates that TopoIII plays an important role in resolving the aberrant structure generated from the arrest of the replication fork. To explore the direct role of PfTopoIII during replication stress, we evaluated the level of PfTopoIII after HU treatment. We exposed synchronous trophozoite-stage parasites with two different doses of HU (2.5 mM and 10 mM) for 6 h. Subsequently, HU was extensively washed, the parasites were returned to the normal media for 26 h. Protein was harvested from all the parasites to perform western blot analysis. We found that PfTopoIII was moderately induced in a dose-dependent manner upon HU treatment, supporting its direct role in mitigating replication stress (Figure 15D). We repeated the experiment twice and quantified the band intensity using Image J software and found that there was a 3.5-fold induction in PfTopoIII expression levels in parasites treated with 10 mM HU (Figure 15D), indicating that to overcome replicative stress conditions the parasite cells tend to increase the protein levels of PfTopoIII. To understand whether the increase in expression occurred due to the stabilization of TopoIII at the protein or transcript level, we extracted RNA from untreated and HU-treated parasites and quantified the *PfTOPOIII* cDNA by real-time RT-PCR. There was a 2.5-fold induction in the expression of *PfTOPOIII* upon HU treatment. Rad51 plays an essential role in replication fork stability and regression (163). Rad51 expression was used as a positive control in our experiment (Figure 15E). The

transcriptional induction of *PfTOPOIII* in response to HU treatment indicates that the increased level of endogenous PfTopoIII is required to promote recovery from replication stress. This finding reveals that PfTopoIII plays a key role in the response to replication stress in the parasite.

A.

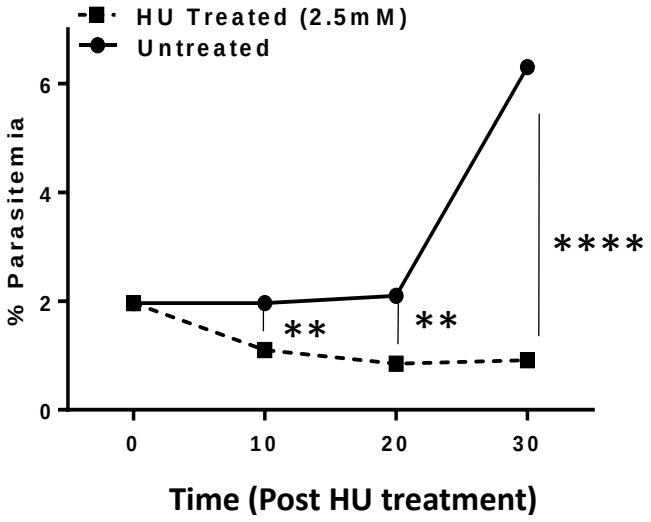
HU Treated (2.5mM)
Untreated
% Parasitemia
0
2
4
6
0
10
20
30
Time (Post HU treatment)
**
**
****

B.

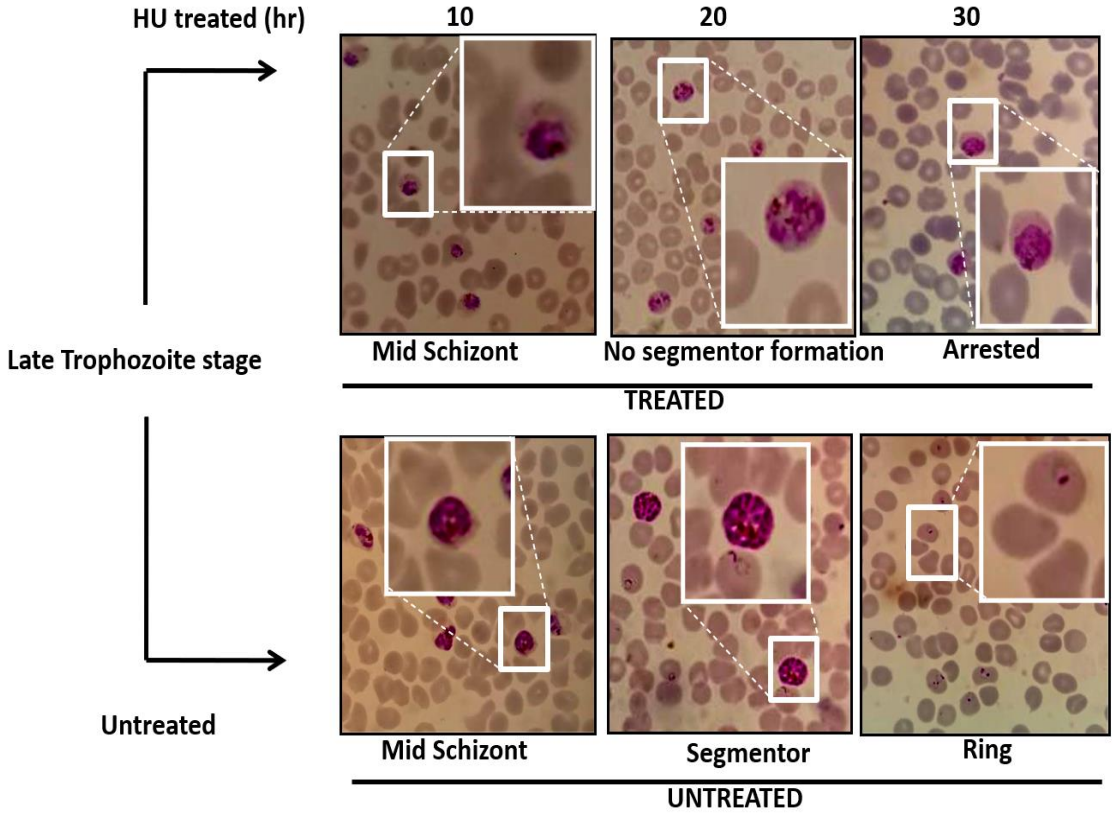
HU treated (hr)
10
20
30
Late Trophozoite stage
Mid Schizont
No segmentor formation
Arrested
TREATED
Untreated
Mid Schizont
Segmentor
Ring
UNTREATED

C.

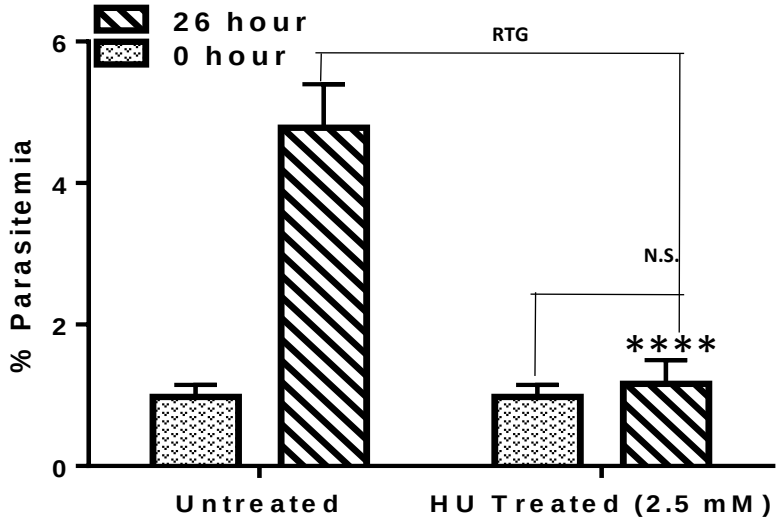
26 hour
0 hour
RTG
N.S.
****
% Parasitemia
0
2
4
6
Untreated
HU Treated (2.5 mM)

D.

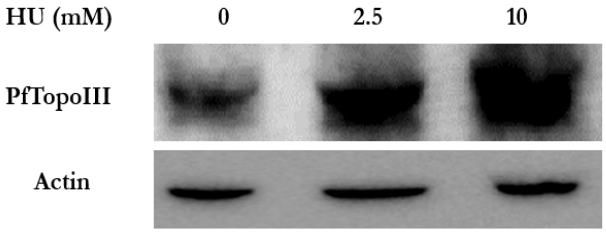
HU (mM)
0
2.5
10
PfTopoIII
Actin

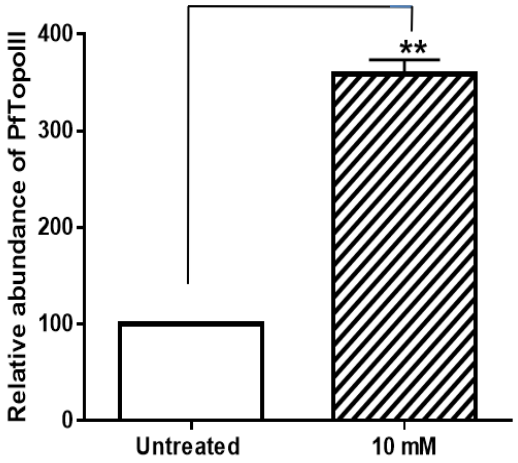
**
Relative abundance of PfTopoIII
0
100
200
300
400
Untreated
10 mM

E.

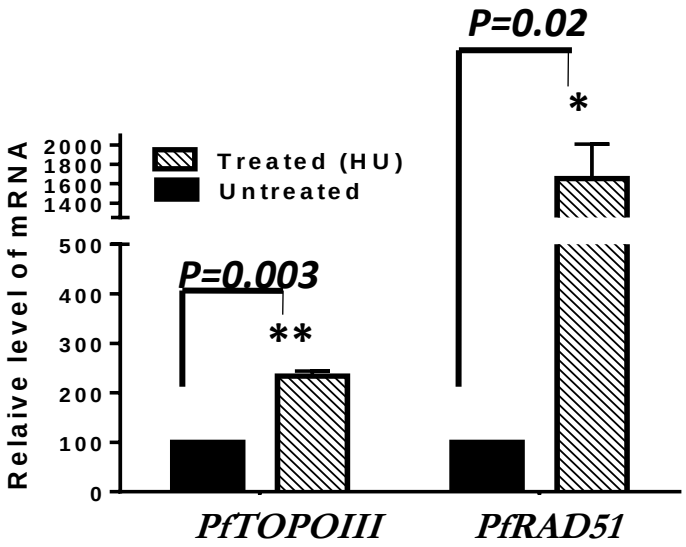

Figure 15. Replication stress induced expression of *PfTOPOIII.* A) Synchronous trophozoite stage specific 3D7 parasites were exposed to 2.5 mM HU for 30 h and parasitaemia was measured for untreated and treated batch at every 10 h intervals. Error bars indicate mean ± SD; n = 3; **** P < 0.0001; ** P < 0.01. B) Morphology of the HU treated parasites was observed under same conditions as A) using Giemsa staining method. The experiment was repeated for more than three times and in each case about 2000 infected RBC has been analysed. One of the representative pictures show that 20th hour post treatment arrests the parasite which is continued for 30th hour, while the untreated parasites form mature schizonts (segmenters) at 20th hour and subsequently forms rings at 30th hour. C) Synchronous trophozoite stage specific 3D7 parasites were exposed to 2.5 mM HU for 6 h, after which HU was extensively washed out and the parasites were subsequently returned to grow (RTG) in normal media. The parasitaemia was measured at the end of 26 h for the untreated and treated batch. Error bars indicate SD; n = 3; **** P < 0.0001; N.S. not significant. D) Untreated and treated parasites (at 2.5 mM and 10 mM HU treatment) were processed in the same way as that described in (C) and were harvested. The total protein was extracted and probed with anti-PfTopoIII antibody. Actin served as a loading control. Quantification of Western blots from three independent experiments was done using Image J software. The band intensities in each lane were normalized against Actin and mean densities were plotted. Error bars indicate mean ± SD; n = 3; ** P < 0.01. E) Synchronized trophozoite stage specific 3D7 parasites were treated with HU and the total RNA was extracted from untreated and treated parasites. Relative abundance of *PfTOPOIII* transcripts by real time RT-PCR revealed significant induction of *PfTOPOIII* upon HU treatment. *PfRAD51* expression was measured as a positive control. The P-value was calculated as 0.003 and 0.02 for *PfTOPOIII* and *PfRAD51* induction respectively using the two-tailed Student's t-test.

3.5.2. PfTopoIII but not *PftopoIII(Δ259–337)* expression rescues the growth defect induced by replication stress

We found that PfTopoIII expression is induced in response to replication stress, probably to counteract the stress, hence, we wanted to determine whether the ectopic expression of PfTopoIII, through a centromeric plasmid, would promote survival in HU-treated parasites. To this end, we compared the growth of three different strains of parasites: 3D7, 3D7 with *PfTopoIII* expression, and 3D7 with *PftopoIII(⊿259–337)* expression. In the first assay, we treated synchronous trophozoite-stage parasites with 2.5 mM HU continuously for 30 h and have measured parasitaemia in intervals of 10 h. We repeated the experiment three times and observed that PfTopoIII expression considerably reduced dose-dependent death of the parasites at the 20th and 30th hours (Figure 16A). Interestingly, the transgenic parasites harbouring *PftopoIII(⊿259–337)* expression plasmid did not show a reversed growth defect and behaved similar to that of the 3D7 parasites (Figure 16B). In the second assay, we exposed the parasites to 2.5 mM HU for 6 h, subsequently, it was extensively washed out and they were returned to normal growth media for 26 h. For each batch of parasites, we have performed three independent assays. We found that the 3D7 parasites were severely affected even with 6 h treatment of HU and their growth remained arrested compared with the untreated parasites. The PfTopoIII transgenic parasite line showed fully rescued survivability and there was no significant difference between the survivability of treated versus untreated parasites (Figure 16C). However, the *PftopoIII(⊿259–337)* parasite line showed a similar trend as that of 3D7 parasites and displayed a significant difference in

survivability compared with untreated parasites (Figure 16C). Hence, the charged domain of PfTopoIII is essential for in vivo function of the enzyme.

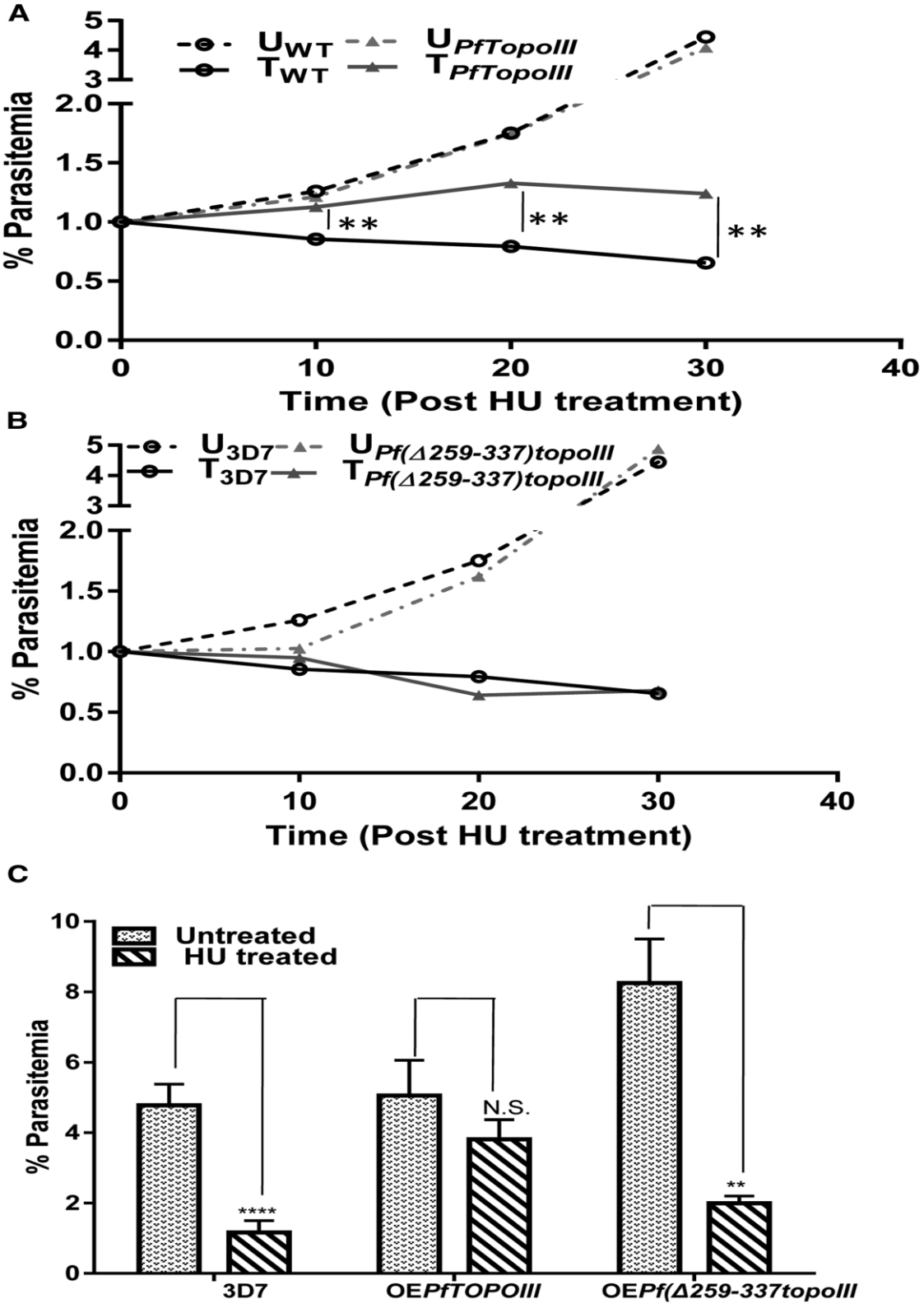
A
U WT
T WT
U PfTopoIII
T PfTopoIII
% Parasitemia
Time (Post HU treatment)
**
**
**
B
U 3D7
T 3D7
U Pf(Δ259-337)topoIII
T Pf(Δ259-337)topoIII
% Parasitemia
Time (Post HU treatment)
C
Untreated
HU treated
% Parasitemia
****
N.S.
**
3D7
OEPfTOPOIII
OEPf(Δ259-337topoIII

Figure 16. *PfTopoIII* but not *PftopoIII(Δ259–337)* expression reverses the replication stress induced growth defect. A) 3D7 and *PfTOPOIII* over-expressing parasites, synchronized at trophozoite stage, were treated with 2.5 mM HU for 30 h. The parasitaemia of each treated and untreated strain was measured after 10 h, 20 h and 30 h time intervals. At each time point, approximately 2000 RBC were counted and the mean parasitaemia was plotted. Error bars indicate mean ± SD; n = 3; ** P < 0.01. B) A similar experiment was performed with 3D7 and *Pf (Δ259–337)topoIII* over-expressing strain with HU treatment for 30 h. More than three independent experiments were conducted and the mean parasitaemia (%) was plotted. C) 3D7, PfTopoIII over-expressing strain and *Pf(Δ259–337)topoIII* over-expressing strain were synchronized at the trophozoite stage and treated with 2.5 mM HU for 6 h. Afterwards, HU was extensively washed and treated parasite strains were subsequently grown in normal media for 26 h following which, parasitaemia was measured. For each strain, minimum three batches of experiments were done and mean values of parasitaemia for untreated and treated condition for each of the three strains were plotted. Error bars indicate SD; n = 3; **** P < 0.0001; ** P < 0.01; N.S. not significant.

CHAPTER 4

DISCUSSION

This is the first study to identify functionally active TopoIII from a malaria parasite. We demonstrated that the spatiotemporal expression of PfTopoIII occurs in the nucleus and in the mitochondria during the actively replicating stage of the parasite. It is noteworthy that in humans, mice, and Drosophila, there is a mitochondrial localization signal at the amino terminal end of TopoIIIα (164) and a nuclear localization signal at the carboxyl terminal end (69). Although *Plasmodium* TopoIII is devoid of any such signal sequences, our subcellular fractionation data, immunofluorescence data, and mitochondrial immunoprecipitation results collectively establish that PfTopoIII is a mitochondrial topoisomerase. This finding again reinforces the notion that the mechanism behind mitochondrial import is poorly understood in malaria parasites.

HU treatment depletes the cellular pool of deoxyribonucleotides and subsequently causes stalling of the replication fork (165). Eventually, there occurs accumulation of joint DNA molecules in the direction opposite to the replication fork, and this results in the formation of so-called chicken foot structures (166) that have serious implications on cell survivability. As these structures resemble Holliday junctions (167), we speculate that if such a condition is generated in *P. falciparum*, PfTopoIII along with its cognate helicases might play an important role in resolving the structures and converting them back into the replication forks. Our study demonstrated the direct role of PfTopoIII in mitigating HU-mediated replication stress. First, PfTopoIII expression is induced in a dose-dependent manner in response to HU treatment. Second, expression of PfTopoIII can completely bypass the HU-induced growth defect in the parasites. It is noteworthy that the HU-mediated aberrant structure is resolved by the dual action of TopoIII and RecQ helicases.

There are two members of the RecQ family of DNA helicases in *Plasmodium*, namely, PfBlm and PfWrn. The absence of either of these enhances the rate of formation of stalled replication forks, indicating that both the members are required for efficient *Plasmodium* DNA replication (168). *E. coli* RecQ helicases interact with TopoIII and help resolve converging replication forks (169). In humans, TopoIIIα can dissolve Holliday structures jointly with Blm but not with Wrn (170). In this study, we determined by yeast two hybrid analysis that PfTopoIII interacts with PfBlm and PfWrn with equal efficiencies and that both helicases are expressed at the active replication stage of the parasite. However, it is necessary to investigate further whether both helicases mobilize a double Holliday junction and the resulting catenated DNA is resolved by PfTopoIII in malaria parasites.

Our study identified a charged domain within PfTopoIII that is indispensable for its *in vivo* function. MDS of PfTopoIII with DNA octamer showed that the enzyme undergoes a conformational change upon DNA binding. At the start of the DNA protein interaction, PfTopoIII-ssDNA adopts a closed conformation similar to that of the apo enzyme (PfTopoIII alone). However, gradually a central cavity is created by the movement of domain III and the Toprim domain so that the DNA can be accommodated. This movement of domains is often referred to as protein-mediated gate dynamics (171) and has an important implication in their biochemical activities. The DNA octamer is stabilized by the hydrogen bonding and stacking interactions between bases and the positively charged residues present in the charged domain of PfTopoIII. Hence, it can be concluded that the charged domain stabilizes the effective binding of PfTopoIII with DNA and thus may play an important role in the catalytic mechanism of PfTopoIII protein. To support the prediction, we

wanted to experimentally determine the DNA binding ability of the charged linker mutant. As PfTopoIII could not be purified, we determined the association of PfTopoIII and its mutant with mtDNA by chromatin immune precipitation as an independent study in our laboratory (172). That study revealed that the removal of the charged region shows significantly poor association with mtDNA compared to the wild-type PfTopoIII. Our genetic study emphasized the essential requirement of this domain for PfTopoIII function. First, the expression of wild-type PfTopoIII fully rescued the slow-growth phenotype and MMS-induced toxicity in yeast, but the expression of mutant *PftopoIII(⊿259–337)* failed to do the same and mimicked the phenotype of the topoisomerase-inactive mutant *PftopoIIIY421F*. We found that the loss of activity in the mutant *PftopoIII(⊿259–337)* strain was not due to poor heterologous expression of *Plasmodium* protein in *S. cerevisiae*. Although the expression of *PftopoIII(⊿259–337)* could not be demonstrated by western blotting analyses, the interaction between *PftopoIII(⊿259–337)* and PfBlm/PfWrn in yeast two-hybrid studies indirectly demonstrated the expression of the mutant protein in yeast. Second, the transgenic mutant parasite line *(PftopoIII(⊿259–337)- GFP)* failed to rescue itself from short-term exposure to replication stress, like the transgenic parasite line PfTopoIII-GFP. Together, our results emphasize the importance of the charged domain in PfTopoIII function. Although this type of charged domain is absent from other eukaryotic TopoIII, a similar kind of multiple positively charged insertions, albeit shorter stretches have been observed in *E. coli* and many other prokaryotic TopoIII sequences (61). A previous experimental study showed that the charged loop present in bacterial TopoIII is essential for decatenation of replication intermediates (61). To date, no inhibitors of TopoIII have been

identified. However, identification of the unique and indispensable charged domain of PfTopoIII qualifies itself as a target against malaria.

CHAPTER 5

TO PREDICT A SMALL MOLECULE INHIBITOR TARGETING PfTopoVIB

5.1 Homology modeling of PfTopoVIB and PfHsp90

The purpose of this study was *in-silico* designing of Radicicol analogs that specifically target PfTopoVIB and not PfHsp90. To that end we carried out homology modeling of both the above proteins through Swiss-Model server (138) and further employed these models for docking analysis. The sequence of *Plasmodium falciparum* TopoVIB was retrieved from Uniprot (ID: Q8ID53) which consists of 561 amino acids. The template search revealed that the most similar protein structure available for the sequence of PfTopoVIB was that of *Sulpholobus shibatae* Topoisomerase VIB (PDB: 2ZBK.D chain). Taking 2ZBK.D chain as the template, the target-template alignment was carried out using BLASTP suite, which predicted the local pairwise sequence identity to be 28.57% and the E-value as 1e-12. For homology modeling, the sequence identity between (20–25)% is considered as the twilight zone (173). Studies have demonstrated that proteins with pairwise sequence identity higher than 25% are similar in 3D structures and have a strong divergent evolutionary relationship (174-180). The E value of 1e-12, obtained for the template from the BLAST tool was considered in the acceptable range as per the recent study(181), which suggests the acceptable threshold of E Value for BLAST as 1e-8. Hence, the 3D structure of 2ZBK.D chain with 28.57% sequence identity was considered as a suitable template for homology modeling of PfTopoVIB. 2ZBK is an X–ray diffraction structure with Radicicol as a native ligand having 3.6 Å resolution. Our study focuses on the ATP-binding domain of PfTopoVIB, known as the Bergerat fold, which spans through 22 to 166 amino acids. This region corresponds to the 11 to 192 amino acids of SsTopoVIB (2ZBK.D chain) with an alignment score range of (50–80) with 42% positives, 29%

identity and 13% gaps. (Figure 17A) shows the sequence alignment between the target PfTopoVIB (Query) and template SsTopoVIB (Subject) in the Bergerat fold. As the aligned region covers the Bergerat fold, we preferred homology modeling over de novo protein structure prediction. It is observed that there is a unique highly charged region (containing a stretch of lysine and glutamic acids) spanning 61^{st} –78^{th} residues in the amino terminal domain of PfTopoVIB. *Plasmodium falciparum* possesses this kind of low complexity charged residues and unstructured region which is a unique feature of parasite protein. However, the biological significance of such low complexity regions remains unknown. Homology based near native model was created for PfTopoVIB (Figure 17B) and it was subjected to 10 steps of energy minimization, using GROMOS 43B1 force field where in each step 20 cycles of steepest descent method was involved. 200 cycles of steepest descent were required to attain the lowest energy model, which was used for further analysis.

The sequence of PfHsp90 was retrieved from the Uniprot database (ID: Q8IL32). For building the near native model of PfHsp90, 3IED (PDB code) was selected as the template. The target-template alignment using blastp suite, predicted the local pairwise sequence identity to be 98% and the E-value as 5e-171 (Figure 17C). The ligand adenylyl phosphoramidate (AMPPN) was removed from 3IED template for building the near native model of PfHsp90 (Figure 17D). The model was subjected to 10 steps of energy minimization to obtain the lowest energy model for further analysis.

A.

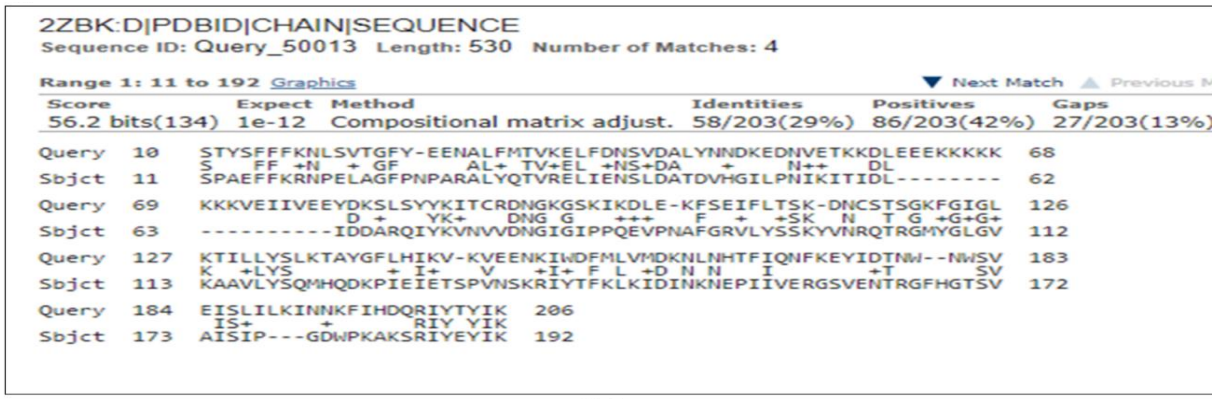

2ZBK:D|PDBID|CHAIN|SEQUENCE
Sequence ID: Query_50013 Length: 530 Number of Matches: 4

Range 1: 11 to 192 Graphics ▼ Next Match ▲ Previous M

Score	Expect	Method	Identities	Positives	Gaps
56.2 bits(134)	1e-12	Compositional matrix adjust.	58/203(29%)	86/203(42%)	27/203(13%)

```
Query  10   STYSFFFKNLSVTGFY-EENALFMTVKELFDNSVDALYNNDKEDNVETKKDLEEEKKKKK  68
            S   FF +N   + GF     AL+ TV+EL +NS+DA    +     N++    DL
Sbjct  11   SPAEFFKRNPELAGFPNPARALYQTVRELIENSLDATDVHGILPNIKITIDL--------  62

Query  69   KKKVEIIVEEYDKSLSYYKITCRDNGKGSKIKDLE-KFSEIFLTSK-DNCSISGKFGIGL  126
                    D  +    YK+   DNG G    +++    F   +  +SK  N   T G +G+G+
Sbjct  63   ----------IDDARQIYKVNVVDNGIGIPPQEVPNAFGRVLYSSKYVNRQTRGMYGLGV  112

Query  127  KTILLYSLKTAYGFLHIKV-KVEENKIWDFMLVMDKNLNHTFIQNFKEYIDTNW--NWSV  183
            K  +LYS     + I+    V    +I+ F L +D N N    I          +T    SV
Sbjct  113  KAAVLYSQMHQDKPIEIETSPVNSKRIYTFKLKIDINKNEPIIVERGSVENTRGFHGTSV  172

Query  184  EISLILKINNKFIHDQRIYTYIK  206
             IS+      +     RIY YIK
Sbjct  173  AISIP---GDWPKAKSRIYEYIK  192
```

B.

D.

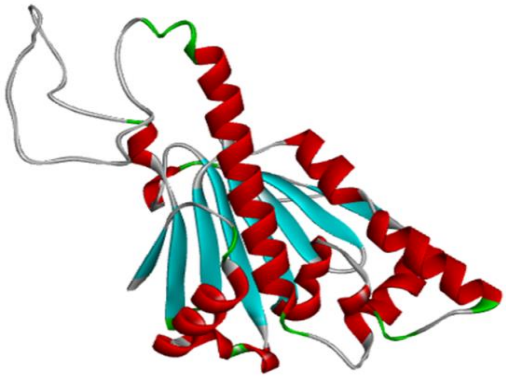

C.

Chain A, Heat shock protein [Plasmodium falciparum 3D7]
Sequence ID: 3IED_A Length: 272 Number of Matches: 1

Range 1: 14 to 272 GenPept Graphics ▼ Next Match ▲ Previous Match

Score	Expect	Method	Identities	Positives	Gaps
498 bits(1283)	5e-171	Compositional matrix adjust.	253/259(98%)	255/259(98%)	0/259(0%)

```
Query  89   REDISSDSSPVEKYNFKAEVNKVMDIIVNSLYTDKDVFLRELISNASDACDKKRIILENN  148
            RE++     SPVEKYNFKAEVNKVMDIIVNSLYTDKDVFLRELISNASDACDKKRIILENN
Sbjct  14   RENLYFQGSPVEKYNFKAEVNKVMDIIVNSLYTDKDVFLRELISNASDACDKKRIILENN  73

Query  149  KLIKDAEVVTNEEIKNETEKEKTENVNESTDKKENVEEEKNDIKKLIIKIKPDKEKKTLT  208
            KLIKDAEVVTNEEIKNETEKEKTENVNESTDKKENVEEEKNDIKKLIIKIKPDKEKKTLT
Sbjct  74   KLIKDAEVVTNEEIKNETEKEKTENVNESTDKKENVEEEKNDIKKLIIKIKPDKEKKTLT  133

Query  209  ITDNGIGMDKSELINNLGTIAQSGTAKFLKQIEEGKADSNLIGQFGVGFYSSFLVSNRVE  268
            ITDNGIGMDKSELINNLGTIAQSGTAKFLKQIEEGKADSNLIGQFGVGFYSSFLVSNRVE
Sbjct  134  ITDNGIGMDKSELINNLGTIAQSGTAKFLKQIEEGKADSNLIGQFGVGFYSSFLVSNRVE  193

Query  269  VYTKKEDQIYRWSSDLKGSFSVNEIKKYDQEYDDIKGSGTKIILHLKEECDEYLEDYKLK  328
            VYTKKEDQIYRWSSDLKGSFSVNEIKKYDQEYDDIKGSGTKIILHLKEECDEYLEDYKLK
Sbjct  194  VYTKKEDQIYRWSSDLKGSFSVNEIKKYDQEYDDIKGSGTKIILHLKEECDEYLEDYKLK  253

Query  329  ELIKKYSEFIKFPIEIWSE  347
            ELIKKYSEFIKFPIEIWSE
Sbjct  254  ELIKKYSEFIKFPIEIWSE  272
```

Figure 17. Bergerat fold of PfTopoVIB has high similarity with SsTopoVIB: A) Pairwise sequence alignment of the Bergerat fold region of PfTopoVIB (Query) and SsTopoVIB (Sbjct); positives show the number of identical amino acids or that have similar chemical properties. B) Homology model of PfTopoVIB was designed using 2ZBK template; 3D structure rendered in solid ribbon and colored according to secondary structure; alpha helices in red, beta sheets in Cyan, coils in white and turns in green. C) Pairwise sequence alignment of the N-terminal domain of PfHsp90 (Query) (Q8IL32) and the template 3IED (Subject). D) Homology model of PfHsp90 created using template 3IED; model

represented in solid ribbon format, colored according to the secondary structure; alpha helices in red, beta sheets in Cyan, coils in white and turns in green

5.2 Modeled structure validation

After designing both the models, it was necessary to investigate whether it can be used for our further studies, and for that we validated our models through PROCHECK, Ramachandran plot and SAVS ERRAT scores. PROCHECK results and Ramachandran plot servers judge the stereo chemical quality and stability of the amino acids present in the respective models. Whereas, SAVS ERRAT gives overall quality factor for non-bonded atomic interactions. Higher scores indicate higher quality and the accepted range is >50 for a high-quality model.

The PROCHECK results (Figure 18A) Ramachandran plot (Figure 18B) for PfTopoVIB revealed that 80.4% of the residues (337 amino acids) were in the most favoured regions, 15.5% (65 amino acids) in the additional allowed region, 2.9% (12 amino acids) in the generously allowed region and 1.2% (5 amino acids) in the disallowed region. The resultant model showed ERRAT score as 81.728 and the final energy as -21297.992 kJ/mol. The PROCHECK results (Figure 18C) and the Ramachandran plot of PfHsp90 model (Figure 18D) revealed that 91.9% of the residues (181 amino acids) were in the most favoured regions, 8.1% (16 amino acids) in the additional allowed region, 0.0% (0 amino acids) in the generously allowed region and 0.0% (0 amino acids) in the disallowed region. The model showed ERRAT score as 81.878 and the final energy was -11965.740 kJ/mol

A.

```
+----------<<<  P  R  O  C  H  E  C  K     S  U  M  M  A  R  Y  >>>----------+
|                                                                             |
| /var/www/PROCHECK/Jobs/4681214/4681214.pdb   1.5              440 residues |
|                                                                             |
*| Ramachandran plot:   80.4% core   15.5% allow    2.9% gener    1.2% disall |
|                                                                             |
*| All Ramachandrans:   39 labelled residues (out of 438)                     |
+| Chi1-chi2 plots:      7 labelled residues (out of 330)                     |
| Side-chain params:    5 better     0 inside      0 worse                    |
|                                                                             |
*| Residue properties: Max.deviation:    19.8             Bad contacts:    7 |
*|                     Bond len/angle:    6.4    Morris et al class:  1  1  2 |
*|     2 D amino acids                                                        |
| G-factors           Dihedrals:  -0.33  Covalent:  -0.15    Overall:  -0.24 |
|                                                                             |
*| Planar groups:    84.0% within limits  16.0% highlighted      10 off graph |
|                                                                             |
+-----------------------------------------------------------------------------+
  + May be worth investigating further.  * Worth investigating further.
```

B

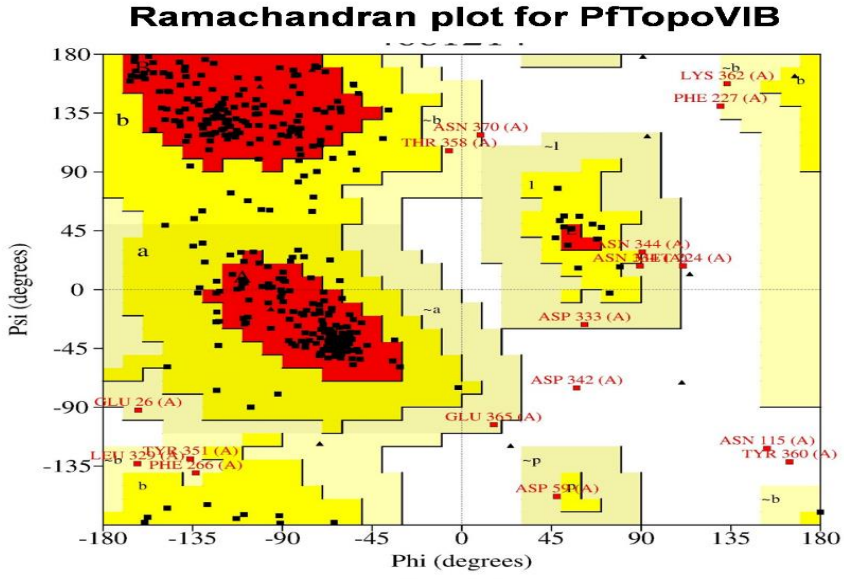

Plot statistics

Residues in most favoured regions [A,B,L]	337	80.4%
Residues in additional allowed regions [a,b,l,p]	65	15.5%
Residues in generously allowed regions [~a,~b,~l,~p]	12	2.9%
Residues in disallowed regions	5	1.2%
Number of non-glycine and non-proline residues	419	100.0%
Number of end-residues (excl. Gly and Pro)	1	
Number of glycine residues (shown as triangles)	16	
Number of proline residues	4	
Total number of residues	440	

Based on an analysis of 118 structures of resolution of at least 2.0 Angstroms and R-factor no greater than 20%, a good quality model would be expected to have over 90% in the most favoured regions.

C.

```
+----------<<<  P  R  O  C  H  E  C  K     S  U  M  M  A  R  Y  >>>----------+
|                                                                             |
| /var/www/PROCHECK/Jobs/4909156/4909156.pdb   1.5              214 residues |
|                                                                             |
| Ramachandran plot:   91.9% core    8.1% allow    0.0% gener    0.0% disall |
|                                                                             |
+| All Ramachandrans:    1 labelled residues (out of 212)                     |
| Chi1-chi2 plots:      0 labelled residues (out of 145)                     |
| Side-chain params:    5 better     0 inside      0 worse                   |
|                                                                             |
+| Residue properties: Max.deviation:     5.8             Bad contacts:    0  |
|                     Bond len/angle:    2.4    Morris et al class:  1  1  2  |
|                                                                             |
| G-factors           Dihedrals:   0.00  Covalent:   0.43    Overall:   0.17 |
|                                                                             |
+| Planar groups:    94.0% within limits   6.0% highlighted       1 off graph |
|                                                                             |
+-----------------------------------------------------------------------------+
  + May be worth investigating further.  * Worth investigating further.
```

D.

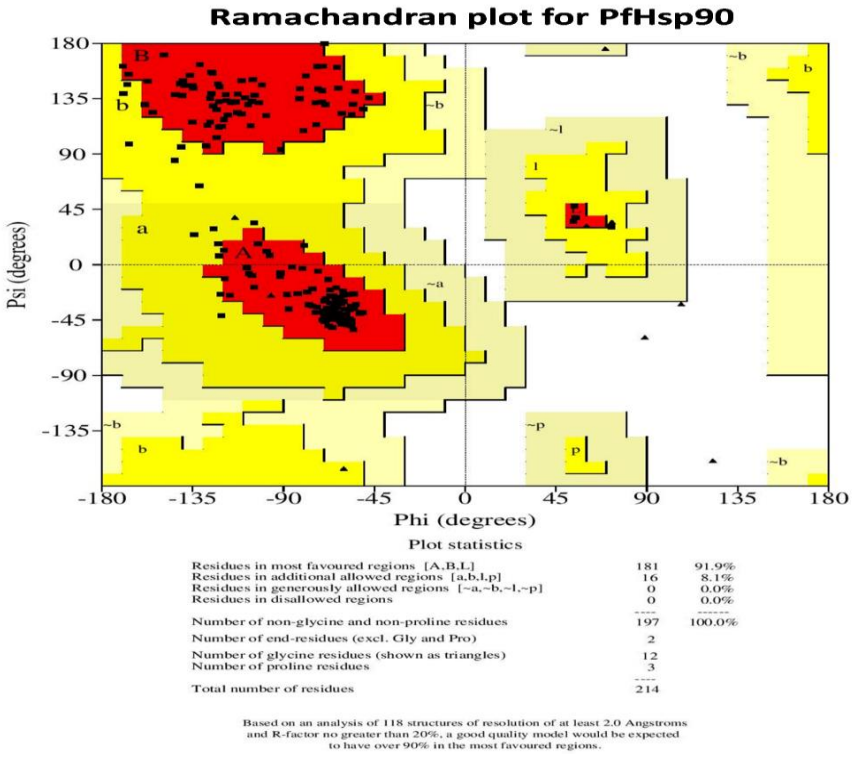

Figure 18: Modeled structure validation A) Procheck result for PfTopoVIB B) Ramachandran plot for PfTopoVIB C) Procheck result for PfHsp90 D) Ramachandran plot for PfHsp90

5.3 In silico binding of Radicicol and ATP to the Bergerat fold of PfTopoVIB and PfHsp90 models

After checking the overall structure of PfTopoVIB and PfHsp90 models, we wanted to validate the structure of the binding pockets, i.e., the Bergerat fold. To that end we used ATP and Radicicol as positive control. We carried out different set of docking studies with our models and the respective crystal structures templates to compare their interactive points.

The crystal structure 2ZBK.D is *Sulpholobus shibatae* Topoisomerase VIB (SsTopoVIB) bound to Radicicol (RDC531). We have presented this structure in (Figure 19A). To validate our docking, we have removed Radicicol from this structure and redocked Radicicol to the apo-structure represented in (Figure 19B). We compared the native pose (Figure 19A) and the newly created docked pose (Figure 19B) by superimposing the RMSD value between the native pose and the docked pose was 1.86 Å (Figure 19C). Our analysis showed that the amino acid Thr170 formed a hydrogen bond, while Ala46, Ile79, Val112 and Phe90 were actively involved in hydrophobic interactions with Radicicol in the 2ZBK-D structure (Figure 19D). Our re-docked structure shows the conservation of the above interactions, in addition, it shows four more contacts including one hydrogen bond with Lys113 and hydrophobic interactions with Gly80, Ala89 and Val112 (Figure 19E). After validating our model, next, we carried out two sets of docking studies using LibDock, one in which both ATP and Radicicol were docked to PfTopoVIB (Figure 19F, G respectively) and in the second set, both the ligands were docked with PfHsp90 respectively (Figure 19H, I). Our study shows that Radicicol binds to the Bergerat fold of PfTopoVIB and PfHsp90 like that of the intrinsic ligand ATP. This also ensured

that the proteins were correctly modeled in silico and had near-native structural topology. The LibDock score for ATP and Radicicol docking to PfTopoVIB were 143.657 and 76.4008 respectively. While 96 different docking poses were obtained for ATP, only 2 different binding poses were obtained for Radicicol. The type of molecular interactions found between PfTopoVIB and ATP/Radicicol and their interatomic distance is tabulated (Table 5). ATP showed 14 molecular interactions in the form of hydrogen bonds and hydrophobic interactions.

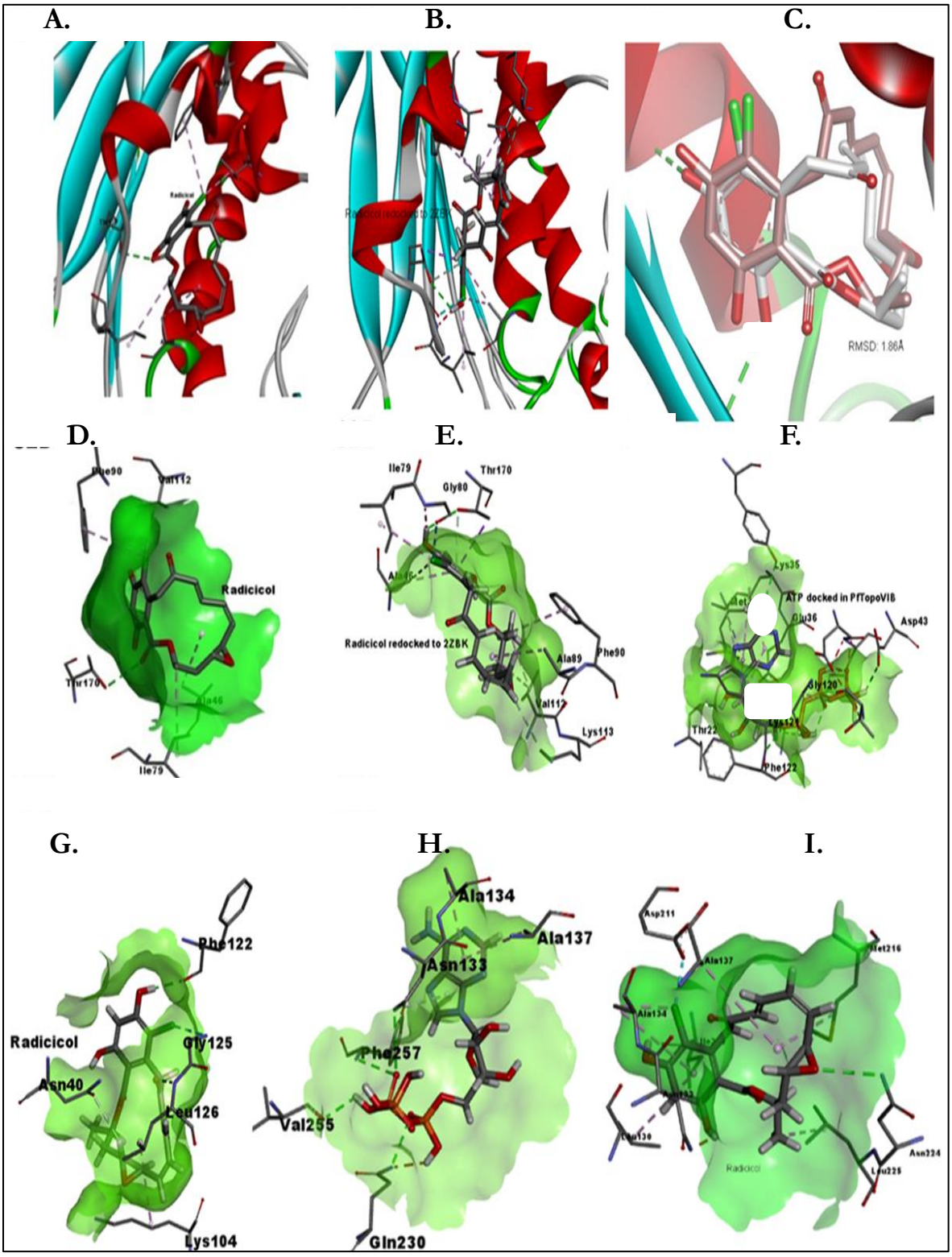
A.
B.
C.
RMSD: 1.86Å
D.
E.
F.
Radicicol
Thr170
Ile79
Radicicol redocked to 2ZBK
Ala89
Phe90
Lys113
ATP docked in PfTopoVIB
Asp43
Phe122
G.
H.
I.
Radicicol
Asn40
Gly125
Leu126
Lys104
Ala134
Ala137
Asn133
Phe257
Val255
Gln230
Asp211
Met216
Asn224
Leu225

Figure 19: *In silico* binding of Radicicol and ATP to the Bergerat fold of PfTopoVIB and PfHsp90 models: A) Radicicol bound to Bergerat fold in *Ss*TopoVIB (2ZBK- D chain). B) Radicicol redocked to *Ss*TopoVIB (*2ZBK- D chain).* C) The native ligand superimposed on the redocked pose of the ligand in the Bergerat fold of 2ZBK- D chain. Protein structure rendered in solid ribbon format in the background and the ligand structures rendered in sticks format with atom-based coloring. D) Native molecular interactions of Radicicol with *Ss*TopoVIB (2ZBK- D chain) E) Molecular interactions of Radicicol when redocked to 2ZBK-D chain. F) - G) ATP and Radicicol interacting with Bergerat fold residues of PfTopoVIB model respectively. H) – I) ATP and Radicicol interacting with Bergerat fold residues of PfHsp90 respectivel

The key amino acids which are involved in conventional hydrogen bonds were Phe122, Asp43 and Thr22 whereas the residues Lys35, Gly120 and Glu36 showed carbon hydrogen bonds. Several hydrophobic interactions were also noted which included a Pi-Sigma bond with Lys35, a Pi-Sulfur bond with Met32 and four Pi-Alkyl bonds, two each with Lys121 and Lys35. Radicicol showed 6 molecular interactions with PfTopoVIB, in which Leu126 formed a conventional hydrogen bond and a hydrophobic interaction through the alkyl group. Phe122 also formed a conventional hydrogen bond. While Asn40 formed a carbon hydrogen bond, Gly125 interacted with the Cl (halogen) of Radicicol and Lys104 made a hydrophobic interaction through the alkyl group. We found that many of the amino acids which interact with Radicicol were conserved between PfTopoVIB and SsTopoVIB. For example, the residues Phe105, Ala44 and Asn40 in PfTopoVIB correspond to that of Phe90, Ala46 and Asn42 in SsTopoVIB.

In the second set of docking studies, we allowed ATP and Radicicol to dock to the in-silico model of PfHsp90 N-terminal domain. Docking resulted in 81 different poses of the ligand ATP with the highest LibDock score of 129.333. 7 molecular interactions were found between ATP and PfHsp90 (Figure 19H). Residues Asn133, Gln230, Phe257 and Val255 were found to form

conventional hydrogen bonds with ATP. Asn133 was also found to possess a Pi-Donor hydrogen bond, whereas Ala134 and Ala137 interacted through the alkyl group (hydrophobic interaction). Radicicol interacted with PfHsp90 in the Bergerat fold with a LibDock score of 91.791 generating 9 different docked poses. The key residues found to interact well with Radicicol were Asn224 through a conventional hydrogen bond, Asp211 through the halogen Cl and the amino acids Ile310, Ala134, Ala137, Met216, Leu225 and Leu130 all through hydrophobic interactions mostly of the alkyl type (Figure 19I). Radicicol when docked with the template PDB structure 3IED, the key residues Ala137, Met207 and Asn215 were identified to interact which corresponds to the residues Ala137, Met216 and Asn224 in the PfHsp90 model. There is a difference of 9 residues in between Met207 and Met216 and also in between Asn215 and Asn224 due to absence of some amino acids in 3IED. As a result, the numbers given to amino acids in PDB is different when compared with our PfHsp90 model.

Name	No. of favorable interactions	Interaction chemistry (residues and atoms involved)	Types of interactions	Inter atomic distance (Å)
ATP	14	A:PHE122:N - ATP:O13	onal HydrogenBond	2.80426
		ATP:H33 - A:ASP43:OD2	onal HydrogenBond	2.75367
		ATP:H43 - A:THR22:O	onal HydrogenBond	2.10041
		A:LYS35:CE - ATP:N23	Carbon Hydrogen Bond	3.21029
		A:GLY120:CA - ATP:O5	Carbon Hydrogen Bond	3.38991
		A:GLY120:CA - ATP:O9	Carbon Hydrogen Bond	3.22957
		ATP:H37 - A:GLU36:OE2	Carbon Hydrogen Bond	2.19205
		ATP:H39 - A:GLU36:OE1	Carbon Hydrogen Bond	2.43497
		A:LYS35:CE – ATP	Hydrophobic (Pi-Sigma)	3.88659
		A:MET32:SD - ATP	Pi-Sulfur	3.78864
		ATP - A:LYS35	Hydrophobic (Pi-Alkyl)	4.97559
		ATP - A:LYS121	Hydrophobic (Pi-Alkyl)	3.54858
		ATP - A:LYS35	Hydrophobic (Pi-Alkyl)	4.37581
		ATP - A:LYS121	Hydrophobic (Pi-Alkyl)	4.80162
Radicicol	6	A:LEU126:N - Ligand_Radicicol:O21	onal HydrogenBond	2.72175
		Ligand_Radicicol:H41 - A:PHE122:O	Conventional Hydrogen Bond	2.15977
		nd_Radicicol:H29 - A:ASN40:OD1	Carbon Hydrogen Bond	2.9883
		A:GLY125:N - Ligand_Radicicol:Cl25	Halogen (Cl, Br, I)	3.15453
		A:LYS104 - Ligand_Radicicol	Hydrophobic (Alkyl)	4.90789
		A:LEU126 - Ligand_Radicicol	Hydrophobic (Alkyl)	4.47298
Analog 2	12	A:LYS127:CE - Analog 2:O20	Carbon Hydrogen Bond	3.10244
		A:PHE122:O - Analog 2:Cl24	Halogen (Cl, Br, I)	3.05922
		A:LYS104:NZ - Analog 2	i-Donor Hydrogen Bond; Electrostatic (Pi-Cation)	3.49079
		A:GLU36:OE1 - Analog 2	Electrostatic (Pi-Anion)	4.79691
		A:GLU36:OE2 - Analog 2	Electrostatic (Pi-Anion)	3.01484
		A:LYS121:N - Analog 2	Pi-Donor Hydrogen Bond	3.7326
		A:LEU126:CD2 - Analog 2	Hydrophobic (Pi-Sigma)	3.63792

		A:PHE105 - Analog 2	Hydrophobic (Pi-Pi T-shaped)	5.57757
		Analog 2 - A:LYS104	Hydrophobic (Pi-Alkyl)	4.74007
		Analog 2 - A:LYS127	Hydrophobic (Pi-Alkyl)	5.3158
		Analog 2 - A:LYS121	Hydrophobic (Pi-Alkyl)	4.08109
		Analog 2 - A:LEU126	Hydrophobic (Pi-Alkyl)	5.41542
Analog 6	8	A:ASN40:ND2 - Analog 6:Cl15	Conventional Hydrogen Bond;Halogen (Cl, Br, I)	3.18295
		A:LEU126:N - Analog 6:Cl15	Conventional Hydrogen Bond; Halogen (Cl, Br, I)	2.65522
		Analog 6:H53 - A:PHE122:O	Conventional Hydrogen Bond	2.22567
		A:LYS127:CE - Analog 6:O22	Carbon Hydrogen Bond	3.42368
		A:GLU36:OE2 - Analog 6	Electrostatic (Pi-Anion)	2.81234
		Analog 6:Cl15 - A:LEU126	Hydrophobic (Alkyl)	4.4957
		Analog 6 - A:LYS35	Hydrophobic (Pi-Alkyl)	4.48007
		Analog 6 - A:LYS121	Hydrophobic (Pi-Alkyl)	4.77203
Analog 7	14	A:LYS104:NZ - Analog 7	Pi-Donor Hydrogen Bond; Electrostatic (Pi-Cation)	3.62644
		A:ASN48:ND2 - Analog 7	Pi-Donor Hydrogen Bond	3.91351
		A:ILE185:CD1 - Analog 7	Hydrophobic (Pi-Sigma)	2.8234
		A:SER41:OG - Analog 7	Pi-Lone Pair	2.76756
		A:ASN40:C,O;SER41:N - Analog 7	Hydrophobic (Amide-Pi Stacked)	4.25484
		Analog 7:Cl24 - A:LYS104	Hydrophobic (Alkyl)	4.58326
		Analog 7:Cl24 - A:LEU126	Hydrophobic (Alkyl)	4.88912
		Analog 7 - A:ALA44	Hydrophobic (Pi-Alkyl)	5.08465
		Analog 7 - A:VAL183	Hydrophobic (Pi-Alkyl)	4.8022
		Analog 7 - A:LEU37	Hydrophobic (Pi-Alkyl)	4.7053
		Analog 7 - A:CYS90	Hydrophobic (Pi-Alkyl)	3.90423
		Analog 7 - A:VAL183	Hydrophobic (Pi-Alkyl)	4.76599
		Analog 7 - A:ALA44	Hydrophobic (Pi-Alkyl)	5.11399
		Analog 7 - A:LYS95	Hydrophobic (Pi-Alkyl)	5.42291

Table 5: Interactions and chemical bonding of ATP, Radicicol and its analogs with PfTopoVIB mode

5.4 Designing of Radicicol analogs and docking to PfTopoVIB and PfHsp90

We conducted this study to potentially generate a specific Radicicol analog for PfTopoVIB to reduce its *in vivo* off-targets. To that end, our strategy was to modify the structure of Radicicol to design novel analogs by substituting the functional groups, which potentially enhance its inhibition against PfTopoVIB and reduce its inhibition of PfHsp90. The reported Structure-Activity Relationship (SAR) of Radicicol (143) was considered for selecting the attachment point for the modification, and various functional groups were identified from relevant literature (144-149). We substituted different functional groups at specific attachment points of Radicicol without disturbing the macrocyclic ring required for the bioactivity of Radicicol.

The 3D structure of Radicicol served as the reference molecule for the in-silico design of 97 different structural analogs using MarvinSketch tool. The analog structures were computationally drawn and designed by modifying different atoms, functional groups and/or side chains of Radicicol, based on its reported Structure–activity relationship (SAR) to alter its biological activity against PfTopoVIB and PfHsp90. We focused on altering or replacing those functional groups of Radicicol that cause higher affinity towards Hsp90. 6498 different conformers were generated for 97 analogs using Biovia DS 4.0. Receptor-ligand docking performed by LibDock protocol against PfTopoVIB protein using 6498 analog conformers returned 3162 docked poses. In the same manner, docking against PfHsp90 protein using 6498 analog conformers returned 2512 docked poses. All the docked poses were analysed and the best docked pose of each ligand towards each protein was identified based on the highest LibDock score and compared with the LibDock score of ATP and Radicicol (Table 6).

Table 6: Comparison of the LibDock score of ATP, Radicicol and its derivatives against PfTopoVIB and PfHsp90 (The number of poses of each analog docked to the protein are given in bracket)

Name	LibDock Score (No. of poses docked)	
	PfTopoVIB	**PfHsp90**
ATP	143.657 (96)	129.333 (81)
Radicicol	76.4008 (2)	91.7911 (9)
Analog 1	105.184 (8)	92.585 (4)
Analog 2	133.823 (9)	**No docked poses**
Analog 3	74.1867 (2)	89.926 (12)
Analog 4	87.0343 (5)	92.2888 (7)
Analog 5	88.8705 (2)	101.406 (14)
Analog 6	108.647 (2)	**No docked poses**
Analog 7	77.5334 (2)	**No docked poses**
Analog 8	84.9003 (2)	98.4773 (7)
Analog 9	87.3219 (2)	98.7025 (11)
Analog 10	92.3465 (1)	104.188 (8)
Analog 11	77.623 (4)	84.8962 (20)
Analog 12	68.6989 (1)	93.066 (5)
Analog 13	73.1041 (3)	89.7777 (2)
Analog 14	82.7546 (3)	90.8558 (5)
Analog 15	88.8888 (15)	96.9247 (52)
Analog 16	76.4399 (2)	90.5099 (5)
Analog 17	76.4532 (1)	95.5775 (20)
Analog 18	76.0733 (1)	106.118 (5)
Analog 19	**No docked poses**	96.8303 (13)
Analog 20	**No docked poses**	66.8629 (2)
Analog 21	77.4023 (5)	96.0849 (7)
Analog 22	83.9107 (5)	105.157 (13)
Analog 23	76.1084 (4)	86.745 (9)
Analog 24	77.7701 (6)	84.7549 (6)
Analog 25	88.8888 (15)	96.9247 (52)
Analog 26	92.0622 (37)	106.204 (15)
Analog 27	113.034 (92)	107.629 (90)
Analog 28	126.111 (81)	111.54 (89)
Analog 29	146.569 (91)	107.773 (30)

Analog 30	116.084 (92)	121.593 (74)
Analog 31	121.53 (95)	119.932 (38)
Analog 32	**No docked poses**	**No docked poses**
Analog 33	124.066 (87)	99.2816 (89)
Analog 34	111.149 (94)	113.188 (86)
Analog 35	104.421(96)	113.064 (81)
Analog 36	89.2511 (26)	80.1705 (2)
Analog 37	87.3713 (14)	93.9307 (22)
Analog 38	100.184 (58)	86.4046 (6)
Analog 39	109.044 (21)	85.967 (21)
Analog 40	91.7332 (27)	92.2866 (33)
Analog 41	106.414 (52)	101.088 (37)
Analog 42	95.2177 (19)	96.2555 (22)
Analog 43	109.439 (11)	93.4571 (13)
Analog 44	108.03 (67)	79.2665 (8)
Analog 45	90.5919 (40)	92.064 (63)
Analog 46	103.04 (56)	97.2199 (71)
Analog 47	86.6312 (10)	96.4127 (15)
Analog 48	103.04 (56)	97.2199 (71)
Analog 49	98.6211 (17)	92.5781 (48)
Analog 50	77.7701 (6)	84.7549 (6)
Analog 51	76.1084 (4)	86.745 (9)
Analog 52	120.296 (60)	115.213 (16)
Analog 53	115.77 (62)	104.267 (23)
Analog 54	86.4992 (2)	90.9012 (23)
Analog 55	**No docked poses**	83.4545 (11)
Analog 56	81.7324 (3)	87.2365 (17)
Analog 57	**No docked poses**	94.1162 (15)
Analog 58	69.6464 (2)	89.5652 (12)
Analog 59	91.3509 (3)	98.6856 (6)
Analog 60	103.441 (38)	105.537 (44)
Analog 61	124.531 (85)	112.673 (81)
Analog 62	105.573 (95)	108.981 (67)
Analog 63	**No docked poses**	**No docked poses**
Analog 64	105.808 (96)	111.198 (79)
Analog 65	127.171 (86)	107.959 (14)
Analog 66	127.312 (77)	112.49 (11)
Analog 67	134.451 (91)	118.745 (88)
Analog 68	80.1883 (1)	80.9545 (6)
Analog 69	94.0426 (26)	97.3786 (18)

Analog 70	96.43 (16)	106.191 (27)
Analog 71	106.638 (11)	114.339 (36)
Analog 72	71.6177 (3)	89.3496 (9)
Analog 73	78.2695 (5)	89.3019 (11)
Analog 74	**No docked poses**	97.7812 (7)
Analog 75	98.4877 (42)	124.62 (70)
Analog 76	128.528 (91)	113.804 (85)
Analog 77	103.528 (36)	89.1453 (3)
Analog 78	126.025 (40)	91.7578 (8)
Analog 79	130.084 (92)	58.4248 (1)
Analog 80	119.39 (93)	126.137 (9)
Analog 81	71.7722 (2)	90.548 (22)
Analog 82	**No docked poses**	89.7058 (6)
Analog 83	93.4051 (5)	106.048 (15)
Analog 84	117.584 (6)	82.8479 (2)
Analog 85	85.9985 (24)	90.4115 (20)
Analog 88	127.677 (89)	105.661 (91)
Analog 89	76.0733 (1)	106.118 (5)
Analog 90	140.878 (84)	119.481 (12)
Analog 91	158.337 (69)	100.199 (2)
Analog 92	103.932 (26)	94.0685 (4)
Analog 93	**No docked poses**	**No docked poses**
Analog 94	100.184 (58)	86.4046 (6)
Analog 95	126.616 (98)	111.055 (14)
Analog 96	82.3439 (1)	37.5413 (1)
Analog 97	87.0725(2)	97.8591 (15)
Analog 98	92.3465 (1)	104.188 (8)
Analog 99	104.634 (92)	105.533 (83)

5.5 Selection of the Radicicol analogs that show specific docking to PfTopoVIB but not to PfHsp90

PfTopoVIB and PfHsp90 share a common structural ATP-binding domain known as the Bergerat fold (94) characterized by a structural motif consisting of an eight stranded mixed beta-sheet in two layers – alpha/beta (111). We carried out this study to select the specific analog for PfTopoVIB binding and sorted them with the following strategy. Out of 97 analogs, 88 molecules interacted with PfTopoVIB within the same binding cavity occupied by Radicicol and ATP, whereas 9 analogs failed to dock. Depending upon the LibDock score of each analog compared to ATP and Radicicol, we classified them into two groups, one with a higher LibDock score than the cut off value 76.4008 and the other with lower scores than the cut off value. In case of PfTopoVIB, we have chosen this cut off value to select those analogs of Radicicol that have a higher chance of binding with PfTopoVIB as compared to the Radicicol. The LibDock score of Radicicol for PfTopoVIB is 76.4 hence all the values that are higher than 76.4 are shortlisted. To that end, 77 analogs were identified with LibDock scores higher than the cut off value and 11 analogs with lower LibDock scores than the cut off. The highest score was obtained for analog 91 (158.337) and the lowest score was obtained for analog 23 (76.108). So, based on docking score, 77 analogs of Radicicol performed better than Radicicol, 11 analogs were poor performers and 9 did not dock at all (Table 6). The same classification criterion was adopted for analysing the docking results of PfHsp90 also. In this case, the cut off value was taken as 91.7911. The LibDock score of Radicicol for PfHsp90 is 91.79; hence the values higher than that of 91.79 are shortlisted. Out of 97 analogs, 78 molecules were found to interact with a higher dock score than the cut off value. 13 analogs

docked with a lower LibDock score and the remaining 6 analogs did not dock to PfHsp90 at all. The highest binding affinity was obtained for analog 80 (126.137) and the lowest for analog 78 (91.757). We focused our work only on those subsets of Radicicol analogs that display higher affinity towards PfTopoVIB and no affinity towards PfHsp90. Hence, although analog 91 shows the highest score for PfTopoVIB, it also shows higher docking score for PfHsp90. Similarly, analog 23 shows a poor score for PfTopoVIB compared to PfHsp90. The analysis of these ligands is beyond the scope of this manuscript. Our criterion for selecting the best analogs was to compare their binding affinity with both the proteins and finally choose those which docks specifically to PfTopoVIB but have little or no binding towards PfHsp90. We observed that out of the 6 analogs which did not dock to PfHsp90, 3 analogs did not dock to PfTopoVIB either, but the other 3 analogs were having higher LibDock scores towards PfTopoVIB. The structures of Radicicol and these three analogs are presented (Figure 20). These three analogs; analog 2, analog 6, and analog 7, with LibDock scores 133.823, 108.647 and 77.533 respectively were selected as the lead molecules. The number of molecules generated, docked and filtered at various step of this study has been summarized in Table 7.

Further, we compared the volume of Radicicol binding pockets between PfTopoVIB and PfHsp90 (Figure 21A, B) using a grid based 'Eraser' algorithm implemented in DS 4.0 and found that the binding pocket volume for PfTopoVIB is (180.625 $Å^3$), much larger than that of PfHsp90 (143 $Å^3$).

Both the pockets were found to contain the residues of the alpha/beta structural motif, where the ATP and Radicicol interacted in our docking studies. We reason that as the size of analog 2 (637.162 Da), analog 6 (516.969 Da) and analog 7 (653.161 Da) are larger than that of ATP (507.181 Da) and Radicicol

(364.777 Da), they are not able to fit properly to the binding site of PfHsp90 which is smaller than the binding pocket of PfTopoVIB.

Table 7: The number of molecules generated, docked and filtered at various step

Virtual screening steps for Radicicol and its analogs	Number of molecules	
3D structure retrieved for Radicicol and ATP from Pubchem	2	
Analogs generated for Radicicol using MarvinSketch	97	
Total number of conformers for Radicicol, 97 analogs and ATP (10 conformers each for 99 molecules)	990	
Structures prepared using Ligand preparation for Docking	962	
3D conformers generated Using DS.4.0 for docking process	6498	
Docking of 6498 structures against target proteins	PfTopoVIB	PfHsp90
No. of poses docked to target proteins at Bergerat fold	3162	2512
No. of analogs failed to dock to the target protein structures	9	6
No. of analogs docked only to PfTopoVIB and not to PfHsp90	3	
No. of lead molecules selected for interaction analysis and molecular dynamics simulation	3	

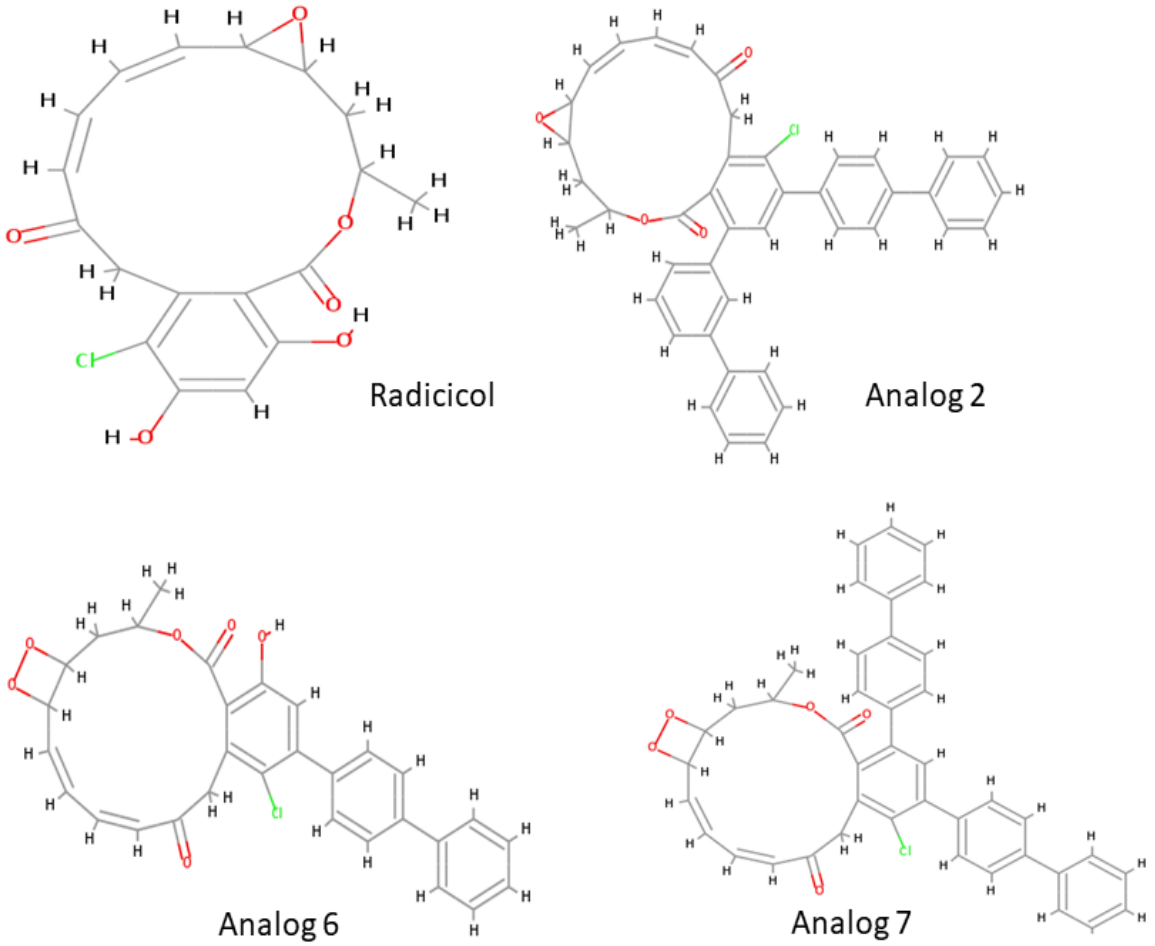

Figure 20: 2D structure of Radicicol and its analogs; 2, 6 and 7 are represented.

A.

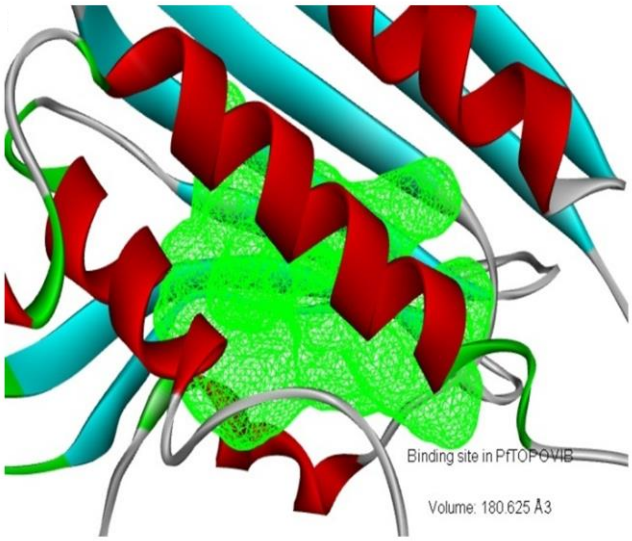
Binding site in PfTOPOVIB
Volume: 180.625 Å3

B.

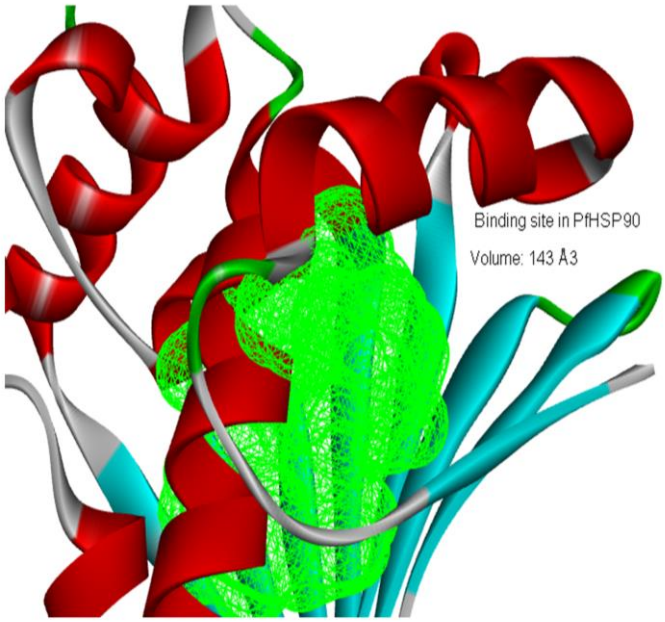
Binding site in PfHSP90
Volume: 143 Å3

Figure 21 A, B. Comparing the volume of Radicicol binding pockets between PfTopoVIB and PfHsp90

The molecular interactions between the lead analogs and PfTopoVIB (Figure 22A-C) were analyzed and compared with that of parent molecule Radicicol. Analog 2 showed 12 interactions, analog 6 showed 8 interactions and analog 7 showed 14 (Table 5). The key amino acids in PfTopoVIB which established contacts with analog 2 were Glu36, Lys104, Phe105, Ly121, Phe122, Leu126 and Lys127. While a carbon hydrogen bond and a hydrophobic Pi-alkyl interaction were formed by Lys127, two hydrophobic interactions (Pi-Sigma and Pi-alkyl) were formed with Leu126. Glu36 showed two electrostatic (Pi-anion) interactions and Lys121 had a Pi-donor hydrogen bond and one hydrophobic interaction of Pi-alkyl type. Lys104 showed a Pi-donor hydrogen bond and a hydrophobic Pi-alkyl interaction. Phe122 established an interaction through the halogen atom Cl of analog 2 and Phe105 formed a Pi-Pi T-shaped hydrophobic interaction. Analog 6 showed three conventional hydrogen bonds with the amino acids Asn40, Leu126 and Phe122. Lys127 formed a carbon hydrogen bond; Glu36 formed an electrostatic Pi-anion linkage; Leu126, Lys35 and Lys121 formed hydrophobic interactions mostly of pi-alkyl type. Analog 7, on the other hand, showed the highest number of hydrophobic interactions, but with a different set of residues present in PfTopoVIB namely Leu37, Asn40, Ala44, Cys90, Lys95, Leu126, Val183 and Ile185. Lys104 formed a Pi-donor hydrogen bond and a hydrophobic interaction through the alkyl group of analog 7. Asn48 also established a Pi-donor hydrogen bond and Ser41 showed a Pi-lone pair interaction with analog 7. When compared to ATP and Radicicol, the amino acids which retained their contacts with analog 2 were Phe122, Glu36, Lys121, Leu 126 and Lys104. The interactions with the residues Lys35, Glu36, Asn40, Lys121, Phe122, Leu126 and Ly127 were common in the case of analog 6. But analog 7 showed contacts with Leu126, Asn40 and Lys104 which were

A-C

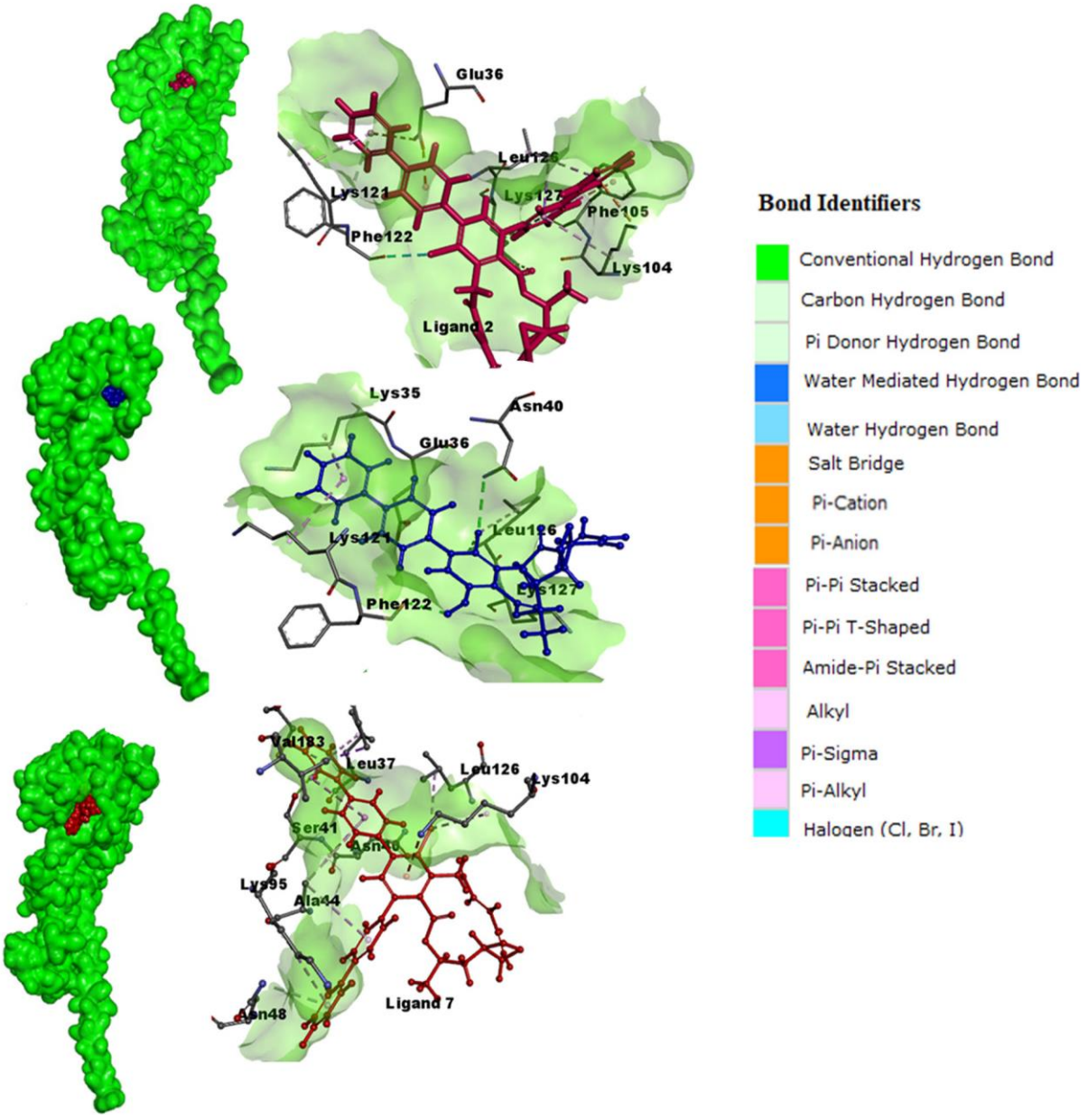

Figure 22 A-C. Molecular interactions of the lead analogs of Radicicol in the Bergerat fold of PfTopoVIB: (A-C) analog 2 (purple), analog 6 (blue) and analog 7 (red) interaction with PfTopoVIB has been presented. The color codes for different bonds also given in the figure.

similar with those found in Radicicol. There were no common contacts found between ATP and analog 7. Phe122 was interacting with ATP, Radicicol, analog 2 and analog 6, but not with analog 7, whereas Leu126 had contact with all others except ATP.

The binding of PfTopoVIB and the lead analogs within the Bergerat fold is illustrated (Figure 23). The 2D interaction diagrams of the lead analogs docked to PfTopoVIB are presented (Figure 24 A-C).

In the present study, we designed 97 analogs of Radicicol and docked all of them with PfTopoVIB and PfHsp90 models. Out of 97 analogs, 88 analogs docked with PfTopoVIB. The criterion for selection was to select those analogs that have higher docking score than Radicicol. In case of PfTopoVIB 78 molecules fulfilled that criteria. We planned to select an analog that should not bind with PfHsp90 molecule. As mentioned above, 6 molecules failed to dock PfHsp90 modeled structure. Those 6 analogs were the potential lead for our study. Out of those 6 only three analogs; analog 2, 6 and 7 showed higher binding with PfTopoVIB model. Hence, we went forward with analog 2, 6 and 7 for M.D simulation study in collaboration with Professor Nair [Department of Computational Biology and Bioinformatics, University of Kerala]. Their data showed a strong evidence that analog 2 is the most stable structure that have greater binding affinity with PfTopoVIB model (182).

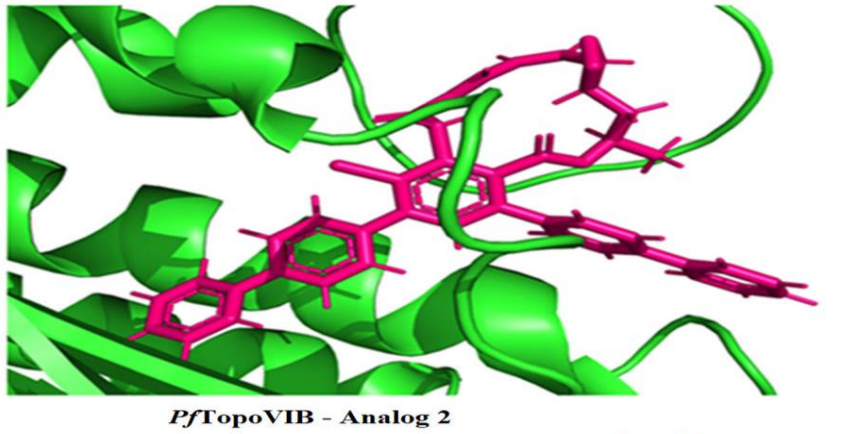

*Pf*TopoVIB - Analog 2

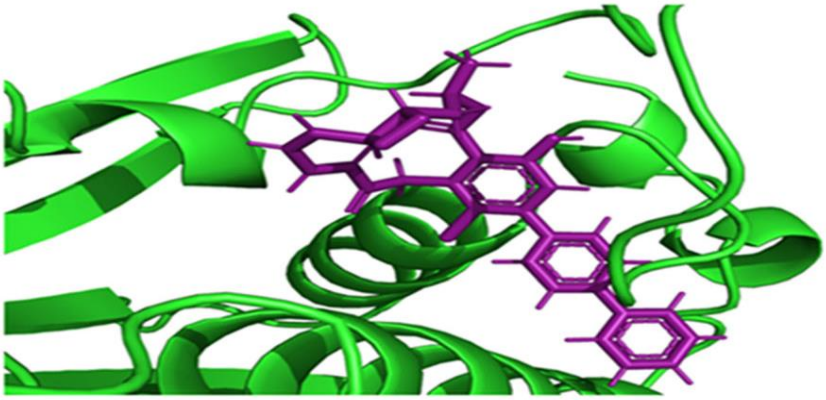

*Pf*TopoVIB - Analog 6

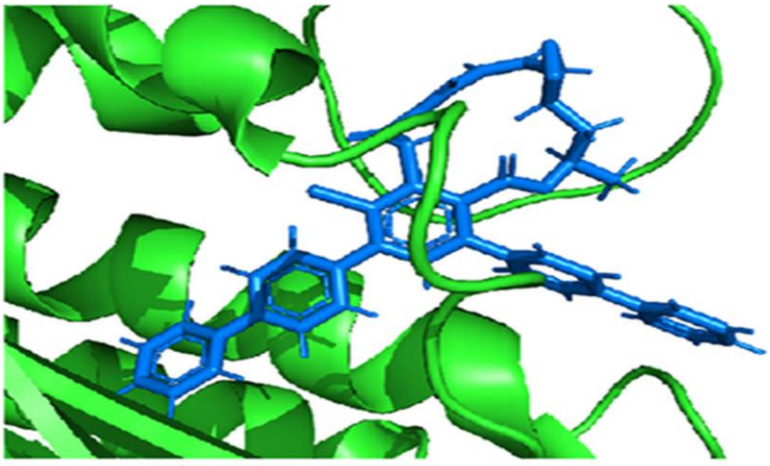

*Pf*TopoVIB - Analog 7

Figure 23. Illustration of binding between PfTopoVIB and the lead analogs: Analog 2 (pink), Analog 6 (purple) and Analog 7 (blue) binding with PfTopoVIB Bergerat fold is represented.

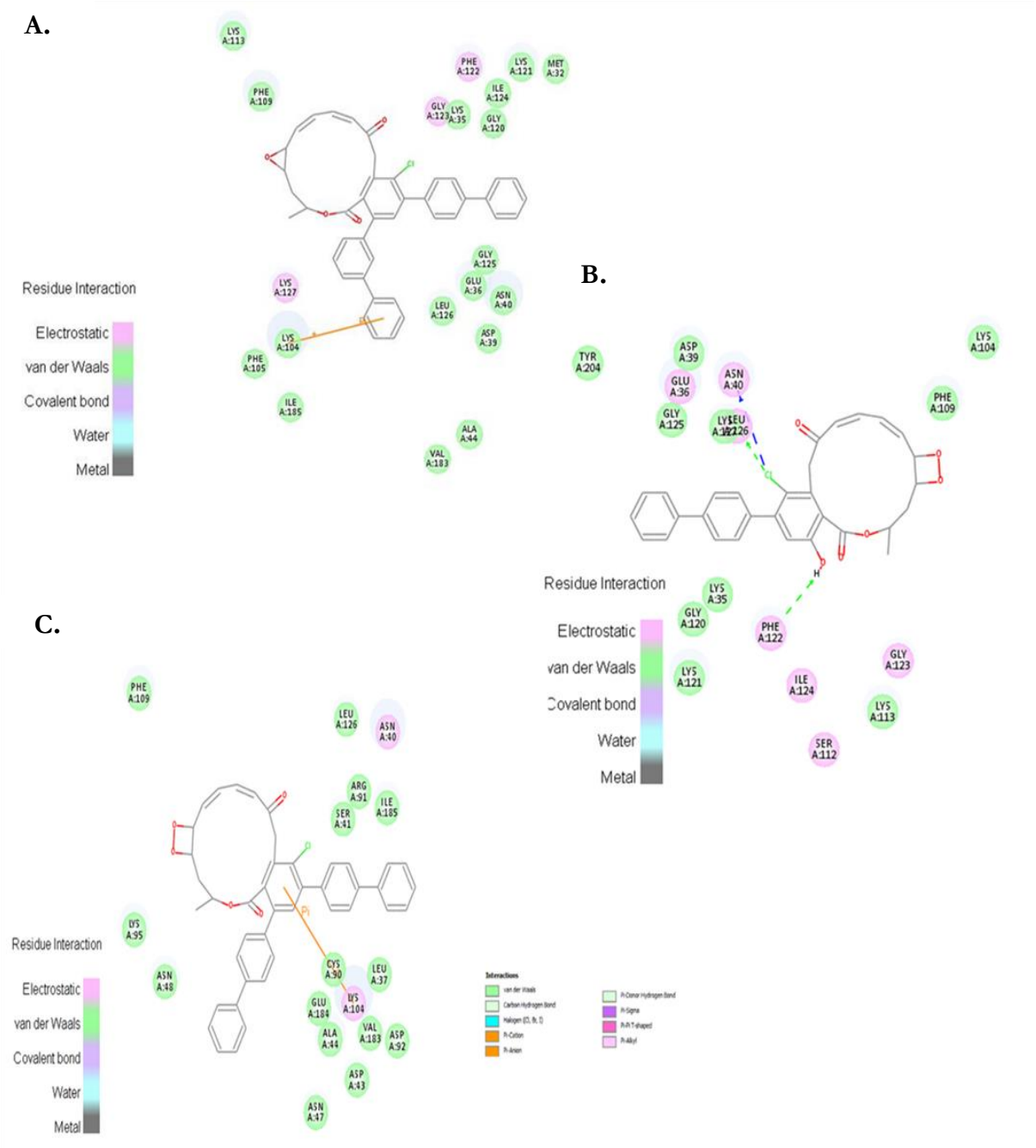

Figure 24 A-C: 2D interaction diagrams of the lead analogs with PfTopoVIB: A) – C) 2D analog interaction diagram of PfTopoVIB with Analog 2, 6 and 7 respectively; color code: purple circles – amino acids with hydrogen bonding, electrostatic or polar interactions; green circles – amino acids in the van der Waals interactions, non-polar; others grey.

CHAPTER 6

DISCUSSION

Plasmodium falciparum possesses a unique Type II topoisomerase TopoVIB, which has potential to be a novel target against malaria. Our previous studies have shown, Radicicol inhibits the schizont to ring transition of the blood stage parasites, indicating a functional role of PfTopoVIB at that stage. Endoreduplication occurs in two other stages of the parasite life cycle namely liver stage and mosquito stage (sexual stage), and PfTopoVIB might be a critical determinant for those stages as well. As most of the replication proteins are essential for the survivability, and generation of conditional knock-outs of PfTopoVIB in *Plasmodium* is technically challenging, it is important to identify highly specific chemical inhibitors of PfTopoVIB in order to delineate the precise biological role of this protein in *Plasmodium*. However, owing to the similarity within the Bergerat ATP-binding fold which is present in both PfTopoVIB and PfHsp90, Radicicol is found to dock at both the structures. Hence, finding a chemical inhibitor that has specificity towards PfTopoVIB is the need of the hour. Through our analysis, we have shortlisted 3 analogs of Radicicol that are predicted to bind specifically to PfTopoVIB and do not bind to PfHsp90. With a collaborative study with Professor Nair [Department of Computational Biology and Bioinformatics, University of Kerala] we have determined the 50 ns molecular dynamics simulations of analog-2, analog-6 and analog-7 with PfTopoVIB. The free energy calculations and the simulation results indicate that analog-2 forms a stable complex with PfTopoVIB (182). Hence, our study shortlists one chemical structure out of 97 that predicts a stable exclusive binding with PfTopoVIB. In analog 2, the two hydroxyl groups present at the C-17 and C-19 position of Radicicol are substituted by two biphenyl groups and the resultant derivative is found to dock with PfTopoVIB with more points of contact and hence found to score better than that of

Radicicol. Hence, analog 2 urges future experimental validation in the biochemical assays of PfTopoVIB and in the *Plasmodium* culture.

REFERENCES

1. Carter, R. and Mendis, K.N. (2002) Evolutionary and historical aspects of the burden of malaria. *Clin Microbiol Rev*, **15**, 564-594.
2. (2019) WORLD MALARIA REPORT.
3. Institute of Medicine Committee on the Economics of Antimalarial, D. (2004) In Arrow, K. J., Panosian, C. and Gelband, H. (eds.), *Saving Lives, Buying Time: Economics of Malaria Drugs in an Age of Resistance*. National Academies Press (US)

4. Jr., O.S., Mitchell VS, Pearson GW and et al. (1991). Institute of Medicine (US) Committee for the Study on Malaria Prevention and Control, Washington (DC).
5. CLA, L. (1978) A newly discovered parasite in the blood of patients suffering from malaria. Parasitic etiology of attacks of malaria. *Tropical Medicine and Parasitology. Classic Investigations*
6. Poinar, G., Jr. (2005) Plasmodium dominicana n. sp. (Plasmodiidae: Haemospororida) from Tertiary Dominican amber. *Systematic parasitology*, **61**, 47-52.
7. IW, S. (1998) A brief history of malaria and discovery of the parasite's life cycle. *Malaria: Parasite Biology, Pathogenesis and Protection*
8. Talman, A.M., Domarle, O., McKenzie, F.E., Ariey, F. and Robert, V. (2004) Gametocytogenesis : the puberty of Plasmodium falciparum. *Malaria Journal*, **3**, 24.
9. Gerald, N., Mahajan, B. and Kumar, S. (2011) Mitosis in the human malaria parasite Plasmodium falciparum. *Eukaryotic cell*, **10**, 474-482.
10. Venugopal, K., Hentzschel, F., Valkiūnas, G. and Marti, M. (2020) Plasmodium asexual growth and sexual development in the haematopoietic niche of the host. *Nature reviews. Microbiology*, **18**, 177-189.
11. Sinden, R.E., Canning, E.U., Bray, R.S. and Smalley, M.E. (1978) Gametocyte and gamete development in Plasmodium falciparum. *Proceedings of the Royal Society of London. Series B, Biological sciences*, **201**, 375-399.
12. Rosenberg, R. and Rungsiwongse, J. (1991) The number of sporozoites produced by individual malaria oocysts. *The American journal of tropical medicine and hygiene*, **45**, 574-577.
13. World Health, O. (2015) *Guidelines for the treatment of malaria*. 3rd ed ed. World Health Organization, Geneva.
14. Nsanzabana, C. (2019) Resistance to Artemisinin Combination Therapies (ACTs): Do Not Forget the Partner Drug! *Tropical medicine and infectious disease*, **4**.
15. Baruch, D.I., Pasloske, B.L., Singh, H.B., Bi, X., Ma, X.C., Feldman, M., Taraschi, T.F. and Howard, R.J. (1995) Cloning the P. falciparum gene encoding PfEMP1, a malarial variant antigen and adherence receptor on the surface of parasitized human erythrocytes. *Cell*, **82**, 77-87.
16. Smith, J.D., Chitnis, C.E., Craig, A.G., Roberts, D.J., Hudson-Taylor, D.E., Peterson, D.S., Pinches, R., Newbold, C.I. and Miller, L.H. (1995) Switches in expression of Plasmodium falciparum var genes correlate with changes in antigenic and cytoadherent phenotypes of infected erythrocytes. *Cell*, **82**, 101-110.
17. Otto, T.D., Gilabert, A., Crellen, T., Böhme, U., Arnathau, C., Sanders, M., Oyola, S.O., Okouga, A.P., Boundenga, L., Willaume, E. *et al.* (2018) Genomes of all known members of a Plasmodium subgenus reveal paths to virulent human malaria. *Nature microbiology*, **3**, 687-697.
18. Mok, S., Ashley, E.A., Ferreira, P.E., Zhu, L., Lin, Z., Yeo, T., Chotivanich, K., Imwong, M., Pukrittayakamee, S., Dhorda, M. *et al.* (2015) Drug resistance. Population

transcriptomics of human malaria parasites reveals the mechanism of artemisinin resistance. *Science (New York, N.Y.)*, **347**, 431-435.

19. Kumar, A., Valecha, N., Jain, T. and Dash, A.P. (2007) Burden of malaria in India: retrospective and prospective view. *The American journal of tropical medicine and hygiene*, **77**, 69-78.
20. Nabi, S. and Qader, S. (2009) Is Global Warming likely to cause an increased incidence of Malaria? *The Libyan journal of medicine*, **4**, 18-22.
21. Zell, R. (2004) Global climate change and the emergence/re-emergence of infectious diseases. *International journal of medical microbiology : IJMM*, **293 Suppl 37**, 16-26.
22. Casares, S., Brumeanu, T.D. and Richie, T.L. (2010) The RTS,S malaria vaccine. *Vaccine*, **28**, 4880-4894.
23. Batista, F.A., Gyau, B., Vilacha, J.F., Bosch, S.S., Lunev, S., Wrenger, C. and Groves, M.R. (2020) New directions in antimalarial target validation. *Expert Opinion on Drug Discovery*, **15**, 189-202.
24. Nilsson, S.K., Childs, L.M., Buckee, C. and Marti, M. (2015) Targeting Human Transmission Biology for Malaria Elimination. *PLoS pathogens*, **11**, e1004871.
25. Gupta, A., Mehra, P., Deshmukh, A., Dar, A., Mitra, P., Roy, N. and Dhar, S.K. (2009) Functional dissection of the catalytic carboxyl-terminal domain of origin recognition complex subunit 1 (PfORC1) of the human malaria parasite Plasmodium falciparum. *Eukaryotic cell*, **8**, 1341-1351.
26. Chalapareddy, S., Bhattacharyya, M.K., Mishra, S. and Bhattacharyya, S. (2014) Radicicol confers mid-schizont arrest by inhibiting mitochondrial replication in Plasmodium falciparum. *Antimicrobial agents and chemotherapy*, **58**, 4341-4352.
27. Chalapareddy, S., Chakrabarty, S., Bhattacharyya, M.K. and Bhattacharyya, S. (2016) Radicicol-Mediated Inhibition of Topoisomerase VIB-VIA Activity of the Human Malaria Parasite Plasmodium falciparum. *mSphere*, **1**.
28. Bodley, A.L., Cumming, J.N. and Shapiro, T.A. (1998) Effects of camptothecin, a topoisomerase I inhibitor, on Plasmodium falciparum. *Biochemical pharmacology*, **55**, 709-711.
29. Carvalho, C., Santos, R.X., Cardoso, S., Correia, S., Oliveira, P.J., Santos, M.S. and Moreira, P.I. (2009) Doxorubicin: the good, the bad and the ugly effect. *Current medicinal chemistry*, **16**, 3267-3285.
30. Andriole, V.T. (2005) The quinolones: past, present, and future. *Clinical infectious diseases : an official publication of the Infectious Diseases Society of America*, **41 Suppl 2**, S113-119.
31. Zhang, G.F., Liu, X., Zhang, S., Pan, B. and Liu, M.L. (2018) Ciprofloxacin derivatives and their antibacterial activities. *European journal of medicinal chemistry*, **146**, 599-612.
32. Watson, J.D. and Crick, F.H. (1953) Genetical implications of the structure of deoxyribonucleic acid. *Nature*, **171**, 964-967.
33. Wang, J.C. (1971) Interaction between DNA and an Escherichia coli protein omega. *Journal of molecular biology*, **55**, 523-533.
34. Horowitz, D.S. and Wang, J.C. (1987) Mapping the active site tyrosine of Escherichia coli DNA gyrase. *The Journal of biological chemistry*, **262**, 5339-5344.
35. Wang, J.C. (1991) DNA topoisomerases: why so many? *The Journal of biological chemistry*, **266**, 6659-6662.
36. Wu, J., Feng, L. and Hsieh, T.S. (2010) Drosophila topo IIIalpha is required for the maintenance of mitochondrial genome and male germ-line stem cells. *Proceedings of the National Academy of Sciences of the United States of America*, **107**, 6228-6233.

37. Deweese, J.E., Osheroff, M.A. and Osheroff, N. (2008) DNA Topology and Topoisomerases: Teaching a "Knotty" Subject. *Biochemistry and molecular biology education : a bimonthly publication of the International Union of Biochemistry and Molecular Biology*, **37**, 2-10.
38. Sissi, C. and Palumbo, M. (2010) In front of and behind the replication fork: bacterial type IIA topoisomerases. *Cellular and molecular life sciences : CMLS*, **67**, 2001-2024.
39. Schvartzman, J.B. and Stasiak, A. (2004) A topological view of the replicon. *EMBO reports*, **5**, 256-261.
40. Goffart, S., Hangas, A. and Pohjoismäki, J.L.O. (2019) Twist and Turn-Topoisomerase Functions in Mitochondrial DNA Maintenance. *International journal of molecular sciences*, **20**.
41. Kikuchi, A. and Asai, K. (1984) Reverse gyrase--a topoisomerase which introduces positive superhelical turns into DNA. *Nature*, **309**, 677-681.
42. Li, Z., Mondragón, A. and DiGate, R.J. (2001) The mechanism of type IA topoisomerase-mediated DNA topological transformations. *Molecular cell*, **7**, 301-307.
43. Dekker, N.H., Rybenkov, V.V., Duguet, M., Crisona, N.J., Cozzarelli, N.R., Bensimon, D. and Croquette, V. (2002) The mechanism of type IA topoisomerases. *Proceedings of the National Academy of Sciences of the United States of America*, **99**, 12126-12131.
44. Kirkegaard, K. and Wang, J.C. (1985) Bacterial DNA topoisomerase I can relax positively supercoiled DNA containing a single-stranded loop. *Journal of molecular biology*, **185**, 625-637.
45. Champoux, J.J. (2001) DNA topoisomerases: structure, function, and mechanism. *Annual review of biochemistry*, **70**, 369-413.
46. Lima, C.D., Wang, J.C. and Mondragón, A. (1994) Three-dimensional structure of the 67K N-terminal fragment of E. coli DNA topoisomerase I. *Nature*, **367**, 138-146.
47. Mondragón, A. and DiGate, R. (1999) The structure of Escherichia coli DNA topoisomerase III. *Structure (London, England : 1993)*, **7**, 1373-1383.
48. Wang, J.C. (2002) Cellular roles of DNA topoisomerases: a molecular perspective. *Nature reviews. Molecular cell biology*, **3**, 430-440.
49. Ahumada, A. and Tse-Dinh, Y.C. (2002) The role of the Zn(II) binding domain in the mechanism of E. coli DNA topoisomerase I. *BMC biochemistry*, **3**, 13.
50. Gardner, M.J., Hall, N., Fung, E., White, O., Berriman, M., Hyman, R.W., Carlton, J.M., Pain, A., Nelson, K.E., Bowman, S. *et al.* (2002) Genome sequence of the human malaria parasite Plasmodium falciparum. *Nature*, **419**, 498-511.
51. Lee, A.H., Symington, L.S. and Fidock, D.A. (2014) DNA repair mechanisms and their biological roles in the malaria parasite Plasmodium falciparum. *Microbiology and molecular biology reviews : MMBR*, **78**, 469-486.
52. Dean, F., Krasnow, M.A., Otter, R., Matzuk, M.M., Spengler, S.J. and Cozzarelli, N.R. (1983) Escherichia coli type-1 topoisomerases: identification, mechanism, and role in recombination. *Cold Spring Harbor symposia on quantitative biology*, **47 Pt 2**, 769-777.
53. Srivenugopal, K.S., Lockshon, D. and Morris, D.R. (1984) Escherichia coli DNA topoisomerase III: purification and characterization of a new type I enzyme. *Biochemistry*, **23**, 1899-1906.
54. Caron, P.R. and Wang, J.C. (1994) Appendix. II: Alignment of primary sequences of DNA topoisomerases. *Advances in pharmacology (San Diego, Calif.)*, **29b**, 271-297.
55. Aravind, L., Leipe, D.D. and Koonin, E.V. (1998) Toprim--a conserved catalytic domain in type IA and II topoisomerases, DnaG-type primases, OLD family nucleases and RecR proteins. *Nucleic acids research*, **26**, 4205-4213.

56. Wilson, T.M., Chen, A.D. and Hsieh, T. (2000) Cloning and characterization of Drosophila topoisomerase IIIbeta. Relaxation of hypernegatively supercoiled DNA. *J Biol Chem*, **275**, 1533-1540.
57. Hanai, R., Caron, P.R. and Wang, J.C. (1996) Human TOP3: a single-copy gene encoding DNA topoisomerase III. *Proceedings of the National Academy of Sciences of the United States of America*, **93**, 3653-3657.
58. Bizard, A.H. and Hickson, I.D. (2020) The many lives of type IA topoisomerases. *J Biol Chem*, **295**, 7138-7153.
59. DiGate, R.J. and Marians, K.J. (1988) Identification of a potent decatenating enzyme from Escherichia coli. *The Journal of biological chemistry*, **263**, 13366-13373.
60. Zhang, H.L., Malpure, S., Li, Z., Hiasa, H. and DiGate, R.J. (1996) The role of the carboxyl-terminal amino acid residues in Escherichia coli DNA topoisomerase III-mediated catalysis. *The Journal of biological chemistry*, **271**, 9039-9045.
61. Li, Z., Mondragón, A., Hiasa, H., Marians, K.J. and DiGate, R.J. (2000) Identification of a unique domain essential for Escherichia coli DNA topoisomerase III-catalysed decatenation of replication intermediates. *Molecular microbiology*, **35**, 888-895.
62. DiGate, R.J. and Marians, K.J. (1992) Escherichia coli topoisomerase III-catalyzed cleavage of RNA. *The Journal of biological chemistry*, **267**, 20532-20535.
63. Plank, J.L., Chu, S.H., Pohlhaus, J.R., Wilson-Sali, T. and Hsieh, T.S. (2005) Drosophila melanogaster topoisomerase IIIalpha preferentially relaxes a positively or negatively supercoiled bubble substrate and is essential during development. *The Journal of biological chemistry*, **280**, 3564-3573.
64. Kwan, K.Y., Moens, P.B. and Wang, J.C. (2003) Infertility and aneuploidy in mice lacking a type IA DNA topoisomerase III beta. *Proceedings of the National Academy of Sciences of the United States of America*, **100**, 2526-2531.
65. Li, W. and Wang, J.C. (1998) Mammalian DNA topoisomerase IIIα is essential in early embryogenesis. *Proceedings of the National Academy of Sciences*, **95**, 1010-1013.
66. Kwan, K.Y. and Wang, J.C. (2001) Mice lacking DNA topoisomerase IIIbeta develop to maturity but show a reduced mean lifespan. *Proceedings of the National Academy of Sciences of the United States of America*, **98**, 5717-5721.
67. Gangloff, S., de Massy, B., Arthur, L., Rothstein, R. and Fabre, F. (1999) The essential role of yeast topoisomerase III in meiosis depends on recombination. *The EMBO journal*, **18**, 1701-1711.
68. Gangloff, S., McDonald, J.P., Bendixen, C., Arthur, L. and Rothstein, R. (1994) The yeast type I topoisomerase Top3 interacts with Sgs1, a DNA helicase homolog: a potential eukaryotic reverse gyrase. *Mol Cell Biol*, **14**, 8391-8398.
69. Wu, J., Feng, L. and Hsieh, T.-s. (2010) Drosophila topo IIIα is required for the maintenance of mitochondrial genome and male germ-line stem cells. *Proceedings of the National Academy of Sciences*, **107**, 6228-6233.
70. Nicholls, T.J., Nadalutti, C.A., Motori, E., Sommerville, E.W., Gorman, G.S., Basu, S., Hoberg, E., Turnbull, D.M., Chinnery, P.F., Larsson, N.G. *et al.* (2018) Topoisomerase 3α Is Required for Decatenation and Segregation of Human mtDNA. *Molecular cell*, **69**, 9-23.e26.
71. Bennett, R.J., Noirot-Gros, M.F. and Wang, J.C. (2000) Interaction between yeast sgs1 helicase and DNA topoisomerase III. *The Journal of biological chemistry*, **275**, 26898-26905.

72. Fricke, W.M., Kaliraman, V. and Brill, S.J. (2001) Mapping the DNA topoisomerase III binding domain of the Sgs1 DNA helicase. *The Journal of biological chemistry*, **276**, 8848-8855.
73. Ahmad, F. and Stewart, E. (2005) The N-terminal region of the Schizosaccharomyces pombe RecQ helicase, Rqh1p, physically interacts with Topoisomerase III and is required for Rqh1p function. *Molecular genetics and genomics : MGG*, **273**, 102-114.
74. Johnson, F.B., Lombard, D.B., Neff, N.F., Mastrangelo, M.A., Dewolf, W., Ellis, N.A., Marciniak, R.A., Yin, Y., Jaenisch, R. and Guarente, L. (2000) Association of the Bloom syndrome protein with topoisomerase IIIalpha in somatic and meiotic cells. *Cancer research*, **60**, 1162-1167.
75. Wu, L., Davies, S.L., North, P.S., Goulaouic, H., Riou, J.F., Turley, H., Gatter, K.C. and Hickson, I.D. (2000) The Bloom's syndrome gene product interacts with topoisomerase III. *The Journal of biological chemistry*, **275**, 9636-9644.
76. Oakley, T.J. and Hickson, I.D. (2002) Defending genome integrity during S-phase: putative roles for RecQ helicases and topoisomerase III. *DNA repair*, **1**, 175-207.
77. Wu, L. and Hickson, I.D. (2003) The Bloom's syndrome helicase suppresses crossing over during homologous recombination. *Nature*, **426**, 870-874.
78. Chang, M., Bellaoui, M., Zhang, C., Desai, R., Morozov, P., Delgado-Cruzata, L., Rothstein, R., Freyer, G.A., Boone, C. and Brown, G.W. (2005) RMI1/NCE4, a suppressor of genome instability, encodes a member of the RecQ helicase/Topo III complex. *The EMBO journal*, **24**, 2024-2033.
79. Chen, C.F. and Brill, S.J. (2007) Binding and activation of DNA topoisomerase III by the Rmi1 subunit. *The Journal of biological chemistry*, **282**, 28971-28979.
80. Kim, R.A. and Wang, J.C. (1992) Identification of the yeast TOP3 gene product as a single strand-specific DNA topoisomerase. *The Journal of biological chemistry*, **267**, 17178-17185.
81. Mullen, J.R., Nallaseth, F.S., Lan, Y.Q., Slagle, C.E. and Brill, S.J. (2005) Yeast Rmi1/Nce4 controls genome stability as a subunit of the Sgs1-Top3 complex. *Mol Cell Biol*, **25**, 4476-4487.
82. Lai, M.S., Seki, M., Ui, A. and Enomoto, T. (2007) Rmi1, a member of the Sgs1-Top3 complex in budding yeast, contributes to sister chromatid cohesion. *EMBO reports*, **8**, 685-690.
83. Lee, C.M., Wang, G., Pertsinidis, A. and Marians, K.J. (2019) Topoisomerase III Acts at the Replication Fork To Remove Precatenanes. *Journal of Bacteriology*, **201**, e00563-00518.
84. Krogh, B.O. and Shuman, S. (2000) Catalytic mechanism of DNA topoisomerase IB. *Molecular cell*, **5**, 1035-1041.
85. Patel, A., Shuman, S. and Mondragón, A. (2006) Crystal structure of a bacterial type IB DNA topoisomerase reveals a preassembled active site in the absence of DNA. *The Journal of biological chemistry*, **281**, 6030-6037.
86. Stewart, L., Redinbo, M.R., Qiu, X., Hol, W.G. and Champoux, J.J. (1998) A model for the mechanism of human topoisomerase I. *Science (New York, N.Y.)*, **279**, 1534-1541.
87. Riou, J.F., Gabillot, M., Philippe, M., Schrevel, J. and Riou, G. (1986) Purification and characterization of Plasmodium berghei DNA topoisomerases I and II: drug action, inhibition of decatenation and relaxation, and stimulation of DNA cleavage. *Biochemistry*, **25**, 1471-1479.
88. Tosh, K. and Kilbey, B. (1995) The gene encoding topoisomerase I from the human malaria parasite Plasmodium falciparum. *Gene*, **163**, 151-154.

89. Tosh, K., Cheesman, S., Horrocks, P. and Kilbey, B. (1999) Plasmodium falciparum:Stage-Related Expression of Topoisomerase I. *Experimental Parasitology*, **91**, 126-132.
90. Wang, J.C. (1998) Moving one DNA double helix through another by a type II DNA topoisomerase: the story of a simple molecular machine. *Quarterly reviews of biophysics*, **31**, 107-144.
91. Brown, P.O. and Cozzarelli, N.R. (1979) A sign inversion mechanism for enzymatic supercoiling of DNA. *Science (New York, N.Y.)*, **206**, 1081-1083.
92. Classen, S., Olland, S. and Berger, J.M. (2003) Structure of the topoisomerase II ATPase region and its mechanism of inhibition by the chemotherapeutic agent ICRF-187. *Proceedings of the National Academy of Sciences of the United States of America*, **100**, 10629-10634.
93. Osheroff, N. (1998) DNA topoisomerases. *Biochimica et biophysica acta*, **1400**, 1-2.
94. Bergerat, A., de Massy, B., Gadelle, D., Varoutas, P.C., Nicolas, A. and Forterre, P. (1997) An atypical topoisomerase II from Archaea with implications for meiotic recombination. *Nature*, **386**, 414-417.
95. Bauer, D.L., Marie, R., Rasmussen, K.H., Kristensen, A. and Mir, K.U. (2012) DNA catenation maintains structure of human metaphase chromosomes. *Nucleic acids research*, **40**, 11428-11434.
96. Durrieu, F., Samejima, K., Fortune, J.M., Kandels-Lewis, S., Osheroff, N. and Earnshaw, W.C. (2000) DNA topoisomerase IIalpha interacts with CAD nuclease and is involved in chromatin condensation during apoptotic execution. *Current biology : CB*, **10**, 923-926.
97. Andrews, C.A., Vas, A.C., Meier, B., Giménez-Abián, J.F., Díaz-Martínez, L.A., Green, J., Erickson, S.L., Vanderwaal, K.E., Hsu, W.S. and Clarke, D.J. (2006) A mitotic topoisomerase II checkpoint in budding yeast is required for genome stability but acts independently of Pds1/securin. *Genes & development*, **20**, 1162-1174.
98. Turley, H., Comley, M., Houlbrook, S., Nozaki, N., Kikuchi, A., Hickson, I.D., Gatter, K. and Harris, A.L. (1997) The distribution and expression of the two isoforms of DNA topoisomerase II in normal and neoplastic human tissues. *British journal of cancer*, **75**, 1340-1346.
99. Raghu Ram, E.V., Kumar, A., Biswas, S., Kumar, A., Chaubey, S., Siddiqi, M.I. and Habib, S. (2007) Nuclear gyrB encodes a functional subunit of the Plasmodium falciparum gyrase that is involved in apicoplast DNA replication. *Molecular and biochemical parasitology*, **154**, 30-39.
100. Dar, M.A., Sharma, A., Mondal, N. and Dhar, S.K. (2007) Molecular cloning of apicoplast-targeted Plasmodium falciparum DNA gyrase genes: unique intrinsic ATPase activity and ATP-independent dimerization of PfGyrB subunit. *Eukaryotic cell*, **6**, 398-412.
101. Dar, A., Prusty, D., Mondal, N. and Dhar, S.K. (2009) A unique 45-amino-acid region in the toprim domain of Plasmodium falciparum gyrase B is essential for its activity. *Eukaryotic cell*, **8**, 1759-1769.
102. Nagano, S., Seki, E., Lin, T.Y., Shirouzu, M., Yokoyama, S. and Heddle, J.G. (2015) Investigating the Roles of the C-Terminal Domain of Plasmodium falciparum GyrA. *PLoS One*, **10**, e0142313.
103. Mudeppa, D.G., Kumar, S., Kokkonda, S., White, J. and Rathod, P.K. (2015) Topoisomerase II from Human Malaria Parasites: EXPRESSION, PURIFICATION, AND SELECTIVE INHIBITION. *The Journal of biological chemistry*, **290**, 20313-20324.
104. Attasart, P., Boonma, S., Sunintaboon, P., Tanwilai, D., Pothikasikorn, J. and Noonpakdee, W.T. (2016) Inhibition of Plasmodium falciparum proliferation in vitro by

double-stranded RNA nanoparticle against malaria topoisomerase II. *Exp Parasitol*, **164**, 84-90.

105. Hartung, F. and Puchta, H. (2000) Molecular characterisation of two paralogous SPO11 homologues in Arabidopsis thaliana. *Nucleic acids research*, **28**, 1548-1554.
106. Aravind, L., Iyer, L.M., Wellems, T.E. and Miller, L.H. (2003) Plasmodium biology: genomic gleanings. *Cell*, **115**, 771-785.
107. Gadelle, D., Krupovic, M., Raymann, K., Mayer, C. and Forterre, P. (2014) DNA topoisomerase VIII: a novel subfamily of type IIB topoisomerases encoded by free or integrated plasmids in Archaea and Bacteria. *Nucleic acids research*, **42**, 8578-8591.
108. Buhler, C., Lebbink, J.H., Bocs, C., Ladenstein, R. and Forterre, P. (2001) DNA topoisomerase VI generates ATP-dependent double-strand breaks with two-nucleotide overhangs. *The Journal of biological chemistry*, **276**, 37215-37222.
109. Corbett, K.D., Benedetti, P. and Berger, J.M. (2007) Holoenzyme assembly and ATP-mediated conformational dynamics of topoisomerase VI. *Nature structural & molecular biology*, **14**, 611-619.
110. Chen, S.H., Chan, N.L. and Hsieh, T.S. (2013) New mechanistic and functional insights into DNA topoisomerases. *Annual review of biochemistry*, **82**, 139-170.
111. Dutta, R. and Inouye, M. (2000) GHKL, an emergent ATPase/kinase superfamily. *Trends Biochem Sci*, **25**, 24-28.
112. Hartung, F., Angelis, K.J., Meister, A., Schubert, I., Melzer, M. and Puchta, H. (2002) An archaebacterial topoisomerase homolog not present in other eukaryotes is indispensable for cell proliferation of plants. *Current biology : CB*, **12**, 1787-1791.
113. An, X.J., Deng, Z.Y. and Wang, T. (2011) OsSpo11-4, a rice homologue of the archaeal TopVIA protein, mediates double-strand DNA cleavage and interacts with OsTopVIB. *PloS one*, **6**, e20327.
114. Robert, T., Nore, A., Brun, C., Maffre, C., Crimi, B., Bourbon, H.M. and de Massy, B. (2016) The TopoVIB-Like protein family is required for meiotic DNA double-strand break formation. *Science (New York, N.Y.)*, **351**, 943-949.
115. Nichols, M.D., DeAngelis, K., Keck, J.L. and Berger, J.M. (1999) Structure and function of an archaeal topoisomerase VI subunit with homology to the meiotic recombination factor Spo11. *Embo j*, **18**, 6177-6188.
116. Keeney, S., Giroux, C.N. and Kleckner, N. (1997) Meiosis-specific DNA double-strand breaks are catalyzed by Spo11, a member of a widely conserved protein family. *Cell*, **88**, 375-384.
117. Celerin, M., Merino, S.T., Stone, J.E., Menzie, A.M. and Zolan, M.E. (2000) Multiple roles of Spo11 in meiotic chromosome behavior. *The EMBO journal*, **19**, 2739-2750.
118. Corbett, K.D. and Berger, J.M. (2003) Emerging roles for plant topoisomerase VI. *Chemistry & biology*, **10**, 107-111.
119. Sugimoto-Shirasu, K., Stacey, N.J., Corsar, J., Roberts, K. and McCann, M.C. (2002) DNA topoisomerase VI is essential for endoreduplication in Arabidopsis. *Current biology : CB*, **12**, 1782-1786.
120. Sugimoto-Shirasu, K. and Roberts, K. (2003) "Big it up": endoreduplication and cell-size control in plants. *Current opinion in plant biology*, **6**, 544-553.
121. Gantt, S.M., Myung, J.M., Briones, M.R., Li, W.D., Corey, E.J., Omura, S., Nussenzweig, V. and Sinnis, P. (1998) Proteasome inhibitors block development of Plasmodium spp. *Antimicrobial agents and chemotherapy*, **42**, 2731-2738.

122. Sturm, A. and Heussler, V. (2007) Live and let die: manipulation of host hepatocytes by exoerythrocytic Plasmodium parasites. *Medical microbiology and immunology*, **196**, 127-133.
123. Corbett, K.D. and Berger, J.M. (2003) Structure of the topoisomerase VI-B subunit: implications for type II topoisomerase mechanism and evolution. *The EMBO journal*, **22**, 151-163.
124. Graille, M., Cladière, L., Durand, D., Lecointe, F., Gadelle, D., Quevillon-Cheruel, S., Vachette, P., Forterre, P. and van Tilbeurgh, H. (2008) Crystal structure of an intact type II DNA topoisomerase: insights into DNA transfer mechanisms. *Structure*, **16**, 360-370.
125. Oestergaard, V.H., Bjergbaek, L., Skouboe, C., Giangiacomo, L., Knudsen, B.R. and Andersen, A.H. (2004) The transducer domain is important for clamp operation in human DNA topoisomerase IIalpha. *The Journal of biological chemistry*, **279**, 1684-1691.
126. Corbett, K.D. and Berger, J.M. (2006) Structural basis for topoisomerase VI inhibition by the anti-Hsp90 drug radicicol. *Nucleic acids research*, **34**, 4269-4277.
127. Gadelle, D., Bocs, C., Graille, M. and Forterre, P. (2005) Inhibition of archaeal growth and DNA topoisomerase VI activities by the Hsp90 inhibitor radicicol. *Nucleic acids research*, **33**, 2310-2317.
128. Chalapareddy, S., Chakrabarty, S., Bhattacharyya, M.K. and Bhattacharyya, S. (2016) Radicicol-Mediated Inhibition of Topoisomerase VIB-VIA Activity of the Human Malaria Parasite Plasmodium falciparum. *mSphere*, **1**, e00025-00015.
129. Stebbins, C.E., Russo, A.A., Schneider, C., Rosen, N., Hartl, F.U. and Pavletich, N.P. (1997) Crystal structure of an Hsp90-geldanamycin complex: targeting of a protein chaperone by an antitumor agent. *Cell*, **89**, 239-250.
130. Soga, S., Neckers, L.M., Schulte, T.W., Shiotsu, Y., Akasaka, K., Narumi, H., Agatsuma, T., Ikuina, Y., Murakata, C., Tamaoki, T. *et al.* (1999) KF25706, a novel oxime derivative of radicicol, exhibits in vivo antitumor activity via selective depletion of Hsp90 binding signaling molecules. *Cancer research*, **59**, 2931-2938.
131. Chalapareddy, S., Bhattacharyya, M.K., Mishra, S. and Bhattacharyya, S. (2014) *Antimicrobial Agents and Chemotherapy*, **58**, 4341.
132. Laskar, S., Bhattacharyya, M.K., Shankar, R. and Bhattacharyya, S. (2011) HSP90 controls SIR2 mediated gene silencing. *PloS one*, **6**, e23406.
133. Longtine, M.S., McKenzie, A., 3rd, Demarini, D.J., Shah, N.G., Wach, A., Brachat, A., Philippsen, P. and Pringle, J.R. (1998) Additional modules for versatile and economical PCR-based gene deletion and modification in Saccharomyces cerevisiae. *Yeast (Chichester, England)*, **14**, 953-961.
134. Jensen, J.B. and Trager, W. (1977) Plasmodium falciparum in culture: use of outdated erthrocytes and description of the candle jar method. *The Journal of parasitology*, **63**, 883-886.
135. Moll, K., Ljungstrom, I., Perlmann, H., Scherf, A. and Wahlgren, M. (2008), , *Malaria Research and Reference Reagent Resource* Vol. Manassas, VA.
136. Bairoch, A. and Apweiler, R. (1997) The SWISS-PROT protein sequence database: its relevance to human molecular medical research. *Journal of molecular medicine (Berlin, Germany)*, **75**, 312-316.
137. Berman, H.M., Westbrook, J., Feng, Z., Gilliland, G., Bhat, T.N., Weissig, H., Shindyalov, I.N. and Bourne, P.E. (2000) The Protein Data Bank. *Nucleic acids research*, **28**, 235-242.

138. Guex, N., Peitsch, M.C. and Schwede, T. (2009) Automated comparative protein structure modeling with SWISS-MODEL and Swiss-PdbViewer: a historical perspective. *Electrophoresis*, **30 Suppl 1**, S162-173.
139. Laskowski, R.A., MacArthur, M.W., Moss, D.S. and Thornton, J.M. (1993) PROCHECK: a program to check the stereochemical quality of protein structures. *Journal of Applied Crystallography*, **26**, 283-291.
140. Van Gunsteren, W.F., et al. (1996), *The GROMOS 96 Manual and User Guide.*, VDF Hochschulverlag AG an der ETH Zürich Zürich,, Vol. 1, pp. 1042
141. Colovos, C. and Yeates, T.O. (1993) Verification of protein structures: patterns of nonbonded atomic interactions. *Protein science : a publication of the Protein Society*, **2**, 1511-1519.
142. Kim, S., Chen, J., Cheng, T., Gindulyte, A., He, J., He, S., Li, Q., Shoemaker, B.A., Thiessen, P.A., Yu, B. *et al.* (2019) PubChem 2019 update: improved access to chemical data. *Nucleic acids research*, **47**, D1102-d1109.
143. Turbyville, T.J., Wijeratne, E.M., Liu, M.X., Burns, A.M., Seliga, C.J., Luevano, L.A., David, C.L., Faeth, S.H., Whitesell, L. and Gunatilaka, A.A. (2006) Search for Hsp90 inhibitors with potential anticancer activity: isolation and SAR studies of radicicol and monocillin I from two plant-associated fungi of the Sonoran desert. *Journal of natural products*, **69**, 178-184.
144. Dutton, B.L., Kitson, R.R., Parry-Morris, S., Roe, S.M., Prodromou, C. and Moody, C.J. (2014) Synthesis of macrolactam analogues of radicicol and their binding to heat shock protein Hsp90. *Organic & biomolecular chemistry*, **12**, 1328-1340.
145. Wang, S., Xu, Y., Maine, E.A., Wijeratne, E.M., Espinosa-Artiles, P., Gunatilaka, A.A. and Molnár, I. (2008) Functional characterization of the biosynthesis of radicicol, an Hsp90 inhibitor resorcylic acid lactone from Chaetomium chiversii. *Chemistry & biology*, **15**, 1328-1338.
146. Pearl, L.H., Prodromou, C. and Workman, P. (2008) The Hsp90 molecular chaperone: an open and shut case for treatment. *The Biochemical journal*, **410**, 439-453.
147. Teo, R.D., Dong, S.S., Gross, Z., Gray, H.B. and Goddard, W.A., 3rd. (2015) Computational predictions of corroles as a class of Hsp90 inhibitors. *Molecular bioSystems*, **11**, 2907-2914.
148. Shinonaga, H., Noguchi, T., Ikeda, A., Aoki, M., Fujimoto, N. and Kawashima, A. (2009) Synthesis and structure-activity relationships of radicicol derivatives and WNT-5A expression inhibitory activity. *Bioorganic & medicinal chemistry*, **17**, 4622-4635.
149. Shiotsu, Y., Neckers, L.M., Wortman, I., An, W.G., Schulte, T.W., Soga, S., Murakata, C., Tamaoki, T. and Akinaga, S. (2000) Novel oxime derivatives of radicicol induce erythroid differentiation associated with preferential G(1) phase accumulation against chronic myelogenous leukemia cells through destabilization of Bcr-Abl with Hsp90 complex. *Blood*, **96**, 2284-2291.
150. BIOVIA. (2019). Dassault Systèmes, San Diego.
151. Smellie, A., Teig, S.L. and Towbin, P. (1995) Poling: Promoting conformational variation. *Journal of Computational Chemistry*, **16**, 171-187.
152. Diller, D.J. and Merz, K.M., Jr. (2001) High throughput docking for library design and library prioritization. *Proteins*, **43**, 113-124.
153. Rao, S.N., Head, M.S., Kulkarni, A. and LaLonde, J.M. (2007) Validation studies of the site-directed docking program LibDock. *Journal of chemical information and modeling*, **47**, 2159-2171.

154. Venkatachalam, C.M., Jiang, X., Oldfield, T. and Waldman, M. (2003) LigandFit: a novel method for the shape-directed rapid docking of ligands to protein active sites. *Journal of molecular graphics & modelling*, **21**, 289-307.
155. Krammer, A., Kirchhoff, P.D., Jiang, X., Venkatachalam, C.M. and Waldman, M. (2005) LigScore: a novel scoring function for predicting binding affinities. *Journal of molecular graphics & modelling*, **23**, 395-407.
156. James, P., Halladay, J. and Craig, E.A. (1996) Genomic libraries and a host strain designed for highly efficient two-hybrid selection in yeast. *Genetics*, **144**, 1425-1436.
157. Govindarajalu, G., Rizvi, Z., Kumar, D. and Sijwali, P.S. (2019) Lyse-Reseal Erythrocytes for Transfection of Plasmodium falciparum. *Scientific reports*, **9**, 19952.
158. Suhane, T., Bindumadhavan, V., Fangaria, N., Nair, A.S., Tabassum, W., Muley, P., Bhattacharyya, M.K. and Bhattacharyya, S. (2019) Glu-108 in Saccharomyces cerevisiae Rad51 Is Critical for DNA Damage-Induced Nuclear Function. *mSphere*, **4**.
159. Harte, W.E., Jr., Swaminathan, S., Mansuri, M.M., Martin, J.C., Rosenberg, I.E. and Beveridge, D.L. (1990) Domain communication in the dynamical structure of human immunodeficiency virus 1 protease. *Proceedings of the National Academy of Sciences of the United States of America*, **87**, 8864-8868.
160. Groth, P., Ausländer, S., Majumder, M.M., Schultz, N., Johansson, F., Petermann, E. and Helleday, T. (2010) Methylated DNA causes a physical block to replication forks independently of damage signalling, O(6)-methylguanine or DNA single-strand breaks and results in DNA damage. *J Mol Biol*, **402**, 70-82.
161. Chakraverty, R.K., Kearsey, J.M., Oakley, T.J., Grenon, M., de La Torre Ruiz, M.A., Lowndes, N.F. and Hickson, I.D. (2001) Topoisomerase III acts upstream of Rad53p in the S-phase DNA damage checkpoint. *Mol Cell Biol*, **21**, 7150-7162.
162. Mitra, P., Banu, K., Deshmukh, Abhijit S., Subbarao, N. and Dhar, Suman K. (2015) Functional dissection of proliferating-cell nuclear antigens (1 and 2) in human malarial parasite Plasmodium falciparum: possible involvement in DNA replication and DNA damage response. *Biochemical Journal*, **470**, 115-129.
163. Zellweger, R., Dalcher, D., Mutreja, K., Berti, M., Schmid, J.A., Herrador, R., Vindigni, A. and Lopes, M. (2015) Rad51-mediated replication fork reversal is a global response to genotoxic treatments in human cells. *Journal of Cell Biology*, **208**, 563-579.
164. Wang, Y., Lyu, Y.L. and Wang, J.C. (2002) Dual localization of human DNA topoisomerase IIIalpha to mitochondria and nucleus. *Proceedings of the National Academy of Sciences of the United States of America*, **99**, 12114-12119.
165. Bianchi, V., Pontis, E. and Reichard, P. (1986) Changes of deoxyribonucleoside triphosphate pools induced by hydroxyurea and their relation to DNA synthesis. *J Biol Chem*, **261**, 16037-16042.
166. Maric, C. and Bénard, M. (2014) Replication forks reverse at high frequency upon replication stress in Physarum polycephalum. *Chromosoma*, **123**, 577-585.
167. Liu, Y. (2016) EEPD1: Breaking and Rescuing the Replication Fork. *PLoS genetics*, **12**, e1005742.
168. Claessens, A., Harris, L.M., Stanojcic, S., Chappell, L., Stanton, A., Kuk, N., Veneziano-Broccia, P., Sterkers, Y., Rayner, J.C. and Merrick, C.J. (2018) RecQ helicases in the malaria parasite Plasmodium falciparum affect genome stability, gene expression patterns and DNA replication dynamics. *PLoS genetics*, **14**, e1007490.
169. Suski, C. and Marians, K.J. (2008) Resolution of converging replication forks by RecQ and topoisomerase III. *Molecular cell*, **30**, 779-789.

170. Wu, L., Chan, K.L., Ralf, C., Bernstein, D.A., Garcia, P.L., Bohr, V.A., Vindigni, A., Janscak, P., Keck, J.L. and Hickson, I.D. (2005) The HRDC domain of BLM is required for the dissolution of double Holliday junctions. *The EMBO journal*, **24**, 2679-2687.
171. Mills, M., Tse-Dinh, Y.C. and Neuman, K.C. (2018) Direct observation of topoisomerase IA gate dynamics. *Nature structural & molecular biology*, **25**, 1111-1118.
172. Bansod, S., Bung, N., Singh, P., Suthram, N., Choudhury, H., Roy, A., Bulusu, G. and Bhattacharyya, S. (2020) Elucidation of an essential function of the unique charged domain of Plasmodium topoisomerase III. *Biochem J*.
173. Chung, S.Y. and Subbiah, S. (1996) A structural explanation for the twilight zone of protein sequence homology. *Structure*, **4**, 1123-1127.
174. Chang, G.S., Hong, Y., Ko, K.D., Bhardwaj, G., Holmes, E.C., Patterson, R.L. and van Rossum, D.B. (2008) Phylogenetic profiles reveal evolutionary relationships within the "twilight zone" of sequence similarity. *Proceedings of the National Academy of Sciences of the United States of America*, **105**, 13474-13479.
175. Walter, F. (1989) R. F. Doolittle, Of URFS and ORFS — a Primer on How to Analyze Derived Amino Acid Sequences. VII + 103 S., 24 Abb., 14 Tab. Mill Valley 1986. University Science Books. ISBN: 0-935702-54-7. *Journal of Basic Microbiology*, **29**, 246-246.
176. Laurents, D.V., Subbiah, S. and Levitt, M. (1994) Different protein sequences can give rise to highly similar folds through different stabilizing interactions. *Protein science : a publication of the Protein Society*, **3**, 1938-1944.
177. Rost, B. (1999) Twilight zone of protein sequence alignments. *Protein Eng*, **12**, 85-94.
178. Sander, C. and Schneider, R. (1991) Database of homology-derived protein structures and the structural meaning of sequence alignment. *Proteins*, **9**, 56-68.
179. Subbiah, S., Laurents, D.V. and Levitt, M. (1993) Structural similarity of DNA-binding domains of bacteriophage repressors and the globin core. *Current biology : CB*, **3**, 141-148.
180. Yang, A.S. and Honig, B. (2000) An integrated approach to the analysis and modeling of protein sequences and structures. III. A comparative study of sequence conservation in protein structural families using multiple structural alignments. *J Mol Biol*, **301**, 691-711.
181. Barghash, A. and Helms, V. (2013) Transferring functional annotations of membrane transporters on the basis of sequence similarity and sequence motifs. *BMC Bioinformatics*, **14**, 343.
182. Bansod, S., Raj, N., R, A., Nair, A.S. and Bhattacharyya, S. (2021) Molecular docking and molecular dynamics simulation identify a novel Radicicol derivative that predicts exclusive binding to Plasmodium falciparum Topoisomerase VIB. *Journal of Biomolecular Structure and Dynamics*, 1-13.

APPENDIX

Cloning of *PfTOPOIII* in *pET28a* vector

PfTOPOIII (Gene ID: PF3D7_1347100) gene has no intron. It was amplified using *Plasmodium falciparum* genomic DNA as template using the forward primer OSB 334 having BamHI restriction site and reverse primer OSB 335 having SalI restriction site. A PCR product of 2.1 kb was initially cloned in TA cloning vector *pTZ57R/T*. The insert was excised out from *pTZ57R/T-PfTOPOIII* clone by digesting it with BamHI and SalI restriction enzymes and cloned into final vector *pET28a*.

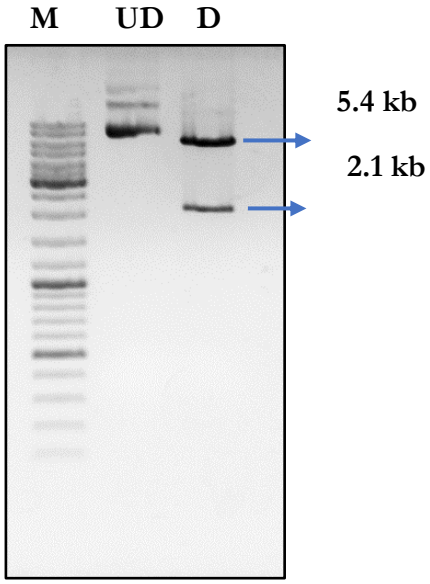

FigA1: Cloning of *PfTOPOIII* in *pET28a* vector: *pET28a-PfTOPOIII* clone was confirmed by restriction digestion with BamHI and SalI in which vector (5.4 kb) and insert (2.1 kb) got separated after double digestion. The clone was further confirmed by plasmid DNA sequencing.
(M: marker, UD: undigested, D: digested)

Cloning of *PfTOPOIII* in yeast expression vector *pTA*

PfTOPOIII insert was excised out from *pTZ57R/T-PfTOPOIII* vector by digesting it with BamHI and SalI restriction enzymes and cloned into the yeast expression vector *pTA* under the control of GPD promoter.

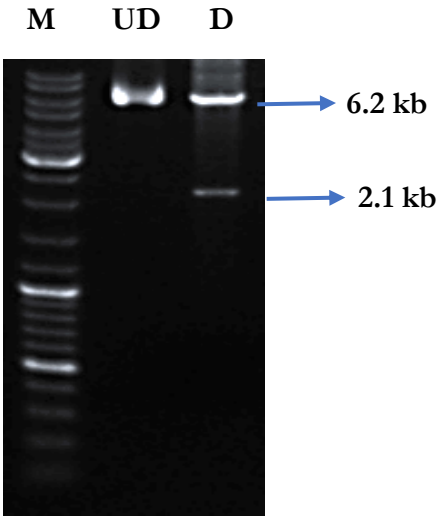

Fig A2: Cloning of *PfTOPOIII* in *pTA* vector: *pTA-PfTOPOIII* clone was confirmed by restriction digestion with BamHI and SalI in which vector (6.2 kb) and insert (2.1 kb) got separated after double digestion. The clone was further confirmed by plasmid DNA sequencing.
(M: marker, UD: undigested, D: digested)

Cloning of *ScTOPOIII* in *pTA* vector

ScTOPOIII was amplified using *S. cerevisae* genomic DNA as template using the forward primer OSB 346 having BamHI restriction site and reverse primer OSB 455 having SalI restriction site. This PCR product of 1.9 kb was digested with BamHI and SalI restriction enzymes and cloned into the yeast expression vector *pTA*.

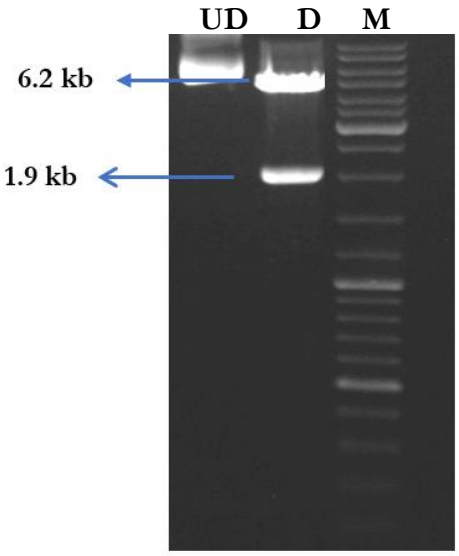

Fig A3: Cloning of *ScTOPOIII* in *pTA* vector: *pTA-ScTOPOIII* clone was confirmed by restriction digestion with BamHI and SalI in which vector (6.2 kb) and insert (1.9 kb) got separated after double digestion. The clone was further confirmed by plasmid DNA sequencing.
(M: marker, UD: undigested, D: digested)

Cloning of *PfY421FtopoIII* in *pTA* vector

PfY421FtopoIII mutant was generated by a splice overlap PCR method. ORF of *PfTOPOIII* was PCR amplified in two fragments. Fragment 1 was amplified using OSB 334 and OSB 452 primer. Fragment 2 was amplified by using the primer pairs OSB 453 and OSB 335). The primers OSB 452 and OSB 453 are bearing the desired mutation in each fragment. These fragments were fused with fusion PCR using OSB 334 and OSB 335 primer. The final fusion product (*PfY421FtopoIII)* was initially cloned in TA cloning vector pTZ57R/T. The insert was excised out from pTZ57R/T-*PfY421FtopoIII* clone by digesting it with BamHI and SalI restriction enzymes and subcloned into final vector *pTA*.

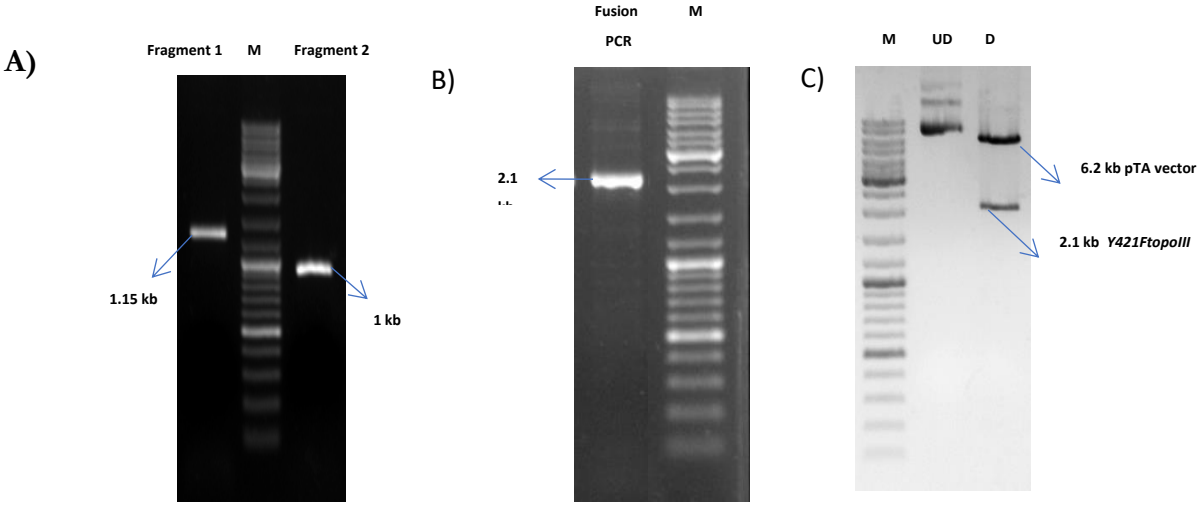

Fig A4: Cloning of *PfY421FtopoIII* in *pTA* vector. *PfY421FtopoIII* amplicon was amplified by splice overlap extension PCR in two fragments 1.15 kb (Fragment 1) and 1 kb (Fragment 2). B) Fusion PCR was done to generate final product length 2.1 kb. C) pTA-*PfY421FtopoIII* clone was confirmed by restriction digestion with BamHI and SalI in which vector (6.2 kb) and insert (2.1 kb) got separated after double digestion.

(M: marker, UD: undigested, D: digested)

Cloning of *Pf(Δ259-337)topoIII* in *pTA* vector

Pf(Δ259-337)topoIII mutant was generated by a splice overlap PCR method. ORF of *PfTOPOIII* was PCR amplified in two fragments. Fragment 1 was amplified using OSB 334, OSB 450 primer. Fragment 2 was amplified by using OSB 451, and OSB 335 bearing the desired deletion. These fragments were fused with fusion PCR using OSB 334 and OSB 335 primer. The final fusion product *Pf(Δ259-337)topoIII* was initially cloned in TA cloning vector pTZ57R/T. The insert was excised out from pTZ57R/T-*Pf(Δ259-337)topoIII* clone by digesting it with BamHI and SalI restriction enzymes and cloned into the vector *pTA*.

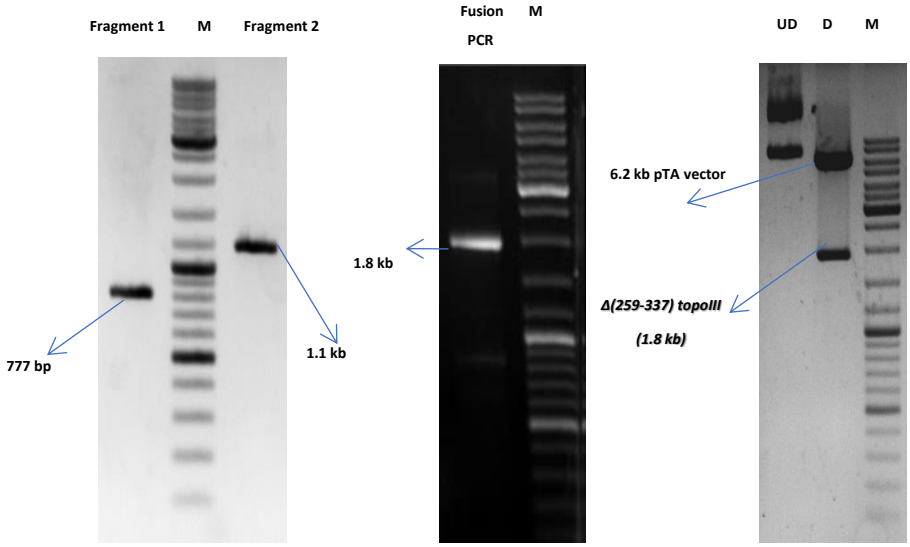

Fig A5: Cloning of *Pf(Δ259-337)topoIII* in *pTA* vector: *Pf(Δ259-337)topoIII* amplicon was amplified by splice overlap extension PCR in two fragments (777 bp and 1.1 kb). B) Fusion PCR was done to generate final product length 1.8 kb. C) pTA+ *Pf(Δ259-337)topoIII* clone was confirmed by restriction digestion with BamHI and SalI in which vector (6.2 kb) and insert (1.8 kb) got separated after double digestion. The clone was further confirmed by plasmid DNA sequencing.
(M: marker, UD: undigested, D: digested)

Cloning of *PfTOPOIII* in *pGBDUC-1* vector

PfTOPOIII insert was excised out from *pTZ57R/T-PfTOPOIII* clone by digesting it with BamHI and SalI restriction enzymes and cloned into the yeast two hybrid bait vector *pGBDUC-1*.

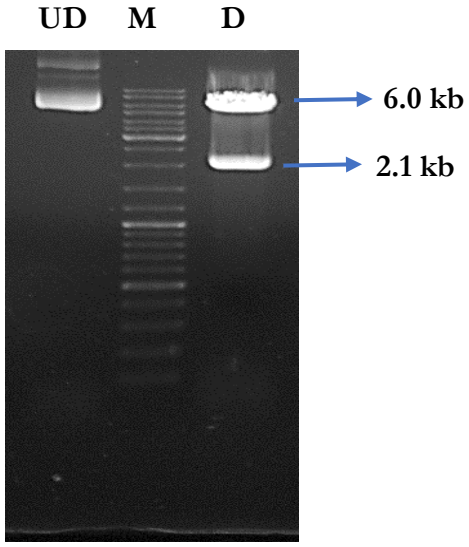

Fig A6: Cloning of *PfTOPOIII* in *pGBDUC-1* vector: *pGBDUC-1-PfTOPOIII* clone was confirmed by restriction digestion with BamHI and SalI in which vector (6 kb) and insert (2.1 kb) got separated after double digestion. The clone was further confirmed by plasmid DNA sequencing.
(M: marker, UD: undigested, D: digested)

Cloning of *Pf(Δ259-337)topoIII* in *pGBDUC-1* vector

pTA-Pf(Δ259-337)topoIII clone was digested with BamHI and SalI restriction enzymes to release the insert. Finally, *Pf(Δ259-337)topoIII* insert was cloned into pGBDUC-1 vector.

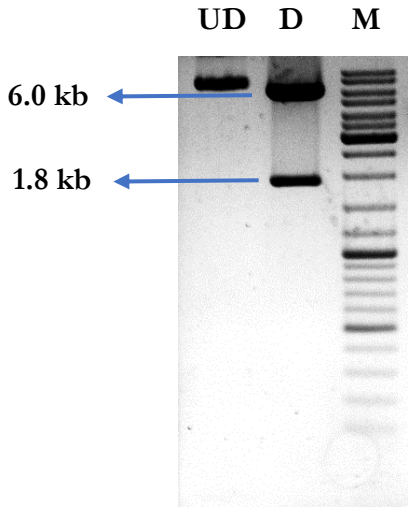

Fig A7: Cloning of *Pf(259-337)topoIII* in *pGDBUC-1* vector: *pGDBUC-1-Pf(259-337)topoIII* clone was confirmed by restriction digestion with BamHI and SalI in which vector (6 kb) and insert (1.8 kb) got separated after double digestion. The clone was further confirmed by plasmid DNA sequencing. (M: marker, UD: undigested, D: digested)

Cloning of *PfTOPOIII* in *P. falciparum* expression vector *pPfCENv3*

PfTOPOIII was amplified using *Plasmodium falciparum* genomic DNA as template using the forward primer OSB 334 having BamHI restriction site flanking and the reverse primer OSB 497 having BglII site after removing the stop codon. We put 2 extra bases before the BglII site so that it will be in frame with the GFP present in the *pPfCENv3* vector. The amplified fragment was first cloned into *pTA* vector. *PfTOPOIII* insert was released by BamHI and BglII digestion and was subcloned in BglII digested *pPfCENv3* vector by non-directional cloning. The cloning was first confirmed by digestion with BglII, which shows a linearlised band near 10.6 kb. Further, the clone was confirmed by digestion with XhoI (4989 position) and BglII (4202 position). The right oriented insert releases the GFP fragment of size 800bp. The wrong orientation clone gives out an insert approx. 2.9 kb.

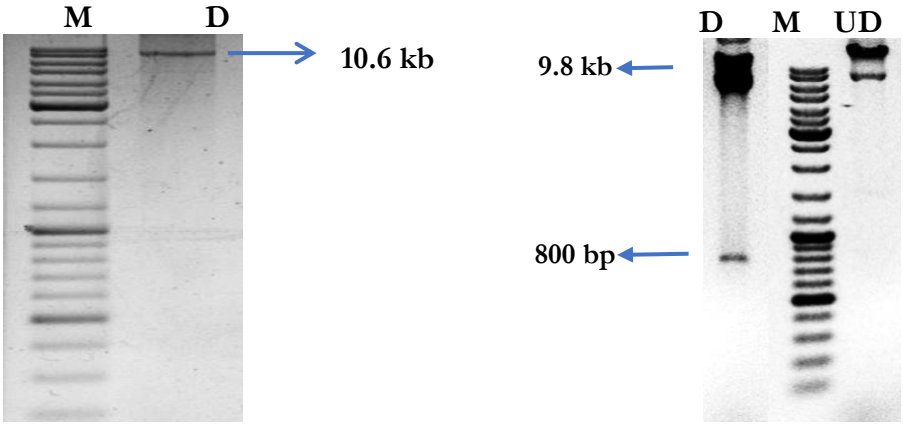

Fig A8: Cloning of *PfTOPOIII* in pCENV3 vector: pCENV3+*PfTOPOIII* clone was confirmed by restriction digestion with BglII in which 10.6 kb size is obtained. The right orientated insert was selected by restriction digestion with BglII and Xho1 which releases GFP (800 bp) after double digestion. The clone was further confirmed by plasmid DNA sequencing.

(M: marker, UD: undigested, D: digested)

Cloning of *Pf(Δ259-337)topoIII* in *P. falciparum* expression vector *pPfCENv3*

Pf(Δ259-337)topoIII was amplified using the forward primer OSB 334 having BamHI restriction site flanking and reverse primer OSB having BglII site without the stop codon. We put 2 extra bases before BglII site so that it will be in frame with the GFP present in *pPfCENv3* vector. *Pf(Δ259-337)topoIII* insert was released by BamHI and BglII digestion and was subcloned in BglII digested *pPfCENv3* vector by non-directional cloning. The cloning was first confirmed by digestion with BglII, which shows a linearlised band near 10.3 kb. Further, the clone was screened by digestion with XhoI and BglII. The right oriented ORF gives out an insert of 800 bp of GFP whereas, the reverse oriented ORF releases a fragment of an approximate size of 2.6 kb.

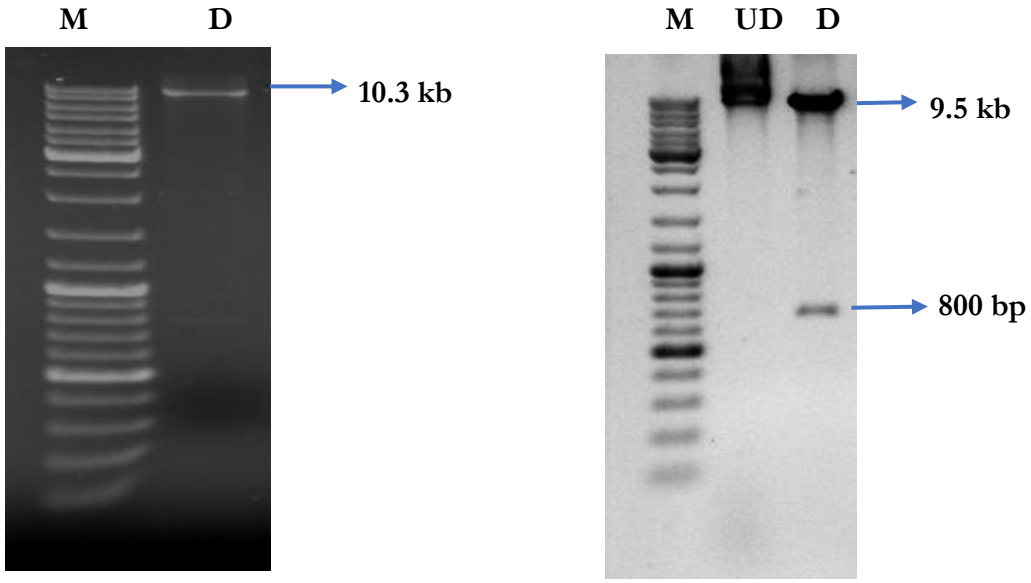

Fig A9: Cloning of *Pf(Δ259-337)topoIII* in pCENV3 vector: pCENV3+ *Pf(Δ259-337)topoIII* clone was confirmed by restriction digestion with BglII in which 10.3 kb size is obtained. Further, the direction was confirmed by restriction digestion with XhoI and BglII in a GFP (800 bp) is released after double digestion. The clone was further confirmed by plasmid DNA sequencing.
(M: marker, UD: undigested, D: digested)

Essential role of Plasmodium Topoisomerase III & its unique charged domain

by Shephali Bansod

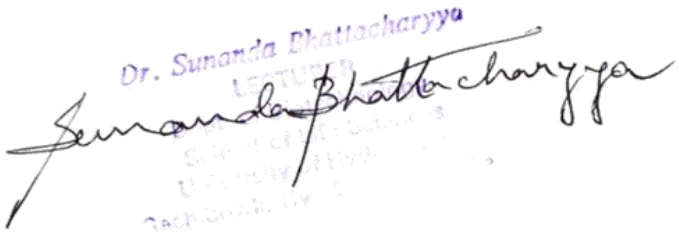

Submission date: 30-Apr-2021 11:48AM (UTC+0530)
Submission ID: 1574176162
File name: soft_copy_Shephali_BAnsod.pdf (565.78K)
Word count: 23892
Character count: 125902

Essential role of Plasmodium Topoisomerase III & its unique charged domain

ORIGINALITY REPORT

27%	14%	16%	17%
SIMILARITY INDEX	INTERNET SOURCES	PUBLICATIONS	STUDENT PAPERS

PRIMARY SOURCES

1	Submitted to University of Hyderabad, Hyderabad Student Paper	13%
2	Tanvi Suhane, Vijayalakshmi Bindumadhavan, Nupur Fangaria, Achuthsankar S. Nair et al. " Glu-108 in Rad51 Is Critical for DNA Damage-Induced Nuclear Function ", mSphere, 2019 Publication	1%
3	aac.asm.org Internet Source	1%
4	www.ncbi.nlm.nih.gov Internet Source	1%
5	Submitted to University of Witwatersrand Student Paper	1%
6	Sureshkumar Chalapareddy, Swati Chakrabarty, Mrinal Kanti Bhattacharyya, Sunanda Bhattacharyya. "Radicicol-Mediated Inhibition of Topoisomerase VIB-VIA Activity of	1%

This is to certify that there are certain part of the thesis belonging to 'material & methods' [#1-4 and #6] as indicated, with a cumulative similarity score of 17%, which must be represented as it it. Hence 17% should be deducted from the total score Thus, the resulting similarity score is 10%

Sunanda Bhattacharyya

LECTURER
Dept. of Biotechnology

Synopsis of the thesis titled

Essential role of *Plasmodium* Topoisomerase III & its unique charged domain

Submitted for the award of

DOCTOR OF PHILOSOPHY

By

SHEPHALI BANSOD (14LTPM01)

Research Supervisor

DR. SUNANADA BHATTACHARYYA

Department of Biotechnology and Bioinformatics
School of Life Sciences
University of Hyderabad
Hyderabad
500046
India

SYNOPSIS

Malaria is a life-threatening disease that severely affects pregnant women and children under five years of age (https://www.who.int/news-room/feature-stories/detail/world-malaria-report-2019). In 2018 alone, there were an estimated 228 million malaria cases and 405000 deaths worldwide. These numbers reflect the urgent requirement of an effective molecular target to suppress this disease. The potential drug target should be essential for parasite survivability and should have little or no homology with its human counterpart.

The *Plasmodium* life cycle is complex as it has to survive within two hosts (humans and mosquitoes). Their genome undergoes various processes like replication, transcription, repair, and recombination, which require a different set of specialized proteins. One such group of proteins necessary for almost all kinds of DNA metabolism are topoisomerases. Studies have shown that the absence of topoisomerases stalls replication fork [1] and causes genome instability [2], which eventually leads to cell death [3].

Topoisomerases are the enzymes involved in solving the topological problems by allowing the passage of one strand of DNA through the other, relieving either the underwinding or overwinding [4]. They are classified into two subfamilies, Type I and Type II Topoisomerase. Type II DNA topoisomerases solve the compact DNA structures by moving one DNA double helix through another in an ATP-dependent fashion. In general, they form transient phospho-tyrosine bonds between the protein and DNA. Type II topoisomerases function to remove super-helical twists from DNA and resolve knotted or tangled duplex molecules during numerous DNA processes. The major ones include recombination and replication [5, 6]. This group is again divided into Type IIA and Type IIB subfamilies. In *Plasmodium,* there are two type IIA topoisomerases, namely, DNA gyrase and topoisomerase II. DNA gyrases are involved in apicoplast replication, whereas topoisomerase II enzymes are essential during nuclear replication [7]. Type IIB topoisomerases are found in archaea and plants but absent in humans. In *Plasmodium*, PfTopoVI is the type IIB topoisomerase that is expressed during the replicative stage of the parasite. As this enzyme is absent in humans, it has a potential for drug target against malaria. It has two subunits, topoisomerase VIA and topoisomerase VIB. A small molecule inhibitor of PfTopoVIB has been identified which can inhibit the decatenation activity of this enzyme [8, 9].

Contrary to Type II topoisomerases, Type I topoisomerase transiently cuts a single strand of DNA and does not require ATP for its function. They are divided into two subclasses based

on the polarity of phospho-tyrosyl bond formed between a catalytic tyrosine residue and a single DNA strand. Type IA subfamily enzyme transiently cuts a single strand of DNA by forming a covalent bond with the catalytic tyrosine residue and 5' phosphate of the DNA, leaving the 3'-OH group free to pass through the intact strand [10]. These enzymes require divalent cation for their activity and relaxes only negative supercoils. They are proficient at catalysing the knotting, unknotting, and interlinking of single-stranded circles and act upon catenation and decatenation of gapped or nicked duplex DNA circles. This group includes topoisomerase I, Topoisomerase III, and reverse gyrase [3]. The Type IB family forms a 3' phospho-tyrosine intermediate leaving 5'-OH to undergo a restrain rotation around the intact DNA strand to relieve the supercoiling. The divalent cation is not required for the transesterification reaction. Unlike the Type IA subfamily, they can efficiently relax both positive and negative supercoils [12].

In the *P. falciparum* genome, two Type I topoisomerases have been identified; topoisomerase I and topoisomerase III. TopoI belongs to the Type IB family, which is expressed at the trophozoite and the schizont stages [13]. Our present study demonstrates the characterization of PfTopoIII, which belongs to the Type IA subfamily.

Earlier studies in other organisms have shown that TopoIII plays an important role during replication [12]. There are two isoforms of topoisomerase III in higher eukaryotes, TopoIIIα and TopoIIIβ. Inactivation of TopoIIIα leads to embryonic lethality in mice [14]. It is essential during the development of *Drosophila melanogaster* [15]. Experimental evidence shows that topoIIIβ$^{-/-}$ leads to infertility (progressive reduction in fecundity), aneuploidy and the reduced the life span in mice [16]. In budding yeast, Δ*topoIII* cells are viable, but their growth rate is reduced by two folds due to the accumulation of cells in the late S/G2 phase of the cell cycle [17]. Besides, yeast homozygous null diploid *topoIII*$^{-}$/*topoIII*$^{-}$ strains are unable to sporulate [17].

In this study, we have determined the function of PfTopoIII in *Plasmodium* biology. We have done the structure-function analysis of this enzyme and identified the presence of a unique charged domain in its structure, which is indispensable for its activity [18].

The *P. falciparum* genome database (http://www.plasmoDB.org) shows the presence of a putative PfTopoIII (Gene ID: PF3D7_1347100) gene. It has no intron, and it is predicted to code a 710 aa protein. Multiple sequence alignment of PfTopoIII with human, mouse, and yeast shows the presence of two aspartates and one glutamate (DxDxE) in its TOPRIM domain, which is conserved across other topoisomerase III sequences [19]. PfTopoIII has a

catalytic tyrosine residue at the 421st position in domain III. There are distinct differences between PfTopoIII and HsTopoIII. HsTopoIII sequence shows a small extension at the amino-terminal end (30 amino-acids long) and an extension at the carboxy-terminal end (360 amino-acid long stretches), which are absent in PfTopoIII. Instead, there is a 79 amino-acid long charged region (259-337) present within domain II of PfTopoIII, which is missing in the human counterpart. This domain has a series of positively charged amino acid residues mostly made up of lysine and arginine. It was earlier reported that *E. coli* Topo III comprises a similar but much smaller 17 amino acid regions rich in lysine and arginine residues [20]. Studies have indicated that the removal of charged domain hampers the decatenation activity of EcTopoIII [20]. To predict the configuration of the charged domain region of PfTopoIII in the presence of DNA, we used in-silico analysis. We have modeled PfTopoIII using I-TASSER server [21] and selected human TopoIIIα as a template (PDB: 4CGY) [22]. A single-strand DNA octamer (CGCAACTT) was placed in the binding site to generate a structure of PfTopoIII bound with DNA. The apo structure and the DNA bound PfTopoIII structure were stimulated for 100 ns using Gromacs 4.5.5 [23] and CHARMM36 force field [24]. It was observed that during the initiation of the simulation, the charged domain interacted with parts of domain III, similar to that of apo structure simulation. Around 34 ns, the charged domain adopted an open conformation to interact with the DNA octamer. At ~46 ns, residues D296, E297, K302, and K304 that are present within the charged domain, started interacting with the DNA octamer to stabilize it. During the latter part of the simulation, the charged domain was in a closed conformation. Thus, the molecular dynamics simulation data predicted that the charged domain of PfTopoIII remains flexible and stabilizes upon binding to the single-stranded DNA. We studied the expression of PfTopoIII in a bacterial system to generate its specific antibody, but the protein could not be expressed in bacteria. Hence, we generated a peptide antibody that was very specific towards the charged domain region of PfTopoIII. Using this antibody, we performed the expression studies within *P. falciparum* asexual development stages, *i.e.*, rings, trophozoites, and schizonts. We measured the mRNA and protein expression levels of PfTopoIII at different developmental stages of the parasite. We found it is highly expressed during the schizont stage, where the parasite DNA is replicated [18].

Studies have shown that HsTopoIII has the mitochondrial localization signal at the N-terminal and a nuclear localization signal at the C-terminal [25]. As mentioned earlier, the PfTopoIII enzyme structure is devoid of any such signal peptides. To understand the localization of PfTopoIII during the replicative stage, we did subcellular fractionation studies. Western blots

of the nuclear and organelle fractions display the presence of PfTopoIII in both the nuclear and mitochondrial fractions. We generated a transgenic parasite harboring PfTopoIII-GFP fusion protein and performed the live-cell imaging using a fluorescence microscope. We detect the localization of the protein in both the nucleus and mitochondria. We have generated another transgenic parasite harboring charged linker deletion mutant of PfTopoIII [PftopoIII$^{(\Delta 259\text{-}337)}$]. Live-cell imaging of this strain shows that the mutant protein is also present in the nucleus and mitochondria, indicating that the charged region is not essential for the nuclear or mitochondrial localization of the protein. Next, to evaluate the *in-vivo* function of PfTopoIII, we performed complementation studies using yeast as a surrogate system. Although ⊿*topoIII* strains are viable in yeast, they show a slow-growth phenotype (SLG) [26]. We created a Δ*topoIII* knockout strain of yeast using a homologous recombination strategy. Further, we created five isogenic strains of ⊿*topoIII* harboring each of *pTA* (Empty), *pTA-ScTopoIII*, *pTA-PfTOPOIII*, *pTA-PftopoIIIY421F,* and *pTA-PftopoIII(Δ259-337)*. We tested whether PfTopoIII can reverse the SLG of Δ*topoIII* strain. Our result showed that PfTopoIII was fully complementing the phenotype and showed similar growth as that of ScTopoIII harboring strain. As expected, the active-site mutant of PfTopoIII (*Y421FtopoIII*) remains non-functional and behaved similar to that of the Δ*topoIII* strain carrying empty plasmid. Surprisingly, the charged linker deletion mutant of PfTopoIII also failed to reverse the SLG phenotype of ⊿*topoIII,* indicating its essential requirement for the function of PfTopoIII [18]. Studies have shown that yeast ⊿*topoIII* strains are sensitive to MMS treatment because MMS methylates DNA which physically blocks the replication fork progression leading to cell death [27]. We wanted to determine whether PfTopoIII expression can reverse the MMS sensitivity of the ⊿*topoIII* strain. To that end, we exposed the above-mentioned isogenic strains to 0.01% and 0.04% MMS for 2 hours, and after that returned them to normal media and scored their survivability. We observed that full-length PfTopoIII could reverse MMS sensitivity in a similar manner as that of ScTopoIII harboring strain, suggesting a direct role of PfTopoIII during replication under stress conditions. On the contrary, the strain expressing PftopoIII^{Y421F} and PftopoIII$^{(\Delta 259\text{-}337)}$ showed severe sensitivity towards MMS, and they behaved similar to that of the ⊿*topoIII* strain. This re-establishes that the charge domain region is indispensable for the functioning of PfTopoIII. To rule out the possibility that loss of complementation is not due to loss of expression, we checked the mRNA and protein expression levels of all the strains used in this study. We observe that *ScTOPOIII*, wild-type *PfTOPOIII*, *PftopoIII$^{(\Delta 259\text{-}337)}$,* and *PftopoIIIY421F* were stably expressing at mRNA and protein level.

TopoIII performs its function via a conserved mechanism. RecQ helicases remodel the DNA into an accessible single-strand conformation suitable for processing only by TopoIII [28] to resolve stalled replication forks. We wanted to check whether PfTopoIII physically interacts with *Plasmodium* RecQ helicases. *Plasmodium falciparum* genome contains two RecQ helicases, namely PfBLM and PfWRN. We performed yeast two-hybrid analysis to evaluate the physical interaction between PfTopoIII and PfBLM/PfWRN. To that end, we cloned *PfBLM* and *PfWRN* in the prey vector as a fusion to the Gal4 activation domain and cloned *PfTOPOIII* in the bait vector as a fusion to the Gal4 DNA binding domain. Our study showed that both PfBLM and PfWRN physically interact with PfTopoIII. We did a similar study using the mutant *PftopoIII*$^{(\Delta 259–337)}$. We cloned the same in the bait vector. We observed that the absence of charged region does not affect the interaction between the PfTopoIII protein and the PfRecQ helicases.

To determine the function of PfTopoIII in parasite replication, we used hydroxyurea (HU) as a replication blocker. HU inhibits the ribonucleotide reductase, an enzyme required for the generation of deoxyribonucleotide triphosphates during the S-phase of the cell cycle [29]. Initially, 2.5 mM HU was given for 30 h (prolonged exposure) at 2% late trophozoite stage parasites, and we measured the survivability after every 10 h of initial treatment. We observed that the untreated parasites had a three-fold increment in parasitaemia at the end of the 30th hour. However, the HU-treated parasites showed severe sensitivity, and their survivability was significantly reduced in a time-dependent manner. We also studied the morphological effects of HU on parasites at three different time intervals. Untreated parasites formed mature schizonts (segmenters) at the end of the 20th hour, which eventually ruptured and produced rings at the end of the 30th hour. However, no such distinct stages were observed in HU-treated parasites. We wanted to study the effects of short-term exposure of HU on parasite survivability. We used 1% trophozoite-stage synchronized parasites and exposed them to 2.5 mM HU for 6 h. Subsequently, HU was extensively washed, and the parasites were returned to grow (RTG) to the normal media for 26 h. We found a 5-fold increase in parasitaemia in untreated parasites. However, this time, the treated parasites did not show any decrease in parasitaemia; instead, they remain arrested in the schizont stage and are defective in the schizont to ring transition. dNTPs are essential substrates for the successful replication of DNA. It was earlier shown that HU treatment causes stalling of the replication fork, which ultimately generates a chicken foot-like structure [30]. We reason that the prolonged presence of such structures may be detrimental to the parasites. It was reported that *S. cerevisiae* displays

severe sensitivity towards HU in *ΔtopoIII* strain [31], which indicates that TopoIII plays an essential role in resolving the aberrant structure generated from the arrest of the replication fork.

In order to determine the direct role of PfTopoIII during replication stress, we determined the endogenous level of PfTopoIII in HU treated parasites. We exposed synchronous trophozoite-stage specific parasites to two different HU doses (2.5 mM and 10 mM) for 6 h, subsequently washed HU, and allowed to grow the parasites in normal growth media for 26 h. We harvested the untreated and treated parasites at the end of 26 h and compared the levels of PfTopoIII in two cases. We found an increase in PfTopoIII protein levels in HU treated parasites in a dose dependent manner. To understand whether the increase in expression occurred due to the stabilization of proteins or increment in *PfTOPOIII* transcript levels, we extracted RNA from the untreated and HU-treated parasites. We quantified the *PfTOPOIII* cDNA by real-time RT-PCR. We detect an induction in the mRNA level of *PfTOPOIII* upon HU treatment. Rad51 plays an essential role in replicating fork stability and regression; hence was used as a positive control [32]. The transcriptional induction of *PfTOPOIII* in response to HU treatment indicates that the increased level of endogenous PfTopoIII is required to promote recovery from replication stress.

An increase in endogenous levels of PfTopoIII in response to HU gave us an indication that PfTopoIII is essential for cell survivability under stress conditions. Hence, we expressed PfTopoIII and PftopoIII$^{(\Delta 259–337)}$ ectopically in 3D7 strain using a centromeric plasmid. We repeated similar experiments, as described above, with the transgenic parasite strain. Firstly, we exposed the parasites to 2.5 mM HU for 30 h and monitored its growth every 10 h. We observed that the transgenic parasites harboring PftopoIII$^{(\Delta 259–337)}$ strain showed a similar sensitivity towards HU treatment as that of 3D7. On the contrary, the transgenic parasites with PfTopoIII over-expression vector, considerably reduced the dose-dependent death of the parasites at the 20th and 30th hours, reinforcing that the full-length PfTopoIII but not the charged domain deletion mutant of PfTopoIII can reverse HU's inhibitory effects. In a different assay, we exposed all the three strains towards 2.5 mM HU for a short duration (6 h) and eventually washed HU and allowed them to grow in normal media for 26 h. We found that as expected, the 3D7 parasites were severely affected even with 6 h treatment of HU, and their growth remained arrested compared with the untreated parasites. The PfTopoIII transgenic parasite line showed no significant difference between the survivability of treated versus untreated parasites and successfully reversed HU's growth defects. However, the

transgenic parasite line harboring PftopoIII$^{(\Delta 259–337)}$ showed a similar trend as that of 3D7 parasites and displayed a significant difference in survivability than the untreated parasites. This is the first study to identify functionally active TopoIII from a malaria parasite. Our study demonstrated a direct role of PfTopoIII in mitigating HU-mediated replication stress [18]. Firstly, PfTopoIII expression is induced in a dose-dependent manner in response to HU treatment. Secondly, expression of PfTopoIII can completely bypass the HU-induced growth defect in the parasites. It was earlier reported that HU treatment depletes the cellular pool of deoxyribonucleotides and there occurs an accumulation of joint DNA molecules in the direction opposite to the replication fork [33] that have serious implications on cell survivability. As these structures resemble Holliday junctions [34], we speculate that if such a condition is generated in *P. falciparum*, PfTopoIII along with its cognate helicases might play an important role in resolving the structures and converting them back into the replication forks.

Our study also identified a charged domain within PfTopoIII that is indispensable for its *in vivo* function. A previous experimental study showed that the charged loop present in bacterial TopoIII is essential for the decatenation of replication intermediates [17]. Our in-silico analysis predicts that the charged domain stabilizes the effective binding of PfTopoIII with DNA and indicates that this domain might play an important role in the catalytic mechanism of PfTopoIII protein. We obtained similar results with our genetic analysis. Firstly, the expression of wild-type PfTopoIII fully rescued the SLG and MMS-induced toxicity in yeast, but the expression of mutant *PftopoIII(∠1259–337)* failed to do the same and mimicked the phenotype of the topoisomerase-inactive mutant *PftopoIIIY421F*. Secondly, the transgenic mutant parasite line harboring *PftopoIII(∠1259–337)-GFP* failed to rescue itself from short-term exposure to replication stress. Together, our results emphasize the importance of the charged domain in the PfTopoIII function [18]. To date, no inhibitors of TopoIII have been identified. However, identification of the unique and indispensable charged domain of PfTopoIII promises itself as a target against malaria.

We also carried out another study where we performed *in-silico* analysis to identify a specific inhibitor of Topoisomerase VIB of *Plasmodium falciparum* [35]. TopoVIB acts as a novel target to treat malaria because it has no human ortholog. Radicicol, an antifungal macro lactone antibiotic, was previously shown to inhibit the function of *Sulpholobus shibatae* TopoVIB by acting as a competitive inhibitor of ATP. Previously, using a yeast-based assay system, we have demonstrated that Radicicol inhibits the decatenation activity of PfTopoVIB [8]. Radicicol

treatment sensitizes the *P. falciparum* parasites with an IC_{50} of 8.5 μM [9]. We observe that Radicicol treatment inhibits the schizont to ring transition of the blood-stage parasites, indicating the significance of PfTopoVI in *Plasmodium* biology.

Studies have shown that PfTopoVIB is a member of the GHKL (Gyrase-Hsp90-Histidine Kinase-MutL) super-family. They all share a small three-dimensional ATP-binding fold known as the Bergerat fold [36]. Due to this similarity within the Bergerat ATP-binding fold, Radicicol was found to dock both PfTopoVIB and PfHsp90 [9]. We used computational biology to design an analog of Radicicol that specifically binds PfTopoVIB and not to PfHsp90. Our strategy was to modify the radicicol structure by adding functional groups to enhance Radicicol attachment to PfTopoVIB and not PfHsp90 [37-42]. To that end, we designed 97 analogs of Radicicol using Marvin sketch version 16.8.8.0 (https://chemaxon.com/products/marvin) and generated 10 conformers of each of those analogs in DS 4.0 [43].

We created homology-based structures for PfTopoVIB and PfHsp90 proteins. The sequences of PfTopoVIB and PfHsp90 were retrieved from the Uniport/Swiss-Prot database [44]. Near-native structures of PfTopoVIB and PfHsp90 were modelled using the automated mode (ProMod3 Version 1.2) integrated with the Swiss-Model server [45]. For the PfTopoVIB model, 2ZBK was used as a template, which is a crystal structure for *S. shibatae* TopoVIB. Similarly, for PfHsp90, homology model 3IED was used as a template. Ramachandran plot for the modeled PfTopoVIB structure revealed that 80.4% of the residues (337 amino acids) were in the most favoured regions, 15.5% (65 amino acids) in the additional allowed region, 2.9% (12 amino acids) in the generously allowed region, and 1.2% (5 amino acids) in the disallowed region. The resultant model showed an ERRAT score of 81.728 and the final energy as -21297.992 kJ / mol. The PROCHECK results and the Ramachandran plot of PfHsp90 model revealed that 91.9% of the residues (181 amino acids) were in the most favoured regions, 8.1% (16 amino acids) in the additional allowed region, 0.0% (0 amino acids) in the generously allowed region and 0.0% (0 amino acids) in the disallowed region. The model showed ERRAT score as 81.878 and the final energy was -11965.740 kJ / mol.

Two sets of docking were carried out in a site-specific manner. The 3D structures of PfTopoVIB and PfHsp90 served as receptors, the 97 Radicicol derivatives and their conformers served as the analog dataset. The docking program LibDock [46, 47] implemented in DS 4.0 performs a high-throughput docking by aligning analog conformations to polar and a polar receptor interaction site(hotspots). ATP was used as a positive control. An empirical scoring function, LigScore [48], was employed to score the docked ligand poses, and the

complexes were ranked and sorted according to the descending order of the LibDock score. Out of 97 analogs, 88 molecules interacted with PfTopoVIB within the same binding cavity occupied by Radicicol and ATP, whereas 9 analogs failed to dock. Depending upon each analog's LibDock score, we classified them into two groups, one with a higher LibDock score than the cut-off value 76.4008 and the other with lower scores than the cut off value. We reason that way we will group those analogs of Radicicol that have a higher chance of binding with PfTopoVIB than the Radicicol. As the LibDock score of Radicicol for PfTopoVIB was 76.4; hence, all those having higher values than 76.4 were shortlisted. Based on the docking score, 77 analogs of Radicicol performed better than Radicicol, 11 analogs were poor performers, and 9 did not dock at all.

The same classification criterion was adopted for analysing the docking results of PfHsp90. In this case, the LibDock score of Radicicol for PfHsp90 is 91.79; hence, the values higher than that of 91.79 were shortlisted. Out of 97 analogs, 78 molecules were found to interact with a higher dock score than the cut-off value. 13 analogs docked with a lower LibDock score, and the remaining 6 analogs did not dock to PfHsp90 at all. Our criterion for selecting the best analogs was comparing their binding affinity with both the proteins and finally choosing those that docks specifically to PfTopoVIB but have little or no binding towards PfHsp90. We observed that out of the 6 analogs which did not dock to PfHsp90, 3 analogs docked with PfTopoVIB and has higher LibDock scores towards PfTopoVIB. These three analogs; analog 2, analog 6, and analog 7, with LibDock scores 133.823, 108.647, and 77.533, were selected as the lead molecules [35].

We performed a 50 ns Molecular Dynamics (MD) simulation study in triplicates for analog2-PfTopoVIB, analog6-PfTopoVIB, and analog7-PfTopoVIB complexes. Analog2-PfTopoVIB was found to be most stable and uniform with an average RMSD value of 0.2 Å. In contrast, analog7-PfTopoVIB and analog6-PfTopoVIB showed fluctuations during simulations [35]. We calculated the binding free energy of each of the three complexes, PfTopoVIB-analog2, PfTopoVIB-analog6 and PfTopoVIB-analog7 at 10 ns intervals for 50 ns. The relative binding energy of analog2 was found to be the lowest, confirming analog2 binding to be the strongest among the studied complexes. In analog2, we substituted two biphenyl groups at the C-17 and C-19 positions of Radicicol. The resultant derivative docked with PfTopoVIB with more contact points and scored better than Radicicol [35]. In future, we plan to validate its inhibitory effect on the activity of PfTopoVIB through the biochemical assays.

REFERENCES

1. Ray Chaudhuri A, Hashimoto Y, Herrador R, et al. Topoisomerase I poisoning results in PARP-mediated replication fork reversal. *Nat Struct Mol Biol*. 2012; 19(4): 417-423. doi:10.1038/nsmb.2258.
2. Drolet M, Brochu J. R-loop-dependent replication and genomic instability in bacteria. *DNA Repair (Amst)*. 2019; 84:10269-1026933. doi:10.1016/j.dnarep.
3. Champoux JJ. DNA topoisomerases: structure, function, and mechanism. *Annu Rev Biochem*. 2001; 70:369-413. doi:10.1146/annurev.biochem.70.1.369.
4. Pommier Y, Sun Y, Huang SN, et al. Roles of eukaryotic topoisomerases in transcription, replication and genomic stability. *Nat Rev Mol Cell Biol*. 2016; 17(11):703-721. doi:10.1038/nrm.2016.111.
5. Osheroff N. DNA topoisomerases. *Biochim Biophys Acta*. 1998; 1;1400(1-3):1-2. doi: 10.1016/s0167-4781(98)00123-7.
6. Wang JC. Cellular roles of DNA topoisomerases: a molecular perspective. *Nat Rev Mol Cell Biol*. 2002; 3(6):430-440. doi:10.1038/nrm831.
7. Raghu Ram EV, Kumar A, Biswas S, et al. Nuclear gyrB encodes a functional subunit of the Plasmodium falciparum gyrase that is involved in apicoplast DNA replication. *Mol Biochem Parasitol*. 2007; 154(1):30-39. doi:10.1016/j.molbiopara.2007.04.001.
8. Chalapareddy S, Chakrabarty S, Bhattacharyya MK, et al. Radicicol-Mediated Inhibition of Topoisomerase VIB-VIA Activity of the Human Malaria Parasite Plasmodium falciparum. *mSphere*. 2016; 1(1). doi:10.1128/mSphere.00025-15.
9. Chalapareddy S, Bhattacharyya MK, Mishra S, et al. Radicicol confers mid-schizont arrest by inhibiting mitochondrial replication in Plasmodium falciparum. *Antimicrob Agents Chemother*. 2014; 58(8):4341-4352. doi:10.1128/AAC.02519-13.
10. Li Z, Mondragón A, DiGate RJ. The mechanism of type IA topoisomerase-mediated DNA topological transformations. *Mol Cell* 2001 Feb; 7(2):301-7. doi: 10.1016/s1097-2765(01)00178-2.
11. Krogh BO, Shuman S. Catalytic mechanism of DNA topoisomerase IB. *Mol Cell* 2000; 5(6):1035-1041. doi:10.1016/s1097-2765(00)80268-3.
12. Bizard AH, Hickson ID. The many lives of type IA topoisomerases. *J Biol Chem*. 2020; 295(20):7138-7153. doi:10.1074/jbc.REV120.008286

13. Tosh K, Cheesman S, Horrocks P, et al. Plasmodium falciparum: stage-related expression of topoisomerase I. *Exp Parasitol*. 1999; 91(2):126-132. doi:10.1006/expr.1998.4362.
14. Li W, Wang JC. Mammalian DNA topoisomerase IIIalpha is essential in early embryogenesis. *Proc Natl Acad Sci U S A*. 1998; 95(3):1010-1013. doi:10.1073/pnas.95.3.1010.
15. Plank JL, Chu SH, Pohlhaus JR, et al. Drosophila melanogaster topoisomerase III alpha preferentially relaxes a positively or negatively supercoiled bubble substrate and is essential during development. *J Biol Chem*. 2005; 280(5):3564-3573. doi:10.1074/jbc.M411337200.
16. Kwan KY, Moens PB, Wang JC. Infertility and aneuploidy in mice lacking a type IA DNA topoisomerase III beta. *Proc Natl Acad Sci U S A*. 2003; 100(5):2526-2531. doi:10.1073/pnas.0437998100.
17. Wallis JW, Chrebet G, Brodsky G, et al. A hyper-recombination mutation in S. cerevisiae identifies a novel eukaryotic topoisomerase. *Cell*. 1989; 58(2):409-419. doi:10.1016/0092-8674(89)90855-6.
18. Bansod S, Bung N, Singh P, et al. Elucidation of an essential function of the unique charged domain of Plasmodium topoisomerase III. 2020; *Biochem J*. 2020; BCJ20200318. doi:10.1042/BCJ20200318.
19. Aravind L, Leipe DD, Koonin EV. Toprim--a conserved catalytic domain in type IA and II topoisomerases, DnaG-type primases, OLD family nucleases and RecR proteins. *Nucleic Acids Res*. 1998; 26(18):4205-4213. doi:10.1093/nar/26.18.4205.
20. Li Z, Mondragón A, Hiasa H, et al. Identification of a unique domain essential for Escherichia coli DNA topoisomerase III-catalysed decatenation of replication intermediates. *Mol Microbiol*. 2000; 35(4):888-895. doi:10.1046/j.1365-2958.2000.01763.x.
21. Yang J, Zhang Y. Protein Structure and Function Prediction Using I-TASSER. *Curr Protoc Bioinformatics*. 2015; 52:5.8.1-5.8.15. 2015 17. doi:10.1002/0471250953.bi0508s52.
22. Bocquet N, Bizard AH, Abdulrahman W, et al. Structural and mechanistic insight into Holliday-junction dissolution by topoisomerase IIIα and RMI1. *Nat Struct Mol Biol*. 2014; 21(3):261-268. doi:10.1038/nsmb.2775.

23. Hess B, Kutzner C, van der Spoel D, et al. GROMACS 4: Algorithms for Highly Efficient, Load-Balanced, and Scalable Molecular Simulation. *J Chem Theory Comput*. 2008; 4(3):435-447. doi:10.1021/ct700301q.

24. Huang J, MacKerell AD Jr. CHARMM36 all-atom additive protein force field: validation based on comparison to NMR data. *J Comput Chem*. 2013; 34(25):2135-2145. doi:10.1002/jcc.23354.

25. Nicholls TJ, Nadalutti CA, Motori E, et al. Topoisomerase 3α Is Required for Decatenation and Segregation of Human mtDNA. *Mol Cell*. 2018; 69(1):9-23.e6. doi:10.1016/j.molcel.2017.11.033.

26. Gangloff S, McDonald JP, Bendixen C, et al. The yeast type I topoisomerase Top3 interacts with Sgs1, a DNA helicase homolog: a potential eukaryotic reverse gyrase. *Mol Cell Biol*. 1994; 14(12):8391-8398. doi:10.1128/mcb.14.12.8391.

27. Groth P, Ausländer S, Majumder MM, et al. Methylated DNA causes a physical block to replication forks independently of damage signalling, O(6)-methylguanine or DNA single-strand breaks and results in DNA damage. *J Mol Biol*. 2010; 402(1):70-82 doi:10.1016/j.jmb.2010.07.010.

28. Wu L, Hickson ID. The Bloom's syndrome helicase suppresses crossing over during homologous recombination. *Nature*.2003; 426(6968):870-874. doi:10.1038/nature02253.

29. Bianchi V, Pontis E, Reichard P. Changes of deoxyribonucleoside triphosphate pools induced by hydroxyurea and their relation to DNA synthesis. *J Biol Chem*. 1986; 261(34):16037-16042.

30. Maric C, Bénard M. Replication forks reverse at high frequency upon replication stress in Physarum polycephalum. *Chromosoma*. 2014; 123(6):577-585. doi:10.1007/s00412-014-0471-z.

31. Chakraverty RK, Kearsey JM, Oakley TJ, et al. Topoisomerase III acts upstream of Rad53p in the S-phase DNA damage checkpoint. *Mol Cell Biol*. 2001; 21(21):7150-7162. doi:10.1128/MCB.21.21.7150-7162.

32. Zellweger R, Dalcher D, Mutreja K, et al. Rad51-mediated replication fork reversal is a global response to genotoxic treatments in human cells. *J Cell Biol*. 2015; 208(5):563-579. doi:10.1083/jcb.201406099.

33. Maric C, Bénard M. Replication forks reverse at high frequency upon replication stress in Physarum polycephalum. *Chromosoma*. 2014; 123(6):577-585. doi:10.1007/s00412-014-0471-z.

34. Liu Y. EEPD1: Breaking and Rescuing the Replication Fork. *PLoS Genet*. 2016; 12(2):e1005742 doi:10.1371/journal.pgen.1005742.

35. Bansod S, Raj N, Amjesh R, et al. Molecular docking and molecular dynamics simulation identify a novel Radicicol derivative that predicts exclusive binding to *Plasmodium falciparum* Topoisomerase VIB. *J Biomol Struct Dyn*. 2021; 1-13. doi:10.1080/07391102.2021.1891970.

36. Dutta R, Inouye M. GHKL, an emergent ATPase/kinase superfamily. *Trends Biochem Sci*. 2000; 25(1):24-28. doi:10.1016/s0968-0004(99)01503-0.

37. Dutton BL, Kitson RR, Parry-Morris S, et al. Synthesis of macrolactam analogues of radicicol and their binding to heat shock protein Hsp90. *Org Biomol Chem*. 2014; 12(8):1328-1340. doi:10.1039/c3ob42211a.

38. Wang S, Xu Y, Maine EA, et al. Functional characterization of the biosynthesis of radicicol, an Hsp90 inhibitor resorcylic acid lactone from Chaetomium chiversii. *Chem Biol*. 2008; 15(12):1328-1338. doi:10.1016/j.chembiol.2008.10.006.

39. Pearl LH, Prodromou C, Workman P. The Hsp90 molecular chaperone: an open and shut case for treatment. Biochem J. 2008; 410(3):439-53. doi: 10.1042/BJ20071640. PMID: 18290764.

40. Teo RD, Dong SS, Gross Z, et al. Computational predictions of corroles as a class of Hsp90 inhibitors. *Mol Biosyst*. 2015; 11(11):2907-2914. doi:10.1039/c5mb00352k.

41. Shinonaga H, Noguchi T, Ikeda A, et al. Synthesis and structure-activity relationships of radicicol derivatives and WNT-5A expression inhibitory activity. *Bioorg Med Chem*. 2009; 17(13):4622-4635. doi:10.1016/j.bmc.2009.04.060.

42. Shiotsu Y, Neckers LM, Wortman I, et al. Novel oxime derivatives of radicicol induce erythroid differentiation associated with preferential G(1) phase accumulation against chronic myelogenous leukemia cells through destabilization of Bcr-Abl with Hsp90 complex. *Blood* 2000; 96(6):2284-2291.

43. Smellie A, Teig SL, Towbin P. Poling: Promoting conformational variation. *J. Comput. Chem* 1995; 16: 171-187 doi:10.1002/jcc.540160205.

44. Bairoch A, Apweiler R. The SWISS-PROT protein sequence database: its relevance to human molecular medical research. *J Mol Med (Berl)*. 1997; 75(5):312-316.

45. Guex N, Peitsch MC, Schwede T. Automated comparative protein structure modeling with SWISS-MODEL and Swiss-PdbViewer: a historical perspective. *Electrophoresis*. 2009; 30 Suppl 1:S162-S173. doi:10.1002/elps.200900140.

46. Diller DJ, Merz KM Jr. High throughput docking for library design and library prioritization. *Proteins*. 2001; 43(2):113-124.

47. Rao SN, Head MS, Kulkarni A, et al. Validation studies of the site-directed docking program LibDock. *J Chem Inf Model*. 2007;47(6):2159-2171. doi:10.1021/ci6004299

48. Krammer A, Kirchhoff PD, Jiang X, et al. LigScore: a novel scoring function for predicting binding affinities. *J Mol Graph Model*. 2005; 23(5):395-407. doi:10.1016/j.jmgm.2004.11.007.

Biochemical Journal (2020) **477** 4745–4767
https://doi.org/10.1042/BCJ20200318

Research Article

Elucidation of an essential function of the unique charged domain of *Plasmodium* topoisomerase III

Shephali Bansod[1], Navneet Bung[2], Priyanka Singh[1], Niranjan Suthram[3], Himashree Choudhury[1], Arijit Roy[2], Gopalakrishnan Bulusu[2] and Sunanda Bhattacharyya[1]

[1]Department of Biotechnology and Bioinformatics, School of Life Sciences, University of Hyderabad, Hyderabad, India; [2]Tata Consultancy Services Limited, Hyderabad, India; [3]Department of Biochemistry, School of Life Sciences, University of Hyderabad, Hyderabad, India

Correspondence: Sunanda Bhattacharyya (sdeb70@gmail.com)

Topoisomerase III (TopoIII) along with RecQ helicases are required for the resolution of abnormal DNA structures that result from the stalling of replication forks. Sequence analyses have identified a putative TopoIII in the *Plasmodium falciparum* genome (PfTopoIII). PfTopoIII shows dual nuclear and mitochondrial localization. The expression and association of PfTopoIII with mtDNA are tightly linked to the asexual replication of the parasite. In this study, we observed that PfTopoIII physically interacts with PfBlm and PfWrn. Sequence alignment and domain analyses have revealed that it contains a unique positively charged region, spanning 85 amino acids, within domain II. A molecular dynamics simulation study revealed that this unstructured domain communicates with DNA and attains a thermodynamically stable state upon DNA binding. Here, we found that the association between PfTopoIII and the mitochondrial genome is negatively affected by the absence of the charged domain. Our study shows that *PfTOPOIII* can completely rescue the slow growth phenotype of the *ΔtopoIII* strain in *Saccharomyces cerevisiae*, but neither *PfY421FtopoIII* (catalytic-active site mutant) nor *Pf(Δ259–337)topoIII* (charged region deletion mutant) can functionally complement *ScTOPOIII*. Hydroxyurea (HU) led to stalling of the replication fork during the S phase, caused moderate toxicity to the growth of *P. falciparum*, and was associated with concomitant transcriptional up-regulation of *PfTOPOIII*. In addition, ectopic expression of *PfTOPOIII* reversed HU-induced toxicity. Interestingly, the expression of *Pf(Δ259–337)topoIII* failed to reverse HU-mediated toxicity. Taken together, our results establish the importance of TopoIII during *Plasmodium* replication and emphasize the essential requirement of the charged domain in PfTopoIII function.

Introduction

Malaria is a life-threatening disease caused by *Plasmodium* parasites. According to the latest report of the World Health Organization, there were 228 million cases of malaria worldwide in 2018 (https://www.who.int/news-room/feature-stories/detail/world-malaria-report-2019). Because the parasite has begun to develop resistance to antimalarial medicines [1–3], it is necessary to identify novel targets that are essential to the parasite's biology. Topoisomerases are attractive targets because they are required for cellular function; indeed they are currently being used to successfully treat bacterial infection [4] and cancer [5]. This group of enzymes is essential for DNA metabolism and plays a crucial role during DNA replication, transcription, recombination, and repair. There are two subgroups of topoisomerases, categorized based on their mode of action: Type I and Type II [6]. PfTopoII [7], PfGyrase [8–10], and PfTopoVI [11,12] are Type II topoisomerases, which have been characterized in detail.

Received: 24 April 2020
Revised: 27 September 2020
Accepted: 26 November 2020

Accepted Manuscript online: 26 November 2020
Version of Record published: 24 December 2020

Biochemical Journal (2020) 477 4745–4767
https://doi.org/10.1042/BCJ20200318

P. falciparum possesses a putative DNA topoisomerase III (TopoIII) as the sole member of the type IA family of topoisomerases, which transiently cleaves single-stranded DNA through the formation of a covalent 5′ phosphotyrosine intermediate, releasing a free 3′-OH end. The parasite has another subclass of topoisomerase I, type IB, which belongs to an evolutionarily distinct class than type IA. A previous study revealed that *PfTOPOIB* mRNA is transcribed at the trophozoite stage but not at the schizont stage [13]. The TopoIB enzyme relaxes both positive and negative supercoils in DNA, cleaves the single-stranded DNA through formation of 3′ phosphotyrosine intermediate, and allows the 5′-OH strand to undergo a restrained rotation around the non-scissile strand [14]. The TopoIB enzyme plays a major role in removing DNA supercoiling during DNA transcription and replication. However, topoisomerase IA performs additional roles besides working as a swivel during DNA replication. Owing to the difference in strand passage activity, Type IA enzymes play an important role in chromosome segregation during DNA replication and also perform regulatory roles in the formation or resolution of recombination intermediates along with the RecQ helicases [15].

Bacteria possess two Type IA topoisomerases, TopoI and TopoIII, which share a high degree of protein sequence similarity except that TopoIII contains a unique 17 amino acid (aa) charged loop present in the central hole of the enzyme. This gives TopoIII a distinct cleavage pattern compared with TopoI [16] and serves as a potent decatenase of replication intermediates [17] but inefficient relaxation of supercoiled DNA [18]. A recent study showed that bacterial TopoIII remains physically associated with the actively replicating fork and unlinks the catenated and precatenated DNA rings that result during DNA replication [19].

Budding yeast cells that lack topoisomerase III are viable; however, their growth rate is reduced by two-fold due to the accumulation of cells in the late S/G2 phase of the cell cycle and show hyper-recombination between repetitive sequences [20]. In addition, yeast homozygous null diploid *topoIII⁻/topoIII⁻* cells are unable to sporulate [20]. There are two homologous genes for TopoIII in vertebrates (TopoIIIα and TopoIIIβ). Inactivation of TopoIIIα leads to embryonic lethality in mice [21].

Yeast TopoIII and human TopoIIIα physically interact with Sgs1 and Blm, respectively, and resolve the double Holliday junctions that are generated within the replicating sister chromosomes during sudden stalling of the replication fork; this subsequently suppresses genetic crossover [22]. TopoIIIα is also required for the decatenation and segregation of human mitochondrial DNA (mtDNA) following replication [23].

Plasmodium mitochondrial and nuclear replication initiates in the late trophozoite stage [24]. It has been demonstrated that mtDNA of *Plasmodium* follows the rolling circle mode of replication like that of *Saccharomyces cerevisiae* [25]. During this process, inter-molecular homologous recombination results in the formation of a circular as well as a lariat-like complex network, which is eventually processed to form linear concatamers of DNA [26]. This suggests the possible involvement of Type I and/or Type II topoisomerases in mtDNA replication, which are essential for proper segregation of mtDNA in newly formed rings; however, to date, there is no report of this.

We investigated the function of TopoIII in *Plasmodium* biology. Our results establish that it plays an important role during the replication of the parasite. We found that the enzyme is expressed specifically during the onset of replication and its dual presence in the nucleus and mitochondria suggests its involvement during the replication of both genomes. Additionally, the stronger association between PfTopoIII and mtDNA during the late schizont stage of the parasite development indicates that it might play a role in mtDNA segregation. Our study also demonstrates a physical association between PfTopoIII and PfRecQ helicases.

Our study points out an important feature toward structure-function relation of PfTopoIII. We have identified a unique highly charged low complexity region (residues 253–336) in PfTopoIII, which is rich in aspartic acid and lysine rich repetitive sequences. It is noteworthy that about half of the ORFs of parasite genome are having repetitive sequences [27] although their role in protein function remains unclear. Using several genetic studies we have concluded that, deletion of this region completely abolishes the function of PfTopoIII. The presence of this unique 85 amino acid region affirms the enzyme as an attractive target for the design of antimalarial agents.

Materials and methods

Plasmids

The sequences of all primers used in this study are tabulated in Supplementary Table S3. *PfTOPOIII*, *PfY421FtopoIII*, and *Pf(Δ259–337)topoIII* were cloned in 2 μ yeast expression vector *pTA* [28] between the BamH1 and SalI restriction sites using the primer pairs OSB 334 and OSB 335. *ScTOPOIII* was cloned in *pTA*

vector using primer pairs OSB 346 and OSB 455. Full-length *PfTOPOIII* and *Pf(Δ259–337)topoIII* were cloned in centromeric *Plasmodium* expression vector pPfCENv3 (a gift from Dr. Puran Singh Sijwali, CCMB, Hyderabad) [29] under the promoter of *PfCAM* using forward primer OSB 334 and the reverse primer OSB 497. *PfTOPOIII* and its mutant were expressed as a C-terminal GFP fusion product. *PfTOPOIII*, and *Pf(Δ259–337)topoIII* were individually subcloned into bait vector *pGBDUC1* between BamHI and SalI restriction sites to create the *pGBDUC1PfTOPOIII* and *pGBDUC1Pf(Δ259–337)topoIII* plasmids. We received the prey plasmids *pGADC1PfBLM* and *pGADC1PfWRN* as a gift from Professor Mrinal K. Bhattacharyya of the University of Hyderabad.

Site-directed mutagenesis

Point mutations and deletion mutations were introduced in *PfTopoIII* using the splice overlap extension (SOE) PCR technique. Primer sets with the required mutations were designed to incorporate mutations in *PfTOPOIII* at the desired locations. *Plasmodium* 3D7 genomic DNA was used as a template and a full-length gene was amplified in two segments to insert a point mutation. To amplify the first and second segments to generate the *PfY421FtopoIII* mutation, the OSB 334/OSB 452 and OSB 453/OSB 335 primer sets were used, respectively. Then full-length *PftopoIII* containing the *Y421F* mutation was amplified using the first two segments along with primer set OSB 334 and OSB 335. Finally *PfY421FtopoIII* mutant was cloned into *pTA* 2 μ yeast expression vector between the BamH1 and SalI sites. After successful cloning, the *PfY421FtopoIII* construct was sequenced to confirm the desired mutation. To generate a Y-to-F mutation at the 421st aa residue, we changed the codons TAC to TTT. Similarly, to generate the *Pf(Δ259–337)topoIII* mutation, the OSB 334/OSB 450 and OSB 451/OSB 335 primer sets were used, respectively, for amplification, as mentioned earlier. Then full-length *PftopoIII* with the deletion of the abovementioned segment was amplified using the first two segments along with the primer set OSB 334/OSB 335. Finally, a *Pf(Δ259–337)topoIII* deletion mutant was cloned into *pTA* 2 μ yeast expression vector between the BamH1 and SalI sites. After successful cloning, the *Pf(Δ259–337)topoIII* construct was sequenced to confirm the desired deletion.

Yeast strains

The strains used in this study are listed in Table 1. The *ΔSctopoIII* strain was generated by homologous recombination-mediated gene knockout. To that end, a deletion cassette [30] with an *HIS3* gene flanked by 40 bp upstream and 40 bp of the 3′ terminal end of *ScTOPOIII* ORF was amplified using the primer set OSB 348/OSB 385. Then the cassette was transformed in the wild-type strain and the transformed colonies were selected using histidine drop-out plates. Individual colonies were screened for *SctopoIII* knockout clone by PCR-mediated confirmation using primer pairs OSB 350 and OSB 385. For a functional complementation study in yeast, we transformed the empty vector (*pTA*), *pTAScTOPOIII, pTAPfTOPOIII*, *pTAPfY421FtopoIII*, and *pTAPf(Δ259–337)topoIII* individually into the *ΔtopoIII* strain to generate SBY2, SBY3, SBY4, SBY5, and SBY6, respectively. To perform yeast two-hybrid analyses, we used a PMY3 strain that harbors empty *pGADC1* and *pGBDUC1* vectors [31]. To study the interaction between PfTopoIII and PfBlm as well as PfWrn, the HCY1 and HCY2 strains were created by transforming Prey-*PfBLM* + Bait-*PfTOPOIII* and Prey-*PfWRN* + Bait *PfTOPOIII* constructs into the PJ69-4A strain, respectively. Similarly, to study the interaction between PftopoIII$^{(\Delta 259-337)}$ and PfBlm as well as PfWrn, strains HCY3 and HCY4 were generated by transforming the Prey-*PfBLM* + Bait-*Pf(Δ259–337)topoIII* and Prey-*PfWRN* + Bait-*Pf(Δ259–337)topoIII* constructs, respectively into the PJ69-4A strain. The strains HCY7, HCY8, HCY9, and HCY10 were used as controls. These strains were generated by transforming empty Prey + Bait-*PfTOPOIII*, Prey-*PfBLM* + empty Bait, Prey-*PfWRN* + empty Bait, and empty Prey + Bait-*Pf(Δ259–337)topoIII* vectors respectively into the PJ69-4A strain.

Synchronization of *P. falciparum in vitro* culture

Synchronization was done following a previously published protocol [32]. Briefly, 10 ml ring-stage parasites were centrifuged at 2500 rpm for 10 min at room temperature. The supernatant was removed using a Pasteur pipette and the pellet was carefully re-suspended in two bed volumes of pre-warmed 5% sorbitol (Sigma) solution at 37°C. The sample was incubated at 37°C for 10 min with intermittent tapping. After that, pre-warmed incomplete medium was added to a volume of 10 ml, and the sample was centrifuged at 3000 rpm for 10 min. The supernatant was removed and the pellet was washed three times with pre-warmed incomplete medium. Then the parasites were allowed to grow normally until the early ring stage, and sorbitol synchronization was

Biochemical Journal (2020) **477** 4745–4767
https://doi.org/10.1042/BCJ20200318

Table 1 Yeast strains

Strain	Genotype	Source
SBY1	*MATα leu2-3,112 trp1-1 can1-100 ura3-1 ade2-1 his3-11,15 [phi+] TOPOIII::HIS3*	This study
SBY2	*MATα leu2-3,112 trp1-1 can1-100 ura3-1 ade2-1 his3-11,15 [phi+] TOPOIII::HIS3 Pta*	This study
SBY3	*MATα leu2-3,112 trp1-1 can1-100 ura3-1 ade2-1 his3-11,15 [phi+] TOPOIII::HIS3 pTAScTOPOIII*	This study
SBY4	*MATα leu2-3,112 trp1-1 can1-100 ura3-1 ade2-1 his3-11,15 [phi+] TopoIII::HIS3 pTAPfTOPOIII*	This study
SBY5	*MATα leu2-3,112 trp1-1 can1-100 ura3-1 ade2-1 his3-11,15 [phi+] TopoIII::HIS3 pTAPfY421FtopoIII*	This study
SBY6	*MATα leu2-3,112 trp1-1 can1-100 ura3-1 ade2-1 his3-11,15 [phi+] TOPOIII::HIS3 pTAPf(Δ259–337)topoIII*	This study
PJ694a	*MATa trpl-901 leu2-3,112 ura3-52 his3-200 ga14Δ ga180Δ LYS2 :: GALI-HIS3 GAL2-ADE2, met2::GAL7-lacZ*	[31]
PMY3	*MATa trpl-901 leu2-3,112 ura3-52 his3-200 ga14Δ ga180Δ LYS2 :: GALI-HIS3 GAL2-ADE2, met2::GAL7-lacZ pGADC1,pGBDUC1*	[31]
HCY1	*MATa trpl-901 leu2-3,112 ura3-52 his3-200 ga14Δ ga180Δ LYS2 :: GALI-HIS3 GAL2-ADE2, met2::GAL7-lacZ pGADC1/PfBLM, pGBDUC1/PfTOPOIII*	This study
HCY2	*MATa trpl-901 leu2-3,112 ura3-52 his3-200 ga14Δ ga180Δ LYS2 :: GALI-HIS3 GAL2-ADE2, met2::GAL7-lacZ pGADC1/PfWRN, pGBDUC1/PfTOPOIII*	This study
HCY3	*MATa trpl-901 leu2-3,112 ura3-52 his3-200 ga14Δ ga180Δ LYS2 :: GALI-HIS3 GAL2-ADE2, met2::GAL7-lacZ pGADC1/PfBLM, pGBDUC1/Pf(Δ259–337)topoIII*	This study
HCY4	*MATa trpl-901 leu2-3,112 ura3-52 his3-200 ga14Δ ga180Δ LYS2 :: GALI-HIS3 GAL2-ADE2, met2::GAL7-lacZ pGADC1/PfWRN, pGBDUC1/Pf(Δ259–337)topoIII*	This study
HCY7	*MATa trpl-901 leu2-3,112 ura3-52 his3-200 ga14Δ ga180Δ LYS2 :: GALI-HIS3 GAL2-ADE2, met2::GAL7-lacZ pGADC1, pGBDUC1/PfTOPOIII*	This study
HCY8	*MATa trpl-901 leu2-3,112 ura3-52 his3-200 ga14Δ ga180Δ LYS2 :: GALI-HIS3 GAL2-ADE2, met2::GAL7-lacZ pGADC1/PfBLM, pGBDUC1*	This study
HCY9	*MATa trpl-901 leu2-3,112 ura3-52 his3-200 ga14Δ ga180Δ LYS2 :: GALI-HIS3 GAL2-ADE2, met2::GAL7-lacZ pGADC1/PfWRN, pGBDUC1*	This study
HCY10	*MATa trpl-901 leu2-3,112 ura3-52 his3-200 ga14Δ ga180Δ LYS2 :: GALI-HIS3 GAL2-ADE2, met2::GAL7-lacZ pGADC1, pGBDUC1/Pf(Δ259–337)topoIII*	This study

performed again to obtain close to 100% synchronized ring-stage parasites. These synchronized parasites were grown further to obtain synchronized trophozoite-stage and synchronized schizont-stage parasites.

Generation of transgenic parasites

For transfection, plasmid DNA was purified using Maxi kit (Qiagen) and was re-suspended in 50 μl cytomix solution (10 mM K_2HPO_4 pH 7.6, 120 mM KCl, 0.15 mM $CaCl_2$, 25 mM HEPES pH 7.6, 2 mM EGTA pH 7.6, 5 mM $MgCl_2$) and kept at 4°C for overnight before transfection. Tightly synchronized ring-stage *P. falciparum* culture (6% parasitemia) was electroporated (Bio-Rad Gene Pulser) with 80–100 μg plasmids. Transfected cells were initially allowed to grow in the absence of drug (normal RPMI media) until the parasitemia reached 4%. Later cells were maintained in media containing Blasticidin (2.4 μg/ml) until transfectants appeared. Transgenic parasites were confirmed by checking the expression of GFP-tagged protein via Western blotting analyses.

Yeast two-hybrid analyses

Yeast two-hybrid analyses were performed as described previously [31]. The strains PMY3, HCY1, HCY2, HCY3, HCY4, HCY7, HCY8, HCY9, and HCY10 were grown in SC-Ura-Leu medium until the logarithmic

phase. Then they were diluted serially and spotted in SC-Ura-Leu and SC-Ura-Leu-His media. The plates were kept at 30°C for 3–4 days. The strain PMY3 was used as the negative control in our study.

Chromatin immunoprecipitation assay

We followed a previously described method [32]. Briefly, synchronized asexual erythrocytic stages (R, T, ES, and LS) of *P. falciparum* 3D7 parasite were cultured in RPMI1640 media. Formaldehyde (37%) was added to the parasite culture to a final concentration of 1% and the sample was incubated at 37°C for 10 min. The sample was sonicated six times (Elma; model-S-60H) at a frequency of 37 kHz for 10 s, followed by 5 min incubation on ice to generate an average DNA fragment size of 1 kb. Then protein–DNA complexes were selectively immunoprecipitated using antiPfTopoIII antibody. Reverse cross-linking was performed using 5 M NaCl. Finally, DNA was extracted using proteinase K-phenol chloroform. We quantified PfTopoIII recruitment to mtDNA using specific primers pairs for different regions of the *P. falciparum* mitochondrial genome, i.e. for A set- OMKB 540, OSB 251; for B set- OSB 493, OSB 495; for C set- OMKB 615, OSB 176; for D set- OMKB 616, OMKB 617; for E set- OMKB 618, OMKB 619; and for F set- OMKB 620, OMKB 541 as shown in Figure 4A. Control antibody used for ChIP was rabbit immunoglobulin G, which acted as a negative control. The IgG values were 0 or negligible. The IgG values were subtracted from the PfTopoIII ChIP value before plotting. To compare the recruitment of wild-type PfTopoIII and mutant PftopoIII$^{(\Delta 259-337)}$ to mtDNA, we used transgenic parasite lines specific to the late schizont stage that express the enzymes as GFP fusion proteins and used anti-GFP antibody to precipitate PfTopoIII-bound DNA.

Real-time PCR analyses

Equal amounts of RNA (10 μg) from ring-, trophozoite- and schizont-stage parasites were first subjected to DNase I (Fermentas) digestion for 15 min at room temperature. Then, DNase I was inactivated by incubation with 25 mM EDTA at 65°C for 10 min. The absence of genomic DNA was verified by amplification with gene-specific primers before the reverse-transcriptase step. Next, each RNA sample was reverse-transcribed with oligo dT primer (Sigma–Aldrich) using reverse transcriptase (Omni Script; Qiagen, Hilden, Germany) [12]. The resulting cDNA was subjected to semi-quantitative reverse transcription (RT)-PCR to detect the transcript level of *P. falciparum TopoIII* in all of the asexual stages. Similarly, the expression of *PfBLM* was measured by amplifying 149 bp gene-specific regions using the primer pairs OMKB 332 and OMKB 333. In addition, *PfWRN* expression was measured by amplifying 225 bp gene-specific regions using the primer pairs OMKB 334 and OMKB335. For real-time PCR, cDNA from each stage was diluted (1 : 50) and used for PCR using an RT-PCR kit (Roche). Real-time analyses were conducted using the Applied Biosystems 7500 Fast Real-Time PCR system. The threshold cycle (C_T) value of the *ARP* transcript of each sample was used to normalize the corresponding C_T values of the *PfTopoIII* transcripts. The normalized C_T values of *PfTOPOIII* from different samples were compared with obtain ΔC_T values. The relative levels of mRNA were deduced from the formula: change in mRNA level = $2^{\Delta CT}$. The primers OSB 337 and OSB 335 were designed to amplify a 254 bp gene-specific region of *PfTOPOIII*, and OSB 94 and OSB 95 were used to amplify a 300 bp gene-specific region of *P. falciparum* aspartate-rich protein (*PfARP*) [12]. To further investigate the mRNA levels of *PfTOPOIII* under HU conditions, RNA was isolated under treated and untreated conditions. The same procedure was followed to check the expression of *PfTOPOIII*. The primers OMKB 198 and OMKB 17 were used to amplify 314 bp gene-specific regions of *PfRAD51*.

Immunofluorescence assay

Plasmodium culture (6% parasitemia in the late-schizont stage) harboring PfTopoIII-GFP expression vector and that harboring PftopoIII$^{(\Delta 259-337)}$-GFP expression vector was stained with DAPI and separately with Mitotracker for 30 min at 37°C prior to imaging. Subsequently, fluorescence levels as assessed via DAPI, Mitotracker, and GFP were observed and captured from live cells using a fluorescence microscope (Axio Observer Z1 with Apotome, Carl Zeiss).

PfTopoIII structure modeling and molecular dynamics

The PfTopoIII structure was modeled using the I-TASSER server [33], employing the 4CGY (PDB ID) structure as a template [34]. For residues with no matching template, I-TASSER performs *ab initio* modeling. To check the stability of the modeled structure, explicit solvent MD simulation was performed using Gromacs 4.5.5 [35] and CHARMM36 force field [36]. The apo-structure was solvated in an octahedron box with a

Biochemical Journal (2020) 477 4745–4767
https://doi.org/10.1042/BCJ20200318

TIP3P water model [37]. The charges on the protein were neutralized by adding chloride ions. NVT- and NPT-position restrained equilibrations were done for 200 ps and 1 ns, respectively. The modeled apo structure was used for 50 ns molecular dynamics (MD) simulations.

A clustering calculation was performed on the last 10 ns of the trajectory from the 50 ns simulation of the PfTopoIII apo-structure. The structure at the center of the largest cluster was chosen as the starting structure for the subsequent simulations. To study the binding of single-stranded DNA in the PfTopoIII structure, the *E. coli* structure was used. The 1I7D (PDB ID) [38] structure was aligned to the PfTopoIII to generate a holo structure with a single-stranded DNA octamer. The holo structure of PfTopoIII was simulated for 100 ns using a similar procedure as mentioned above. VMD 1.9.2 [39] and Gromacs 4.5.5 [35] were used to analyze the trajectories. The root-mean-square fluctuations (RMSFs) of the Cα atoms of the entire protein were calculated by using the g_rmsf module of Gromacs.

Phylogenetic analyses

The TopoIII sequences of various organisms (*P. falciparum*, *S. cerevisiae*, human, mouse, *E. coli*, *V. cholerae*, *V. nereis*, *E. lignolyticus* and *S. enterica*) were obtained from Uniprot [40] and PlasmoDB [41]. Then multiple sequence alignment (MSA) was performed using ClustalW [42]. A phylogenetic tree was constructed using fasttree [43] as implemented in Genomenet (http://www.genome.jp) [44].

Subcellular fractionation

Samples (60 ml) of 8% parasitized erythrocytes specific to the late-schizont stage were harvested and treated with 0.15% saponin to free parasites from red blood cells (RBCs). The standard protocol for subcellular fractionation was followed [12].

MMS sensitivity assay

SBY2, SBY3, SBY4, SBY5, and SBY6 were tested for DNA damage sensitivity. All strains were grown overnight in tryptophan dropout synthetic medium at 30°C. The next day, secondary culture was grown until 0.5 OD_{600} at 30°C. After OD_{600} reached to 0.5, the culture was divided into three sets. One set of cells was treated with 0.01% (vol/vol) methyl methanesulfonate (MMS) (Sigma–Aldrich), and the second set of cells was treated with 0.04% MMS and grown at 30°C for 2 h. The third set was continuously grown at 30°C for 2 h without MMS. After this process, approximately 1000 untreated and 1000 treated cells were spread on selective media and incubated at 30°C for 2–3 days.

HU sensitivity assay

In survivability assays, HU (Sigma) was added to the highly synchronized late-trophozoite stage of *P. falciparum* culture (∼1% parasitaemia) at a concentration of 2.5 mM for 30 h at 37°C. Parasitemia was determined via Giemsa staining (Sigma) at every 10 h by counting at least 2000 RBCs. For each strain, 3–4 independent assays were conducted. In return-to-growth assays, 1% synchronized parasites were treated with 2.5 mM HU for 6 h. After 6 h treatment with HU, cells were washed twice and allowed to grow for 26 h in complete media. Then 6 h and 26 h slides were prepared for both HU-treated and untreated samples and parasitemia was measured. This experiment was repeated three times in 3D7 and in strains over-expressing *PftopoIII*$^{(\Delta 259-337)}$*-GFP* and *PfTOPOIII-GFP*.

Western blotting

Parasite proteins were extracted from the ring, trophozoite, and schizont stages of the parasite and were loaded on SDS polyacrylamide gels. A polyvinylidene difluoride (PVDF) membrane was used for transfer, as described previously [28]. The primary antibodies used were mouse antihAct1 antibody (Abcam) and rabbit antiPfTopoIII antibody (KR Instruments and Chemicals) at 1 : 5000 dilutions. For subcellular fractionation, we used rabbit antiHistone H3 antibody (Imperial Life Sciences) and mouse antiCytochrome C antibody (Allied Scientific) at 1 : 5000 and 1 : 3000 dilutions, respectively. For secondary antibodies, horseradish peroxide-conjugated antirabbit antibody (Promega) and antimouse antibody (Santa Cruz Biotechnology Inc. CA, U.S.A.) were used at 1 : 10 000 dilution. To check the expression of the PfTopoIII in the yeast surrogate system, proteins were isolated from the SBY3, SBY4, and SBY5 strains. The primary antibody against antiScActin (Abcam) was used at a concentration of 1 : 10 000 dilutions. The western blots were developed using a chemiluminescent detection system (Pierce). Every experiment was repeated at least three times and band intensities were

quantified using Image J software. Mean relative densities were plotted using GraphPad prism. To detect the transgenic parasite, we used rabbit anti-GFP antibody (Allied Scientific Products) at 1 : 5000 dilutions. To further study the effects of HU on protein levels of PfTopoIII, western blotting analyses were performed on 20 ml *Plasmodium* cultures. The culture was divided equally into two groups: samples treated with 10 mM HU and kept for 20 h at 37°C and an untreated group. After 20 h, parasitized erythrocytes specific to the late-schizont stage were harvested, treated with 0.15% saponin, and washed three times with 1× PBS; then protein was isolated by using standard procedures.

Results

A unique charged domain in PfTopoIII

The *P. falciparum* genome database (http://www.plasmoDB.org) shows the presence of a putative PfTopoIII (Gene ID: PF3D7_1347100) gene. It has no intron and it is predicted to code a 710 aa protein. Multiple sequence alignment of PfTopoIII showed significant homology in the catalytic TOPRIM domain (aa 5 to 150) across various TopoIII sequences (Figure 1) with two conserved aspartates at positions 118 and 120 and one conserved glutamate at position 122 (red box in the figure). The catalytic tyrosine residue of the enzyme is located at position 421 (blue star) within a highly conserved GYISYPRTET sequence (green box). PfTopoIII lacks a stretch of 30 aa residues at the N-terminal end and an extended 362 aa at the C-terminal domain that are present in human and mouse TopoIIIα. These extended N-terminal and C-terminal regions are also absent from ScTopoIII. However, there is a unique charged aa containing region spanning residues 253 to 336, which is absent from other eukaryotic TopoIII. It showed 75% sequence identity with *Plasmodium berghei* TopoIII and 35–39% sequence identity with other orthologs of TopoIII (Supplementary Table S1). The UniProt IDs for TopoIII orthologs are presented in Supplementary Table S2.

TopoIII protein sequences obtained from both eukaryotic and prokaryotic organisms were aligned using ClustalW (see Methods). In our phylogenetic analyses, prokaryotic and eukaryotic sequences formed two distinct branches from the root. The TopoIII sequence from *P. falciparum* was close to ScTopoIII and human TopoIIIα (Supplementary Figure S1A), while the TopoIII sequences from *E. coli*, *V. cholerae*, *V. nereis*, *E. lignolyticus* and *S. enterica* were clustered together. *PfTOPOIII* with 2133 base pairs was PCR amplified using 3D7 *P. falciparum* genomic DNA as a template (Supplementary Figure S1B) and was subsequently cloned into pET28a bacterial expression vector and was sequenced.

PfTopoIII expression is tightly linked with the replication of the parasite

We isolated RNA from various synchronized asexual stages of the parasite (ring, trophozoite, and schizont) and performed semi-quantitative RT-PCR and real-time RT-PCR. Our semi-quantitative results indicated that *PfTOPOIII* transcript is expressed in the schizont stage of the parasite (Figure 2A). Aspartate-rich protein (ARP), which is constitutively expressed at all stages of the parasite, was used as a loading control. Real-time RT-PCR analyses showed that the schizont stage of the parasite expressed more than 30-fold greater *PfTOPOIII* transcript compared with the ring and trophozoite stages, indicating its direct role during the replication of the parasite (Figure 2B).

To investigate the expression of PfTopoIII at the protein level, we raised antibody against the enzyme. *PfTOPOIII* was cloned in a bacterial expression vector using histidine tag. However, it could not be expressed under various conditions. Hence, we designed a peptide spanning residues 281–300 of PfTopoIII (DSNNYSDETDDYYGDEKK) and raised antibodies against the peptide. Immune sera analyses showed a specific band near 75 kDa (Figure 2C, right blot), which was absent when probed with pre-immune sera (Figure 2C, left blot). Using this specific antibody, we performed western blotting to investigate the stage-specific expression of the protein. We found that PfTopoIII is expressed specifically in the schizont stage (Figure 2D). Actin was used as a loading control. Thus, the expression profiles at the transcript level and protein level corroborated each other.

Subcellular localization of PfTopoIII

To examine the localization of PfTopoIII in the parasite, the distribution of endogenous PfTopoIII was studied by subcellular fractionation as well as by fluorescence microscopy. We conducted three independent subcellular fractionations of the parasite culture, and one representative image is presented in Figure 3A. We found that PfTopoIII was present both in the nuclear as well as in the organelle fraction. Histone H3 and cytochrome C

PORTLAND PRESS

Biochemical Journal (2020) **477** 4745–4767
https://doi.org/10.1042/BCJ20200318

Figure 1. Sequence analysis results shows the identification of a unique charged domain in PfTopoIII.

Multiple sequence alignment of PfTopoIII (*P. falciparum*), PbTopoIII (*Plasmodium berghei*), HsTopoIIIα (*Homo sapiens*), MmTopoIIIα (*Mus musculus*) and ScTopoIII (*Saccharomyces cerevisiae*) shows the presence of two conserved aspartate residues and one glutamate residue in the toprim domain (red box). Moreover, one conserved tyrosine residue (represented by a blue star) is present in the catalytic domain (green box).

were used as nuclear and mitochondrial protein markers, respectively. We generated a transgenic parasite line expressing PfTopoIII-GFP. Western blotting analyses of synchronous parasites in the schizont stage confirmed the expression of PfTopoIII-GFP (Figure 3B) in the parasite. The localization of the GFP-tagged protein was studied by live-cell imaging using a fluorescence microscope (Carl Zeiss). We found that PfTopoIII-GFP showed distinct nuclear foci and was co-localized with DAPI (Figure 3C). PfTopoIII-GFP was also co-localized with MitoTracker dyes (Figure 3D). These results correlate with the subcellular fractionation analyses and confirm its presence in both the nucleus and mitochondria of the parasite.

PfTopoIII interacts with the mitochondrial genome

To determine whether PfTopoIII is associated with mtDNA, we conducted mtDNA immunoprecipitation (mtDNA-IP) assays on four synchronized developmental stages of the parasite, namely, the ring (R), trophozoite (T), early schizont (ES), and late schizont (LS) stages. We designed six sets of primers (A–F) in such a way that PCR amplification of immune-precipitated samples with each set of primers gave rise to fragments of similar length (1 kb). The position of each primer set is presented in Figure 4A and their sequences are listed

Biochemical Journal (2020) 477 4745–4767
https://doi.org/10.1042/BCJ20200318

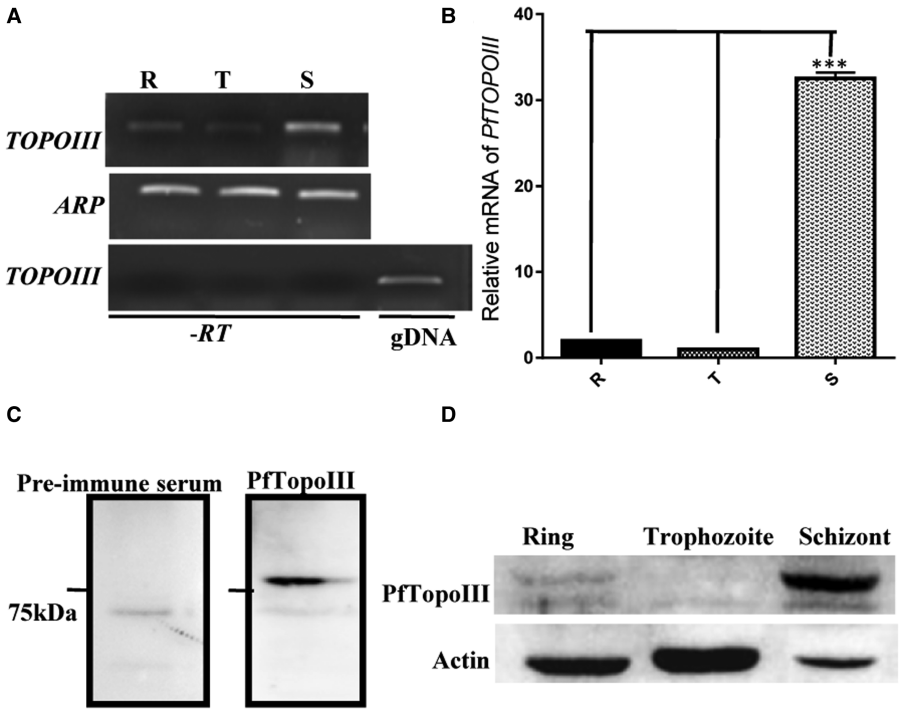

Figure 2. PfTopoIII expression is tightly linked with the replication of the parasite.

(**A**) RT-PCR analysis with RNA isolated from the rings (R), trophozoites (T) and schizonts (S) stages. PCR amplification was done using *PfTOPOIII* and *ARP* (Aspartate rich protein) specific primers which amplify 254 bp and 300 bp specific to the 3′ end of the transcript, respectively. The bottom panel shows the lack of a *PfTOPOIII* band in the absence of reverse transcriptase (–RT). Genomic DNA (gDNA) served as a positive control. (**B**) Real-time RT-PCR shows the relative abundance of *PfTOPOIII* at various stages of the parasites. Error bars indicate mean ± SD; $n = 3$; $P = 0.0003$. (**C**) Western blotting analyses of parasite cell extracts with pre-immune serum (left blot) and with an antibody raised against PfTopoIII (right blot). The molecular weight marker is indicated on the left. (**D**) Stage dependent expression of *PfTopoIII* in *P. falciparum* lysate has been shown: R, middle rings; T, early/mid trophozoite; S, mid/late schizont. Actin served as a loading control.

in Supplementary Table S3. Considering that, in *P. falciparum*, linear mtDNA of 6 kb unit length forms multimers in a head-to-tail fashion [26], the primer sets corresponding to A–E were used to amplify the internal DNA sequence within each monomer of linear mtDNA. On the other hand, the primer set F was used to amplify the junctional sequence spanning two monomeric mtDNAs. We found that the relative occupancy of PfTopoIII to the F site of mtDNA was much higher compared with the other sites. In addition, PfTopoIII recruitment was negligible in the R, T and ES stages but enhanced in the LS stage (Figure 4B). Together, these results suggest that PfTopoIII might be involved in the segregation of mtDNA of the parasite in the late-schizont stage.

Molecular dynamic simulations indicate that the flexible charged domain of PfTopoIII stabilizes upon DNA binding

We modeled PfTopoIII using the I-TASSER server by selecting human TopoIIIα as a template (PDB ID: 4CGY) (Figure 5A). Domain analyses of PfTopoIII indicated the presence of an extra charged region within domain II that was disordered and away from the DNA binding region. The stability of the structure was evaluated via MDS for 50 ns. During the simulations, the PfTopoIII structure was stable but the charged region showed large fluctuations (data not shown). In a 50 ns apo-PfTopoIII simulation, the charged domain remained away from the DNA binding region (Supplementary Figure S2).

To understand whether the charged domain had any role in DNA binding, we compared it to the structure of *E. coli* TopoIII, which has a charged loop similar to that of PfTopoIII [17]. To that end, the structure of *E.*

Biochemical Journal (2020) **477** 4745–4767
https://doi.org/10.1042/BCJ20200318

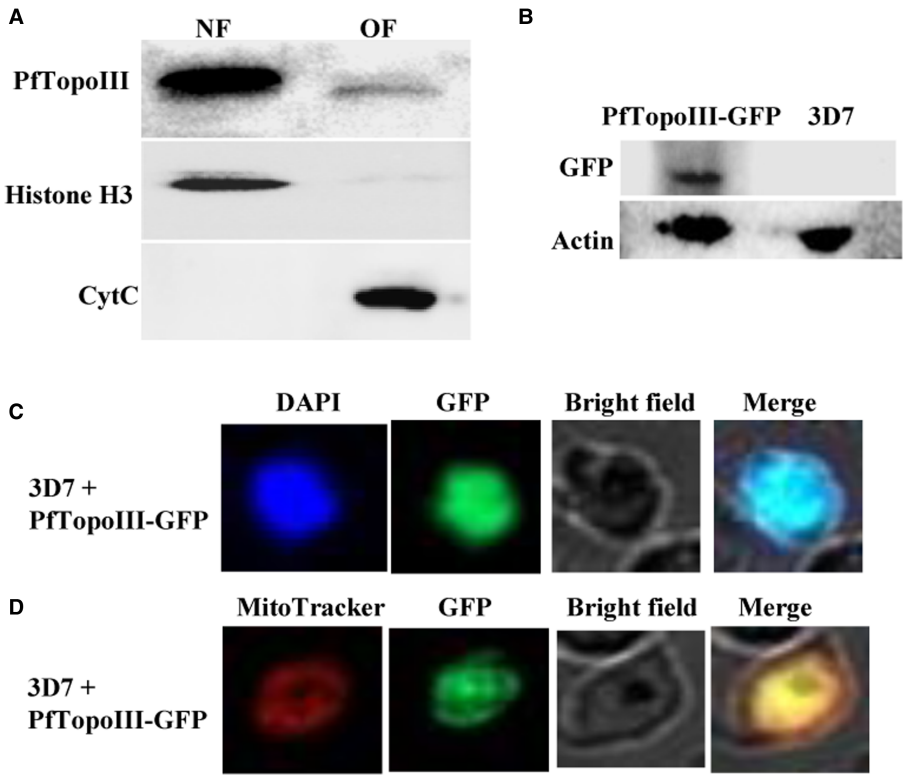

Figure 3. Subcellular localization of PfTopoIII.

(**A**) Western blotting analyses of the nuclear (NF) and organelle fractions (OF) of 3D7 parasite infected RBC were done using anti-PfTopoIII antibody. Histone H3 and Cytochrome C were used as the nuclear and mitochondrial markers, respectively. (**B**) Western blotting analyses of the total protein extracted from 3D7 and a transgenic parasite strain harboring PfTopoIII-GFP expression vector were performed using anti-GFP antibody. Actin served as a loading control. (**C** and **D**) Fluorescence microscopy shows the expression of PfTopoIII-GFP at the late schizont stage. Parasite nucleus was stained with DAPI (blue) while parasite mitochondria were stained with MitoTracker Red (red).

coli TopoIII (PDB ID: 1I7D) with a single-stranded DNA octamer (5′-CGCAACTT 3′) was aligned to the PfTopoIII and the single-stranded DNA octamer was placed in the binding site to generate a structure of PfTopoIII bound with DNA. The holo structure of PfTopoIII was simulated for 100 ns using a similar procedure as mentioned above. RMSFs of the PfTopoIII-DNA complex were computed for the Cα atoms of complete protein to capture the dynamics of individual amino acids. From the RMSF plot, the maximum fluctuations were observed in parts of the charged domain, the Toprim domain, and domain III (Supplementary Figure S3A). Other fluctuations were also observed in the amino and carboxyl-terminal of the protein (Supplementary Figure S3A). In principal component analyses (PCA), used to identify the dominant motions during the simulations [45], both, PC1 and PC2 showed major fluctuations in the charged domain with similar direction, towards the bindings site of single-stranded DNA (Supplementary Figure S3B). PC1 also showed fluctuations in parts of Toprim and domain III, which are in the opposite direction, indicating the opening of a central hole of the PfTopoIII protein (Supplementary Figure S3B). From these observations, it can be inferred that there are two major conformational changes in the protein. First, domain III and Toprim domain open up to accommodate the oligonucleotide, and then the charged domain comes closer to and interacts with the oligonucleotide.

The distance between the centers of mass of domain III (residues 380–511) and parts of Toprim domain (residues 12–26 and 152–163) were computed to quantify the movement between these two domains (Figure 5B). The domains moved by a distance of 7 Å compared with the PfTopoIII modeled structure (Figure 5B).

In the RMSF and PCA analyses, the charged domain showed high flexibility during MDS. The conformations of the charged domain could largely be clustered into four bins, as can be seen in the free energy

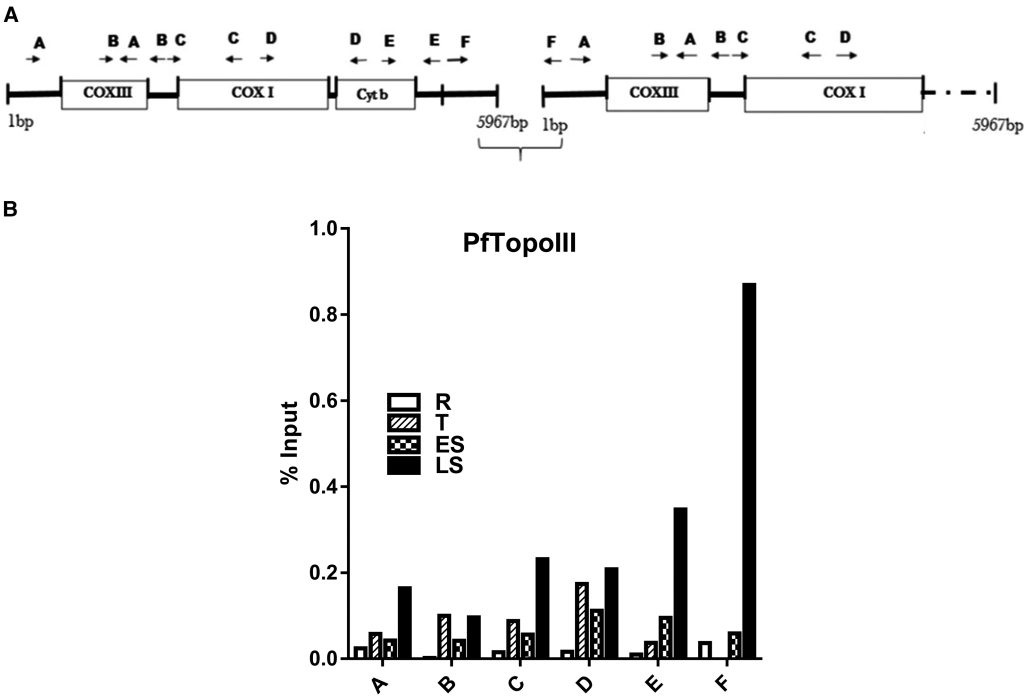

Figure 4. PfTopoIII interacts with mitochondrial genome.

(**A**) The 6-kb long mitochondrial DNA (mtDNA) of *P. falciparum* exists as a linear tandem array joining in a head to tail manner as shown. The map displays three different genes encoded by *Plasmodium* mitochondrial genome *COXIII*, *CYTb* and *COXI* and the position of different primer sets from A to F; each set of primers covers ∼1 kb length and together cover the whole mtDNA. (**B**) The graph displays the occupancy of PfTopoIII on mtDNA as % input on the Y-axis with respect to the different regions of the mitochondrial genome on the X-axis [A–F] covering the entire mtDNA.

landscape (FEL) plot (Figure 5C). During the start of the simulation, the charged domain interacted with parts of domain III, similar to the apo-structure simulation (Figure 5D, red). Around 34 ns, the domain adopted an open conformation to interact with the DNA octamer (Figure 5D, black). At ∼46 ns, residues D296, E297, K302, and K304 started interacting with the oligonucleotide (Figure 5D,E). During the latter part of the simulation, the charged domain was in a closed conformation. The charged and aromatic residues in the charged domain interacted with and stabilized the DNA octamer (Figure 5D,E). The residues from this domain (K302, K301, K299 and others) formed hydrogen bonds and stacked interactions with the nitrogenous bases of the DNA octamer (Figure 5E). These interactions helped to stabilize and place the DNA octamer in the cavity for further processing (Supplementary video S1 and S2). Thus, the MDS and the structural data established that the charged domain of PfTopoIII stabilizes the binding of single-stranded DNA.

PftopoIII$^{(\Delta 259–337)}$ shows a poor association with mtDNA

To determine the functional significance of the charged domain of PfTopoIII, we generated a transgenic parasite that expressed mutant PftopoIII-GFP with a deletion of 259–337 charged aa residues from PfTopoIII. We conducted immunoprecipitations of mtDNA from the synchronous schizont stage of the parasite harboring the mutant PftopoIII$^{(\Delta 259–337)}$-GFP protein and that harboring the wild-type PfTopoIII-GFP protein. The experiment were repeated twice; the recruitment of mutant PftopoIII$^{(\Delta 259–337)}$ towards E and F regions of mtDNA were measured and compared with that with the wild-type PfTopoIII (Figure 6A). The mutant PftopoIII$^{(\Delta 259–337)}$ protein showed a significantly decreased association with the mtDNA compared with the wild-type protein. Western blotting analyses confirmed the expression of mutant PftopoIII$^{(\Delta 259–337)}$-GFP protein in the parasite (Figure 6B). To rule out the possibility that the decreased association was due to defective mitochondrial trafficking of the mutant PftopoIII, we performed live cell imaging of the mutant parasite-infected cells and

Biochemical Journal (2020) **477** 4745–4767
https://doi.org/10.1042/BCJ20200318

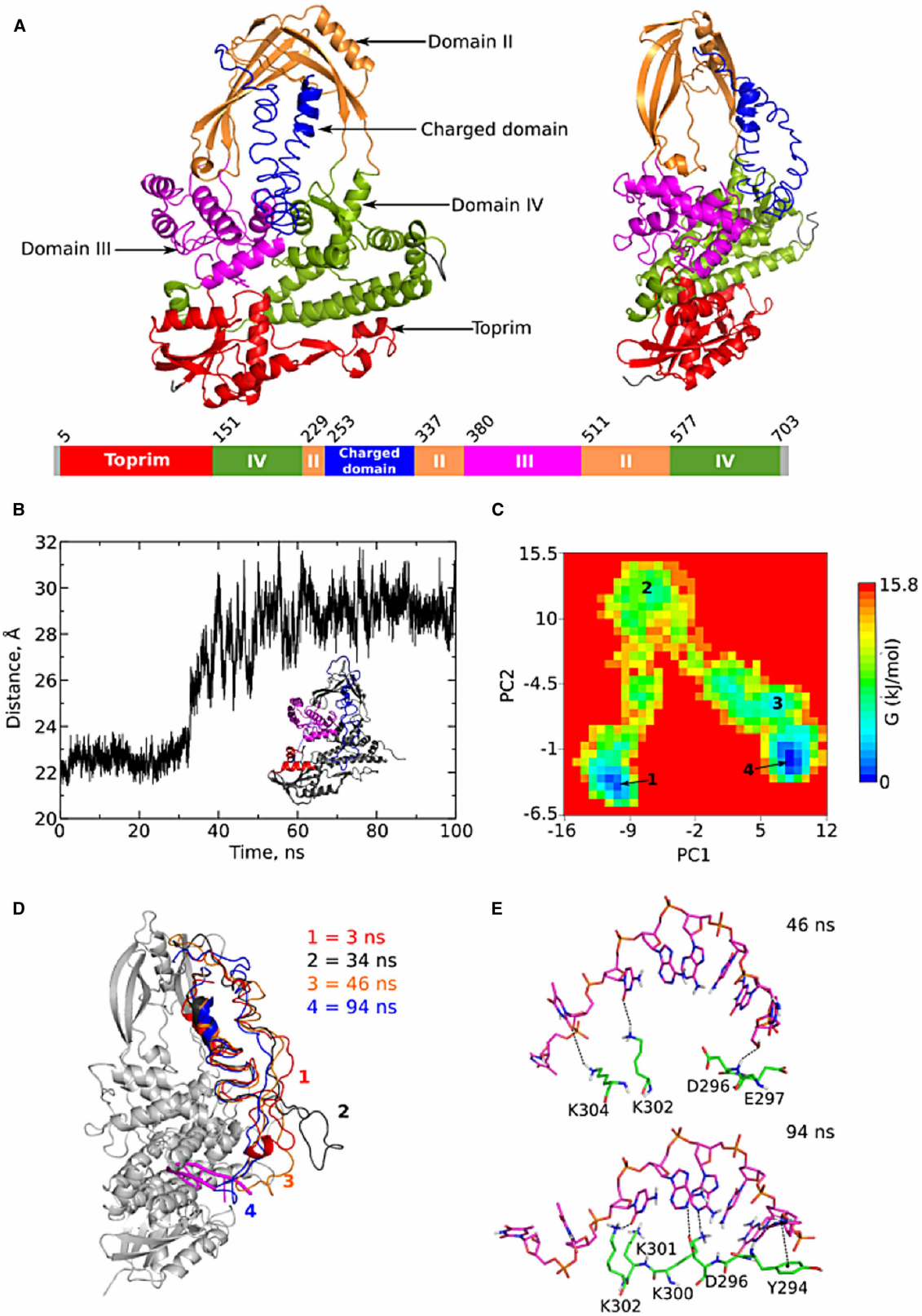

Figure 5. Molecular dynamic simulations indicate that the charged domain of PfTopoIII remains flexible and stabilizes upon DNA binding.

Part 1 of 2

(**A**) Structure of PfTopoIII modeled using the I-TASSER. The toprim domain and domain III are colored in red and magenta,

Figure 5. Molecular dynamic simulations indicate that the charged domain of PfTopoIII remains flexible and stabilizes upon DNA binding. Part 2 of 2

respectively. The domains II and IV are colored in orange and green, respectively. The charged domain which is a part of domain II is shown in blue. (**B**) Graph showing the distance between the centers of mass of parts of toprim (residues 12–26 and 152–163 shown in red) and domain III (residues 380–511 shown in magenta) during the simulation of PfTopoIII holo structure. (**C**) Free energy landscape (FEL) with respect to principal components 1 and 2. (**D**) Major conformations of charged domain (residues 251–337) sampled during 100 ns simulation obtained from FEL have been shown in red, black, orange and blue color, respectively. E. Interactions of charged domain (green) with the DNA octamer (magenta) have been shown.

observed that the mutant protein was co-localized with DAPI as well as with MitoTracker, like that of the wild-type protein (Figure 6C,D).

PfTOPOIII complements the function of *ScTOPOIII* but *Pf(Δ259–337)topoIII* does not

To decipher the *in vivo* role of PfTopoIII, we used *S. cerevisiae* as a surrogate model system. To determine whether full-length PfTopoIII can reverse the slow-growth phenotype of *ΔtopoIII* yeast strain, we deleted *TOPOIII* from the *S. cerevisiae* genome and transformed *ScTOPOIII* expressing vector (*pTA-ScTOPOIII*) into the knock-out strain. This strain served as a positive control in our study. We cloned *PfTOPOIII* in yeast expression vector (*pTA-PfTOPOIII*) and transformed it into *ΔtopoIII* to generate an isogenic strain. We grew each strain in fresh liquid media from overnight culture and monitored their growth for 15 h at regular intervals. We found that full-length PfTopoIII fully rescued the slow-growth phenotype of the *ΔtopoIII* strain to the same extent as that of ScTopoIII (Figure 7A). To confirm that the growth recovery was not due to any compensatory mechanism, we created an isogenic strain where the putative active tyrosine of PfTopoIII (at the 421st position) was mutated to phenylalanine. The mutant was unable to suppress the slow-growth phenotype of *ΔtopoIII* strain, confirming the role of this active tyrosine inside this yeast strain (Figure 7A). To rule out the possibility that loss of complementation is not due to loss of expression of PftopoIII^{Y421F}, we checked the expression of wild-type *PfTOPOIII* and *PftopoIIIY421F* both at the RNA level (Figure 7B) and at the protein level (Figure 7C). Both proteins were stably maintained in the *ΔtopoIII* strain.

Next, we investigated whether the charged domain present in PfTopoIII is essential for its function. To that end, we made a charged domain deletion mutant of *PftopoIII* by deleting 259–337 aa and transformed *pTA-PftopoIII*$^{(\Delta 259-337)}$ into the *ΔtopoIII* strain to check whether it would show PfTopoIII-like activity. This mutant failed to rescue the slow-growth phenotype of the *ΔtopoIII* strain in liquid medium, suggesting that the charged domain was essential for functional complementation (Figure 7A). To rule out the possibility that loss of function of the mutant protein was due to the loss of expression of the mutant protein, we studied the mRNA expression of *pTA-PftopoIII*$^{(\Delta 259-337)}$; it was detected at the same level as that of other test strains (Figure 7B). However, we could not check its expression at the protein level as the peptide antibody was raised against the charged region of PfTopoIII. This experiment emphasizes the importance of the charged region in PfTopoIII function.

PfTopoIII interacts with PfBlm and PfWrn

We have a used yeast two-hybrid assay to monitor the interaction between PfTopoIII and the RecQ helicases of *Plasmodium*. We subcloned *PfTOPOIII* in bait vector as a fusion to the Gal4 DNA binding domain and *PfBLM*/*PfWRN* individually to the prey vector as a fusion to the Gal4 activation domain (Figure 8A). The recombinant bait and prey vectors were transformed in PJ69-4A and the interaction between PfTopoIII and RecQ helicases were scored by monitoring both *HIS3* and *ADE2* reporter gene activity. We found that PfTopoIII, PfBlm, and PfWrn individually did not self-activate the reporter gene activity, as they failed to grow in medium lacking histidine (Figure 8B, rows 2–4). However, PfTopoIII interacted with PfBlm as well as with PfWrn as they grew in such medium (Figure 8B, rows 5 and 6). No growth was observed in adenine dropout medium indicating that their interaction was not strong enough to induce the expression of sufficient adenine (data not shown). We also addressed whether the presence of the charged domain in PfTopoIII is essential for mediating the interaction with RecQ helicases. We found that the mutant PftopoIII$^{(\Delta 259-337)}$ interacted with both PfBlm and PfWrn with the same efficiency as that of the full-length protein (Figure 8B, rows 8 and 9), indicating that the charged domain is dispensable for the interaction with RecQ helicases. Next, we checked

Biochemical Journal (2020) **477** 4745–4767
https://doi.org/10.1042/BCJ20200318

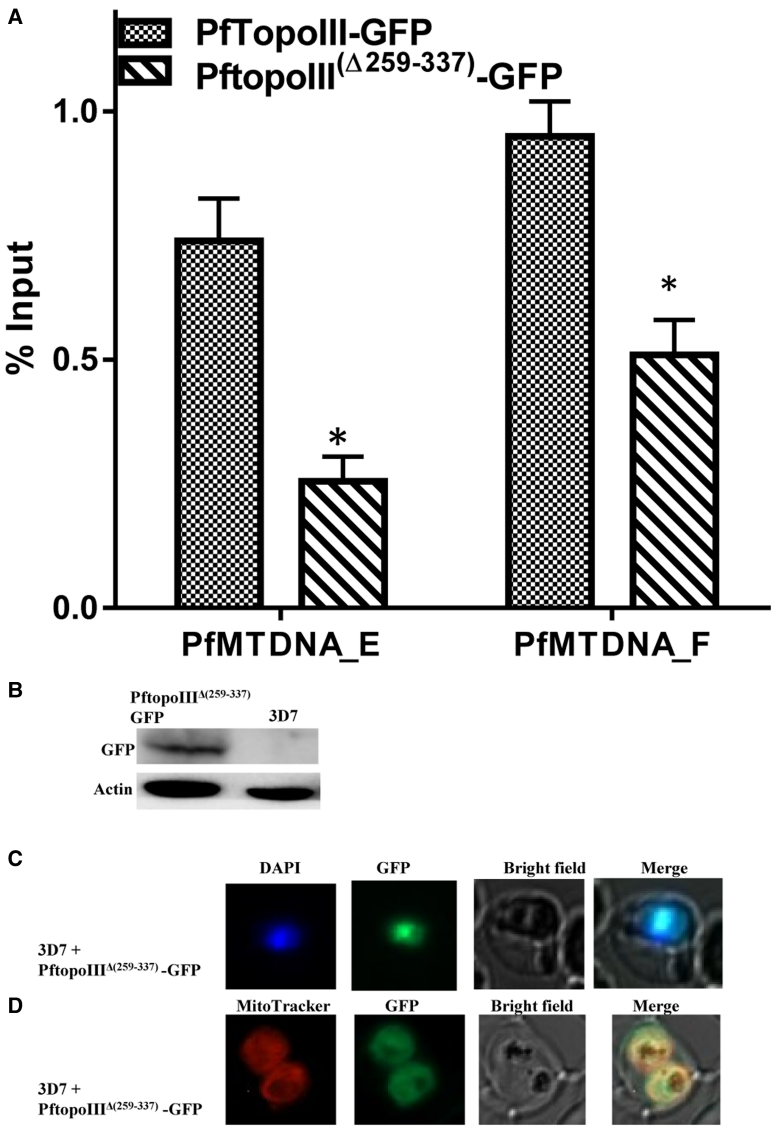

Figure 6. PftopoIII$^{(\Delta 259–337)}$ shows poor association with mtDNA.

(**A**) The mtChIP analyses show the recruitment of PfTopoIII-GFP in comparison with PftopoIII$^{(\Delta 259–337)}$-GFP to two different loci (E and F) of the mitochondrial genome. Error bars indicate mean ± SD; $n = 2$; * $P < 0.05$. (**B**) Immunoblot shows the expression of mutant PftopoIII$^{(\Delta 259–337)}$-GFP protein in the transgenic parasite line. (**C** and **D**) Fluorescence microscopic images show the localization of PftopoIII$^{(\Delta 259–337)}$-GFP. Parasite nucleus was stained with DAPI (blue) and parasite mitochondria were stained with MitoTracker Red (red).

whether *PfBLM* and *PfWRN* were expressed in the schizont stage of the parasite along with *PfTopoIII*. Semi-quantitative RTPCR indicated that both RecQ helicases were abundantly expressed along with *PfTOPOIII* at the asexual replicative stage of the parasite (Figure 8C).

Replication block-induced sensitivity in *ΔtopoIII* is rescued by ectopic expression of full-length PfTopoIII but not by the charged domain mutant protein

MMS modifies the DNA by adding methyl groups and the methylated DNA subsequently physically blocks replication forks [46]. It has been earlier reported that TopoIII along with Sgs1 can eliminate the obstacle

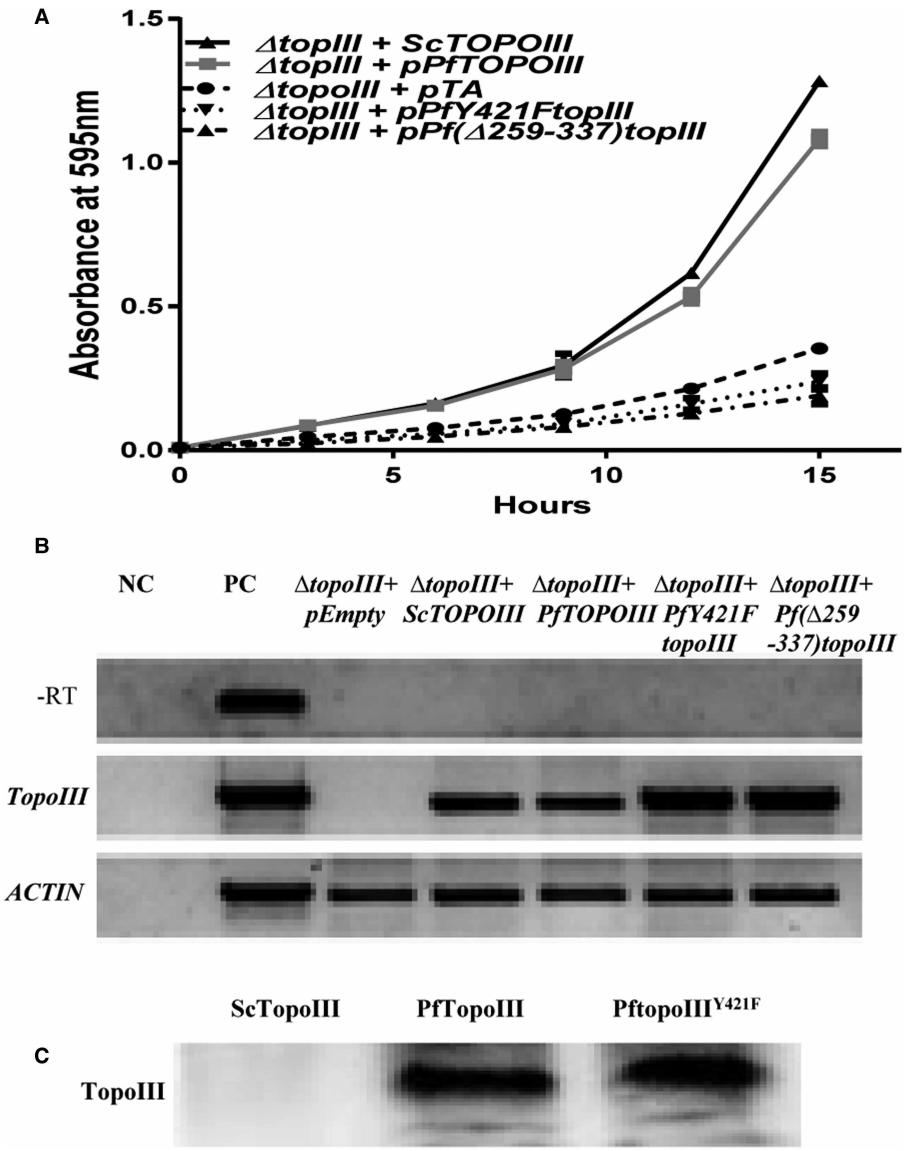

Figure 7. *PfTOPOIII* can complement the function of *ScTOPOIII*, but *Pf(Δ259–337)topoIII* cannot.

(**A**) *S. cerevisiae Δtopo*III strain was individually transformed with empty vector, vector expressing *ScTOPOIII*, *PfTOPOIII*, *PfY421FtopoIII* and *Pf(Δ259–337)topoIII*. Growth rate of all the strains were measured in liquid synthetic medium lacking tryptophan and the OD_{595} was plotted against time. The results shown represent the mean of three independent experiments. (**B**) The expression of *TOPOIII* from the above mentioned strains was monitored using gene specific primers; Actin served as positive control. NC denotes negative control, i.e. *ScTOPOIII* PCR amplification without genomic DNA and PC denotes positive control i.e. *ScTOPOIII* PCR amplification with genomic DNA as a template. (**C**) Total protein was isolated from the strains as indicated at the top and probed with PfTopoIII specific antibody.

during replication fork progression and that deletion of *TOPOIII* causes MMS sensitivity in a dose-dependent manner [47]. We assessed whether PfTopoIII could suppress the cytotoxic effects of DNA alkylating agent in a yeast model system. To that end, we exposed the test strains to different concentrations of MMS (0.01% and 0.04%) for 2 h, and then returned them to normal media. The percent survivability of each strain at each concentration of MMS is plotted in Figure 9. Full-length PfTopoIII completely rescued the MMS sensitivity of the *ΔtopoIII* strain to the same as that of ScTopoIII, whereas $PftopoIII^{Y421F}$ and $PftopoIII^{(\Delta 259-337)}$ did not. Hence the Y421 residue of the catalytic domain and the charged aa-rich region of PfTopoIII are indispensable for its function.

Biochemical Journal (2020) **477** 4745–4767
https://doi.org/10.1042/BCJ20200318

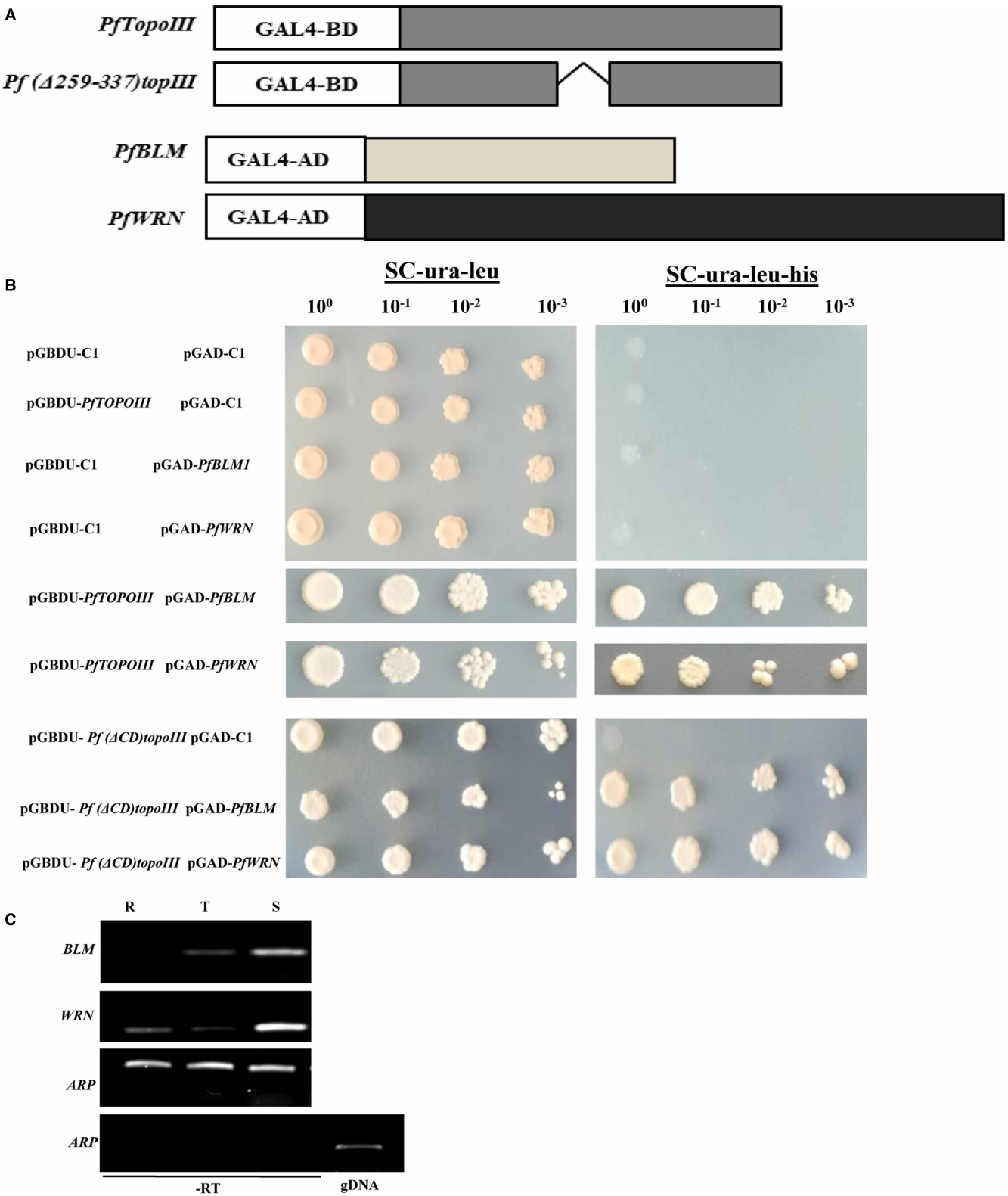

Figure 8. PfTopoIII interacts with PfBlm and PfWrn. Part 1 of 2

(**A**) The schematic representation showing that full length PfTopoIII and PftopoIII$^{(\Delta 259–337)}$ were fused to the Gal4 DNA binding domain generating chimeric constructs in *pGBDUC1* bait vector. Similarly, PfBlm and PfWrn were fused to Gal4 activation domain to generate chimeric constructs in *pGADC1* prey vector. (**B**) Yeast two-hybrid assays were performed in PJ69-4A strain using *HIS3* as a reporter gene. The left panel represents the

Figure 8. PfTopoIII interacts with PfBlm and PfWrn. Part 2 of 2

spotting of equal number of cells with serial dilution in the medium lacking leucine and uracil while the right panel scores the interaction between respective pairs. (**C**) Semi quantitative RT-PCR shows the expression of *PfBLM* and *PfWRN* at the ring (R), trophozoite (T) and schizont (S) stage of the parasite. Aspartate-Rich Protein (ARP) was used as a loading control. PCR without reverse transcriptase (–RT) does not show any amplification except for the positive control i.e. genomic DNA (gDNA).

Replication stress-induced expression of *PfTOPOIII*

HU inhibits ribonucleotide reductase, an enzyme that is required for the generation of deoxyribonucleotide triphosphates during the S-phase of the cell cycle. We studied the effects of prolonged HU-mediated replication stress on malaria parasites. We used synchronized 2% trophozoite-stage parasites exposed to 2.5 mM HU to induce replication stress, as established in a previous study [48]. The growth of the parasites was measured in 10 h time intervals (post HU treatment) and compared with that of untreated parasites. The experiment was repeated three times and the survivability at each time point was plotted (Figure 10A). We found a three-fold increase in parasitemia in untreated parasites at the end of the 30th hour, however, the HU-treated parasites showed severe sensitivity and their survivability was significantly reduced in a time-dependent manner. We also studied the morphology and development in each group at three different time intervals (Supplementary Figure S4). Untreated parasites mostly form mature schizonts (segmenters) at the end of 20th hour eventually ruptured and produced rings at the end of the 30th hour, which caused an increase in parasitemia (Supplementary Figure S4). However, HU treatment caused an arrest in the development of the parasite; mature schizonts could not develop and eventually died. Next, we studied the effects of short-term exposure to HU on parasite survivability. We used synchronized 1% trophozoite-stage parasites and exposed them to 2.5 mM HU for 6 h. Subsequently, HU was extensively washed and the parasites were returned to normal media and allowed to grow for 26 h. We found a 5-fold increase in parasitemia in untreated parasites (Figure 10B). However, treated parasites did not show a decrease in survivability; rather their growth was arrested and they remained at the same developmental stage as that at which they started (Figure 10B). It was reported that *ΔtopoIII* condition in *Saccharomyces cerevisiae* displays severe sensitivity towards HU [47], which indicates that TopoIII plays an important role in resolving the aberrant structure generated from the arrest of the replication fork. To explore the direct role of PfTopoIII during replication stress, we evaluated the level of PfTopoIII after HU treatment. We exposed synchronous trophozoite-stage parasites to two different doses of HU (2.5 mM and 10 mM) for 6 h. Subsequently, HU was extensively washed, the parasites were returned to the normal media for 26 h and then extracted proteins both groups. We found that PfTopoIII was moderately induced in a dose-dependent manner upon HU treatment, supporting its direct role in mitigating replication stress (Figure 10C). We repeated the experiment twice and quantified the band intensity using Image J software. We found that there was a 3.5-fold induction in PfTopoIII expression in parasites treated with 10 mM

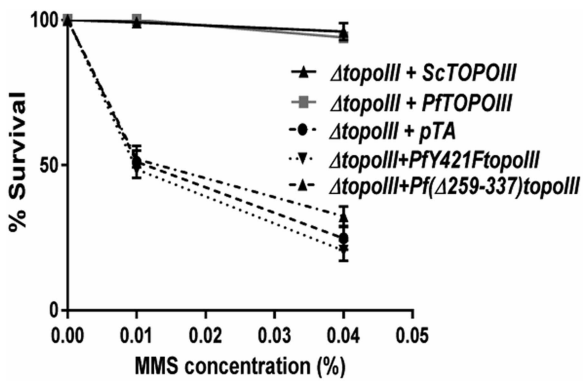

Figure 9. Replication block induced DNA damage sensitivity in *ΔtopoIII* yeast cells is rescued by expression of full length *PfTOPOIII* but not by the expression of mutant protein with deletion in its charged domain.

Isogenic strains, as indicated, were grown to early log phase and exposed to 0.01% MMS and 0.04% MMS treatment. The percent survival of each strain was determined. Error bars indicate mean ± SD; $n = 3$.

Biochemical Journal (2020) **477** 4745–4767
https://doi.org/10.1042/BCJ20200318

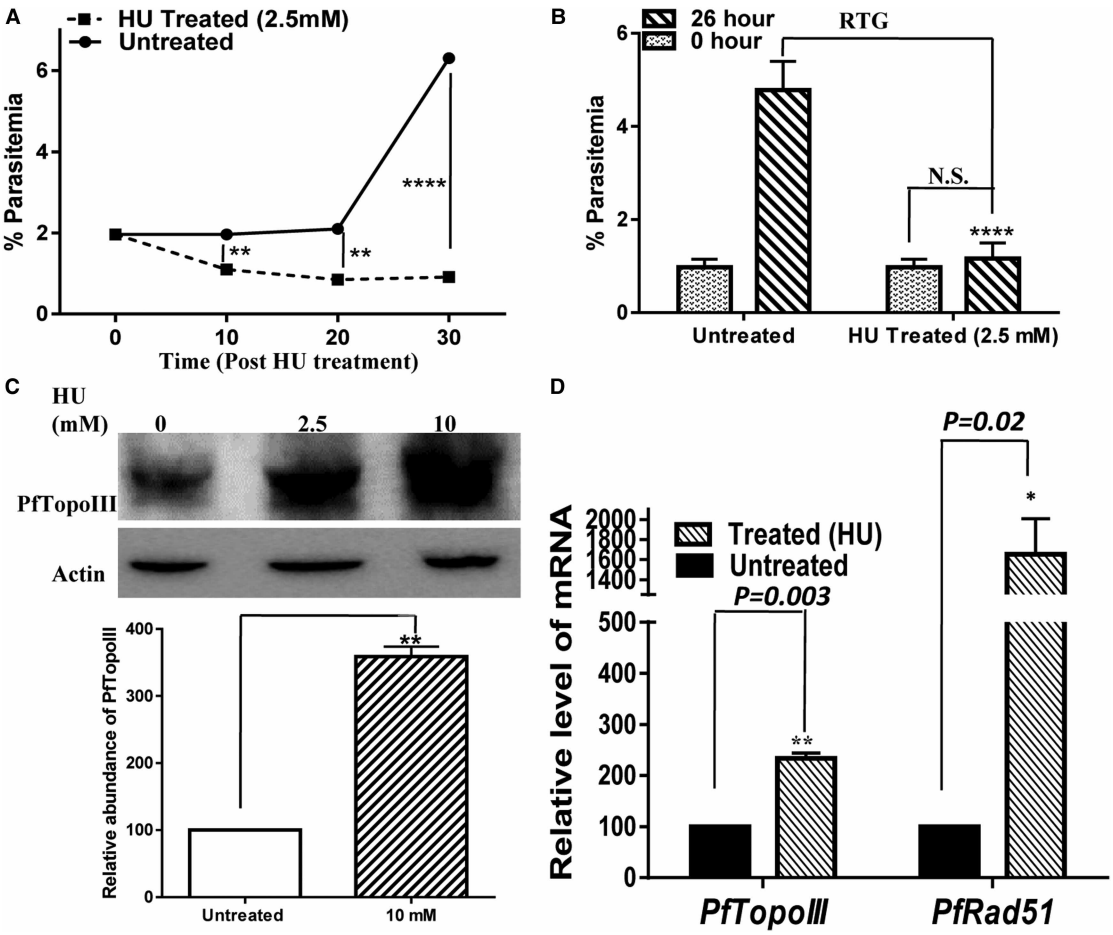

Figure 10. Replication stress induced expression of *PfTOPOIII*.

(**A**) Synchronous trophozoite stage specific 3D7 parasites were exposed to 2.5 mM HU for 30 h and parasitemia was measured for untreated and treated batch at every 10 h intervals. Error bars indicate mean ± SD; $n = 3$; **** $P < 0.0001$; ** $P < 0.01$. (**B**) Synchronous trophozoite stage specific 3D7 parasites were exposed to 2.5 mM HU for 6 h, after which HU was extensively washed out and the parasites were subsequently returned to grow (RTG) in normal media. The parasitemia was measured at the end of 26 h for the untreated and treated batch. Error bars indicate SD; $n = 3$; **** $P < 0.0001$; N.S. not significant. (*C*) Untreated and treated parasites (at 2.5 mM and 10 mM HU treatment) were processed in the same way as that described in (**B**) and were harvested. The total protein was extracted and probed with anti-PfTopoIII antibody. Actin served as a loading control. Quantification of Western blots from three independent experiments was done using Image J software. The band intensities in each lane were normalized against Actin and mean densities were plotted. Error bars indicate mean ± SD; $n = 3$; ** $P < 0.01$. (**D**) Synchronized trophozoite stage specific 3D7 parasites were treated with HU and the total RNA was extracted from untreated and treated parasites. Relative abundance of *PfTOPOIII* transcripts by real time RT-PCR revealed significant induction of *PfTOPOIII* upon HU treatment. *PfRad51* expression was measured as a positive control. The *P*-value was calculated as 0.003 and 0.02 for *PfTOPOIII* and *PfRAD51* induction respectively using the two-tailed Student's *t*-test.

HU (Figure 10C). To understand whether the increase in expression occurred due to the stabilization of proteins or at the transcript level, we extracted RNA from untreated and HU-treated parasites and quantified the *PfTOPOIII* cDNA by real-time RT-PCR. There was a 2.5-fold induction in the expression of *PfTOPOIII* upon HU treatment. Rad51 plays an essential role in replication fork stability and regression [49]. Rad51 expression was used as a positive control in our experiment (Figure 10D). The transcriptional induction of *PfTOPOIII* in response to HU treatment indicates that the increased level of endogenous PfTopoIII is required to promote recovery from replication stress. This finding reveals that PfTopoIII plays a key role in the response to replication stress in the parasite.

Biochemical Journal (2020) 477 4745–4767
https://doi.org/10.1042/BCJ20200318

PfTopoIII but not PftopoIII$^{(\Delta 259–337)}$ expression rescues the growth defect induced by replication stress

Because we found that PfTopoIII expression is induced in response to replication stress, probably to counteract the stress, we wanted to determine whether the ectopic expression of PfTopoIII, through a centromeric plasmid, would promote survival in HU-treated parasites. To this end, we compared the growth of three different strains of parasites: 3D7, 3D7 with PfTopoIII expression, and 3D7 with PftopoIII$^{(\Delta 259–337)}$ expression. In the first assay, we treated synchronous trophozoite-stage parasites with 2.5 mM HU continuously for 30 h and have measured parasitemia in intervals of 10 h. We repeated the experiment three times and observed that PfTopoIII expression considerably reduced dose-dependent death of the parasites at the 20th and 30th hours (Figure 11A). Interestingly, the transgenic parasites harboring PftopoIII$^{(\Delta 259–337)}$ expression plasmid did not show a reversed growth defect and behaved similar to that of the 3D7 parasites (Figure 11B). In the second assay, we exposed the parasites to 2.5 mM HU for 6 h, subsequently, it was extensively washed out and they were returned to normal growth media for 26 h. We found that the 3D7 parasites were severely affected even with 6 h treatment of HU and their growth remained arrested compared with the untreated parasites. The PfTopoIII transgenic parasite line showed fully rescued survivability and there was no significant difference between the survivability of treated versus untreated parasites (Figure 11C). However, the PftopoIII$^{(\Delta 259–337)}$ parasite line showed a similar trend as that of 3D7 parasites and displayed a significant difference in survivability compared with untreated parasites (Figure 11C). Hence, the charged domain of PfTopoIII is essential for *in vivo* function of the enzyme.

Discussion

This is the first study to identify functionally active TopoIII from a malaria parasite. We demonstrated that the spatiotemporal expression of PfTopoIII occurs in the nucleus and in the mitochondria during the actively replicating stage of the parasite. It is noteworthy that in humans, mice, and *Drosophila,* there is a mitochondrial localization signal at the amino terminal end of TopoIIIα [50] and a nuclear localization signal at the carboxyl terminal end [51]. Although *Plasmodium* TopoIII is devoid of any such signal sequences, our subcellular fractionation data, immunofluorescence data, and mitochondrial immunoprecipitation results collectively establish that PfTopoIII is a mitochondrial topoisomerase. This finding again reinforces the notion that the mechanism behind mitochondrial import is poorly understood in malaria parasites.

Human TopoIIIα is required for the maintenance of mtDNA, and TopoIIIα-depleted cells show a significant loss of monomeric mtDNA and form large catenated networks [23]. *Plasmodium* mitochondria undergo a rolling circle mode of replication to form a complex network of linear concatamers during active replication of the parasite [26]. Consistent with this notion, the specific association between PfTopoIII at the terminal end of mtDNA during the final stage of parasite replication indicates its likely involvement in the decatenation of the catenated mtDNA to aid in mtDNA segregation.

HU treatment depletes the cellular pool of deoxyribonucleotides and subsequently causes stalling of the replication fork [52]. Eventually, there occurs accumulation of joint DNA molecules in the direction opposite to the replication fork, and this results in the formation of so-called chicken foot structures [53] that have serious implications on cell survivability. As these structures resemble Holliday junctions [54], we speculate that if such a condition is generated in *P. falciparum*, PfTopoIII along with its cognate helicases might play an important role in resolving the structures and converting them back into the replication forks. Our study demonstrated the direct role of PfTopoIII in mitigating HU-mediated replication stress. First, PfTopoIII expression is induced in a dose-dependent manner in response to HU treatment. Second, expression of PfTopoIII can completely bypass the HU-induced growth defect in the parasites. It is noteworthy that the HU-mediated aberrant structure is resolved by the dual action of TopoIII and RecQ helicases. There are two members of the RecQ family of DNA helicases in *Plasmodium*, namely, PfBlm and PfWrn. The absence of either of these enhances the rate of formation of stalled replication forks, indicating that both the members are required for efficient *Plasmodium* DNA replication [55]. *E. coli* RecQ helicases interact with TopoIII and help resolve converging replication forks [56]. In humans, TopoIIIα can dissolve Holliday structures jointly with Blm but not with Wrn [57]. In this study, we found that PfTopoIII interacts with PfBlm and PfWrn with equal efficiency and that both helicases are expressed at the active replication stage of the parasite. However, it is necessary to investigate further whether both helicases mobilize a double Holliday junction and the resulting catenated DNA is resolved by PfTopoIII in malaria parasites.

Biochemical Journal (2020) **477** 4745–4767
https://doi.org/10.1042/BCJ20200318

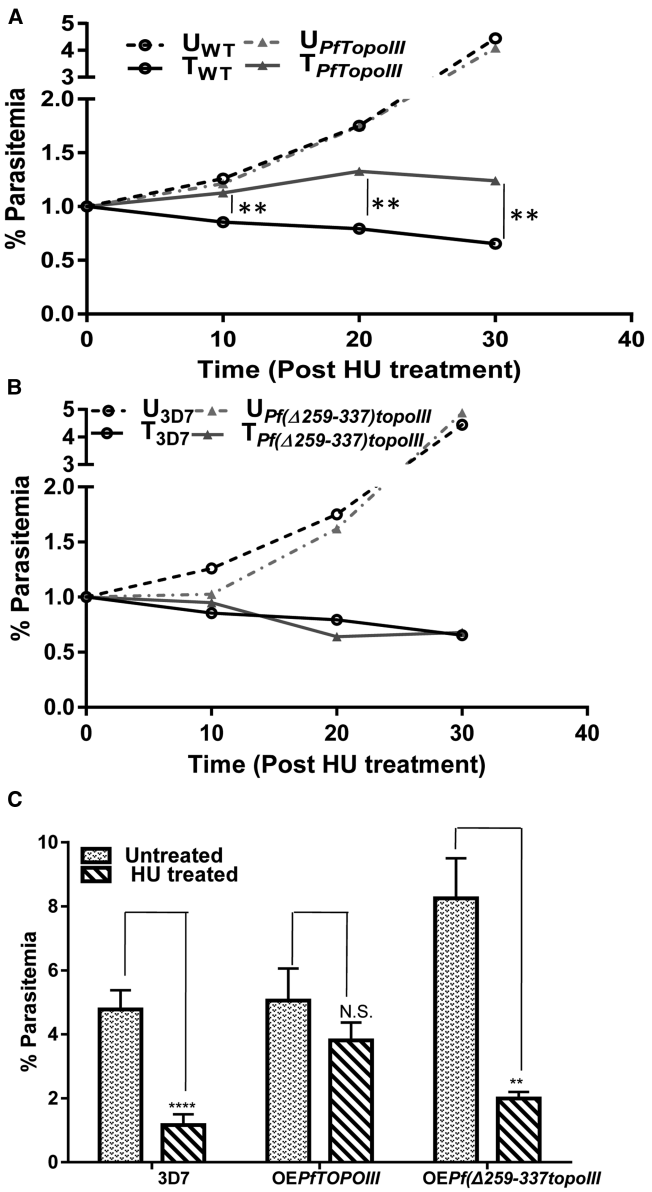

Figure 11. PfTopoIII but not PftopoIII$^{(\Delta 259–337)}$ expression reverses the replication stress induced growth defect.
(**A**) 3D7 and *PfTOPOIII* over-expressing parasites, synchronized at trophozoite stage, were treated with 2.5 mM HU for 30 h. The parasitemia of each treated and untreated strain was measured after 10 h, 20 h and 30 h time intervals. At each time point, approximately 2000 RBC were counted and the mean parasitemia was plotted. Error bars indicate mean ± SD; $n = 3$; ** $P < 0.01$. (**B**) A similar experiment was performed with 3D7 and *Pf (Δ259–337)topoIII* over-expressing strain with HU treatment for 30 h. More than three independent experiments were conducted and the mean parasitemia (%) was plotted. (**C**) 3D7, *PfTopoIII* over-expressing strain and *Pf(Δ259–337)topoIII* over-expressing strain were synchronized at the trophozoite stage and treated with 2.5 mM HU for 6 h. Afterwards, HU was extensively washed and treated parasite strains were subsequently grown in normal media for 26 h following which, parasitemia was measured. For each strain, minimum three batches of experiments were done and mean values of parasitemia for untreated and treated condition for each of the three strains were plotted. Error bars indicate SD; $n = 3$; **** $P < 0.0001$; ** $P < 0.01$; N.S. not significant.

Our study identified a charged domain within PfTopoIII that is indispensable for its *in vivo* function. MDS of PfTopoIII with DNA octamer showed that the enzyme undergoes a conformational change upon DNA binding. At the start of the DNA protein interaction, PfTopoIII-ssDNA adopts a closed conformation similar

to that of the apo enzyme (PfTopoIII alone). However, gradually a central cavity is created by the movement of domain III and the Toprim domain so that the DNA can be accommodated. This movement of domains is often referred to as protein-mediated gate dynamics [58] and has an important implication in their biochemical activities. The DNA octamer is stabilized by the hydrogen bonding and stacking interactions between bases and the positively charged residues present in the charged domain of PfTopoIII. Hence, it can be concluded that the charged domain stabilizes the effective binding of PfTopoIII with DNA and thus may play an important role in the catalytic mechanism of PfTopoIII protein. This is supported by our study, which reveals that the removal of the charged region, as in PftopoIII$^{(\Delta 259-337)}$ shows lesser association with mtDNA in the transgenic parasites. Our genetic study emphasized the essential requirement of this domain for PfTopoIII function. First, the expression of wild-type PfTopoIII fully rescued the slow-growth phenotype and MMS-induced toxicity in yeast, but the expression of mutant PftopoIII$^{(\Delta 259-337)}$ failed to do the same and mimicked the phenotype of the topoisomerase-inactive mutant PftopoIII^{Y421F}. We found that the loss of activity in the mutant PftopoIII$^{(\Delta 259-337)}$ strain was not due to poor heterologous expression of *Plasmodium* protein in *S. cerevisiae*. Although the expression of PftopoIII$^{(\Delta 259-337)}$ could not be demonstrated by western blotting analyses, the interaction between PftopoIII$^{(\Delta 259-337)}$ and PfBlm/PfWrn in yeast two-hybrid studies indirectly demonstrated the expression of the mutant protein in yeast. Second, the transgenic mutant parasite line (PftopoIII$^{(\Delta 259-337)}$-GFP) failed to rescue itself from short-term exposure to replication stress, like the transgenic parasite line PfTopoIII-GFP. Together, our results emphasize the importance of the charged domain in PfTopoIII function. Although this type of charged domain is absent from other eukaryotic TopoIII, a similar kind of multiple positively charged insertions, albeit shorter stretches have been observed in *E. coli* and many other prokaryotic TopoIII sequences [17]. A previous experimental study showed that the charged loop present in bacterial TopoIII is essential for decatenation of replication intermediates [17]. To date, no inhibitors of TopoIII have been identified. However, identification of the unique and indispensable charged domain of PfTopoIII qualifies itself as a target against malaria.

Competing Interests

The authors declare that there are no competing interests associated with the manuscript.

Funding

The work is supported by grants from the Department of Science and Engineering Research Board (DST-SERB), India [EMR/2017/001173].

Author Contributions

S.B. conceived the idea, designed the experiments, guided and wrote the paper. S.Ba., P.S., N.S. and H.C. have conducted all the experiments. N.B. has done all the computational work. A.R. and G.B. have planned and guided the computational work. A.R. has written a part of the paper related to computational study.

Acknowledgements

The work was supported by the Department of Science and Engineering Research Board (DST-SERB), India [EMR/2017/001173] to S.B. S.Ba. was supported by the Senior Research Fellowships from Council for Scientific and Industrial Research (CSIR), India. P.S. was supported by the Junior Research Fellowships from Council for Scientific and Industrial Research (CSIR), India. N.S. was supported by the Senior Research Fellowships from University Grants Commission (UGC). H.C. was supported by the MSc. thesis grant, Department of Biotechnology, India. We acknowledge UGC-SAP for funding the Department of Biotechnology and Bioinformatics, University of Hyderabad to procure Fluorescence microscope, which was used in the present study. We thank Professor Mrinal K Bhattacharyya for helpful discussions and for critical reading of the manuscript.

Abbreviations

ARP, Aspartate-rich protein; ES, early schizont; FEL, free energy landscape; HU, Hydroxyurea; LS, late schizont; MD, molecular dynamics; MMS, methyl methanesulfonate; PCA, principal component analyses; RBCs, red blood cells; RMSFs, root-mean-square fluctuations; RT, reverse transcription.

Biochemical Journal (2020) **477** 4745–4767
https://doi.org/10.1042/BCJ20200318

References

1 Rathod, P.K., McErlean, T. and Lee, P.C. (1997) Variations in frequencies of drug resistance in *Plasmodium falciparum*. *Proc. Natl Acad. Sci. U.S.A.* **94**, 9389–9393 https://doi.org/10.1073/pnas.94.17.9389

2 Ariey, F., Witkowski, B., Amaratunga, C., Beghain, J., Langlois, A.C., Kim, S. et al. (2014) A molecular marker of artemisinin-resistant *Plasmodium falciparum* malaria. *Nature* **505**, 50–55 https://doi.org/10.1038/nature12876

3 Miller, L.H., Ackerman, H.C., Su, X.Z. and Wellems, T.E. (2013) Malaria biology and disease pathogenesis: insights for new treatments. *Nat. Med.* **19**, 156–167 https://doi.org/10.1038/nm.3073

4 Widdowson, K. and Hennessy, A. (2010) Advances in structure-based drug design of novel bacterial topoisomerase inhibitors. *Future Med. Chem.* **2**, 1619–1622 https://doi.org/10.4155/fmc.10.250

5 Nitiss, J.L. (2009) Targeting DNA topoisomerase II in cancer chemotherapy. *Nat. Rev. Cancer* **9**, 338–350 https://doi.org/10.1038/nrc2607

6 Wang, J.C. (1996) DNA topoisomerases. *Annu. Rev. Biochem.* **65**, 635–692 https://doi.org/10.1146/annurev.bi.65.070196.003223

7 Mudeppa, D.G., Kumar, S., Kokkonda, S., White, J. and Rathod, P.K. (2015) Topoisomerase II from human malaria parasites. Expression, purification and selective inhibition. *J. Biol. Chem.* **290**, 20313–20324 https://doi.org/10.1074/jbc.M115.639039

8 Raghu Ram, E.S.V., Kumar, A., Biswas, S., Kumar, A., Chaubey, S., Siddiqi, M.I. et al. (2007) Nuclear gyrB encodes a functional subunit of the *Plasmodium falciparum* gyrase that is involved in apicoplast DNA replication. *Mol. Biochem Parasitol.* **154**, 30–39 https://doi.org/10.1016/j.molbiopara.2007.04.001

9 Dar, M.A., Sharma, A., Mondal, N. and Dhar, S.K. (2007) Molecular cloning of apicoplast-targeted *Plasmodium falciparum* DNA gyrase genes: unique intrinsic ATPase activity and ATP-independent dimerization of *Pf*GyrB subunit. *Eukaryot. Cell* **6**, 398–412 https://doi.org/10.1128/EC.00357-06

10 Gupta, A., Mehra, P., Deshmukh, A., Dar, A., Mitra, P., Roy, N. et al. (2009) Functional dissection of the catalytic carboxyl-terminal domain of origin recognition complex subunit 1 (*Pf*ORC1) of the human malaria parasite *Plasmodium falciparum*. *Eukaryot. Cell* **8**, 1341–1351 https://doi.org/10.1128/EC.00170-09

11 Chalapareddy, S.K., Chakrabarty, S., Bhattacharyya, M. and Bhattacharyya, S. (2016) Radicicol-mediated inhibition of topoisomerase VIB-VIA activity of the human malaria parasite *Plasmodium falciparum*. *mSphere* **1**, e00025-15 https://doi.org/10.1128/mSphere.00025-15

12 Chalapareddy, S.K., Bhattacharyya, M.K., Mishra, S. and Bhattacharyya, S. (2014) Radicicol confers mid-schizont arrest by inhibiting mitochondrial replication in *Plasmodium falciparum*. *Antimicrob. Agents Chemother.* **58**, 4341–4352 https://doi.org/10.1128/AAC.02519-13

13 Tosh, K., Chessman, S., Horrocks, P. and Kilbey, B. (1999) *Plasmodium falciparum*: stage related expression of topoisomerase I. *Exp. parasitol.* **91**, 126–132 https://doi.org/10.1006/expr.1998.4362

14 Stewart, L., Redinbo, M.R., Qiu, X., Hol, W.G.J. and Champoux, J.J. (1998) A model for the mechanism of human topoisomerase I. *Science* **279**, 1534–1541 https://doi.org/10.1126/science.279.5356.1534

15 Plank, J. and Hsieh, T.S. (2009) Helicase-appended topoisomerases: new insight into the mechanism of directional strand transfer. *J. Biol. Chem.* **284**, 30737–30741 https://doi.org/10.1074/jbc.R109.051268

16 Dean, F., Krasnow, M., Otter, R., Matzuk, M., Spengler, S. and Cozzarelli, N. (1983) *Escherichia coli* type-1 topoisomerases: identification, mechanism, and role in recombination. *Cold Spring Harb. Symp. Quant. Biol.* **49**, 769–777 https://doi.org/10.1101/SQB.1983.047.01.088

17 Zhiyu, L., Mondragón, A., Hiasa, H., Marians, K. and DiGate, R.J. (2002) Identification of a unique domain essential for *Escherichia coli* DNA topoisomerase III -catalysed decatenation of replication intermediates. *Mol. Microbiol.* **35**, 888–895 https://doi.org/10.1046/j.1365-2958.2000.01763.x

18 DiGate, R.J. and Marians, K.J. (1988) Identification of a potent decatenating enzyme from *Escherichia coli*. *J. Biol. Chem.* **263**, 13366–13373 PMID:2843517

19 Lee, C.M., Wang, G., Pertsinidis, A. and Marians, K.J. (2019) Topoisomerase III acts at the replication fork to remove precatenanes. *J. Bacteriol.* **201**, e00563-18 https://doi.org/10.1128/JB.00563-18

20 Wallis, J., Chrebet, G., Brodsky, G., Rolfe, M. and Rothstein, R. (1989) A hyper-recombination mutation in *S.cerevisiae* identifies a novel eukaryotic topoisomerase. *Cell* **58**, 409–419 https://doi.org/10.1016/0092-8674(89)90855-6

21 Hanai, R., Caron, P.R. and Wang, J.C. (1996) Human TOP3: A single-copy gene encoding DNA topoisomerase III. *Proc. Natl Acad. Sci. U.S.A.* **93**, 3653–3657 https://doi.org/10.1073/pnas.93.8.3653

22 Oakley, T.J. and Hickson, I.D. (2002) Defending genome integrity during S-phase: putative roles for RecQ helicases and topoisomerase III. *DNA Repair* **1**, 175–207 https://doi.org/10.1016/S1568-7864(02)00002-2

23 Nicholls, T.J., Nadalutti, C.A., Motori, E., Sommerville, E., Gorman, G., Basu, S. et al. (2018) Topoisomerase 3α is required for decatenation and segregation of human mtDNA. *Mol. Cell* **69**, 9–23.e6 https://doi.org/10.1016/j.molcel.2017.11.033

24 Preiser, P., Wilson, R., Moore, P., McCready, S., Hajibagheri, M., Blight, K. et al. (1996) Recombination associated with replication of malarial mitochondrial DNA. *EMBO J.* **15**, 684–693 https://doi.org/10.1002/j.1460-2075.1996.tb00401.x

25 Maleszka, R., Skelly, P.K. and Clark- walker, G.D. (1991) Rolling circle replication of DNA in yeast mitochondria. *EMBO J.* **10**, 3923–3929 https://doi.org/10.1002/j.1460-2075.1991.tb04962.x

26 Wilson, R.J. and Williamson, D.H. (1997) Extrachromosomal DNA in the apicomplexa. *Microbil. Mol. Biol. Rev.* **61**, 1–16 https://doi.org/10.1128/.61.1.1-16.1997

27 Mendes, T.A., Lobo, F.P., Rodrigues, T.S., Rodrigues-Luiz, G.F., da Rocha, W.D., Fujiwara, R.T. et al. (2013) Repeat-enriched proteins are related to host cell invasion and immune evasion in parasitic protozoa. *Mol. Biol. Evol.* **30**, 951–963 https://doi.org/10.1093/molbev/mst001

28 Laskar, S., Bhattacharyya, M., Shankar, R. and Bhattacharyya, S. (2011) HSP90 controls SIR2 mediated gene silencing. *PLoS ONE* **8**, e23406 https://doi.org/10.1371/journal.pone.0023406

29 Govindarajalu, G., Rizvi, Z., Kumar, D. and Sijwali, P.S. (2019) Lyse-reseal erythrocytes for transfection of *Plasmodium falciparum*. *Sci. Rep.* **9**, 19952 https://doi.org/10.1038/s41598-019-56513-9

30 Longtine, M.S., Mc kenzie, III, A., Demarini, D.J., Shah, N., Wach, A., Brachat, A. et al. (1998) Additional modules for versatile and economical PCR-based gene deletion and modification in *Saccharomyces cerevisiae*. *Yeast* **14**, 953–961 https://doi.org/10.1002/(SICI)1097-0061(199807)14:10<953::AID-YEA293>3.0.CO;2-U

31 Suhane, T., Bindumadhavan, V., Fangaria, N., Nair, A., Tabassum, W., Muley, P. et al. (2019) Glu-108 in *Saccharomyces cerevisiae* Rad51 is critical for DNA damage-induced nuclear function. *mSphere* **4**, e00082-19 https://doi.org/10.1128/mSphere.00082-19

32 Moll, K., Ljungstrom, I., Perlmann, H., Scherf, A. and Wahlgren, M. (2008) *Methods in Malaria Research*, Malaria Research and Reference Reagent Resource Center/ATCC, Manassas, VA
33 Yang, J. and Zhang, Y. (2015) Protein structure and function prediction using I-TASSER. *Curr. Protoc. Bioinformatics* **52**, 5–8 https://doi.org/10.1002/0471250953.bi0508s52
34 Bocquet, N., Bizard, A.H., Abdulrahman, W., Larsen, N.B., Faty, M., Cavadini, S. et al. (2014) Structural and mechanistic insight into Holliday-junction dissolution by topoisomerase IIIα and RMI1. *Nat. Struct. Mol. Biol.* **21**, 261–268 https://doi.org/10.1038/nsmb.2775
35 Hess, B., Kutzner, C., Spoel, D.V. and Lindahl, E. (2008) GROMACS 4: Algorithms for highly efficient, load-balanced, and scalable molecular simulation. *J. Chem. Theory Comput.* **4**, 435–447 https://doi.org/10.1021/ct700301q
36 Huang, J. and MacKerell, Jr, A.D. (2013) CHARMM36 all-atom additive protein force field: Validation based on comparison to NMR data. *J. Comput. Chem.* **34**, 2135–2145 https://doi.org/10.1002/jcc.23354
37 Jorgensen, W.L., Chandrasekhar, J., Madura, J.D., Impey, R.W. and Klein, M.L. (1983) Comparison of simple potential functions for simulating liquid water. *J. Chem. Phys.* **79**, 926–935 https://doi.org/10.1063/1.445869
38 Changela, A., DiGate, R.J. and Mondragon, A. (2001) Crystal structure of a complex of a type IA DNA topoisomerase with a single-stranded DNA molecule. *Nature* **441**, 1077–1081 https://doi.org/10.1038/35082615
39 Humphrey, W., Dalke, A. and Schulten, K. (1996) VMD: visual molecular dynamics. *J. Mol. Graph.* **14**, 33–38 https://doi.org/10.1016/0263-7855(96)00018-5
40 The UniProt Consortium. (2017) Uniprot: the universal protein knowledgebase. *Nucleic Acids Res.* **45**, D158–D169 https://doi.org/10.1093/nar/gkw1099
41 Aurrecoechea, C., Brestelli, J., Brunk, B.P., Dommer, J., Fischer, S., Gajria, B. et al. (2009) PlasmoDB: a functional genomic database for malaria parasites. *Nucleic Acids Res.* **37**, D539–D543 https://doi.org/10.1093/nar/gkn814
42 Thompson, J.D., Higgins, D.G. and Gibson, T.J. (1994) CLUSTAL w: improving the sensitivity of progressive multiple sequence alignment through sequence weighting, position-specific gap penalties and weight matrix choice. *Nucleic Acids Res.* **22**, 4673–4680 https://doi.org/10.1093/nar/22.22.4673
43 Price, M.N., Dehal, P.S. and Arkin, A.P. (2009) Fasttree: computing large minimum evolution trees with profiles instead of a distance matrix. *Mol. Biol. Evol.* **26**, 1641–1650 https://doi.org/10.1093/molbev/msp077
44 Kanehisa, M., Goto, S., Kawashima, S. and Nakaya, A. (2002) The KEGG databases at genomeNet. *Nucleic Acids Res.* **30**, 42–46 https://doi.org/10.1093/nar/30.1.42
45 Harte, W.E., Swaminathan, S., Mansuri, M.M., Martin, J.C., Rosenberg, I.E. and Beveridge, D.L. (1990) Domain communication in the dynamical structure of human immunodeficiency virus 1 protease. *Proc. Natl Acad. Sci. U.S.A.* **87**, 8864–8868 https://doi.org/10.1073/pnas.87.22.8864
46 Groth, P., Ausländer, S., Majumder, M.M., Schultz, N., Johansson, F., Petermann, E. et al. (2010) Methylated DNA causes a physical block to replication forks independently of damage signalling, O(6)-methylguanine or DNA single-strand breaks and results in DNA damage. *J. Biol. Chem.* **402**, 70–82 https://doi.org/10.1016/j.jmb.2010.07.010
47 Chakraverty, R.K., Kearsey, J.M., Oakley, T., Grenon, J., Ruiz, M., Lowndes, M.A.T. et al. (2001) Topoisomerase III acts upstream of Rad53p in the S-Phase DNA damage checkpoint. *Mol. Cell. Biol.* **21**, 7150–7162 https://doi.org/10.1128/MCB.21.21.7150-7162.2001
48 Mitra, P., Banu, K., Deshmukh, A.S., Subbarao, N. and Dhar, S.K. (2015) Functional dissection of proliferating-cell nuclear antigen (1 and 2) in human malarial parasite *Plasmodium falciparum*: possible involvement in DNA replication and DNA damage response. *Biochem. J.* **470**, 115–129 https://doi.org/10.1042/BJ20150452
49 Zellweger, R., Dalcher, D., Mutreja, K., Berti, M., Schmid, J.A., Herrador, R. et al. (2015) Rad51-mediated replication fork reversal is a global response to genotoxic treatments in human cells. *J. Cell Biol.* **208**, 563–579 https://doi.org/10.1083/jcb.201406099
50 Wang, Y., Lyu, Y.L. and Wang, J.C. (2002) Dual localization of human DNA topoisomerase IIIα to mitochondria and nucleus. *Proc. Natl Acad. Sci. U.S.A.* **99**, 12114–12119 https://doi.org/10.1073/pnas.192449499
51 Wu, J., Feng, L. and Hsieh, T. (2010) Drosophila topo IIIα is required for the maintenance of mitochondrial genome and male germ-line stem cells. *Proc. Natl Acad. Sci. U.S.A.* **107**, 6228–6233 https://doi.org/10.1073/pnas.1001855107
52 Bianchi, V., Pontis, E. and Reichard, P. (1986) Changes of deoxyribonucleoside triphosphate pools induced by hydroxyurea and their relation to DNA synthesis. *J. Biol. Chem.* **261**, 16037–16042 PMID:3536919
53 Chrystelle, M. and Bénard, M. (2014) Replication forks reverse at high frequency upon replication stress in *Physarum polycephalum*. *Chromosoma* **123**, 577–585 https://doi.org/10.1007/s00412-014-0471-z
54 Liu, Y. (2016) EEPD1: breaking and rescuing the replication fork. *PLoS Genet.* **12**, e1005742 https://doi.org/10.1371/journal.pgen.1005742
55 Claessens, A., Harris, L.M., Stanojcic, S., Chappell, L., Stanton, A., Kuk, N. et al. (2018) Recq helicases in the malaria parasite *Plasmodium falciparum* affect genome stability, gene expression patterns and DNA replication dynamics. *PLoS Genet.* **14**, e1007490 https://doi.org/10.1371/journal.pgen.1007490
56 Suski, C. and Marians, K. (2008) Resolution of converging replication forks by RecQ and topoisomerase III. *Mol. Cell* **30**, 779–789 https://doi.org/10.1016/j.molcel.2008.04.020
57 Wu, L., Chan, K.L., Ralf, C., Bernstein, D.A., Garcia, P.L., Bohr, V.A. et al. (2005) The HRDC domain of BLM is required for the dissolution of double Holliday junctions. *EMBO J.* **24**, 2679–2687 https://doi.org/10.1038/sj.emboj.7600740
58 Mills, M., Tse-Dinh, Y. and Neuman, K.C. (2018) Direct observation of topoisomerase IA gate dynamics. *Nat. Struct. Mol. Biol.* **25**, 1111–1118 https://doi.org/10.1038/s41594-018-0158-x

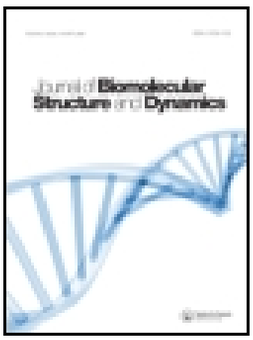

Taylor & Francis
Taylor & Francis Group

Journal of Biomolecular Structure and Dynamics

ISSN: (Print) (Online) Journal homepage: https://www.tandfonline.com/loi/tbsd20

Molecular docking and molecular dynamics simulation identify a novel Radicicol derivative that predicts exclusive binding to *Plasmodium falciparum* Topoisomerase VIB

Shephali Bansod, Navya Raj, Amjesh R, Achuthsankar S. Nair & Sunanda Bhattacharyya

To cite this article: Shephali Bansod, Navya Raj, Amjesh R, Achuthsankar S. Nair & Sunanda Bhattacharyya (2021): Molecular docking and molecular dynamics simulation identify a novel Radicicol derivative that predicts exclusive binding to *Plasmodium falciparum* Topoisomerase VIB, Journal of Biomolecular Structure and Dynamics, DOI: 10.1080/07391102.2021.1891970

To link to this article: https://doi.org/10.1080/07391102.2021.1891970

JOURNAL OF BIOMOLECULAR STRUCTURE AND DYNAMICS
https://doi.org/10.1080/07391102.2021.1891970

Molecular docking and molecular dynamics simulation identify a novel Radicicol derivative that predicts exclusive binding to *Plasmodium falciparum* Topoisomerase VIB

Shephali Bansod[a]*, Navya Raj[b]*, Amjesh R[c], Achuthsankar S. Nair[d] and Sunanda Bhattacharyya[a]

[a]Department of Biotechnology and Bioinformatics, School of Life Sciences, University of Hyderabad, Hyderabad, Telangana, India; [b]Department of Health Informatics, College of Health Sciences, Saudi Electronic University, Dammam, Kingdom of Saudi Arabia; [c]Rajiv Gandhi Centre for Biotechnology, Thiruvananthapuram, Kerala, India ; [d]Department of Computational Biology and Bioinformatics, University of Kerala, Thiruvananthapuram, Kerala, India

Communicated by Ramaswamy H. Sarma

ABSTRACT

Plasmodium falciparum harbors a unique type II topoisomerase, Topoisomerase VIB (*Pf*TopoVIB), expressed specifically at the actively replicating stage of the parasite. An earlier study showed that Radicicol inhibits the decatenation activity of *Pf*TopoVIB and thereby arrests the parasites at the schizont stage. Radicicol targets a unique ATP-binding fold called the Bergerat fold, which is also present in the N-terminal domain of the heat shock protein 90 (*Pf*Hsp90). Hence, Radicicol may manifest off-target activity within the parasite. We speculate that the affinity of Radicicol towards *Pf*TopoVIB could be enhanced by modifying its structure so that it shows preferential binding towards *Pf*TopoVIB but not to *Pf*Hsp90. Here, we have performed the docking and affinity studies of 97 derivatives (structural analogs) of Radicicol and have identified 3 analogs that show selective binding only to *Pf*TopoVIB and no binding with *Pf*Hsp90 at all. Molecular dynamics simulation study was performed for 50 ns in triplicate with those 3 analogs and we find that one of them shows a stable association with Radicicol. This study identifies the structural molecule which could be instrumental in blocking the function of *Pf*TopoVIB and hence can serve as an important inhibitor for malaria pathogenesis.

Abbreviations: AM1-BCC: Atomic charges1-bond charge corrections; Basic Local Alignment Search Tool - Protein; (BLASTP); CGenFF: CHARMM General Force Field; CHARMM36 FF: CHARMM36 additive force field; CHARMM36: Chemistry at Harvard Macromolecular Mechanics 36; DS: Discovery Studio; farPPI: Fast Amber Rescoring for Protein-Protein Interacting Inhibitors; ff14SB: Force field 14 Stony Brook; GAFF2: General AMBER Force Field; GPU: Graphics processing unit; GROMOS: GROningen MOlecular Simulation; GSK299423: GlaxoSmithKline 299423; IC_{50}: Half maximal inhibitory concentration; IUPAC: International Union of Pure and Applied Chemistry; MM/PB (GB) SA: Molecular Mechanics/Poisson–Boltzmann or generalized Born and surface area continuum solvation; NPT: ensembles: moles (N), pressure (P) and temperature (T); PDB: Protein Data Bank; RMSD: Root-Mean-Square Deviation; SMTL: Swiss-Model Template Library; SAVES: Structural Analysis and Verification Server; SAR: Structure-Activity Relationship; TIP3P: transferable intermolecular potential with 3 points; UniProtKB: Universal Protein Knowledgebase; UCLA-DOE: University of California, Los Angeles-Department of Energy; WHO: World Health Organization

ARTICLE HISTORY
Received 8 November 2020
Accepted 13 February 2021

KEYWORDS
Plasmodium Topoisomerase VIB; Radicicol; Bergerat fold; homology modeling; MD simulation

Introduction

The apicomplexan parasite *Plasmodium falciparum* causes the most severe form of human malaria. According to the latest WHO report (https://www.who.int/news-room/fact-sheets/detail/malaria), there are 228 million cases of malaria in 2018, of which 405,000 deaths are reported. Although malaria is an old-world disease only a few anti-malaria drugs are available which can kill the parasite (Tse et al., 2019). Further, parasites have developed resistance against the anti-malarial drugs Chloroquine and Artemisinin which subsequently have increased the mortality rate of malaria throughout the world. Hence, it is of utmost importance to develop new anti-malarial drugs. The approaches may include identification of new targets, rational drug design, repurposing of drugs and identification of natural products having anti-malarial activity (Newman & Cragg, 2016; Vale et al., 2020).

Topoisomerases are attractive targets as it constitutes one of the most important enzyme-family that maintains the super helicity of DNA and thereby is essential for DNA replication, transcription and DNA repair. Earlier studies have

CONTACT Sunanda Bhattacharyya sdeb70@gmail.com; sbtsl@uohyd.ernet.in Department of Biotechnology and Bioinformatics, School of Life Sciences, University of Hyderabad, Gachibowli, Telangana 500046, India
*These authors have contributed equally to the work.

Supplemental data for this article can be accessed online at https://doi.org/10.1080/07391102.2021.1891970.

identified that Ciprofloxacin targets the Type II topoisomerase of bacteria namely DNA Gyrase and topoisomerase IV, thereby is used to treat various kinds of bacterial infections (Mitscher, 2005; Widdowson & Hennessy, 2010). A recent study has established that GSK299423 exhibits 57-fold selectivity towards the *P. falciparum* type II topoisomerase than the human counterpart (Mudeppa et al., 2015). Using a yeast-based assay system, we have shown that *Pf*TopoVIA-VIB can decatenate the catenated DNA. Moreover Radicicol, an antifungal macrolactone antibiotic causes inhibition of the decatenation activity of *Pf*TopoVIB in a dose-dependent manner (Chalapareddy, 2016).

Topoisomerase VI is a type IIB topoisomerase which was first identified in an archaeal species *Sulpholobus shibatae* (*Ss*TopoVI). It has two subunits: Topoiosmerase VIA and VIB which forms a heterotetramer (A_2B_2) in its active state. Structural studies revealed the striking similarities in the ATP binding motifs of TopoVIB and the members of the GHKL (Gyrase-Hsp90-Histidine Kinase-MutL) super-family. They all share a small three-dimensional ATP-binding fold known as the Bergerat fold. The core ATP binding domain (amino acids 22 to 166) of *Pf*TopoVIB is homologous to that present in the GHKL ATPases and is composed of three small motifs (B1, B2, and B3) that constitute the Bergerat fold (Chalapareddy, 2016). It has been demonstrated that Radicicol competes with ATP for binding to the *Ss*TopoVIB monomers, thereby inhibits the dimerization of *Ss*TopoVIB ATPase domain and ATP hydrolysis, which subsequently hampers the strand passage reaction of the enzyme (Corbett & Berger, 2006). *Plasmodium falciparum* expresses both subunits of topoisomerase VI in the replicative stage of the parasite. In *Plasmodium* infected erythrocyte, Radicicol causes the growth inhibition of parasites with an IC_{50} of 8.5 μM (Chalapareddy et al., 2014). It was observed that Radicicol induces over-expression of *Pf*TopoVIB and results in the inhibition of schizont stage to ring stage transition in *Plasmodium*. This underscores the significance of *Pf*TopoVI in *Plasmodium* biology. As most of the replication proteins are essential for the survivability, and generation of conditional knock-outs in *Plasmodium* is technically challenging, it is important to identify highly specific chemical inhibitors of *Pf*TopoVIB in order to delineate the precise biological role of this protein in *Plasmodium*. However, owing to the similarity within the Bergerat ATP-binding fold which is present in both *Pf*TopoVIB and *Pf*Hsp90, Radicicol is found to dock at both the structures (Chalapareddy et al., 2014). Our present study aims at identifying the analogs of Radicicol that could reduce its off-target activity. We plan to identify some specific analogs of Radicicol that would bind specifically to the *Pf*TopoVIB but not to *Pf*Hsp90. Using the bioinformatics approaches, we have designed 97 analogs of Radicicol and they are allowed to dock on *Pf*TopoVIB as well as on *Pf*Hsp90. Analysis of the results revealed three such analogs that have a very strong affinity for *Pf*TopoVIB, and they do not exhibit any binding with *Pf*Hsp90. The validation of the docked complexes is done using molecular dynamics simulations which identifies one analog that shows stable ligand-protein interactions. This derivative of Radicicol can serve as a tool to decipher the biological function of *Plasmodium* topoisomerase VIB.

Materials and methods

Comparative structure modeling and validation of PfTopoVIB and PfHsp90

The crystal or solution structure for *Pf*TopoVIB is not solved yet. In case of *Pf*Hsp90, although two crystal structures are solved, they are not of the full-length protein. Hence, homology-based structure modeling was carried out for both of the proteins. The sequences of *Pf*TopoVIB and *Pf*Hsp90 were retrieved from the UniProtKB/Swiss-Prot database (Bairoch & Apweiler, 1997) and suitable templates were selected from the SMTL, a large structural database of experimentally determined protein structures, derived from the PDB (Berman et al., 2000). Target-template sequence alignment was carried out using BLAST P suite (https://blast.ncbi.nlm.nih.gov/Blast.cgi?PAGE=Proteins). Near native structures of *Pf*TopoVIB and *Pf*Hsp90 were modeled using the automated mode (ProMod3 Version 1.2) integrated in the Swiss-Model server (Guex et al., 2009). Necessary energy minimization steps were also carried out for the predicted models using the GROMOS 43B1 force field (Van Gunsteren, 1996) implemented in the Swiss-PDB viewer (http://www.expasy.org/spdbv). The validation of both the modelled structures were carried out using the PROCHECK server (Laskowski et al., 1993) and the Ramachandran plot (http://services.mbi.ucla.edu/SAVES/Ramachandran/). PROCHECK server checks the stereochemical quality of the modelled structures and the Ramachandran plot shows the residue-by-residue quality and stability of the favored and the disallowed regions in the protein model. ERRAT scores (Colovos & Yeates, 1993) were also predicted for the homology models through the Structural Analysis and the Verification Server (SAVES) (https://servicesn.mbi.ucla.edu/SAVES) of UCLA-DOE Lab.

Design and preparation of Radicicol analogs

The 3D structure of Radicicol, downloaded from the PubChem compound database (Kim et al., 2019) was used as the reference molecular scaffold for the *in-silico* design of different derivatives (structural analogs). MarvinSketch tool (https://chemaxon.com/products/marvin), version 16.8.8.0 was used to draw the analogs by modifying different atoms, functional groups and/or side chains of Radicicol. Our strategy was to modify the structure of Radicicol and design novel analogs by substituting the functional groups which potentially enhance its inhibition against *Pf*TopoVIB and reduce its inhibition of *Pf*Hsp90. The reported Structure-Activity Relationship (SAR) of Radicicol (Turbyville et al., 2006) was considered for selecting the attachment point for the modification and various functional groups were identified from relevant literature (Dutton et al., 2014; Pearl et al., 2008; Shinonaga et al., 2009; Shiotsu et al., 2000; Teo et al., 2015; Wang et al., 2008). We substituted various functional groups at specific attachment points of Radicicol, without

disturbing the macrocyclic ring which is required for the bioactivity of Radicicol. The designed analogs were saved along with their 10 conformers each for further preparation. 'Prepare ligand' protocol in Biovia Discovery Studio (DS) 4.0 (BIOVIA, 2019) was used to prepare the analog dataset, which optimizes the charges of common groups, adds hydrogen atoms, generates tautomers/isomers and removes duplicate/bad conformers. 'Generate Conformations' protocol, using a quasi-exhaustive systematic search method (FAST conformation generation method) (Smellie et al., 1995) employed in DS 4.0 was used to create all the possible diverse 3D conformers of each analog and all the resulting diverse conformers were stored as a single file for further docking step.

Structure based virtual screening of Radicicol analogs against PfTopoVIB and PfHsp90

Along with Radicicol and its analogs, Adenosine triphosphate (ATP) molecule (downloaded from PubChem compound database) was also used as the positive control for docking studies. Since ATP binds to the monomeric form of TopoVIB we have used the monomers of *Pf*TopoVIB and *Pf*Hsp90 as our template for our docking studies. Two sets of docking were carried out in a site-specific manner, where the 3D structures of *Pf*TopoVIB and *Pf*Hsp90 served as the receptors and the Radicicol derivatives with their conformers served as the analog dataset. The docking program LibDock (Diller & Merz, 2001; Rao et al., 2007) implemented in DS 4.0 performs a high-throughput docking by aligning analog conformations to polar and apolar receptor interaction sites (hotspots). The binding site cavities were analyzed for both the target protein structures using the 'Eraser algorithm' (Venkatachalam et al., 2003) implemented in DS 4.0. A grid with coordinates of −9.153 Å, −79.659 Å and 25.38 Å for X, Y and Z respectively with spacing of 0.5 Å was used for positioning the binding site. In case of *Pf*Hsp90, the grid coordinates of 21.963, 32.991 and 14.764 for X, Y and Z respectively with spacing of 0.5 Å was used. The grid covered the Bergerat fold residues, which were specified as the target protein site features (termed as HotSpots) by the LibDock program for calculating the binding affinity of analogs with the receptors. Receptor-analog docking study was performed using LibDock protocol against *Pf*TopoVIB as well as *Pf*Hsp90. An empirical scoring function, LigScore (Krammer et al., 2005) was employed to score the docked ligand poses, and the complexes were ranked and sorted according to the descending order of the LibDock score. The best docked pose for each analog towards each protein was identified based on the highest LibDock score and compared with the LibDock score of ATP and Radicicol. The lead molecules were selected based on higher LibDock score and specific docking with *Pf*TopoVIB and little or no docking with *Pf*Hsp90. The interacting amino acids of the complexes were analyzed and the types of molecular interactions including conventional hydrogen bonds, carbon-hydrogen bonds, electrostatic interactions and hydrophobic interactions were noted.

Molecular dynamics (MD) simulation of the best docked pose of lead ligand-protein complexes

Molecular dynamics simulations were performed for the top three analogs using Gromacs software 5.1.4 (Lindahl et al., 2001; Van Der Spoel et al., 2005). The analog-protein complexes were subjected to 50 ns molecular dynamics simulation in triplicate to validate the stability of the complex and also to estimate the variation and conformational changes in the protein-analog interactions. For simulation, the standard CHARMM36 FF which includes parameters for the protein and other bio-molecules were employed (Lee et al., 2016). The parameter for the analogs was generated using CGenFF (Vanommeslaeghe et al., 2010). Protein-analog complexes were kept in a periodic rectangular box and solvated with TIP3P water molecules. In order to neutralize the charge 0.15 M KCl ions were added to the system. The system was then equilibrated with NPT ensembles and was subjected to 50,000 steps minimization using the steepest descent method for 1000 ps at 300 K. To maintain the temperature, Berendsen thermostat with tc = 1.0 ps and Parrinello-Rahman barostat with tp = 2.0 ps were used. The Van der Waals interactions were described using a Lennard Jones function with a cut off of 1.0 nm. Molecular dynamics simulations were performed in triplicate for each system using a GPU SERVER with Intel® Xeon® Gold 6154 3.0 G,18 core 256 GB RAM with dual NVIDIA Tesla™ V100 GPU 32GB PCI-E.

Binding free energy calculation

We calculated the free energy of the *Pf*TopoVIB bound to each of the three lead analogs. For that, we used the snapshots collected from trajectories, that resulted from the MD simulations. We used the Web server farPPI which employs the MM/PB (GB) SA approaches with the GAFF2 and ff14SB force field combination and the PB3 procedure (Wang et al., 2019). It uses a ready-to-dock benchmark database (2P2I database, ver. 2.0, 28-03-2018) and a ready-to-rescore benchmark dataset, which contains 900 binding poses for 184 protein-ligand complexes. The docked pose file and the receptor file are the input. The partial charge of ligand is assigned by AM1-BCC method via the antechamber module of Amber. The calculated binding free energy is based on the equation; Energy Binding = Energy Complex – Energy Ligand – Energy Receptor.

Results

Homology modeling of PfTopoVIB and PfHsp90

The sequence of *Plasmodium falciparum* TopoVIB retrieved from Uniprot (ID: Q8ID53) consists of 561 amino acids. The template search revealed that the most similar protein structure available for the sequence of *Pf*TopoVIB was that of *Sulpholobus shibatae* Topoisomerase VIB (PDB: 2ZBK.D chain). Taking 2ZBK.D chain as the template, the target-template alignment was carried out using BLASTP suite, which predicted the local pairwise sequence identity to be 28.57% and the E-value as 1e-12. For homology modeling, the sequence

identity between (20–25)% is considered as the twilight zone (Chung & Subbiah, 1996). Studies have demonstrated that proteins with pairwise sequence identity higher than 25% are similar in 3D structures and have a strong divergent evolutionary relationship (Chang et al., 2008; Doolittle, 1986; Laurents et al., 1994; Rost, 1999; Sander & Schneider, 1991; Subbiah et al., 1993; Yang & Honig, 2000). The E value of 1e-12, obtained for the template from the BLAST tool was considered in the acceptable range as per the recent study (Barghash & Helms, 2013), which suggests the acceptable threshold of E Value for BLAST as 1e-8. Hence, the 3D structure of 2ZBK.D chain with 28.57% sequence identity was considered as a suitable template for homology modeling of *Pf*TopoVIB. 2ZBK is an X–ray diffraction structure with Radicicol as a native ligand having 3.6 Å resolution. Our study focuses on the ATP-binding domain of *Pf*TopoVIB, known as the Bergerat fold, which spans through 22 to 166 amino acids. This region corresponds to the 11 to 192 amino acids of *Ss*TopoVIB (2ZBK.D chain) with an alignment score range of (50–80) with 42% positives, 29% identity and 13% gaps. Figure 1(A) shows the sequence alignment between the target *Pf*TopoVIB (Query) and template *Ss*TopoVIB (Subject) in the Bergerat fold. As the aligned region covers the Bergerat fold, we preferred homology modeling over *de novo* protein structure prediction. It is observed that there is a unique highly charged region (containing a stretch of lysines and glutamic acids) spanning 61st–78th residues in the amino-terminal domain of *Pf*TopoVIB. *Plasmodium falciparum* possesses this kind of low complexity charged residues and unstructured region which is a unique feature of parasite protein. However, the biological significance of such low complexity regions remains unknown. Homology based near-native model was created for *Pf*TopoVIB (Figure 1(B)) and subjected to 10 steps of energy minimization, using GROMOS 43b1 force field where in each step 20 cycles of steepest descent method was involved. 200 cycles of steepest descent were required to attain the lowest energy model, which was used for further analysis.

The sequence of *Pf*Hsp90 was retrieved from the Uniprot database (ID: Q8IL32). For building the near native model of *Pf*Hsp90, 3IED (PDB code) was selected as the template. The target-template alignment using blastp suite, predicted the local pairwise sequence identity to be 98% and the E-value as 5e-171 (Figure 1(C)). The ligand adenylyl phosphoramidate (AMPPN) was removed from 3IED template for building the near native model of *Pf*Hsp90 (Figure 1(D)). The model was subjected to 10 steps of energy minimization to obtain the lowest energy model for further analysis.

Modeled structure validation

The PROCHECK results (Supplementary Material) and the results of the Ramachandran plot (Figure S1(A)) validate the stereo chemical quality and stability of the predicted *Pf*TopoVIB model. Ramachandran plot for *Pf*TopoVIB revealed that 80.4% of the residues (337 amino acids) were in the most favored regions, 15.5% (65 amino acids) in the additional allowed region, 2.9% (12 amino acids) in the generously allowed region and 1.2% (5 amino acids) in the disallowed region. The resultant model showed ERRAT score as 81.728 and the final energy as −21297.992 kJ/mol. The PROCHECK results (Supplementary Material) and the Ramachandran plot of *Pf*Hsp90 model (Figure S1(B)) revealed that 91.9% of the residues (181 amino acids) were in the most favored regions, 8.1% (16 amino acids) in the additional allowed region, 0.0% (0 amino acids) in the generously allowed region and 0.0% (0 amino acids) in the disallowed region. The model showed ERRAT score as 81.878 and the final energy was −11965.740 kJ/mol.

In silico *binding of Radicicol and ATP to the Bergerat fold of* Pf*TopoVIB and* Pf*Hsp90 models*

The crystal structure 2ZBK.D has *Sulpholobus shibatae* Topoisomerase VIB (*Ss*TopoVIB) bound to Radicicol (RDC531). We have presented this structure in Figure S2(A). To validate our docking, we have removed Radicicol from this structure and redocked Radicicol to the apo-structure represented in Figure S2(B). We compared the native pose (Figure S2(A)) and the newly created docked pose (Figure S2(B)) by superimposing, the RMSD value between the native pose and the docked pose was 1.86 Å (Figure S2(C)). Our analysis showed that the amino acid Thr170 formed a hydrogen bond, while Ala46, Ile79, Val112 and Phe90 were actively involved in hydrophobic interactions with Radicicol in the 2ZBK-D structure (Figure S2(D)). Our re-docked structure shows the conservation of the above interactions, in addition, it shows four more contacts including one hydrogen bond with Lys113 and hydrophobic interactions with Gly80, Ala89 and Val112 (Figure S2(E)).

After validating our model, next, we carried out two sets of docking studies using LibDock, one in which both ATP and Radicicol were docked to *Pf*TopoVIB (Figure S2(F,G), respectively) and in the second set, both the ligands were docked with *Pf*Hsp90 (Figure S2(H,I)). Our study shows that Radicicol binds to the Bergerat fold of *Pf*TopoVIB and *Pf*Hsp90 like that of the intrinsic ligand ATP. This also ensured that the proteins were correctly modeled *in silico* and had near-native structural topology. The LibDock score for ATP and Radicicol docking were 143.657 and 76.4008 respectively (Table SI). While 96 different docking poses were obtained for ATP, only 2 different binding poses were obtained for Radicicol. The type of molecular interactions found between *Pf*TopoVIB and ATP/Radicicol and their interatomic distance is tabulated (Table SII). ATP showed 14 molecular interactions in the form of hydrogen bonds and hydrophobic interactions. The key amino acids which are involved in conventional hydrogen bonds were Phe122, Asp43 and Thr22 whereas the residues Lys35, Gly120 and Glu36 showed carbon hydrogen bonds. Several hydrophobic interactions were also noted which included a Pi-Sigma bond with Lys35, a Pi-Sulfur bond with Met32 and four Pi-Alkyl bonds, two each with Lys121 and Lys35.

Radicicol showed 6 molecular interactions with *Pf*TopoVIB, in which Leu126 formed a conventional hydrogen bond and a hydrophobic interaction through the alkyl group. Phe122

1A

2ZBK:D|PDBID|CHAIN|SEQUENCE
Sequence ID: Query_50013 Length: 530 Number of Matches: 4

Range 1: 11 to 192 Graphics ▼ Next Match ▲ Previous M

Score	Expect	Method	Identities	Positives	Gaps
56.2 bits(134)	1e-12	Compositional matrix adjust.	58/203(29%)	86/203(42%)	27/203(13%)

```
Query  10   STYSFFFKNLSVTGFY-EENALFMTVKELFDNSVDALYNNDKEDNVETKKDLEEEKKKKK  68
            S   FF +N  + GF     AL+ TV+EL +NS+DA   +    N++   DL
Sbjct  11   SPAEFFKRNPELAGFPNPARALYQTVRELIENSLDATDVHGILPNIKITIDL--------  62

Query  69   KKKVEIIVEEYDKSLSYYKITCRDNGKGSKIKDLE-KFSEIFLTSK-DNCSTSGKFGIGL  126
                      D +   YK+   DNG G   +++   F  +  +SK  N  T G +G+G+
Sbjct  63   ----------IDDARQIYKVNVVDNGIGIPPQEVPNAFGRVLYSSKYVNRQTRGMYGLGV  112

Query  127  KTILLYSLKTAYGFLHIKV-KVEENKIWDFMLVMDKNLNHTFIQNFKEYIDTNW--NWSV  183
            K  +LYS      + I+   V   +I+ F L +D N N   I       +T      SV
Sbjct  113  KAAVLYSQMHQDKPIEIETSPVNSKRIYTFKLKIDINKNEPIIVERGSVENTRGFHGTSV  172

Query  184  EISLILKINNKFIHDQRIYTYIK  206
             IS+      +     RIY YIK
Sbjct  173  AISIP---GDWPKAKSRIYEYIK  192
```

1B

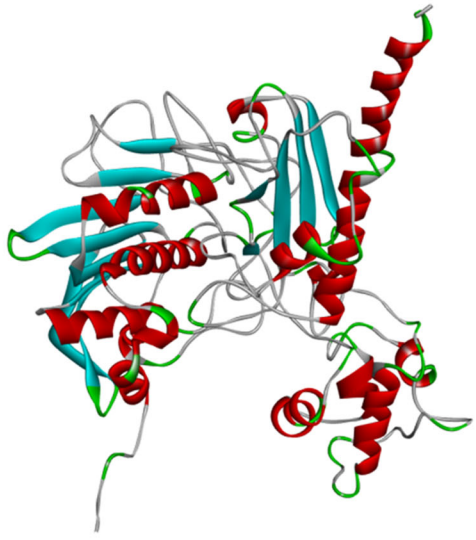

1C

1D

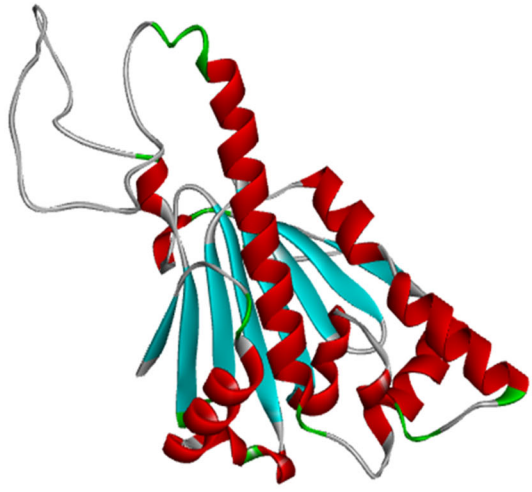

Chain A, Heat shock protein [Plasmodium falciparum 3D7]
Sequence ID: 3IED_A Length: 272 Number of Matches: 1

Range 1: 14 to 272 GenPept Graphics ▼ Next Match ▲ Previous Match

Score	Expect	Method	Identities	Positives	Gaps
498 bits(1283)	5e-171	Compositional matrix adjust.	253/259(98%)	255/259(98%)	0/259(0%)

```
Query  89   REDISSDSSPVEKYNFKAEVNKVMDIIVNSLYTDKDVFLRELISNASDACDKKRIILENN  148
            RE++    SPVEKYNFKAEVNKVMDIIVNSLYTDKDVFLRELISNASDACDKKRIILENN
Sbjct  14   RENLYFQGSPVEKYNFKAEVNKVMDIIVNSLYTDKDVFLRELISNASDACDKKRIILENN  73

Query  149  KLIKDAEVVTNEEIKNETEKEKTENVNESTDKKENVEEEKNDIKKLIIKIKPDKEKKTLT  208
            KLIKDAEVVTNEEIKNETEKEKTENVNESTDKKENVEEEKNDIKKLIIKIKPDKEKKTLT
Sbjct  74   KLIKDAEVVTNEEIKNETEKEKTENVNESTDKKENVEEEKNDIKKLIIKIKPDKEKKTLT  133

Query  209  ITDNGIGMDKSELINNLGTIAQSGTAKFLKQIEEGKADSNLIGQFGVGFYSSFLVSNRVE  268
            ITDNGIGMDKSELINNLGTIAQSGTAKFLKQIEEGKADSNLIGQFGVGFYSSFLVSNRVE
Sbjct  134  ITDNGIGMDKSELINNLGTIAQSGTAKFLKQIEEGKADSNLIGQFGVGFYSSFLVSNRVE  193

Query  269  VYTKKEDQIYRWSSDLKGSFSVNEIKKYDQEYDDIKGSGTKIILHLKEECDEYLEDYKLK  328
            VYTKKEDQIYRWSSDLKGSFSVNEIKKYDQEYDDIKGSGTKIILHLKEECDEYLEDYKLK
Sbjct  194  VYTKKEDQIYRWSSDLKGSFSVNEIKKYDQEYDDIKGSGTKIILHLKEECDEYLEDYKLK  253

Query  329  ELIKKYSEFIKFPIEIWSE  347
            ELIKKYSEFIKFPIEIWSE
Sbjct  254  ELIKKYSEFIKFPIEIWSE  272
```

Figure 1. Bergerat fold of *Pf*TopoVIB has high similarity with *Ss*TopoVIB: (A) Pairwise sequence alignment of the Bergerat fold region of *Pf*TopoVIB (Query) and *Ss*TopoVIB (Sbjct); positives show the number of identical amino acids or that have similar chemical properties; (B) Homology model of *Pf*TopoVIB designed using 2ZBK template; 3D structure rendered in solid ribbon and colored according to secondary structure; alpha helices in red, beta sheets in Cyan, coils in white and turns in green; (C) Pairwise sequence alignment of the N-terminal domain of *Pf*Hsp90 (Query) (Q8IL32) and the template 3IED (Subject); (D) Homology model of *Pf*Hsp90 created using template 3IED; model represented in solid ribbon format, colored according to the secondary structure; alpha helices in red, beta sheets in Cyan, coils in white and turns in green.

also formed a conventional hydrogen bond. While Asn40 formed a carbon hydrogen bond, Gly125 interacted with the Cl (halogen) of Radicicol and Lys104 made a hydrophobic interaction through the alkyl group. We found that many of the amino acids which interact with Radicicol were conserved between *Pf*TopoVIB and *Ss*TopoVIB. For example, the residues Phe105, Ala44 and Asn40 in *Pf*TopoVIB correspond to that of Phe90, Ala46 and Asn42 in *Ss*TopoVIB.

In the second set of docking studies, we allowed ATP and Radicicol to dock to the *in-silico* model of *Pf*Hsp90 N-terminal domain. Docking resulted in 81 different poses of the ligand ATP with the highest LibDock score of 129.333. 7 molecular interactions were found between ATP and *Pf*Hsp90 (Figure S2(H)). Residues Asn133, Gln230, Phe257 and Val255 were found to form conventional hydrogen bonds with ATP. Asn133 was also found to possess a Pi-Donor hydrogen bond, whereas Ala134 and Ala137 interacted through the alkyl group (hydrophobic interaction). Radicicol interacted with *Pf*Hsp90 in the Bergerat fold with a LibDock score of 91.791 generating 9 different docked poses. The key residues found to interact well with Radicicol were Asn224 through a conventional hydrogen bond, Asp211 through the halogen Cl and the amino acids Ile310, Ala134, Ala137, Met216, Leu225 and Leu130 all through hydrophobic interactions mostly of the alkyl type (Figure S2(I)). Radicicol when docked with the template PDB structure 3IED, the key residues Ala137, Met207 and Asn215 were identified to interact which corresponds to the residues Ala137, Met216 and Asn224 in the *Pf*Hsp90 model. There is a difference of 9 residues in between Met207 and Met216 and also in between Asn215 and Asn224. This is because some amino acids were absent in 3IED, so the numbers given to amino acids in PDB is different when compared with our *Pf*Hsp90 model.

Designing of Radicicol analogs and docking to PfTopoVIB and PfHsp90

The 3D structure of Radicicol served as the reference molecule for the *in-silico* design of 97 different structural analogs using MarvinSketch tool. The analog structures were computationally drawn and designed by modifying different atoms, functional groups and/or side chains of Radicicol, based on its reported Structure–activity relationship (SAR) to alter its biological activity against *Pf*TopoVIB and *Pf*Hsp90. We focused on altering or replacing those functional groups of Radicicol that cause higher affinity towards Hsp90. The IUPAC nomenclature, of all the 97 analogs are tabulated (Table SIII). 6498 different conformers were generated for 97 analogs using Biovia DS 4.0. Receptor-ligand docking performed by LibDock protocol against *Pf*TopoVIB protein using 6498 analog conformers returned 3162 docked poses. In the same manner, docking against *Pf*Hsp90 protein using 6498 analog conformers returned 2512 docked poses. All the docked poses were analyzed and the best docked pose of each ligand towards each protein was identified based on the highest LibDock score and compared with the LibDock score of ATP and Radicicol (Table SI).

Selection of the Radicicol analogs that show specific docking to PfTopoVIB but not to PfHsp90

*Pf*TopoVIB and *Pf*Hsp90 share a common structural ATP-binding domain known as the Bergerat fold (Bergerat et al., 1997) characterized by a structural motif consisting of an eight-stranded mixed beta-sheet in two layers – alpha/beta (Dutta & Inouye, 2000). Out of 97 analogs, 88 molecules interacted with *Pf*TopoVIB within the same binding cavity occupied by Radicicol and ATP, whereas 9 analogs failed to dock. Depending upon the LibDock score of each analog compared to ATP and Radicicol, we classified them into two groups, one with a higher LibDock score than the cut off value 76.4008 and the other with lower scores than the cut off value. In case of *Pf*TopoVIB, we have chosen this cut off value to select those analogs of Radicicol that have a higher chance of binding with *Pf*TopoVIB as compared to the Radicicol. The LibDock score of Radicicol for *Pf*TopoVIB is 76.4 hence all the values that are higher than 76.4 are shortlisted. To that end, 77 analogs were identified with LibDock scores higher than the cut off value and 11 analogs with lower LibDock scores than the cut off. The highest score was obtained for analog 91 (158.337) and the lowest score was obtained for analog 23 (76.108). So, based on docking score, 77 analogs of Radicicol performed better than Radicicol, 11 analogs were poor performers and 9 did not dock at all (Table SI).

The same classification criterion was adopted for analyzing the docking results of *Pf*Hsp90 also. In this case, the cut off value was taken as 91.7911. The LibDock score of Radicicol for *Pf*Hsp90 is 91.79; hence the values higher than that of 91.79 are shortlisted. Out of 97 analogs, 78 molecules were found to interact with a higher dock score than the cut off value. 13 analogs docked with a lower LibDock score and the remaining 6 analogs did not dock to *Pf*Hsp90 at all. The highest binding affinity was obtained for analog 80 (126.137) and the lowest for analog 78 (91.757). We focused our work only on those subsets of Radicicol analogs that display higher affinity towards *Pf*TopoVIB and no affinity towards *Pf*Hsp90. Hence, although analog 91 shows the highest score for *Pf*TopoVIB, it also shows higher docking score for *Pf*Hsp90. Similarly, analog 23 shows a poor score for *Pf*TopoVIB compared to *Pf*Hsp90. The analysis of these ligands is beyond the scope of this manuscript. Our criterion for selecting the best analogs was to compare their binding affinity with both the proteins and finally choose those which docks specifically to *Pf*TopoVIB but have little or no binding towards *Pf*Hsp90. We observed that out of the 6 analogs which did not dock to *Pf*Hsp90, 3 analogs did not dock to *Pf*TopoVIB either, but the other 3 analogs were having higher LibDock scores towards *Pf*TopoVIB. The structures of Radicicol and these three analogs are presented (Figure 2). These three analogs; analog 2, analog 6, and analog 7, with LibDock scores 133.823, 108.647 and 77.533 respectively were selected as the lead molecules. The number of molecules generated, docked and filtered at various step of this study has been summarized in Table 1.

Further, we compared the volume of Radicicol binding pockets between *Pf*TopoVIB and *Pf*Hsp90 (Figure S3) using a

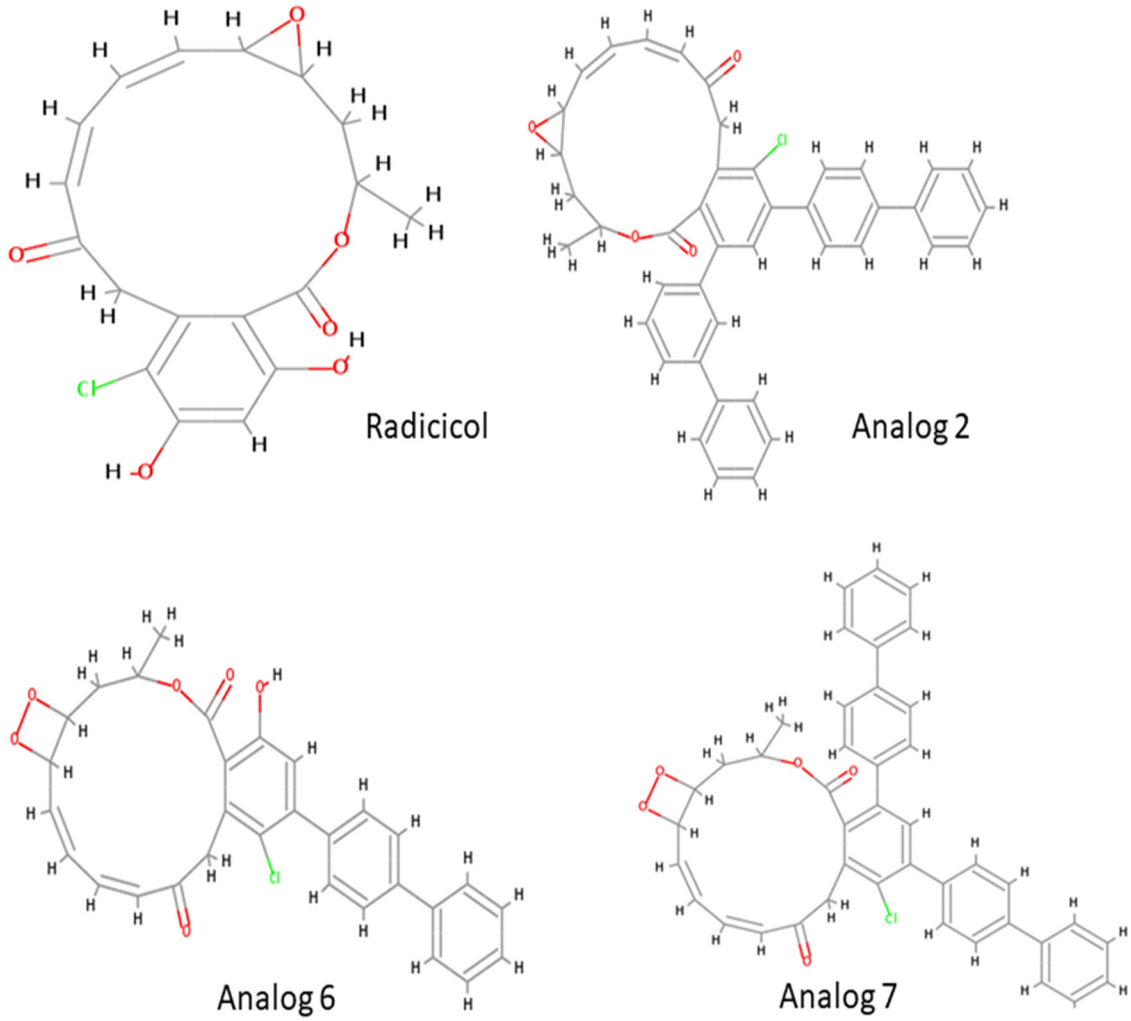

Figure 2. 2D structure of Radicicol and the lead analogs: 2D structure of Radicicol and its analogs; 2, 6 and 7 are represented.

Table 1. The number of molecules generated, docked and filtered at various step.

Virtual screening steps for Radicicol and its analogs	Number of molecules	
3D structure retrieved for Radicicol and ATP from Pubchem	2	
Analogs generated for Radicicol using MarvinSketch	97	
Total number of conformers for Radicicol, 97 analogs and ATP (10 conformers each for 99 molecules)	990	
Structures prepared using Ligand preparation for Docking	962	
3D conformers generated Using DS.4.0 for docking process	6498	
Docking of 6498 structures against target proteins	*Pf*TopoVIB	*Pf*Hsp90
No. of poses docked to target proteins at Bergerat fold	3162	2512
No. of analogs failed to dock to the target protein structures	9	6
No. of analogs docked only to *Pf*TopoVIB and not to *Pf*Hsp90	3	
No. of lead molecules selected for interaction analysis and molecular dynamics simulation	3	

grid based 'Eraser' algorithm implemented in DS 4.0 and found that the binding pocket volume for *Pf*TopoVIB is (180.625 Å^3), much larger than that of *Pf*Hsp90 (143 Å^3). Both the pockets were found to contain the residues of the alpha/beta structural motif, where the ATP and Radicicol interacted in our docking studies. We reason that as the size of analog 2 (637.162 Da), analog 6 (516.969 Da) and analog 7 (653.161 Da) are larger than that of ATP (507.181 Da) and Radicicol (364.777 Da), they are not able to fit properly to the binding site of *Pf*Hsp90 which is smaller than the binding pocket of *Pf*TopoVIB.

The molecular interactions between the lead analogs and *Pf*TopoVIB (Figure 3(A–C)) were analyzed and compared with that of parent molecule Radicicol. Analog 2 showed 12 interactions, analog 6 showed 8 interactions and analog 7 showed 14 (Table SII). The key amino acids in *Pf*TopoVIB which established contacts with analog 2 were Glu36, Lys104, Phe105, Ly121, Phe122, Leu126 and Lys127. While a carbon hydrogen bond and a hydrophobic Pi-alkyl interaction were formed by Lys127, two hydrophobic interactions (Pi-Sigma and Pi-alkyl) were formed with Leu126. Glu36 showed two electrostatic (Pi-anion) interactions and Lys121 had a Pi-donor hydrogen bond and

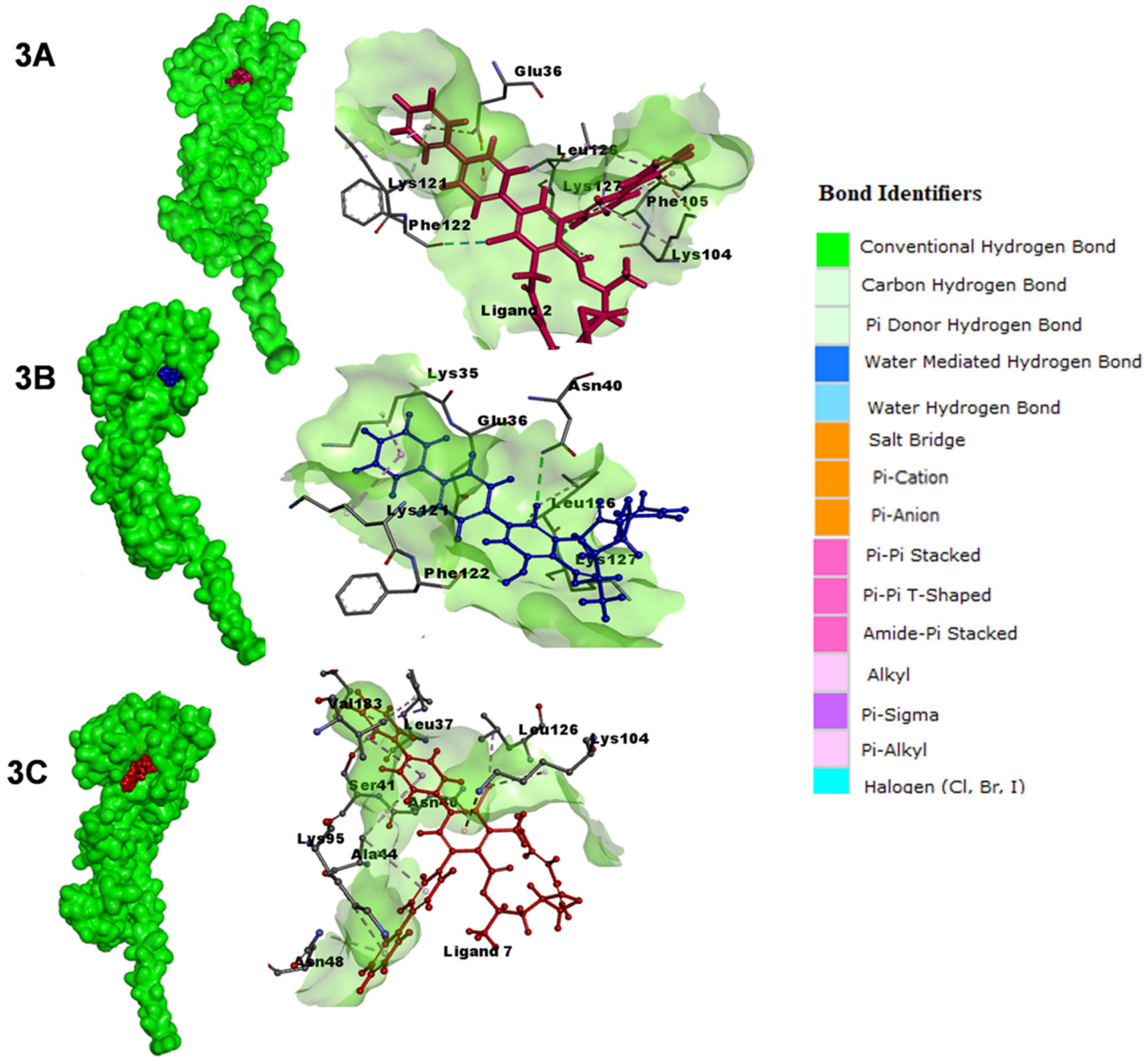

Figure 3. Molecular interactions of the lead analogs of Radicicol in the Bergerat fold of *Pf*TopoVIB: (A–C) analog 2 (purple), analog 6 (blue) and analog 7 (red) interaction with *Pf*TopoVIB has been presented. The color codes for different bonds also given in the figure.

one hydrophobic interaction of Pi-alkyl type. Lys104 showed a Pi-donor hydrogen bond and a hydrophobic Pi-alkyl interaction. Phe122 established an interaction through the halogen atom Cl of analog 2 and Phe105 formed a Pi-Pi T-shaped hydrophobic interaction. Analog 6 showed three conventional hydrogen bonds with the amino acids Asn40, Leu126 and Phe122. Lys127 formed a carbon hydrogen bond; Glu36 formed an electrostatic Pi-anion linkage; Leu126, Lys35 and Lys121 formed hydrophobic interactions mostly of pi-alkyl type. Analog 7, on the other hand, showed the highest number of hydrophobic interactions, but with a different set of residues present in *Pf*TopoVIB namely Leu37, Asn40, Ala44, Cys90, Lys95, Leu126, Val183 and Ile185. Lys104 formed a Pi-donor hydrogen bond and a hydrophobic interaction through the alkyl group of analog 7. Asn48 also established a Pi-donor hydrogen bond and Ser41 showed a Pi-lone pair interaction with analog 7. When compared to ATP and Radicicol, the amino acids which retained their contacts with analog 2 were Phe122, Glu36, Lys121, Leu 126 and Lys104. The interactions with the residues Lys35, Glu36, Asn40, Lys121, Phe122, Leu126 and Ly127 were common in the case of analog 6. But analog 7 showed contacts with Leu126, Asn40 and Lys104 which were similar with those found in Radicicol. There were no common contacts found between ATP and analog 7. Phe122 was interacting with ATP, Radicicol, analog 2 and analog 6, but not with analog 7, whereas Leu126 had contact with all others except ATP. The binding of *Pf*TopoVIB and the lead analogs within the Bergerat fold is illustrated (Figure 4). The 2D interaction diagrams of the lead analogs docked to *Pf*TopoVIB are presented (Figure S4(A–C)).

Molecular dynamic simulation of best docked protein-analog complexes

The stability of analog 2-*Pf*TopoVIB, analog 6-*Pf*TopoVIB and analog 7-*Pf*TopoVIB complexes have been evaluated through

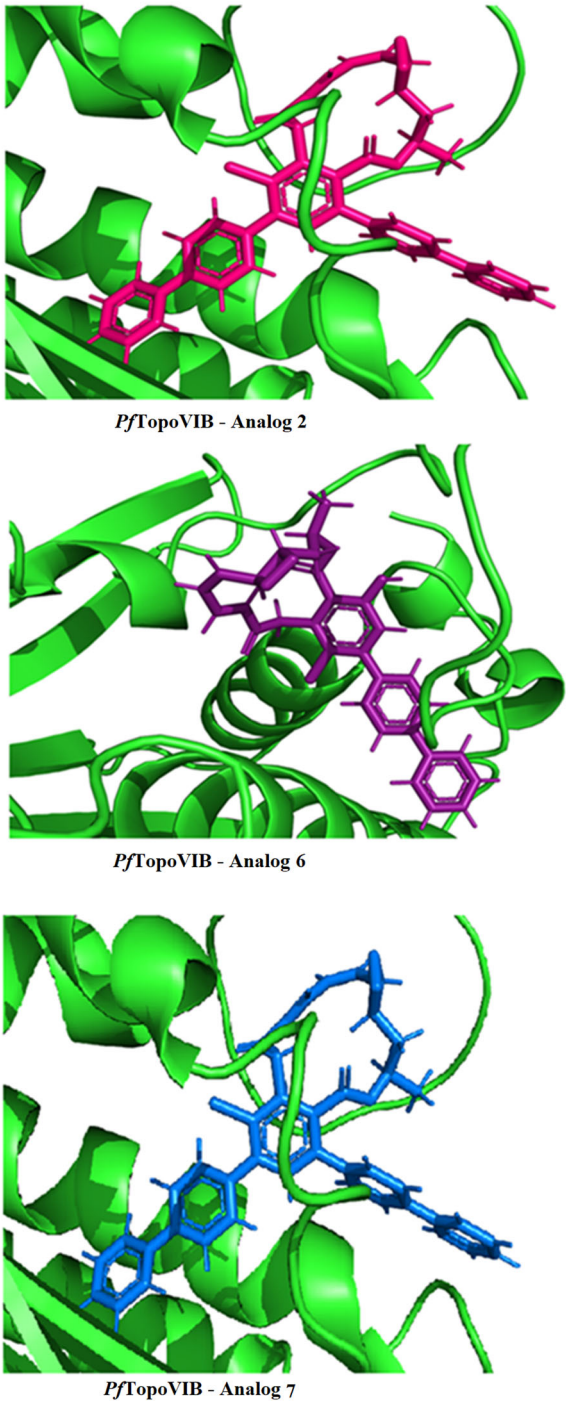

Figure 4. Illustration of binding between *Pf*TopoVIB and the lead analogs: Analog 2 (pink), Analog 6 (purple) and Analog 7 (blue) binding with *Pf*TopoVIB Bergerat fold is represented.

50 ns Molecular Dynamics (MD) simulation. The MD simulations for each analog-*Pf*TopoVIB complex were conducted in triplicate. The RMSD values of all the complexes (Figure 5(A)) and the backbone RMSD are shown (Figure 5(B)). After 50 ns run the analog 7-*Pf*TopoVIB has shown fluctuation towards the end of the simulation, which shows that the protein-analog complex is not stable. In case of analog 6-*Pf*TopoVIB, unusual fluctuations were observed between the 30 ns and 50 ns time points indicating weak stability of the complex. A steady RMSD plot is observed for the analog 2-*Pf*TopoVIB complex, indicating that this analog-protein complex is highly stable throughout the run. We have performed three independent simulations for each of the three analogs and the RMSD of all replicates for each protein analog complex are presented (Figure S5). In all the three runs, analog 2-*Pf*TopoVIB was stable and uniform with an average RMSD value of 0.2 Å, whereas analog 7-*Pf*TopoVIB and analog 6-*Pf*TopoVIB were fluctuating, which indicates that analog 2-*Pf*TopoVIB was more stable as compared to the other complexes.

We have calculated the binding free energy of each of the three complexes; *Pf*TopoVIB-analog 2, *Pf*TopoVIB-analog 6 and *Pf*TopoVIB-analog 7 at 10 ns intervals (0 ns, 10 ns, 20 ns, 30 ns, 40 ns, and 50 ns), as described in the 'Materials & Methods' section and it has been presented in Table 2. The negative values obtained for our analogs show that they have a tight binding with the receptor. The relative binding energy of analog 2 is the lowest indicating strongest among the studied complexes. A detailed flowchart for the steps of virtual screening carried out in our study is given in Figure 6.

The post-MD intermolecular interactions were monitored for the most stable complex, *Pf*TopoVIB-analog 2 (Figure 7). Majority of the contacts formed between the analog and protein residues in the docked complex were found to be retained after 50 ns MD simulation run. The residue Phe122 retained the interaction through halogen (Cl) and Phe105 retained the Pi-Pi T shaped hydrophobic interaction. Lys127 and Lys121 were found to maintain the carbon hydrogen bonds; Lys127 also had a hydrophobic pi-alkyl bond. Leu126 was found to interact with a pi-sigma and a pi-alkyl bond whereas Glu36 retained the two pi-anion interactions. The residues Asn40, Ala44, Lys104, Phe105 and Leu126 which showed strong interaction with Radicicol were found to interact well with analog 2 and retained their interactions post MD simulation as well. Though Lys113, Gly123, Val183 and Ile185 didn't interact, the residues Met32, Lys35, Asp39, Phe109, Ile124, Gly120, Gly125 and Lys127 retained their contacts with analog 2 during post MD simulation. The analysis of the interacting residues in post MD simulation suggests stronger binding thereby stabilizing the complex.

Discussion

Plasmodium falciparum possesses this unique type II topoisomerase TopoVIB, which acts as a novel target to treat malaria. Our previous studies have shown, Radicicol treatment inhibits the endoreduplication of the blood stage parasites, indicating a functional role of *Pf*TopoVIB at that stage. Endoreduplication occurs in two other stages of the parasite life cycle namely liver stage and mosquito stage (sexual stage), and *Pf*TopoVIB might be a critical determinant for those stages as well. Apart from its role in mitotic replication, it might be involved in meiotic recombination along with *Pf*TopoVIA, an ortholog of Spo11. Hence, finding a chemical inhibitor that has specificity towards *Pf*TopoVIB is the need of the hour. Our work shortlists one chemical structure out of 97 that predicts a stable exclusive binding with *Pf*TopoVIB.

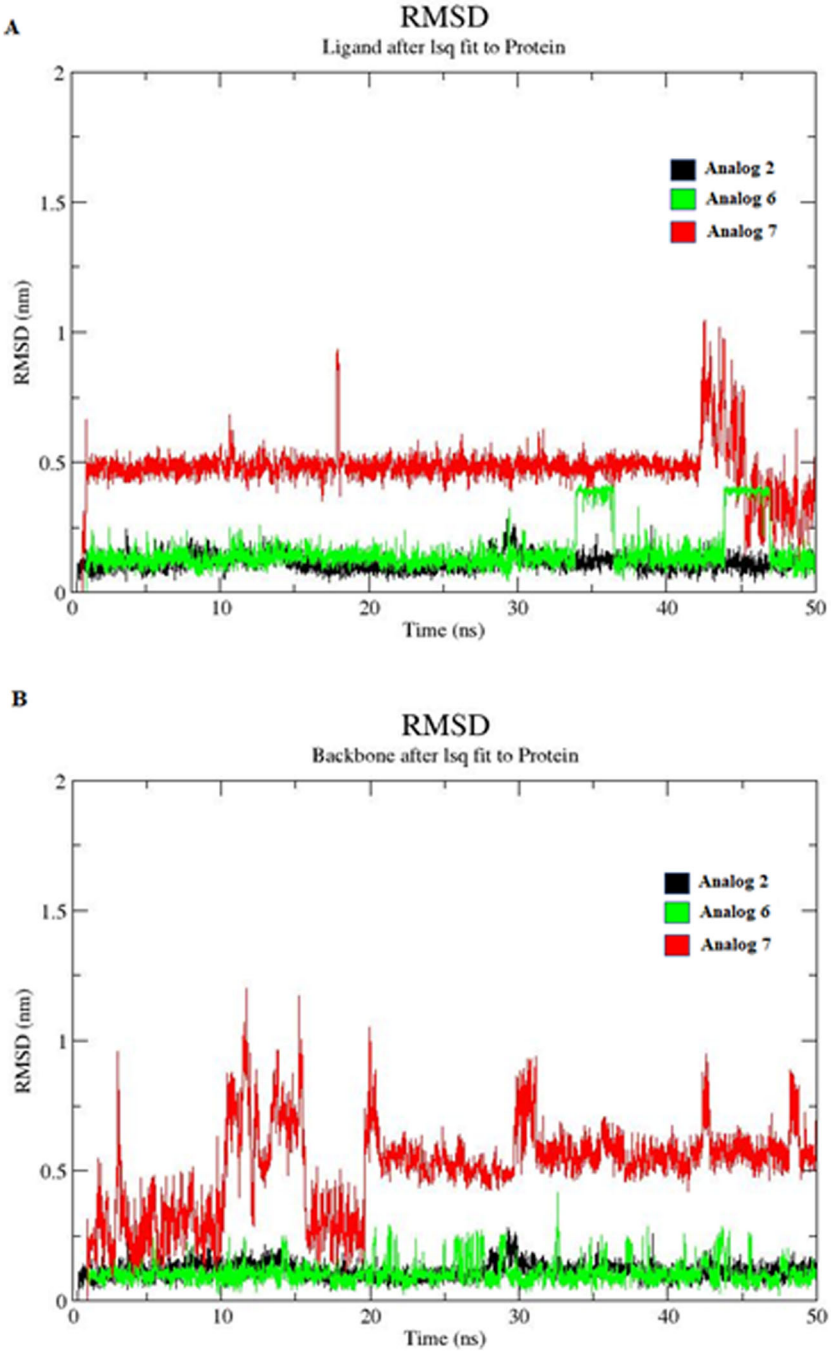

Figure 5. RMSD versus time plots for MD simulated complexes of *Pf*TopoVIB with the lead analogs: (A) RMSD versus time plots of Analog 2-*Pf*TopoVIB (black); Analog 6-*Pf*TopoVIB (green) and Analog 7-*Pf*TopoVIB (red) complexes during 50 ns simulation run. RMSD were plotted using alpha carbon atoms. (B) RMSD vs time plots of backbone of Analog 2-*Pf*TopoVIB (black), Analog 6-*Pf*TopoVIB (green) and Analog 7-*Pf*TopoVIB (red) complexes during 50 ns simulation run.

Table 2. The calculated energy parameters for each of the receptor-ligand complexes.

Ligand name	LibDock score	Binding free energy 0 ns (kcal/mol)	Binding free energy 10 ns (kcal/mol)	Binding free energy 20 ns (kcal/mol)	Binding free energy 30 ns (kcal/mol)	Binding free energy 40 ns (kcal/mol)	Binding free energy 50 ns (kcal/mol)
Analog 2	133.823	−11.5	−12.65	−13.01	−10.43	−12.96	−13.7
Analog 6	108.647	−9.59	−10.47	−11.23	−7.53	−9.89	−7.05
Analog 7	77.5334	−5.23	−3.67	−6.09	−5.97	−6.73	−4.63

In analog 2, the two hydroxyl groups present at the C-17 and C-19 position of Radicicol are substituted by two biphenyl groups and the resultant derivative is found to dock with *Pf*TopoVIB with more points of contact and hence found to score better than that of Radicicol. Free energy calculation and 50 ns molecular dynamics simulations indicate

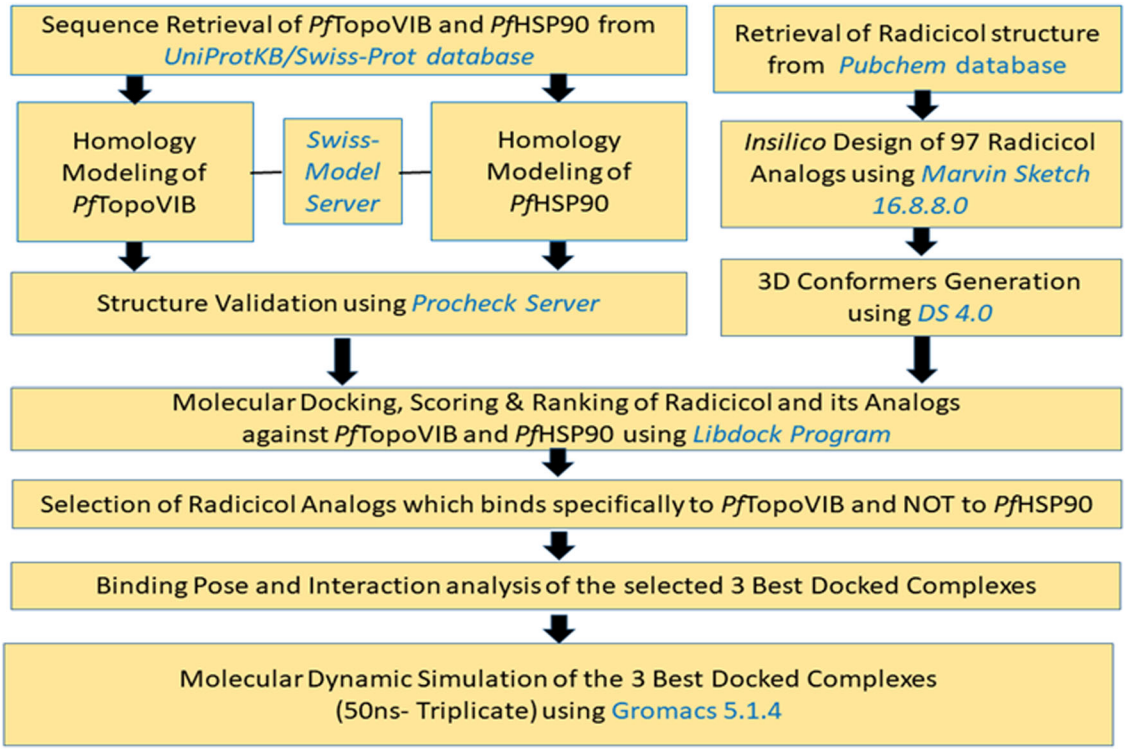

Figure 6. A detailed flowchart for the virtual screening steps.

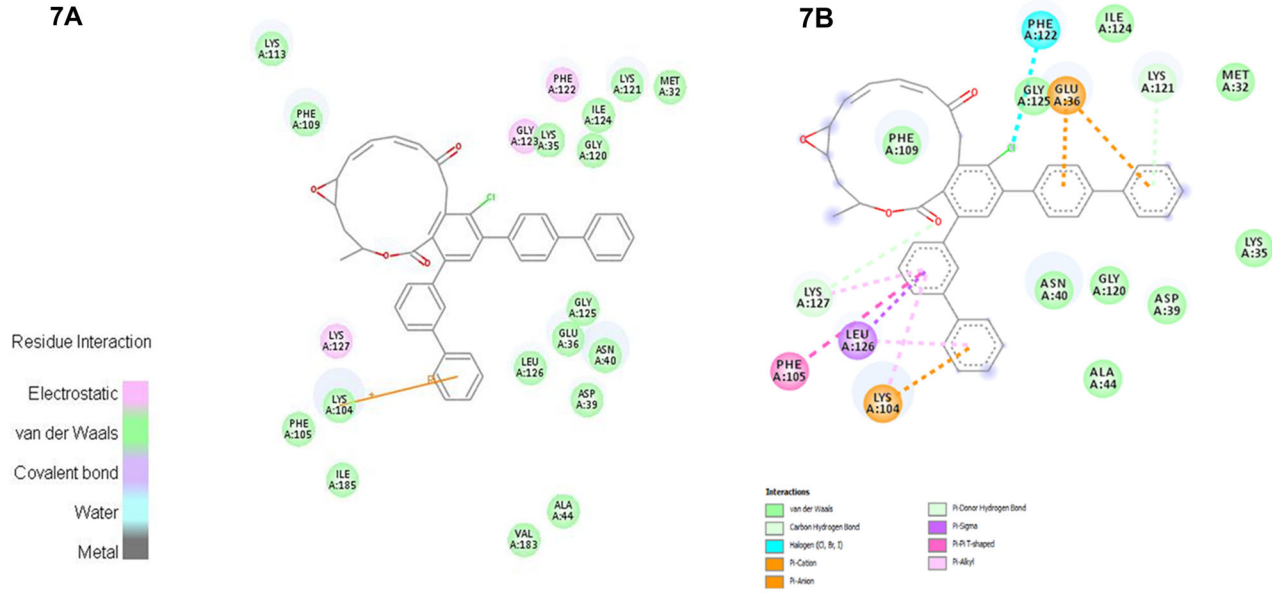

Figure 7. Comparison of 2-dimensional interaction diagrams of Analog 2 with *Pf*TopoVIB pre- and post-50 ns MD simulation run: (A) Analog 2 interacting with *Pf*TopoVIB before MD simulation; (B) Analog 2 interacting with *Pf*TopoVIB post 50 ns MD simulation; the essential amino acid residues at the Bergerat fold are tagged in circles. The purple circles show the amino acids which participate in hydrogen bonding, electrostatic or polar interactions and the green circles show the amino acids which participate in the van der Waals interactions, non-polar and others in grey.

that analog-2 forms a stable complex with *Pf*TopoVIB. Hence analog 2 urge future experimental validation in the biochemical assays of *Pf*TopoVIB and in the *Plasmodium* culture.

Acknowledgements

Our sincere gratitude to Ms. Devika Raj and Dr. Anand Krishnamurthy (Dassault Systemes, Chennai, India) for the support extended during simulation studies. The authors acknowledge the Campus Computing Facility (CCF) at the Central Laboratory for Instrumentation and Facilitation, University of Kerala for providing the HPC cluster facility to carry out this research work.

Disclosure statement

The authors of this paper declare that there is no conflict of interest.

Funding

The work was supported by the Department of Science and Engineering Research Board (DST-SERB), India [SERB/F/7827/2018-2019] to Sunanda Bhattacharyya. Ms. Shephali Bansod is supported by the Senior Research Fellowships from Council for Scientific and Industrial Research (CSIR), India. AR is a recipient of the SERB National Post-Doctoral Fellowship award (PDF/2017/001652) from Department of Science and Technology (DST), India.

References

Bairoch, A., & Apweiler, R. (1997). The SWISS-PROT protein sequence database: Its relevance to human molecular medical research. *Journal of Molecular Medicine (Berlin, Germany)*, *75*(5), 312–316.

Barghash, A., & Helms, V. (2013). Transferring functional annotations of membrane transporters on the basis of sequence similarity and sequence motifs. *BMC Bioinformatics*, *14*(1), 343. https://doi.org/10.1186/1471-2105-14-343

Bergerat, A., de Massy, B., Gadelle, D., Varoutas, P. C., Nicolas, A., & Forterre, P. (1997). An atypical topoisomerase II from Archaea with implications for meiotic recombination. *Nature*, *386*(6623), 414–417. https://doi.org/10.1038/386414a0

Berman, H. M., Westbrook, J., Feng, Z., Gilliland, G., Bhat, T. N., Weissig, H., Shindyalov, I. N., & Bourne, P. E. (2000). The protein data bank. *Nucleic Acids Research*, *28*(1), 235–242. https://doi.org/10.1093/nar/28.1.235

BIOVIA. (2019). *Dassault Systèmes, Discovery studio client 4.0*. Dassault Systèmes.

Chalapareddy, S. (2016). Radicicol-mediated inhibition of topoisomerase VIB-VIA activity of the human malaria parasite *Plasmodium falciparum*. *mSphere*, *1*(1), e00025-15.

Chalapareddy, S., Bhattacharyya, M. K., Mishra, S., & Bhattacharyya, S. (2014). Radicicol confers mid-schizont arrest by inhibiting mitochondrial replication in *Plasmodium falciparum*. *Antimicrobial Agents and Chemotherapy*, *58*(8), 4341–4352. https://doi.org/10.1128/AAC.02519-13

Chang, G. S., Hong, Y., Ko, K. D., Bhardwaj, G., Holmes, E. C., Patterson, R. L., & van Rossum, D. B. (2008). Phylogenetic profiles reveal evolutionary relationships within the "twilight zone" of sequence similarity. *Proceedings of the National Academy of Sciences*, *105*(36), 13474–13479. https://doi.org/10.1073/pnas.0803860105

Chung, S. Y., & Subbiah, S. (1996). A structural explanation for the twilight zone of protein sequence homology. *Structure*, *4*(10), 1123–1127. https://doi.org/10.1016/S0969-2126(96)00119-0

Colovos, C., & Yeates, T. O. (1993). Verification of protein structures: Patterns of nonbonded atomic interactions. *Protein Science*, *2*(9), 1511–1519. https://doi.org/10.1002/pro.5560020916

Corbett, K. D., & Berger, J. M. (2006). Structural basis for topoisomerase VI inhibition by the anti-Hsp90 drug radicicol. *Nucleic Acids Research*, *34*(15), 4269–4277. https://doi.org/10.1093/nar/gkl567

Diller, D. J., & Merz, K. M. Jr., (2001). High throughput docking for library design and library prioritization. *Proteins: Structure, Function, and Genetics*, *43*(2), 113–124. https://doi.org/10.1002/1097-0134(20010501)43:2<113::AID-PROT1023>3.0.CO;2-T

Doolittle, R. F. (1986). *Of Urfs and Orfs: Primer on how to analyze derived amino acid sequences*. University Science Books.

Dutta, R., & Inouye, M. (2000). GHKL, an emergent ATPase/kinase superfamily. *Trends in Biochemical Sciences*, *25*(1), 24–28. https://doi.org/10.1016/S0968-0004(99)01503-0

Dutton, B. L., Kitson, R. R. A., Parry-Morris, S., Roe, S. M., Prodromou, C., & Moody, C. J. (2014). Synthesis of macrolactam analogues of radicicol and their binding to heat shock protein Hsp90. *Organic & Biomolecular Chemistry*, *12*(8), 1328–1340. https://doi.org/10.1039/c3ob42211a

Guex, N., Peitsch, M. C., & Schwede, T. (2009). Automated comparative protein structure modeling with SWISS-MODEL and Swiss-PdbViewer: A historical perspective. *Electrophoresis*, *30 Suppl 1*, S162–S73. https://doi.org/10.1002/elps.200900140

Kim, S., Chen, J., Cheng, T., Gindulyte, A., He, J., He, S., Li, Q., Shoemaker, B. A., Thiessen, P. A., Yu, B., Zaslavsky, L., Zhang, J., & Bolton, E. E. (2019). PubChem 2019 update: Improved access to chemical data. *Nucleic Acids Research*, *47*(D1), D1102–D1109. https://doi.org/10.1093/nar/gky1033

Krammer, A., Kirchhoff, P. D., Jiang, X., Venkatachalam, C. M., & Waldman, M. (2005). LigScore: A novel scoring function for predicting binding affinities. *Journal of Molecular Graphics & Modelling*, *23*(5), 395–407. https://doi.org/10.1016/j.jmgm.2004.11.007

Laskowski, R. A., MacArthur, M. W., Moss, D. S., & Thornton, J. M. (1993). PROCHECK: A program to check the stereochemical quality of protein structures. *Journal of Applied Crystallography*, *26*(2), 283–291. https://doi.org/10.1107/S0021889892009944

Laurents, D. V., Subbiah, S., & Levitt, M. (1994). Different protein sequences can give rise to highly similar folds through different stabilizing interactions. *Protein Science*, *3*(11), 1938–1944. https://doi.org/10.1002/pro.5560031105

Lee, J., Cheng, X., Swails, J. M., Yeom, M. S., Eastman, P. K., Lemkul, J. A., Wei, S., Buckner, J., Jeong, J. C., Qi, Y., Jo, S., Pande, V. S., Case, D. A., Brooks, C. L., MacKerell, A. D., Klauda, J. B., & Im, W. (2016). CHARMM-GUI input generator for NAMD, GROMACS, AMBER, OpenMM, and CHARMM/OpenMM simulations using the CHARMM36 additive force field. *Journal of Chemical Theory and Computation*, *12*(1), 405–413. https://doi.org/10.1021/acs.jctc.5b00935

Lindahl, E., Hess, B., & van der Spoel, D. (2001). GROMACS 3.0: A package for molecular simulation and trajectory analysis. *Journal of Molecular Modeling*, *7*(8), 306–317. https://doi.org/10.1007/s008940100045

Mitscher, L. A. (2005). Bacterial topoisomerase inhibitors: Quinolone and pyridone antibacterial agents. *Chemical Reviews*, *105*(2), 559–592. https://doi.org/10.1021/cr030101q

Mudeppa, D. G., Kumar, S., Kokkonda, S., White, J., & Rathod, P. K. (2015). Topoisomerase II from human malaria parasites: Expression, purification, and selective inhibition. *The Journal of Biological Chemistry*, *290*(33), 20313–20324. https://doi.org/10.1074/jbc.M115.639039

Newman, D. J., & Cragg, G. M. (2016). Natural products as sources of new drugs from 1981 to 2014. *Journal of Natural Products*, *79*(3), 629–661. https://doi.org/10.1021/acs.jnatprod.5b01055

Pearl, L. H., Prodromou, C., & Workman, P. (2008). The Hsp90 molecular chaperone: An open and shut case for treatment. *The Biochemical Journal*, *410*(3), 439–453. https://doi.org/10.1042/BJ20071640

Rao, S. N., Head, M. S., Kulkarni, A., & LaLonde, J. M. (2007). Validation studies of the site-directed docking program LibDock. *Journal of Chemical Information and Modeling*, *47*(6), 2159–2171. https://doi.org/10.1021/ci6004299

Rost, B. (1999). Twilight zone of protein sequence alignments. *Protein Engineering*, *12*(2), 85–94. https://doi.org/10.1093/protein/12.2.85

Sander, C., & Schneider, R. (1991). Database of homology-derived protein structures and the structural meaning of sequence alignment. *Proteins*, *9*(1), 56–68. https://doi.org/10.1002/prot.340090107

Shinonaga, H., Noguchi, T., Ikeda, A., Aoki, M., Fujimoto, N., & Kawashima, A. (2009). Synthesis and structure-activity relationships of radicicol derivatives and WNT-5A expression inhibitory activity. *Bioorganic & Medicinal Chemistry*, *17*(13), 4622–4635. https://doi.org/10.1016/j.bmc.2009.04.060

Shiotsu, Y., Neckers, L. M., Wortman, I., An, W. G., Schulte, T. W., Soga, S., Murakata, C., Tamaoki, T., & Akinaga, S. (2000). Novel oxime derivatives of radicicol induce erythroid differentiation associated with preferential G(1) phase accumulation against chronic myelogenous leukemia cells through destabilization of Bcr-Abl with Hsp90 complex. *Blood*, *96*(6), 2284–2291. https://doi.org/10.1182/blood.V96.6.2284.h8002284_2284_2291

Smellie, A., Teig, S. L., & Towbin, P. (1995). Poling: Promoting conformational variation. *Journal of Computational Chemistry*, *16*(2), 171–187. https://doi.org/10.1002/jcc.540160205

Subbiah, S., Laurents, D. V., & Levitt, M. (1993). Structural similarity of DNA-binding domains of bacteriophage repressors and the globin core. *Current Biology: CB*, *3*(3), 141–148. https://doi.org/10.1016/0960-9822(93)90255-M

Teo, R. D., Dong, S. S., Gross, Z., Gray, H. B., & Goddard, W. A. (2015). Computational predictions of corroles as a class of Hsp90 inhibitors. *Molecular BioSystems*, *11*(11), 2907–2914. https://doi.org/10.1039/c5mb00352k

Tse, E. G., Korsik, M., & Todd, M. H. (2019). The past, present and future of anti-malarial medicines. *Malaria Journal*, *18*(1), 93. https://doi.org/10.1186/s12936-019-2724-z

Turbyville, T. J., Wijeratne, E. M. K., Liu, M. X., Burns, A. M., Seliga, C. J., Luevano, L. A., David, C. L., Faeth, S. H., Whitesell, L., & Gunatilaka, A. A. L. (2006). Search for Hsp90 inhibitors with potential anticancer activity: Isolation and SAR studies of radicicol and monocillin I from two plant-associated fungi of the Sonoran desert. *Journal of Natural Products*, *69*(2), 178–184. https://doi.org/10.1021/np058095b

Vale, V. V., Cruz, J. N., Viana, G. M. R., Póvoa, M. M., Brasil, D. d S. B., & Dolabela, M. F. (2020). Naphthoquinones isolated from *Eleutherine plicata* herb: In vitro antimalarial activity and molecular modeling to investigate their binding modes. *Medicinal Chemistry Research*, *29*(3), 487–494. https://doi.org/10.1007/s00044-019-02498-z

Van Der Spoel, D., Lindahl, E., Hess, B., Groenhof, G., Mark, A. E., & Berendsen, H. J. C. (2005). GROMACS: Fast, flexible, and free. *Journal of Computational Chemistry*, *26*(16), 1701–1718. https://doi.org/10.1002/jcc.20291

Van Gunsteren, W. F. (1996). *Biomolecular simulation: The GROMOS 96 manual and user guide*. VDF Hochschulverlag AG an der ETH Zürich Zürich. 1042 p.

Vanommeslaeghe, K., Hatcher, E., Acharya, C., Kundu, S., Zhong, S., Shim, J., Darian, E., Guvench, O., Lopes, P., Vorobyov, I., & Mackerell, A. D. (2010). CHARMM general force field: A force field for drug-like molecules compatible with the CHARMM all-atom additive biological force fields. *Journal of Computational Chemistry*, *31*(4), 671–690. https://doi.org/10.1002/jcc.21367

Venkatachalam, C. M., Jiang, X., Oldfield, T., & Waldman, M. (2003). LigandFit: A novel method for the shape-directed rapid docking of ligands to protein active sites. *Journal of Molecular Graphics & Modelling*, *21*(4), 289–307. https://doi.org/10.1016/S1093-3263(02)00164-X

Wang, S., Xu, Y., Maine, E. A., Wijeratne, E. M. K., Espinosa-Artiles, P., Gunatilaka, A. A. L., & Molnár, I. (2008). Functional characterization of the biosynthesis of radicicol, an Hsp90 inhibitor resorcylic acid lactone from Chaetomium chiversii. *Chemistry & Biology*, *15*(12), 1328–1338. https://doi.org/10.1016/j.chembiol.2008.10.006

Wang, Z., Wang, X., Li, Y., Lei, T., Wang, E., Li, D., Kang, Y., Zhu, F., & Hou, T. (2019). farPPI: A webserver for accurate prediction of protein-ligand binding structures for small-molecule PPI inhibitors by MM/PB(GB)SA methods. *Bioinformatics (Oxford, England)*, *35*(10), 1777–1779. https://doi.org/10.1093/bioinformatics/bty879

Widdowson, K., & Hennessy, A. (2010). Advances in structure-based drug design of novel bacterial topoisomerase inhibitors. *Future Medicinal Chemistry*, *2*(11), 1619–1622. https://doi.org/10.4155/fmc.10.250

Yang, A. S., & Honig, B. (2000). An integrated approach to the analysis and modeling of protein sequences and structures. III. A comparative study of sequence conservation in protein structural families using multiple structural alignments. *Journal of Molecular Biology*, *301*(3), 691–711. https://doi.org/10.1006/jmbi.2000.3975